Thermal Wave Inverse Problems: Depth Profilometry of Hardened Steels and Diffraction Tomography of Sub-Surface Defects in Metals

by

Lena Nicolaides

A thesis submitted in conformity with the requirements
for the degree of Doctor of Philosophy
Graduate Department of Mechanical and Industrial Engineering
University of Toronto

National Library
of Canada

Acquisitions and
Bibliographic Services

395 Wellington Street
Ottawa ON K1A 0N4
Canada

Bibliothèque nationale
du Canada

Acquisitions et
services bibliographiques

395, rue Wellington
Ottawa ON K1A 0N4
Canada

Your file Votre référence

Our file Notre référence

0-612-53793-5

Thermal wave inverse problems: Depth profilometry of hardened steels and
diffraction tomography of subsurface defects in metals

by Lena Nicolaides

Doctor of Philosophy, 2000
Department of Mechanical and Industrial Engineering
University of Toronto

Abstract

Depth profilometry of hardened steels and Thermal-wave Slice Diffraction Tomography (TSDT) of sub-surface defects in metals are important thermal wave inverse problems. The imaging parameters in thermal wave inverse problems are the material thermal inhomogeneities.

Depth profilometry is an inverse problem that retrieves thermal diffusivity along the depth of a sample. It is well established that in hardened steels thermal diffusivity anticorrelates with microhardness, allowing depth profilometry to be used as a tool to measure microhardness. Depth profilometry also has the unique advantage, over conventional methods, of being non-destructive. Current techniques have not separately addressed the effects of different heat treatments on the thermal diffusivity profile of steels, and therefore, the exact nature of the anticorrelation between thermal diffusivity and microhardness is not properly understood. Carburizing and quenching are widely used for the heat treatment of industrial steel, and it is important to understand their effects on thermal diffusivity profiles. This thesis presents a thorough examination of the actual mechanism by which thermal diffusivity depth profiles are affected by first carburizing and then quenching. The common process in both these heat treatments is the diffusion of carbon. Two novel observations are made: first, it is found that the shape of the thermal diffusivity profile is dominated by carbon diffusion, and second, the absolute thermal diffusivity is a function of microstructure. Furthermore, a novel method of accounting for surface roughness of the samples is developed, which models roughness as white noise of random spatial distribution in the frequency domain. This extends the suitability of depth profilometry to industrial applications.

Thermal-wave Slice Diffraction Tomography (TSDT) is a photothermal imaging technique for non-destructive detection of sub-surface cross-sectional defects in opaque solids in the very-near-surface region (μm-mm). Conventional reconstructions of the well-posed propagating wave-field tomographies cannot be applied to the ill-posed thermal wave problem. A regularization method, such as Tikhonov regularization, is used to invert the almost singular matrices resulting from the ill-posedness of the inverse thermal wave problem. Multiplicity of solutions, which is inherent to ill-posed problems, is resolved by adopting the L-curve method for optimization. For tomographic imaging of sub-surface defects, a new high-resolution radiometric setup is constructed, which reduces the broadening of images associated with previous low-resolution setups.

In summary, two important thermal-wave problems, namely, the depth profilometry and diffraction tomography, were studied in this work. Several improvements to existing methods were implemented, making them attractive for industrial applications.

Acknowledgments

Thank you God for giving me the ability and strength to complete this work.

In my graduate work I was very fortunate to have Professor Andreas Mandelis as my supervisor. His guidance and support throughout my thesis research have made a profound difference in my scientific career. He has been my *father of science* and his never ending devotion to research has been an inspiration.

I would like to thank Dr. C. Beingessner and S. Ghai for their metallurgical insight and also for the heat treatment of the samples; Dr. D. Rose for kindly sending the silicon nitride sample; Prof. Mostaghimi and Dr. L. Pershin for the usage of the surformeter. Also, I would like to thank Prof. Eric Miller for the discussions on inverse problems.

Through the years, many researchers came through the photothermal lab and I would like to thank them all for the scientific discussions and their friendship. Especially, I would like to mention M. Munidasa, F. Funak, A. Salnick, J. Garcia, M. Rodriguez, and S. Paoloni. I would like to thank my student Yan Chen for all her help and my friends Sujata, Maha, Audrey, Ghada and Jennifer for their invaluable support.

Finally, I acknowledge the exceptional support of my parents, brother and sister that made this work possible. I would especially like to thank Michael, for his unselfish devotion to my dream.

Table of Contents

Nomenclature

$\mathbf{A}$	Complex matrix
c	Specific heat
F	Object function
f	Modulation frequency
G	Green function
I	Incident optical irradiance
k	Thermal conductivity
q	Complex wave number
R	Thermal wave reflection coefficient
S	Surface
T	Spatial temperature
V	Volume
w	Beam size radius
α	Thermal diffusivity
λ	Thermal wavelength
μ	Thermal diffusion length
ν	Phase
ρ	Mass density
σ	Regularization parameter
ϕ	Thermal wave flux
ω	Angular frequency
A-R	Anti-Reflecting
AOM	Acousto-Optic Modulator
SNR	Signal-to-Noise Ratio
TSDT	Thermal wave Slice Diffraction Tomography
WKBJ	Wentzel-Kramers-Brillouin-Jeffreys
a.u	Arbitrary Units
AC	Alternating Current

List of Figures

Figure:

List of Tables

Table:

Chapter 1

Introduction to Thermal-Wave Inverse problems

1.1 History

Photothermal methods involve generating and propagating heat by absorbing modulated radiation. These methods date back to as early as 1880 when Alexander Graham Bell [1] invented the "photophone". This device converted sound waves into a modulating beam of light, transmitted the light through the air, and reconverted the light into sound waves at the receiving end. The transmission was performed in open air which often blocked and scattered the lightwaves, causing Bell to eventually abandon the idea of the photophone. The principle of the photophone was only redeveloped as late as 1976 with the Rosencwaig and Gersho theory [2,3], which described the photoacoustic effect. Their theory resulted in the birth of photothermal detection methods. Today, there are numerous photothermal detection schemes applied to a variety of applications. It has been said by photothermal scientists that the photothermal principle is a solution in search of a problem.

1.2 Thermal Wave Forward Theory

1.2.1 One-Dimensional Formulation

When an energy source is focused onto the surface of an opaque solid material, the material will absorb some of the incident energy. This will, in turn, produce a localized heat flow in the material followed by a non-radiative de-excitation process [4]. If this energy source is modulated, a periodic heat flow is produced in the material. The resulting periodic heat flow in the material is a *diffusive* process that produces a periodic temperature distribution called a *thermal wave* (Figure 1.1).

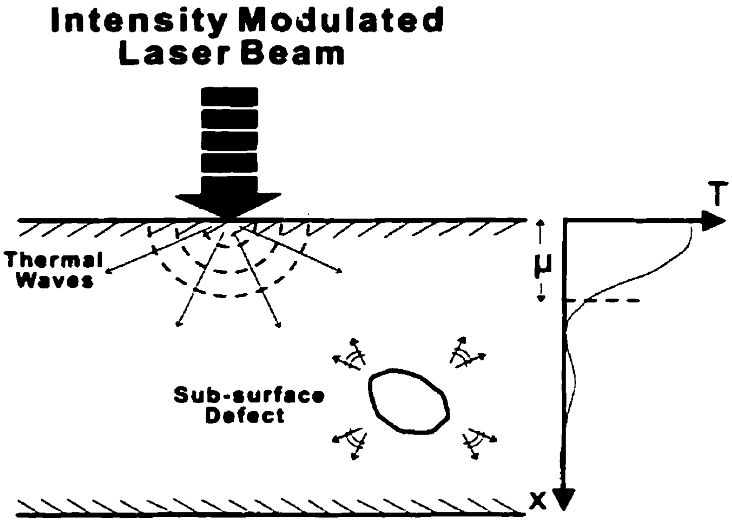

Figure 1.1 Schematic picture of periodic heat diffusion in an opaque solid.

The characteristics of a thermal wave and its behavior can be understood by considering the simplest geometry. Time-dependent heat flow is governed by the one-dimensional heat diffusion equation [5],

$$\kappa \frac{\partial^2}{\partial x^2} T(x,t) = \rho c \frac{\partial T(x,t)}{\partial t} \tag{1.1}$$

where T is the temperature excursion from the equilibrium, ρ, c and k are the mass density, specific heat and thermal conductivity of the medium, respectively. The temperature excursion T, is generated by a periodic source, represented by $e^{-i\omega t}$, where ω is the angular frequency of the heat source. Equation (1.1) can be written in the form of a pseudo-wave Helmholz equation by using a Fourier transformation as follows,

$$\frac{d^2}{dx^2}T(x,\omega)-q^2T(x,\omega)=0 \tag{1.2}$$

where q is the complex wave number,

$$q=\frac{1+i}{\mu}, \tag{1.3a}$$

and μ is the thermal diffusion length also referred to as the damping constant, and is equal to the wavelength of the wave, λ_{th}, divided by 2π.

$$\mu=\frac{\lambda_{th}}{2\pi}=\sqrt{\frac{a}{\pi f_c}} \tag{1.3b}$$

$$\text{with } a=\frac{\kappa}{\rho c} \tag{1.3c}$$

where α is the thermal diffusivity and gives a measure of the rate of heat propagation in a material and f_c is the modulating frequency. Equation (1.2) can be solved to obtain the one-dimensional thermal wave response in a uniform, homogeneous, isotropic material, propagating in the positive x-direction [5] as

$$T(x,t) = T_0 \exp(i(qx - \omega t)), \tag{1.4}$$

where T_0 is the surface temperature produced by the source. Thermal waves are heavily damped, as can be seen by equation (1.4) which shows a decay in the amplitude of a thermal wave with distance from the surface of the material. Equation (1.4) also shows that the penetration depth can change by altering the modulation frequency. For low frequencies, a deep penetration is observed, and for high frequencies, a shallow penetration is observed [6].

Another interesting property of thermal waves is that they are thought to "reflect" between media of different thermal characteristics. The thermal wave reflection coefficient R, for the interface between medium 1 (bulk) and 2 (air) is given by [7]

$$R_{21} = \frac{1 - b_{21}}{1 + b_{21}} \tag{1.5}$$

where

$$b_{21} = \sqrt{\frac{(\rho c \kappa)_2}{(\rho c \kappa)_1}} = \sqrt{\frac{e_2}{e_1}} \tag{1.6}$$

and, e_2 and e_1 are the thermal effusivities of media 2 and 1, respectively. The thermal effusivity is the preferred property when referring to thermal boundaries.

It is important to note that in reality thermal waves *do not reflect* as rays do in optical fields. However, the fact that the thermal wave interface can be mathematically modeled using a reflection coefficient has led to the misconception in the photothermal community that thermal waves actually reflect [8]. Such modeling [9] has evolved merely for mathematical convenience and it has also been reinforced by strong agreement between theory and experiment. The existence of reflection phenomenon in thermal waves was first explained by Shen and Mandelis [10]. Mandelis argued, that according to Fourier's law of heat conduction,

$$\boldsymbol{F}(\boldsymbol{r},t) = -k\nabla T(\boldsymbol{r},t), \tag{1.7}$$

where $\boldsymbol{F}$ is the thermal flux, T is temperature, and k is the thermal conductivity of the material, conduction heat transfer is unidirectional and only activated by existing temperature gradients that generate net heat fluxes in appropriate directions of a material. Therefore, unlike conventional propagating wave fields, thermal waves cannot sustain reflections at boundaries where thermophysical properties change abruptly. Instead the rate of forward propagation at the boundary increases ($e_2 > e_1$) or decreases ($e_2 < e_1$) according to the thermal properties of the boundary. Mandelis further explained [11] that the diffusion equation is a parabolic (i.e., first-order in time) rather than hyperbolic (i.e., second-order in time) differential equation. Propagating waves such as sound waves are represented by a hyperbolic differential equation. In the hyperbolic differential equation, which has two characteristic curves (squared-law), both forward and backward propagation are supported. This is significant, since a parabolic differential equation has only one characteristic curve (linear-law) and thus cannot support backward propagation. Strictly speaking, the terminology of "reflection" and "refraction" at interfaces is inaccurate in the context of thermal waves. Mandelis correctly defined two new terms, namely, thermal-energy accumulation (forward flux decrease), and thermal-energy depletion (forward flux increase) for heat diffusion waves. In summary, thermal wave reflections at interfaces are not physically possible because of the unidirectional (thermal gradient driven) and non-squared-law nature of thermal diffusion waves.

1.2.2 Experimental Methods

1.2.2.1 Thermal Wave Imaging

A basic application of the photothermal principle is thermal wave imaging, which is a technique used to uncover sub-surface defects of opaque solids. The imaging can be achieved using intensity-modulated heat sources such as lasers or particle beams and detectors such as microphones, ultrasonic transducers, infrared detectors and laser probes [12]. The first evidence that thermal waves could be used in imaging was given by Wong et al. [13] in 1978, who later developed a new imaging technique called Scanning Photoacoustic Microscopy (SPAM) [14]. In this technique, a modulated heat source scanned the surface of the sample, producing heat at each point that was then detected by a photoacoustic cell.

The basic ingredients for a thermal microscope include a source of energy, a physical scatterer, and a detector of the radiation scattered [12]. A convenient source of energy is the laser beam, which can be easily modulated and focused to yield a coherent localized energy source. The physical scatterer is the sub-surface defect object. For an image to be formed, either the source of energy or the detector must be localized. Thermal wave imaging generally involves the use of a localized source. The contrast in thermal wave images is controlled by scatterers located within a fraction of a thermal wavelength away from the source. Thus, when the thermal wavelength is varied, the region of the specimen that contributes to the image also changes. The heavily damped nature of thermal waves makes them well-suited to the non-destructive evaluation of near sub-surface defects in opaque solids, ranging from a few micrometers to several millimeters.

Moreover, due to their heavily damped nature, thermal waves can achieve resolutions much higher than those possible with a conventional microscope. The maximum resolution of a conventional microscope is diffraction-limited. This means that the resolution is roughly equal to the wavelength of light used. The diffraction limit is derived for the far-field (Fraunhofer) diffraction approximations, which assume a large distance between the source and observation point. Since thermal waves operate in the extreme-near-field limit (i.e., distances of the order or smaller than the wavelength), the thermal wavelength does not become the limiting factor of resolution [15], making it possible to achieve much higher resolutions. The resolution can also be increased with increasing frequency, however an increased frequency is accompanied by a low signal-to-noise ratio (SNR). Therefore, it is important to seek a compromise between resolution and SNR. In addition, the resolution of a thermal microscope also depends on several other parameters, the most important being the beam spot size. If the beam spot is not smaller than the defect, the image will broaden [15].

Thermal wave microscopes come in several different forms, each with associated advantages and disadvantages, depending on the nature of the source and the detector. As mentioned before, all thermal microscopes have a localized heat source, but differ in that the detectors may be local or non local to a greater or lesser degree. For example, the focused infrared detector is a local point temperature detector; the collinear mirage-effect laser probe is a line detector; and the microphone maybe an area detector [12]. The most prominent of these thermal wave detection methods are described briefly below.

1.2.2.2 Thermal Wave Detection Techniques

a) *Photoacoustic gas-cell detection*

Photoacoustic gas-cell detection [13-14,16-22] is historically the earliest method, and uses a microphone to detect the pressure variations in a volume of gas enclosed in a cell, while a focused modulated laser beam is scanned over the surface of the sample. The technique can be thought of as imaging with a point source and an area detector. An advantage of this technique is that it lends itself readily to theoretical analysis. This is due to the planar symmetry of the detection scheme, which allows the use of plane-wave scattering theory [22]. This symmetry, unfortunately, precludes the detection of closed vertical cracks [12]. It is, however, applicable to detection of complex shapes, since the cell can be designed to fit the sample. A serious disadvantage of the photoacoustic gas-cell detection method is that the sample must be enclosed in an airtight cell. Therefore, it is essentially a contact method. It is also a destructive method due to sample dimension limitations. A further disadvantage is that the frequency range is limited by the audio response range of the microphone, which is about 10kHz.

b) Piezoelectric detection

Piezoelectric detection [23-26] monitors the modulated thermal expansion of a sample by attaching a piezoelectric solid to it. The modulating laser beam generates thermo-elastic waves that propagate through the sample. These waves are picked up by the piezoelectric detector and are converted into a measurable voltage [23]. This technique measures both thermal and acoustic expansions of the material. Most piezoelectric detection systems use an optical beam scanning method in which the laser scans the sample. An advantage of the method is that a wide range of frequencies is allowed. There are two major difficulties with this method. First, the detector must be physically bonded to the sample without affecting the quality of the sample and second the acoustic and thermal modes must be deconvoluted.

c) Pyroelectric detection

In pyroelectric detection [27,28], a temperature modulation can be converted directly into an electric signal by use of the pyroelectric effect [27]. This technique consists of using a thin pyroelectric film in direct contact with a solid sample on which a modulated monochromatic light beam is incident. Following the absorption of the incident light, the temperature of the sample fluctuates and, through heat diffusion, the temperature at the sample-pyroelectric film interface fluctuates. As a result of this temperature fluctuation, a pyroelectric signal proportional to the temperature change in the film is produced. The first pyroelectric thermal wave image was obtained by Baumann et al. [29]. An advantage of pyroelectric detection is that it needs very little incident laser power (~mW) because it senses the sample back-surface temperature directly. In recent years, pyroelectric detection has been used as a non-contact technique [10].

d) Optical beam deflection (Mirage) method

The optical beam deflection technique otherwise known as Mirage detection was first introduced by Boccara et al. [30]. This technique avoids the difficulties that arise from sample-detector contact. The method uses a laser probe for detection and, is therefore a line detector method. The modulated heating of the sample produces a periodic heating of the gas (air) adjacent to the sample causing a periodic variation in the index of refraction of the gas [4]. The change in the refractive index of the air deflects the probe laser, which is measured by a position sensitive optical detector [31]. The optical beam deflection technique is a non-contact method and can operate over a wide frequency range. A disadvantage of this technique is the practical difficulty of maintaining two laser positions (pump and probe), and especially when controlling the height of the probe beam during a scan [12]. The requirement that the sample must have a flat or cylindrical surface further limits the method.

e) Photothermal radiometric detection (PTR)

In photothermal radiometric detection, [32-35] variations in the local surface temperature are measured with a focused infrared detector. The first method based on the infrared emission from the specimen was described by Nordal and Kanstad [32]. The source is a modulated laser beam focused on the surface. The thermal microscope consists of a point source and a point detector, providing one of the highest resolution methods in the extreme-near-field. Photothermal radiometric imaging was demonstrated by Busse [33] using a Golay infrared detector. The method was later extended by Busse and Renk [35] for stereoscopic depth localization of sub-surface defects using a combination of localized heating and detection. An advantage of this technique is that it does not depend on heat flow into air. The analysis is not complicated by the presence of air, which may cause phase delays and signal magnitude changes. However, variations in surface emissivity can obscure the amplitude of the thermal wave image. Photothermal radiometric detection is the experimental method that was chosen in this work to be used for the frequency scanning and cross-sectional imaging of a sample, as described in chapters 4 and 7, respectively.

1.3 Thermal Wave Inverse Theory

In the preceding sections, the thermal wave forward theory was described as a method for obtaining experimental data which when combined with a theoretical model can be used to describe the behavior of thermal waves. This can be referred to as the *forward process*. The simplest application of a forward process is the determination of thermal diffusivity of a homogeneous material. The process involves experimentally obtaining the surface temperature distribution and fitting a theoretical formulation to the experimental "forward" data. The fitting parameter directly yields the homogenous thermal diffusivity. However, there exists another class of problems where the required variable cannot be directly obtained by forward fitting. An example would be a material with near-surface inhomogeneities or subsurface defects. In such cases, a numerical technique is required to invert or reconstruct the sought parameter from the forward process. This can be referred to as the *inverse process*. It is important to note that the thermal wave inverse problem is an ill-posed problem in that small perturbations in data can lead to large artifacts in the reconstruction. This is unlike the well-posed propagation wave field problems where conventional reconstructions can be applied. To solve the ill-posed thermal problem, regularization procedures such as Tikhonov regularization are used. This is explained in detail in Chapter 7.

In recent years, rapid advances in computer hardware and software have led to an increase interest in solving thermal wave inverse problems. There are two main types of thermal inhomogeneities ideal for inverse problem implementation (Figure 1.2). The first is a continuously varying thermal inhomogeneity (known as Type A), and the second is a thermal sub-surface defect (known as Type B). In the case of continuously inhomogeneous materials, the goal is to reconstruct the thermal diffusivity (conductivity) profiles. The point of interest with a sub-surface defect is the identification of the exact location and shape of the defect at a cross-section. The continuously thermal inhomogeneous problem can be treated using a one-dimensional geometry, whereas the sub-surface defect problem requires a three-dimensional geometry. In this study, two thermal wave inverse problems as applied to opaque materials will be investigated in the frequency-domain. The first problem is a one-dimensional depth profilometric problem (Type A), and the second problem is a three-dimensional thermal wave diffraction tomography problem (Type B). A review of these problems is presented in the following sections.

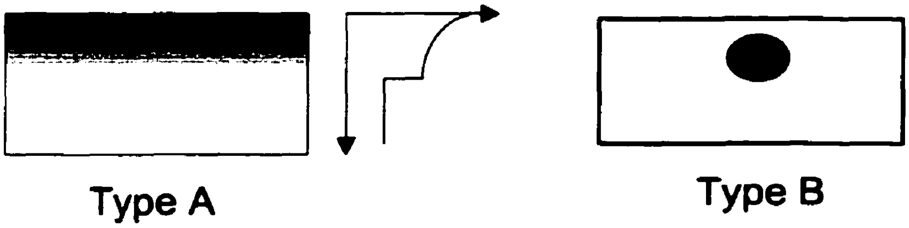

Figure 1.2

	Thermal Inhomogeneities	Inverse Problem
Type A	continuously inhomogeneous	1-D (depth profilometry)
Type B	sub-surface defect	3-D (thermal wave tomography)

1.3.1 Depth Profilometry

Depth profilometry (Type A inverse problem) is an important inverse problem where the thermal diffusivity profile is inverted from the experimental surface information. Thermal diffusivity is a property that depends on the microstructural properties of a material and can thus be used to identify changes that take place in a material as a result of surface modification processes, such as, laser processing, case hardening, and coating deposition. For determining the metallurgical properties of case treated materials, depth profilometry offers an important advantage over existing techniques by being a non-destructive method.

With inhomogeneous materials, the photothermal amplitude and phase signal channels carry information about any heat transport disruption or change below the surface. These changes must be interpreted with appropriate models, in order to yield reliable reconstructions of the spatially variant thermal diffusivity of a sample. A good review dating up to 1996 on the depth profilometric problem was composed by Mandelis et al. [36] and is summarized below. The first attempt to study the properties of surface hardened steel in terms of an inverse process was made by Jaarinen and Luukkala [37], who developed a numerical technique based on the solution of the thermal-wave equation using a two-dimensional finite difference grid. A theoretical formulation of the depth profilometric problem was first described by Vidberg et al. [38]. The authors measured the radial variation of the surface temperature of a heated point at a single modulation frequency. The thermal conductivity and heat capacity profiles were reconstructed using Pade approximants for the inversion of spatial Laplace transforms. The model was only valid for nonconventional experimental geometries and the reconstructed profiles were not always numerically reliable. In a later publication [39], the well-known Hamilton-Jacobi formalism from Classical Mechanics was introduced into the thermal-wave problem by treating the AC temperature field as a Thermal Harmonic Oscillator (THO) [40] and inverting the amplitude and phase of the experimental data by matching it to explicit theoretical expressions for a semi-infinite material. Experimental inversions were obtained for a liquid crystal octylcyanobiphenyl (8CB) [41] using this method with a WKBJ type approximation. Further inversions with semi-infinite laser-processed solids were reported later [42,43]. The method was very sensitive to the presence of experimental noise and was not valid in all physical limiting cases. An inversion procedure for a finite thickness problem has also been reported based on the same THO approach [40]. Glorieux et al. [44], then proposed a model that assumed locally constant or linearly-dependent thermal conductivity on depth where the solid was divided up into a virtual incremental discrete-layer system and, in each layer, forward and reverse thermal-wave equations were set up for constant conductivity. The theory presents problems with the treatment of finite-thickness materials, since it ignores the multiple inter-reflections of the thermal wave between the two boundaries (surfaces) of the material. Fivez and Thoen reported yet another version [45] of the foregoing inversion problem with a linear dependence of the local (incremental) thermal conductivity with depth. Explicit expressions were derived and matched with experimental data, and the results of the inversions were in agreement with those obtained by Ma et al. [42]. The major disadvantage of this approach is its inability to treat semi-infinite solids, since the explicit formulas depend on the boundedness of the derived Bessel and Neumann functions. Instead, the approach requires flat profiles in the bulk of the material under investigation. This is because several combinations of these functions utilized in this approach become infinite in value as the depth increases without bound. A theoretical approach by Lan et al. [46] combines the approaches of both prior papers [44,45]. In this paper, a mirror anticorrelation was found between thermal diffusivity and quenched steels. The method has improved strengths from Ref. [44,45], but it is subject to some combination shortcomings: a flat profile of the thermal conductivity at large distances [47] (i.e., at "infinity") to induce boundedness, and the lack of a theoretical basis to treat multiple thermal-wave reflections from the opposite surfaces of finitely-thick samples. In a theoretical paper [48], Fivez and Thoen presented a new analytical approach to the inverse problem that is valid for semi-infinite solids at sufficiently high frequencies, but shows significant deviations of reconstructed thermophysical profiles from the expected values at low frequencies (equivalent to large depths in a sample).

A good overview of one-dimensional ill-posed inverse problems was given by Power and Prystay [49]. The authors introduced the expectation-minimum principle as a robust method of recovery of the heat flux profile. In a companion paper Power and Prystay [50] found that the expectation-minimum principle had an improved resolution over the zero-order Tikhonov regularization. A different approach was developed by Glorieux and Thoen [51] using neural networks, in which the reconstruction was obtained by observation of the signal and thus on a 'learning' relation between profile-signal examples. The accuracy of such a method depends on the training of the neural network. Mandelis et al. [36] further formulated a complete generalized expression for the thermal-wave field in an inhomogeneous bounded solid. The method improved on the previously derived formulas based on the THO approach [39,42,52] by ensuring proper convergence to limiting cases. Another numerical methodology was developed by Aleshin and Vysloush [53] who attempted to develop a general inverse problem-solving algorithm with the use of Tikhonov regularization. A method by Kolarov and Velinov [54] developed the depth profilometric problem based on the Riccati first-order differential equation. A numerical method was presented to solve the general Riccati equation in real time. In this formulation, in the limit of infinitesimally thin layers, the recursion used in most works is replaced by a non-linear Ricatti equation. LiVoti et al. [55] also developed a similar formulation using a Singular-Value-Decomposition (SVD) regularized inversion method. Xu et al. [56] presented a regularized chi-square minimization technique. Munidasa et al. [57] applied the THO method [36] on quenched steels and found an anticorrelation between thermal diffusivity and microhardness. However, no explanation was given on the thermal diffusivity mechanism. This was a preliminary study which tested the technique under laboratory conditions. Although the samples used were rough, the roughness response on the experimental data was neglected.

Walther and Aleshin [58] developed a method which combines laterally-scanned and frequency-resolved measurements for the inspection of inhomogeneous samples by making use of a Tikhonov stabilizer function. A lateral scan can be rigorous, experimentally increasing the ill-posedness of the problem since more dimensions are introduced. Miller et al. [59] recently introduced a numerical reconstruction method based on an adaptive multi-scale algorithm with no approximations to the heat diffusion equation. An exact physical model is used which allows the profile reconstruction process to be formulated as a non-linear inverse scattering problem. The method is currently being tested on experimental data. In summary, the depth profilometric methods described above can be divided into three main categories: 1) reconstructing the profile using a slicing methodology or WKBJ type approximation with minimization methods, 2) using a matrix-based formulation and reconstructing in terms of regularization (Expectation Minimum, Tikhonov, SVD), and 3) neural network methods which do not require analytical formulation for the forward problem.

1.3.2 Thermal Wave Slice Diffraction Tomography

Thermal Wave Slice Diffraction Tomography (TSDT) (Type B inverse problem), is a photothermal imaging technique for Non-Destructive Evaluation (NDE), leading to the detection of sub-surface cross-sectional defects in opaque solids in the very-near-surface region (μm-mm). Thermal wave tomography refers to cross-sectional imaging of an object upon reconstruction from its projections from different directions. This calls for an inversion technique which can reconstruct the thermal defect from experimental cross-sectional data. Images obtained by thermal wave imaging are two-dimensional "projections" of sub-surface features. These images are projections in the sense that they are formed by mapping the sample surface temperature in a two-dimensional raster without regard to the actual depth position of scatterers. Although work has been done in obtaining depth information on sub-surface features [35,60] and depth profiling of layered samples using equivalent experimental techniques, no studies have been reported until recently about obtaining tomographic images using thermal waves. A photothermal method based on the mirage effect was utilized to obtain depth information of defects using a tomographic like procedure [61]. However, due to the line-integral nature of the probe beam, this technique did not yield proper tomographic imaging.

The first rigorous implementation of TSDT detected scan data by photopyroelectric detection [62], followed by reconstruction using an algorithm based on the ray-like propagation of thermal waves [63,64]. The instrumentation involved attaching a thin pyroelectric film to the back of a sample with a remote metal tip detection geometry. Since both the modulated heating source and detector were localized, they were scanned independently to perform a limited angle tomographic scan. A reconstruction method based on the ray-like propagation of thermal wave in one-dimension calculated average values of thermal diffusivity using phase data. Each imaged cross-section was divided into rectangular pixels and thermal diffusivity values for individual pixels were calculated. All the reconstructed images showed an extensive elongation of the defect cross-section along the vertical direction. The limitations of this method suggested that a diffractive propagation procedure be considered for thermal waves.

A high-fidelity ray-based tomographic imaging reconstruction method for photopyroelectric thermal detection was later demonstrated by Yarai et al. [65]. The experimental method improved on the scan data resolution from the previous works [63,64]. High signal-to-noise ratio detection and resolution were possible by using a film of high pyroelectric coefficient, a very-high-power laser diode and a very-small diameter metal probe tip. The bypass transmission ratio of a thermal wave was calculated between every laser and probe tip position along the defect by using the detected phase signal. The cross-sectional area to be imaged was divided into a picture pixel matrix. Every pixel was classified into "1" or "0" according to summed values of the bypass transmission ratio; a larger value than a certain threshold level was classified as "1". The reconstruction technique presented by Yarai et al. was not necessarily a better technique than the previous one discussed here. Classification of pixels into "1" and "0" increased image contrast, but it did not indicate the true sample shape. This method also suffered from the assumption of ray-like-propagation.

Unlike electromagnetic or acoustic tomography, thermal wave tomography suffers from two drawbacks. First, propagation distances of the thermal wave are short, and second the thermal wave vector is complex, lying along the 45° line in the complex plane [66]. Therefore, the conventional reconstruction used in well-posed propagating wave-field tomographies [67] cannot be applied to the thermal wave problem. To overcome the limitations of a ray optic tomographic reconstruction, Pade and Mandelis [68,69] developed a method taking into account the diffractive and heavily damped nature of thermal waves. The problem approximated the wave field with the two-dimensional Green function and used Tikhonov regularization to deal with the ill-conditioning of thermal waves. The limitation of this method was that it only addressed the physical behavior of thermal waves approximately. The technique, however resulted in adequate reconstructions of cross-sections away from the incident laser source where a strong singularity was pronounced. To avoid the strong two-dimensional singularity at the origin, a three-dimensional formulation of the problem was needed. More recently, Nicolaides and Mandelis [70] implemented a rigorous mathematical model representing the behavior of three-dimensional thermal waves. The method was based on a theoretical expression of Green function for the three-dimensional Helmholtz pseudowave equation [71]. A major limitation of the above work was that an optimization procedure was not implemented to overcome the problem of multiple solutions, which is inherent to ill-posed problems. In a companion paper, Nicolaides et al. [72] successfully reconstructed thermal defects using photothermal radiometry. The experimental technique was made truly non-contact by obtaining cross-sectional scans with photothermal-radiometric detection. However, the use of low resolution photothermal radiometric experimental setup, resulted in reconstructed images that were broadened.

A new numerical technique for solving the forward problem [71] in the wavelet space has recently been developed by Miller et al. [73]. This technique uses a wavelet-based regularization method to better resolve the edge structures of defects relative to reconstructions obtained with smoothness-type regularization. In the future, the experimental data obtained in this thesis will be tested with Miller's formalism.

1.4 Objectives

The literature review presented in the previous sections has set the stage for the objectives of this thesis. The overall objective was to overcome the above described limitations of depth profilometry and thermal wave diffraction tomography. Since these techniques are distinct thermal wave inverse problems, they are treated separately. In the following sections the objectives relating to each problem are described.

1.4.1 Depth Profilometry

The non-destructive nature of depth profilometry offers significant advantages over currently used conventional microhardness techniques. The first objective of this thesis is to explain the correlation between thermal diffusivity and the heat treatment of steels, keeping in mind the anticorrelation between thermal diffusivity and microhardness in quenched steel as observed by Munidasa et al. [57]. This thesis considers not only the effects of quenching on the thermal diffusivity profiles, but also the effects of carburizing. Carburizing is the absorption and diffusion of carbon into solid ferrous alloys by heating. The microstructure of the near-surface region is altered producing carbon gradients and is therefore of interest when studying the effects of carburizing on thermal diffusivity. Furthermore, Munidasa et al. [57] neglected to include the effects of surface roughness on the obtained experimental data. In the context of a laboratory study, neglecting surface roughness does not appear to be a severe limitation because rough samples can be easily polished. However, as an on-line industrial application, sample polishing would be time consuming. These reasons validate the importance of incorporating the effects of roughness on the forward experimental data. The study of surface roughness in hardened steels has driven the second objective of the thesis which is to take into account the influence of surface roughness on experimentally gathered data. It is also important to analyze a sufficiently large number of samples so that statistical variations can be documented. This served as a third objective of this thesis.

1.4.2 Thermal Wave Slice Diffraction Tomography

Multiplicity of solutions is inherent to ill-posed problems. Earlier works have used a "brute-force" approach [70,72] to obtain a single solution. However, in order to pinpoint a reasonable solution, it is important to adapt a rigorous optimization approach. This is especially important if TSDT can be successfully implemented for an industrial application. Incorporating a suitable optimization algorithm in TSDT formed the fourth objective of this thesis.

The fifth and final objective of this thesis was to construct a high resolution photothermal radiometric experimental setup. The purpose of such a high resolution setup is to overcome the problem of image broadening associated with the low resolution setup [72].

1.5 Outline of Thesis

This thesis is divided into two main parts. The first part (Chapters 2-5) deals with the depth profilometric problem, while the second part (Chapters 6-9) presents the thermal wave tomography problem.

Chapter 2 sets the theoretical basis for the depth profilometric problem and develops a theoretical model to treat a rough layer on an inhomogeneous semi-infinite substrate. Chapter 3 outlines the numerical methodology used and implements the theoretical development of Chapter 2. In Chapter 4, the low resolution photothermal radiometric setup is explained and the experimental data obtained are presented and discussed. Chapter 5 includes the reconstructions of the data presented in Chapter 4 by way of eliminating roughness in a novel manner.

Chapter 6 presents the theoretical basis for thermal wave diffraction tomography, and also presents a theoretical expression for the three-dimensional Green function and the incident temperature field. In Chapter 7, the numerical aspects of the thermal wave diffraction problem are discussed and the technique used to optimize the inversion is presented. Chapter 8 describes the construction of the high resolution experimental setup. Although not outlined in the objectives of this thesis, an application of high resolution off-set imaging of cracks is also developed. Tomographic experiments are also presented in Chapter 8, which, in turn, are used for real tomographic inversions, as described in Chapter 9. Chapter 10 presents the overall conclusions of this thesis as well as recommendations for future work.

Chapter 2

Forward Process: Depth Profilometry

2.1 Introduction

Depth profilometry is a one-dimensional inverse problem where the thermal diffusivity profile is inverted from a modulated temperature surface information. Before the inverse problem can be solved the forward problem must be developed. The depth profilometric *forward* problem is based on formulating a one-dimensional temperature distribution model of a thermal wave field from a homogeneous layer on top of a semi-infinite inhomogeneous layer. The top homogeneous layer is introduced into the model so as to account for the thermal response due to the surface conditions (roughness) of the sample. In this way the effects of roughness can be deconvolved to recover the sample's true thermal inhomogeneities. Previous depth profilometry models treated the surface thermal wave response of a smoothed surface [36] and did not account for roughness.

In this chapter the standard (Green function method) one-dimensional treatment of the thermal-wave equation will be presented for a homogeneous sample. This will be followed by a presentation of the thermal wave field in an inhomogeneous layer in terms of treating the thermal wave as a thermal harmonic oscillator (THO) and thus implementing the Hamilton-Jacobi formalism [40] from classical mechanics. The thermal wave theory of a homogeneous layer on top of a semi-infinite inhomogeneous layer will be developed as the depth profilometric solution to the forward problem.

2.2 General Solution of the Thermal Wave Field in a Homogeneous Solid

The general form of the heat diffusion equation in Cartesian coordinates for the temperature distribution $T(\boldsymbol{r},t)$ with a thermal source $q(\boldsymbol{r},t)$ is

$$\nabla^2 T(\boldsymbol{r},t) - \frac{1}{\alpha}\frac{\partial}{\partial t}T(\boldsymbol{r},t) = -\frac{1}{k}q(\boldsymbol{r},t) \tag{2.1}$$

where α is the thermal diffusivity and k is the thermal conductivity, both of which are assumed to not vary in space. Applying the temporal Fourier transform, equation (2.1) transforms into the frequency domain as follows,

$$\nabla^2 \Theta(\boldsymbol{r},\omega) - \sigma^2(\omega)\Theta(\boldsymbol{r},\omega) = -\frac{1}{k}Q(\boldsymbol{r},\omega) \tag{2.2}$$

where $\Theta(\boldsymbol{r},\omega)$ is the wideband Fourier transform of $T(\boldsymbol{r},t)$, which is assumed to exist as

$$\Theta(\boldsymbol{r},\omega) = \int_{-\infty}^{+\infty} T(\boldsymbol{r},t)e^{-i\omega t}dt, \tag{2.3a}$$

and

$$\sigma(\omega) = (1+i)\sqrt{\frac{\omega}{2\alpha}} \tag{2.3b}$$

where σ is the complex wavenumber, and ω represents the angular modulation frequency. To obtain the conventional thermal-wave behavior, the wideband spectral equation (2.2) must be reduced to a single spectral component form by assuming harmonic thermal excitation at some specific frequency $f_0=\omega_0/2\pi$ [5]. The temperature function for a single spectral component of the Fourier field after an inverse Fourier transform, equation (2.3a) becomes

$$T(\boldsymbol{r},t)=\frac{1}{2\pi}\int_{-\infty}^{+\infty}\Theta(\boldsymbol{r},\omega)\delta(\omega-\omega_0)e^{i\omega t}d\omega=\Theta(\boldsymbol{r},\omega_0)e^{i\omega_0 t}\equiv T(\boldsymbol{r},\omega_0), \tag{2.4}$$

where $\delta(\omega-\omega_0)$ is the Dirac delta function, which is used to show that the harmonic field peaks infinitely at the single component $\omega=\omega_0$. By trivially substituting ω for ω_0 and using equation (2.4), equation (2.2) can be written as the thermal-wave field equation

$$\nabla^2 T(\boldsymbol{r},\omega)-\sigma^2(\omega)T(\boldsymbol{r},\omega)=-\frac{1}{k}Q(\boldsymbol{r},\omega), \tag{2.5}$$

where $T(\boldsymbol{r},\omega=\omega_0)$ is assumed to exist and is well defined at the spectral component of interest ω_0. Following a Green function methodology [5] which is based on solving for a homogeneous boundary problem, the solution to equation (2.5) is,

$$\begin{aligned}T(\boldsymbol{r},\omega)&=\frac{a}{k}\iiint_{V_0}Q(\boldsymbol{r}_0,\omega)G(\boldsymbol{r}\,|\,\boldsymbol{r}_0;\omega)dV_0\\&+a\oint_{S_0}[G(\boldsymbol{r}\,|\,\boldsymbol{r}_0^s;\omega)\nabla_0 T(\boldsymbol{r}^s,\omega)-T(\boldsymbol{r}^s,\omega)\nabla_0 G(\boldsymbol{r}\,|\,\boldsymbol{r}_0^s;\omega)]\bullet d\boldsymbol{S}_0\end{aligned} \tag{2.6}$$

where $\boldsymbol{r}$ and $\boldsymbol{r}_0$ are the observation and source coordinates, respectively. $\boldsymbol{S}_0$ is the surface surrounding the source volume V_0 and $\boldsymbol{r}_0^s$ is a coordinate point on $\boldsymbol{S}_0$. $G(\boldsymbol{r}\,|\,\boldsymbol{r}_0^s;\omega)$ is the associated Green function that depends on the geometry boundaries. The thermal diffusivity and conductivity are assumed to be independent of the coordinate in V_0.

2.3 One-Dimensional Thermal Wave Field of Homogeneous Semi-Infinite Solid with Prescribed Surface Flux at x=0

The AC thermal wave flux prescribed at x=0 is given by

$$F(0,\omega)=\frac{1}{2}F_0e^{i\omega t} \tag{2.7}$$

where F_0 is the incident flux. The associated Green function must satisfy a homogeneous Neumann boundary condition at the source coordinate $x_0=0$ as shown below,

$$\frac{\partial}{\partial x_0}G_0(x-x_0,\omega)=0. \tag{2.8}$$

In the absence of a bulk source, equation (2.6) reduces in one-dimension to

$$\begin{aligned}T(x,\omega)&=aG(x|0;\omega)\left[\frac{\partial}{\partial x_0}T(x;\omega)|_{x_0=0}\right]\\&=a\left(-\frac{e^{-\sigma x}}{\sigma}\right)\left[-\frac{F_0}{2k}e^{i\omega t}\right]=F_0\frac{\sqrt{a}}{k\sqrt{\omega}}e^{-(\sigma x+i\frac{\pi}{4})}e^{i\omega t}=F_0\frac{1}{e\sqrt{\omega}}e^{-(\sigma x+i\frac{\pi}{4})}e^{i\omega t}\end{aligned} \tag{2.9}$$

where $e = k/\sqrt{\alpha}$ is the thermal effusivity of the semi-infinite material. It can be seen by the equation that for high thermal effusivity a low thermal signal is expected since the thermal power is conducted away into the bulk of the material. The resulting thermal field exhibits the well-known π/4 phase lag with respect to the input thermal wave flux predicted for semi-infinite geometries [5,40].

2.4 The Hamilton-Jacobi Thermal Wave Oscillator: Solution to an Inhomogeneous Semi-Infinite Solid

A mathematical formalism for the description of the propagation of thermal waves in solids has been pioneered by Mandelis (1985) [39,40]. The method is based on the analogy between thermal waves and classical mechanics by expressing the heat conduction equation in the Hamilton-Jacobi formulation. As outlined above, the AC temperature field can be written as

$$T(x,t) = T(x)e^{-i\omega t} \tag{2.10}$$

which yields the Fourier-Helmholtz equation

$$\frac{d}{dx}\left[k(x)\frac{d}{dx}T(x)\right] - i\omega\rho(x)c(x)T(x) = 0, \tag{2.11}$$

with continuously variable thermal conductivity, $k(x)$, density $\rho(x)$, and specific heat $c(x)$. For a semi-inifinite medium, the boundary conditions at x=0 are,

$$T(x=0)=T_0 \tag{2.12a}$$

$$-k(x)\frac{dT(x)}{dx}|_{x=0}=Q_0 \tag{2.12b}$$

where Q₀ is the thermal flux prescribed on the surface (x=0). Equation (2.11) satisfies the Euler equation

$$\frac{\partial L}{\partial T}-\frac{d}{dx}\frac{\partial L}{\partial(dT/dx)}=0, \tag{2.13}$$

with the Langrangian L, corresponding to [74]

$$L=\frac{1}{2}k(x)\left(\frac{dT(x)}{dx}\right)^2+i\omega\rho(x)c(x)T^2(x) \tag{2.14}$$

and yielding the Hamiltonian

$$\begin{aligned} H(x,T,p_T)&=p_T\left(\frac{dT(x)}{dx}\right)-L \\ &=\frac{p_T^2}{2k(x)}-\frac{1}{2}\omega\varrho(x)c(x)T^2(x), \end{aligned} \tag{2.15}$$

where p_n is the generalized momentum defined by

$$p_T(x)=\frac{\partial L}{\partial(dT/dx)}=k(x)\,\frac{dT(x)}{dx} \tag{2.16}$$

Equations (2.15) and (2.16) show that the generalized coordinate and momentum are the field temperature and heat flux, respectively. For an appropriate Hamiltonian, the canonical transformation is required, such that both coordinate and momentum will be constants of the motion. The thermal-harmonic-oscillator canonical Hamiltonian (constant of motion) is then derived as

$$H(p_T,\tau) = \tfrac{1}{2}p_T^2 - \frac{i\omega}{2}\tau^2, \tag{2.17}$$

which is analogous to the classical canonical Hamiltonian function $H(p_T,\tau) = p_T^2/2m + K\tau^2/2$ with the following effective physical assignations of a harmonic oscillator

$$\tau \equiv [k(x)\rho(x)c(x)]^{1/4}T(x) = [e(x)]^{1/2}T(x); \qquad \text{(position)}, \tag{2.18a}$$

$$p_T \equiv k(x)\,\frac{dT(x)}{dx}; \qquad \text{(momentum)}, \tag{2.18b}$$

$$m^{-1} \equiv \lim_{L\to\infty}\left(\frac{1}{L}\int_0^L \frac{dy}{\sqrt{a_s(y)}}\right); \qquad \text{(inertia)}, \tag{2.18c}$$

$$K = -i\omega; \qquad \text{(spring constant)}. \tag{2.18d}$$

where $e(x) = \sqrt{k(x)\rho(x)c(x)}$ is the material thermal effusivity. Finally, the temperature field $T(x)$ in equation (2.18a) may be written as [40],

$$T(x) = \frac{1}{2\sqrt{e(x)}}[C_1e^{H(x)} - C_2e^{-H(x)}]. \tag{2.19}$$

The exponent $H(x)$, is defined as

$$H(x) = \int_0^x \sigma(y,\omega)dy = \int_0^x (1+i)\left(\frac{\omega}{2a(y)}\right)^{1/2} dy, \tag{2.20}$$

where $\alpha(y)$ is the depth thermal diffusivity distribution of the solid and C_1 and C_2 are integration constants [40] ,

$$C_1 = \frac{P_{T_0}}{\sqrt{\omega}} e^{-i\pi/4} + \tau_0, \text{ and} \tag{2.21b}$$

$$C_2 = \frac{P_{T_0}}{\sqrt{\omega}} e^{-i\pi/4} - \tau_0, \tag{2.21b}$$

where P_{T0} and τ_0 can be determined by boundary (equations (2.12a) and (2.12b)) and limiting conditions. The material under investigation is assumed to be opaque in that its optical penetration depth is much shorter than the shortest thermal diffusion length, $\mu = \sqrt{2a/\omega}$.

2.5 Discrete Homogeneous Layer on a Semi-Infinite Inhomogeneous Layer

The regions surrounding the investigated inhomogeneous layer (x>0) include an air-solid homogeneous interface (x=-d) and a solid-backing interface (x=0) as shown in Figure 2.1.

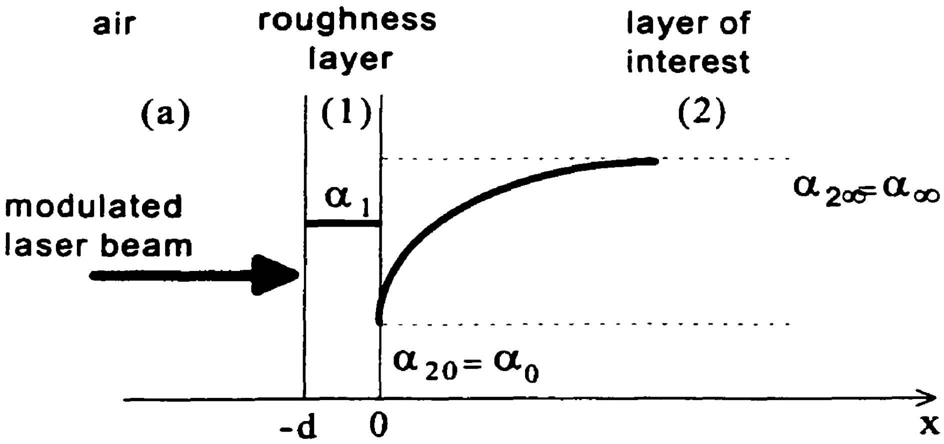

Figure 2.1 Depth profilometric region under investigation.

The AC temperature fields in each region air (a), roughness layer (1) and investigated inhomogeneous layer (2) are:

$$T_a(x,\omega) = D\,e^{\sigma_0(x+d)} \qquad ;\ x \le -d \Rightarrow\ x+d \le 0 \quad (2.22a)$$

$$T_1(x,\omega) = B\,e^{\sigma_1 x} + C\,e^{-\sigma_1 x} \qquad ;\ -d \le x \le 0 \quad (2.22b)$$

$$T_2(x,\omega) = \frac{1}{2\sqrt{e_2(x)}}\left[C_1 e^{H_2(x)} - C_2 e^{-H_2(x)}\right] \qquad ;\ 0 \le x \le \infty \quad (2.22c)$$

Equation (2.22a) is the bounded (finite as $x \to -\infty$) solution to the thermal-wave equation for a homogeneous semi-infinite medium (shown in Section 2.3) [5] and equation (2.22b) is the solution for a finite homogeneous region. In equations (2.22a) and (2.22b) σ_j is the complex wave number defined in equation (2.4), where α_j is the thermal diffusivity of the j-th medium (j:1,2). Equation (2.22c) is the result of treating the inhomogeneous layer thermal wave field in terms of the Hamilton-Jacobi formulation as shown in Section 2.3, and applying the appropriate subscript, 2, to the expressions for identifying the investigated layer. Constants D, B, and C depend on the boundary and limiting conditions of the system, and C_1 and C_2 are as defined in equations (2.20a) and (2.20b), respectively.

The boundary conditions for the regions at $x=-d$ and x=0 are the continuity of temperature and the continuity of heat flux:

$$T_1(x=-d,\omega) = T_0(x=-d,\omega), \quad (2.23a)$$

$$-k_1\frac{dT_1(x=-d,\omega)}{dx} + k_0\frac{dT_0(x=-d,\omega)}{dx} = \tfrac{1}{2}Q_0 e^{i\omega t}, \quad (2.23b)$$

$$T_1(x=0,\omega) = T_2(x=0,\omega), \quad (2.24c)$$

$$k_1 \frac{dT_1(x=0,\omega)}{dx} = k_2 \frac{dT_2(x=0,\omega)}{dx}, \tag{2.24d}$$

where Q_0 represents the thermal source fluence at the material surface [W/m^2] assuming 100% laser power absorption. In the limit $x \to \infty$, the AC temperature, $T_2(x)$, generated should be zero. Applying this condition to equation (2.22c) yields

$$\frac{P_{T0}\, e^{-i\pi/4}}{\sqrt{\omega}} = -\tau_0 \left(\frac{1 + e^{-2H_2(\infty)}}{1 - e^{-2H_2(\infty)}} \right). \tag{2.25}$$

Substituting equation (2.25) to (2.22c) gives

$$T_2(x) = \frac{\tau_0}{\sqrt{e_2(x)}} \left[\frac{e^{-H_2(x)} - e^{-[2H_2(\infty) - H_2(x)]}}{1 - e^{-2H_2(\infty)}} \right]. \tag{2.26}$$

In order to use this with the boundary conditions, the first derivative of $T_2(x)$ with respect to x is written as

$$\begin{aligned} \frac{d}{dx} T_2(x) = {} & \frac{\tau_0}{\sqrt{e_2(x)}} \frac{d}{dx} \left[\frac{e^{-H_2(x)} - e^{-[2H_2(\infty) - H_2(x)]}}{1 - e^{-2H_2(\infty)}} \right] \\ & + \tau_0 \left[\frac{e^{-H_2(x)} - e^{-[2H_2(\infty) - H_2(x)]}}{1 - e^{-2H_2(\infty)}} \right] \frac{d}{dx} [e_2^{-1/2}(x)]. \end{aligned} \tag{2.27}$$

An approximation is now made by neglecting the second part of equation (2.26) and setting the thermal effusivity derivative equal to zero:

$$\frac{d}{dx}[e_2^{-1/2}(x)] \approx 0. \tag{2.28}$$

This assumption amounts to a requirement for nonsteep local variations of the effusivity (WKBJ approximation). This is easily satisfied when the thermophysical field is evaluated at small incremental depth slices where it is not expected that local steep diffusivity gradients may exist [39,59]. Solving for the constants by using the boundary conditions and substituting in equation (2.26), the temperature distribution at layer (2) becomes:

$$\begin{aligned} T_2(x) = {} & \frac{Q_0\sqrt{R_2(x)}}{k_2(0)\sigma_2(0)}\left[\frac{e^{-H_2(x)} - e^{-[2H_2(\infty)-H_2(x)]}}{1 - e^{-2H_2(\infty)}}\right] \\ & \times\left[\frac{b_{21}(0)e^{-\sigma_1 d}}{(1+b_{21}(0)F_2)-(1-b_{21}(0)F_2)e^{-2\sigma_1 d}}\right] \end{aligned} \tag{2.29}$$

where,

$$F_2 = \frac{1+e^{-2H_2(\infty)}}{1-e^{-2H_2(\infty)}}, \tag{2.29a}$$

$$b_{21}(0) = \frac{k_2(0)\sigma_2(0)}{k_1\sigma_1} = b_{201}, \text{ and} \tag{2.29b}$$

$$R_2(x) = \frac{e_2(0)}{e_2(x)}. \tag{2.29c}$$

In deriving equation (2.29) the air-solid interface was assumed to be negligible. This is a valid assumption, since in most cases the thermal coupling coefficient is much less than 1 ($R_{air,1} \ll 1$ near adiabatic conditions). Similarly, by substitution, the temperature distribution in the homogeneous layer (1) from equation (2.22b) becomes:

$$T_1(x) = \frac{Q_0}{2k_1\sigma_1}\left[\frac{e^{-\sigma_1(x+d)} + \Gamma_{21}(0)e^{-\sigma_1(d-x)}}{1 - \Gamma_{21}(0)e^{-2\sigma_1 d}}\right] \tag{2.30}$$

where,

$$\Gamma_{21}(0) = \frac{1 - b_{21}(0)F_2}{1 + b_{21}(0)F_2}. \tag{2.31}$$

Although it will be seen that the results are valid for arbitrary thermal diffusivity depth profiles, for this analysis the following simple simulated functional dependence of the solid inhomogeneous region thermal diffusivity is assumed [36]:

$$a_2(x) = a_s(x) = a_0\left(\frac{1 + \Delta e^{-qx}}{1 + \Delta}\right)^2 \tag{2.32}$$

such that $a_s(\infty) = a_\infty$, $a_s(0) = a_0$ and

$$\Delta = \sqrt{\frac{a_0}{a_\infty}} - 1. \tag{2.32a}$$

The parameter q is a constant that determines the rate of thermophysical decay if $a_0 > a_\infty$ or growth if $a_0 < a_\infty$. By defining a form for the inhomogeneous thermal diffusivity the integral for $H(x)$, equation (2.20), gives $H_2(\infty) \to \infty$, which is also valid for a constant homogeneous thermal diffusivity in layer (2). Thus from equation (2.29a), $F_2 = 1$, and from equation (2.31), $\Gamma_{21}(0) = \gamma_{21}(0) = \gamma_{201}$. The resulting temperature, for the inhomogeneous layer (2) from equation (2.29), simplifies to

$$\begin{aligned} T_2(x) &= \frac{Q_0\sqrt{R_2(x)}}{k_2(0)\sigma_2(0)}\frac{b_{21}(0)\,e^{-\sigma_1 d - H_2(x)}}{(1+b_{21}(0)) - (1-b_{21}(0))e^{-2\sigma_1 d}} \\ &= \frac{Q_0\sqrt{R_2(x)}}{k_1\sigma_1}\frac{e^{-\sigma_1 d - H_2(x)}}{(1+b_{21}(0))(1-\gamma_{21}(0)e^{-2\sigma_1 d})}. \end{aligned} \tag{2.33}$$

The superposition principle is implemented in solving the complete expression for the thermal wave field in an inhomogeneous solid bounded by the regions shown in Figure 2.1. According to this principle, any complicated linear boundary-value problem can have a solution written as a linear combination of solutions to a number of simpler boundary value problems. The general solution of the thermal wave field for the regions shown in Figure 2.1 is then,

$$T(x) = aT_2(x,\omega) + bT_0(x,\omega) + cT_\infty(x,\omega), \tag{2.34}$$

where T_0 and T_∞ are the temperature distributions with constant thermal diffusivities α_0 and α_∞ in layer (2), respectively, and the expressions are

$$T_0(x,\omega) = \frac{Q_0\, e^{-\sigma_1 d - \sigma_{20} x}}{k_1\sigma_1(1+b_{201})(1-\gamma_{201}e^{-2\sigma_1 d})}, \tag{2.35a}$$

$$T_\infty(x,\omega) = \frac{Q_0\, e^{-\sigma_1 d - \sigma_{2\infty} x}}{k_1\sigma_1(1+b_{2\infty 1})(1-\gamma_{2\infty 1}e^{-2\sigma_1 d})}, \tag{2.35b}$$

where b_{201} and γ_{201} are as defined in equation (2.29b) and (2.31) (F_2=1), respectively. $b_{2\infty 1}$ and $\gamma_{2\infty 1}$ are defined similarly by replacing 0 with ∞ in equations (2.29b) and (2.31), respectively.

2.5.1 Determination of the Constants (a, b, c)

Constants a, b and c are determined by the various limiting case requirements of the problem.

2.5.1.1 At Large Distance: $x \to \infty$

Since equation (2.32) gives a constant diffusivity profile of a_∞ at very large distances from the surface, $T(x,\omega) \simeq T_\infty(x,\omega)$ in this limit and equation (2.34) leads to

$$\lim_{x\to\infty}\left\{a\frac{T_2(x,\omega)}{T_\infty(x,\omega)}+b\frac{T_0(x,\omega)}{T_\infty(x,\omega)}+c\right\}=1. \tag{2.36a}$$

Substituting equations (2.33), (2.35a) and (2.35b) to (2.36a), and by setting b=0 to satisfy boundness, results in

$$a=(1-c)\frac{Z}{\sqrt{R_2(x)}}e^{-\sigma_{2\infty}J_\infty}, \tag{2.36b}$$

where

$$J_\infty=\tfrac{1}{2q}\ln(|\frac{a_{20}}{a_{2\infty}}|), \tag{2.36c}$$

$$Z=\frac{(1+b_{201})(1-\gamma_{201}e^{-2\sigma_1 d})}{(1+b_{2\infty 1})(1-\gamma_{2\infty 1}e^{-2\sigma_1 d})} \tag{2.36d}$$

2.5.1.2 Very High Frequency: $\omega \to \infty$

In this limit the penetration depth of the thermal wave is zero, which results in

$$T(0,\omega\to\infty)=T_0(0,\omega). \tag{2.37}$$

Substituting (2.36b) in equation (2.34) and since $\sigma_{2\infty} \to \infty$ as $\omega \to \infty$, it can be shown that

$$c = \frac{T_0(0,\omega)}{T_\infty(0,\omega)} \tag{2.38}$$

2.5.1.3 Very Low Frequency: $\omega \rightarrow 0$

In this limit the penetration depth is infinite resulting in

$$T(0,\omega \rightarrow 0) = T_\infty(0,\omega). \tag{2.39}$$

Substituting (2.36b) and (2.38) in equation (2.34) and since $\sigma_{2\infty} \rightarrow 0$ as $\omega \rightarrow 0$, it can be shown that

$$\left(1 - \frac{T_0(0,\omega)}{T_\infty(0,\omega)}\right)\frac{Z}{\sqrt{R_2(\infty)}} = \frac{T_\infty(0,\omega)}{T_0(0,\omega)} = Z \tag{2.40}$$

which results in

$$R_2(\infty) = 1. \tag{2.41}$$

Finally, substituting all the determined constants from equations (2.38) and (2.41) in equation (2.34) and calculating the field at the front surface $x = -d$,

$$\begin{aligned} T_1(-d,\omega) &= T(0,\omega)\frac{e^{\sigma_1 d}}{1+\gamma_{201}}(1+\gamma_{201}e^{-2\sigma_1 d}) \\ &= \frac{Q_0}{2k_1\sigma_1}\left[\frac{1+\gamma_{201}e^{-2\sigma_1 d}}{1-\gamma_{201}e^{-2\sigma_1 d}}\right](1+(Z-1)e^{-\sigma_{2\infty}J_\infty}) \end{aligned} \tag{2.42}$$

where d cannot $\rightarrow \infty$.

2.6 One and Three Dimensional Formulation for a Homogeneous Layer on a Semi-Infinite Homogeneous Layer

In this thesis, rough homogeneous semi-infinite samples in a one-dimensional geometry were also examined. The samples served as a tool for ensuring that a one-dimensional experimental response was obtained. To correct the experimental data for any three-dimensionalities the theoretical model of a homogeneous layer with a homogeneous semi-infinite substrate is also derived.

Equation (2.42) can be reduced to the well known one-dimensional formulation [3] of a homogeneous layer on a semi-infinite system by setting the inhomogeneous layer to homogeneous, i.e $a_0 = a_\infty$ and therefore Z=1. The resulting equation is:

$$T(-d,\omega) = \frac{Q_0}{2k_1\sigma_1}\left[\frac{1+\gamma_{21}e^{-2\sigma_1 d}}{1-\gamma_{21}e^{-2\sigma_1 d}}\right], \tag{2.43}$$

where γ_{201} becomes γ_{21} with $F_2=1$ as defined in equation (2.40).

Let us prove the one-dimensionality of the depth profilometric experiments. A three-dimensional formulation for a homogeneous layer on a homogeneous semi-infinite substrate is developed. In a three-dimensional formulation the thermal wave field, as generated by a volume source of a Gaussian laser beam incident normal to the surface, must be taken into consideration. Figure 2.2 shows the three dimensional geometry in cartersian coordinates with a Gaussian beam.

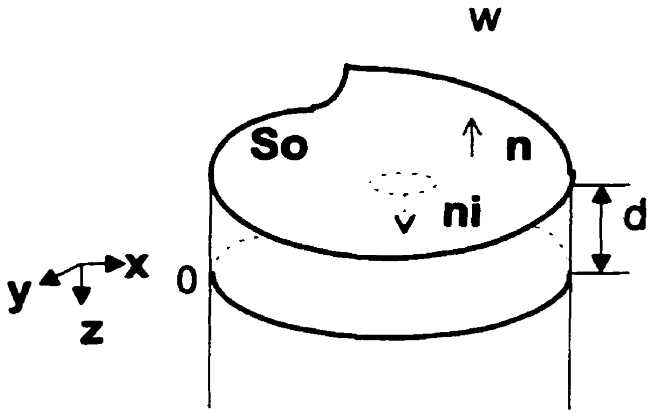

Figure 2.2 Depth profilometric three dimensional region under investigation.

The Gaussian beam is $e^{\frac{-r^2}{w^2}}$, w is the beam spot size, and $r^2=x^2+y^2$. The one-dimensional formulation of equation (2.43) can be converted to three dimensions by integrating over the Bessel function of order zero with the use of one-dimensional Green function by Hankel transformation

$$T(r,-d,\omega)=\frac{Q_0 w^2}{k_1}\int_0^{\infty}\frac{1}{v_1(\lambda)}\left[\frac{1+\Gamma_{21}(\lambda)e^{-2v_1(\lambda)d}}{1-\Gamma_{21}(\lambda)e^{-2v_1(\lambda)d}}\right]e^{-\lambda^2 w^2/4}J_0(\lambda r)\lambda d\lambda \tag{2.44}$$

where,

$$\Gamma_{21}(\lambda)=\frac{1-\xi_{21}(\lambda)}{1+\xi_{21}(\lambda)},$$

$$\xi_{21}(\lambda)=\frac{k_2 v_2(\lambda)}{k_1 v_1(\lambda)},$$

and,

$$v_{1,2}(\lambda)=\sqrt{\lambda^2+\sigma_{1,2}^2}\,.$$

Chapter 3

Inverse Process: Depth Profilometric Numerical Method

3.1 Introduction

In this chapter, the inversion method for depth profilometric reconstruction is outlined. This is a minimization based method and the numerical procedure is outlined in Section 3.2. In Section 3.3, simulation results are presented. Numerical considerations are presented in Section 3.4.

3.2 Numerical Method

The amplitude and phase are experimentally obtained and they correspond to the surface temperature distribution, $T(0,\omega)$. The theoretical values of the data pair are calculated by

$$T(0,\omega) = |M(\omega)| e^{i\Delta\phi(\omega)}, \tag{3.1}$$

where $M(\omega)$ is the amplitude and $\Delta\phi(\omega)$ is the phase at an angular frequency ω. At each frequency the amplitude and phase are used to calculate α_0 and q of equation (2.32) with α_∞ representing the known bulk thermal diffusivity. Although a profile of the form of equation

(2.32) is assumed, the actual profile is updated at each frequency by recalculating new parameters of α_0 and q. In this way, the validity of equation (2.42) becomes more general than the assumed profile of equation (2.32). Arbitrary depth profiles may be reconstructed by numerically determining the optimal pair of α_0 and q so that the profile sought locally results in the experimentally observed thermal-wave signal amplitude and phase data. Therefore, at each ω_j a system of two equations and two unknowns is solved.

The reconstruction method used to solve for the parameters $\alpha_{0(j)}$ and q_j is a multidimensional secant method, known as Broyden's method [36,75], and is based on minimizing the difference between the experimental and theoretical data for amplitude phase as follows,

$$\left|M_{\exp}(\omega_j)\right| - \left|M_{th}(\omega_j)\right| = 0, \tag{3.2a}$$

$$\left|\Delta\Phi_{\exp}(\omega_j)\right| - \left|\Delta\Phi_{th}(\omega_j)\right| = 0, \tag{3.2b}$$

The calculation of the depth parameter x_j is performed based on the fact that as modulation frequency decreases the thermal wave probing depth increases. Starting at the highest frequency ω_0, the shortest depth is the shortest thermal diffusion length, i.e.,

$$x_0 = \sqrt{\frac{2a_0}{\omega_0}} \tag{3.3}$$

The next (lower) frequency ω_{j+1}, corresponds to an increased thermal wave depth

$$x_{j+1} = x_j + \sqrt{\frac{2a_{s(j)}}{\omega_{j+1}}} - \sqrt{\frac{2a_{s(j)}}{\omega_j}} \ , \tag{3.4}$$

which is then substituted in equation (2.32) to calculate $\alpha_{s(j+1)}$. Once $\alpha_{s(j+1)}$ is calculated the method returns to recursively calculate the increased thermal wave depth as,

$$x_{j+1} = x_j + \sqrt{\frac{2a_{s(j+1)}}{\omega_{j+1}}} - \sqrt{\frac{2a_{s(j)}}{\omega_j}}\,. \tag{3.4}$$

Therefore, the depth of each "slice" depends on ω_j and $\alpha_{s(j)}(x_j)$. The expression for $\alpha_{(j)}$, equation (2.32), is used for analytical consistency. The true profile is built up by individual slice profiles as seen in Figure 3.1, with x_1 being the first slice corresponding to the highest frequency. In reconstructing depth profiles from data it is important to first find a reliable set of initial values for α_0 and q. This can be achieved by finding the best theoretical fit, using equation (2.42) (forward problem) to the first few end points (high frequency) using a single profile of the form of equation (2.32).

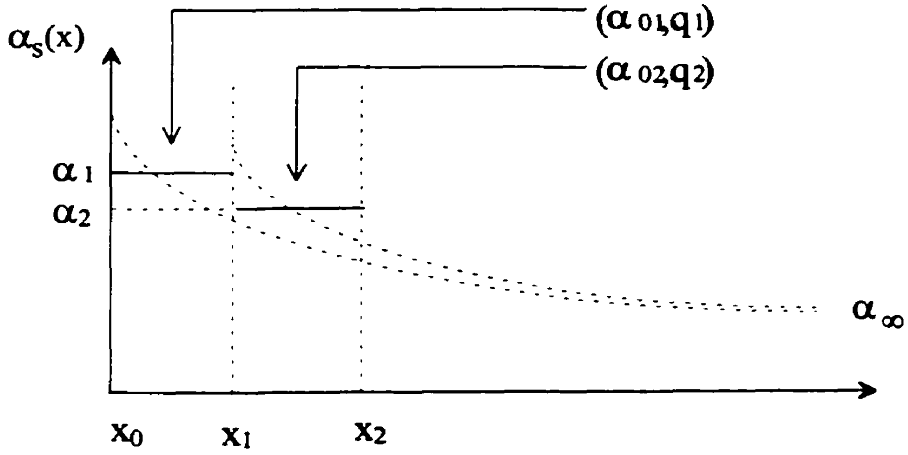

Figure 3.1 Depth profilometric profile calculation.

3.2.1 Detailed Description of the Inversion Method

The numerical solution is obtained by using the following steps:

Step 1. Initializing the theoretical amplitudes.

Since the experimental data amplitude ratio $|M_{exp}(\omega_j)|$ differs from the theoretical one, the experimental data are multiplied by a "scaling constant" which is calculated as a ratio between theoretical and experimental data amplitudes for the highest frequency, using initial values of $\alpha_{0(1)}$ and $q_{(1)}$. An approximate set of initial values, $\alpha_{0(1)}$ and $q_{(1)}$, can be obtained by fitting the high frequency experimental data to the theoretically simulated data corresponding to a single exponential profile (forward problem).

Step 2. Scaling data amplitudes.

In order to eliminate data error for the highest frequency, a scale constant is used which is in the range of ±5% of the initial one. These errors may result from improper $\alpha_{0(1)}$ and $q_{(1)}$ values, roundoff errors and inhomogeneities in the reference sample, and most importantly the effect of reflectivity and/or emissivity of the surfaces of both the reference and the sample. The process is started with the lower value and then step three is applied.

Step 3. Search for local $\alpha_{0(j)}$ and $q_{(j)}$.

This is the main step of the numerical search for solutions to equation (2.42). To be able to calculate the thermal diffusivity $\alpha(x)_{(j)}$ and depth $x_{(j)}$ corresponding to frequency $\omega_{(j)}$ one has to find unknown parameters $\alpha_{0(j)}$ and $q_{(j)}$. A customized two dimensional Broyden's method [36,75] is used. The procedure is customized to avoid run-time errors and singularities in Broyden's two-dimensional line search procedure so that it can be used in conjunction with equation (2.42). The method searches for $\alpha_{0(j)}$ and $q_{(j)}$ to satisfy the minimum conditions $|M_{exp}(\omega_j)| - |M(\omega_j)| = 0$ and $\Delta\phi_{exp}(\omega_j) - \Delta\phi(\omega_j) = 0$ for each angular frequency ω_j. The procedure starts with the highest frequency ω_1. The procedure also has the ability to search for solutions from the lowest frequency. If no solution is found for some of the frequencies, the scaling constant is increased by 1% and the procedure returns to step two above. If the scaling constant reaches the upper boundary of the allowed range and still no solution has been found for each of the frequencies, the procedure returns to step one where the initial $\alpha_{0(j)}$ is increased by 1%. When solutions are found for a specified number of frequencies the procedure advances to step four.

Step 4. Calculation of $\alpha(x)_{(j)}$ and depth $x_{(j)}$.

After all local values of $\alpha_{0(j)}$ and $q_{(j)}$ are known, the thermal diffusivity profile of the sample is calculated. Starting at the highest frequency $\omega_{(1)}$, where a solution was found, the corresponding $\alpha_{0(1)}$ and $q_{(1)}$ are used for determining the thermal diffusivity and the shallowest depth using the algorithm outlined in equations (3.3)-(3.5). In this algorithm a smooth continuity is applied wherein if $\alpha(x)_{(j)}$ significantly differs from the neighboring $\alpha(x)_{(j+1)}$, the scaling constant is increased by 1% and the program returns to step two. This entire procedure takes a few seconds on a Pentium II 266MHz, provided that a reasonable set of initial parameters is given.

The numerical code to solve the minimization problem was originally written in C++ by Frank Funak [36], and it was modified in this work to solve for the new forward theory of homogeneous layer with inhomogeneous semi-inifinite substrate developed in Chapter 2. The forward problem (written in C++) was also linked with an Excel spreadsheet to expedite the forward fitting which is used as an initial guess for the high frequencies. In this process, the numerical calculations are made in C++ as a built-in function in Excel so that the end user can modify parameters in real time.

3.3 Numerical simulations

In order to test the numerical method simulations were performed. Three basic reconstructions were performed for a homogeneous sample with no roughness, and an increasing and a decreasing inhomogeneous profile with no roughness. The reconstruction case which includes roughness is addressed along with the limitations in Chapter 4. The inhomogeneity was formulated with one exponential as given by equation (2.32). Figure 3.1 shows the three simulated profiles and the corresponding reconstructions in a geometry consisting of an inhomogeneous semi-infinite substrate. The first profile constructed is of a homogenous semi-infinite solid with $\alpha=12.5\text{x}10^{-6}\text{m}^2/\text{s}$. The second profile is of an inhomogeneous semi-infinite solid with $\alpha_0=11\text{x}10^{-6}\text{m}^2/\text{s}$, $a_\infty=12.5\text{x}10^{-6}\text{m}^2/\text{s}$ and $q=1000\text{m}^{-1}$. The third profile is an inhomogeneous semi-infinite solid of decreasing profile and with $\alpha_0=12.5\text{x}10^{-6}\text{m}^2/\text{s}$, $a_\infty = 11\text{x}10^{-6}\text{m}^2/\text{s}$, and $q=1000\text{m}^{-1}$. The reconstructions are in agreement with the original profiles created by using a single exponential as seen in Figure 3.2. The reconstruction of the homogeneous sample is $\alpha_0=12.49\text{x}10^{-6}\text{m}^2/\text{s}$ with a 0.08% precision. The increasing and decreasing profiles are less reproducible at the low frequencies.

3.4 Numerical Considerations

In reconstructing thermal diffusivity profiles, the bulk thermal diffusivity is needed *a priori*. This is the value to which the profile will eventually converge. A reconstruction is initiated by forward fitting of α_0, q and α_∞ to the experimental data. The value of the bulk thermal diffusivity α_∞, is kept constant and α_0 and q are searched for a solution to the slicing increment. In this way, α_∞ serves as a means of setting the absolute thermal diffusivity value of the profile and thus reducing the ill-conditioning of the problem. If for some reason a lower value of α_∞ is given then the initial guess of α_0 and q will change accordingly. The final reconstruction is a thermal diffusivity profile with the same shape but lower absolute value and shallower depth as shown in Figure 3.3. In conclusion, the shape of the profile is defined by the relative change of the experimental data, whereas the absolute value and depth are defined by α_∞.

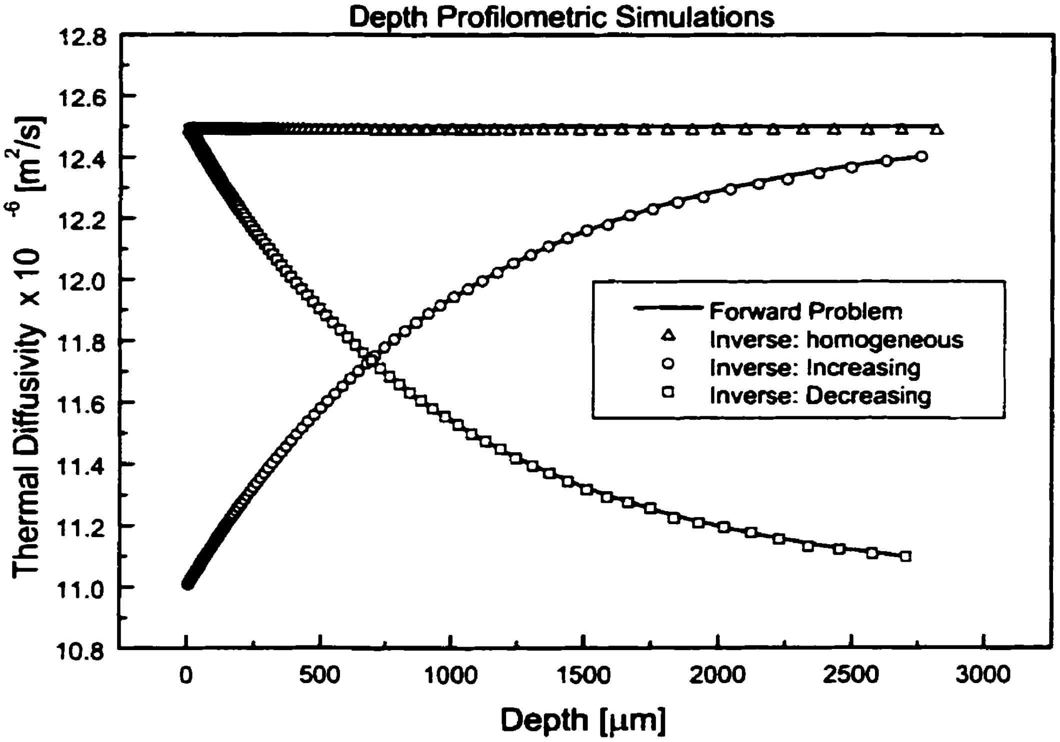

Figure 3.2 Simulated (solid lines) and reconstructions for a homogeneous (triangle), inhomogeneous increasing (circle) and inhomogeneous decreasing (square) profile.

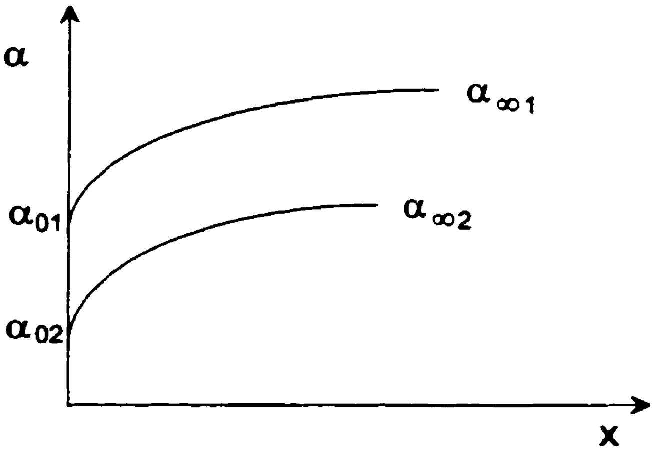

Figure 3.3 Reconstruction of the same forward data with two different bulk thermal diffusivities.

Chapter 4

Depth Profilometric Experimental Method and Data

4.1 Introduction

In this chapter, the experimental methodology for acquiring the frequency scan data for depth profilometry is explored. The data is obtained at a constant spatial position and the frequency is scanned. The current experimental method is based on photothermal radiometric detection, which has the flexibility for both backpropagation and transmission measurements. This is a truly non-contact method. Section 4.2 explains the fundamentals of photothermal radiometry and presents the low resolution experimental system used. In Section 4.3 the types of experimental samples and heating treatment performed are cited. The heating treatments of carburizing and quenching are explained. In Section 4.4 the experimental data for carburized and quenched samples are presented and the significance of the forward data is discussed.

4.2 Experimental Method

4.2.1 Photothermal-Radiometric Detection

Photothermal-radiometric detection is a non-contact technique. The temperature modulation causes a variation in the thermal emissions, which are monitored using an infrared detector. This radiation process is governed by the Stefan-Boltzmann law that relates the total flux of emitted radiation density, W, to the temperature, T, of the emitter surface given by

$$W = \varepsilon\sigma T^4, \tag{4.1}$$

where ε is the emissivity of the surface and $\sigma = 5.67 \times 10^{-8}$ $Wm^{-2}K^{-4}$ is the Stefan-Boltzmann constant. Due to modulated heating by a focused laser beam, the increment $\delta W(\omega)$ of the local thermal radiation emitted from the surface (for $\delta T << T_0$) is given by

$$\delta W(\omega) = 4\varepsilon\sigma\, T_0^3\, \delta T(\omega), \tag{4.2}$$

where T_0 is the static surface temperature, δT is the modulated temperature excursion, and ω is the modulation angular frequency.

Radiometric imaging can be used in two different detection modes: a) Front Surface Detection (Backpropagation/Reflection) and b) Rear Surface Detection (Transmission) [76]. In backpropagation, both the generation and detection of thermal waves take place on the same side of the sample as shown in Figure 4.1(a). Infrared emission from a thermally excited beam location is focused onto an infrared detector using infrared optics. Precautions must be taken to prevent scattered modulated high-intensity laser light from getting into the detector. This could produce false signals at the same frequency as the thermal waves. The scattered laser light may be removed by using a lowpass germanium filter at the detector aperture. In this detection mode, subsurface features are exposed by the backscatter thermal waves that produce a change in temperature at the front surface. Backpropagation is particularly suitable for detecting near surface (up to two thermal diffusion lengths) defects, but there is no limit on specimen thickness. In transmission, thermal waves are generated and detected on opposite sides of the sample, as shown in Figure 4.1(b). The thermal wave transmission method is useful for samples with a thickness of up to four thermal diffusion lengths (μ).

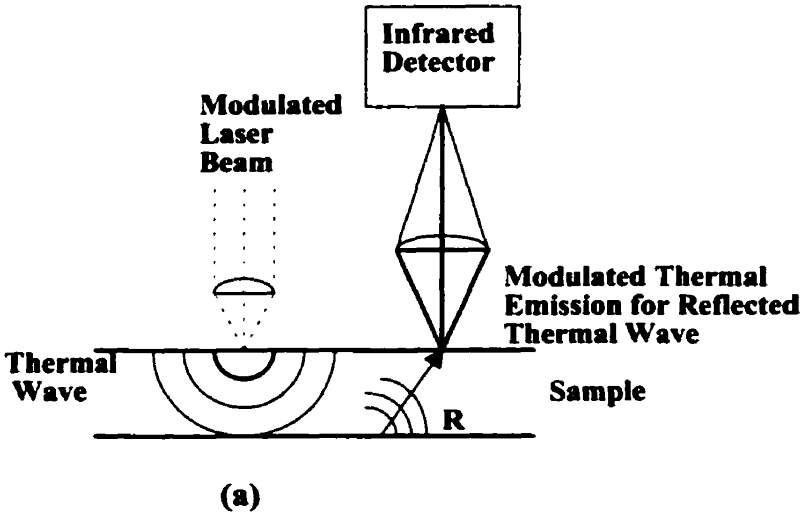

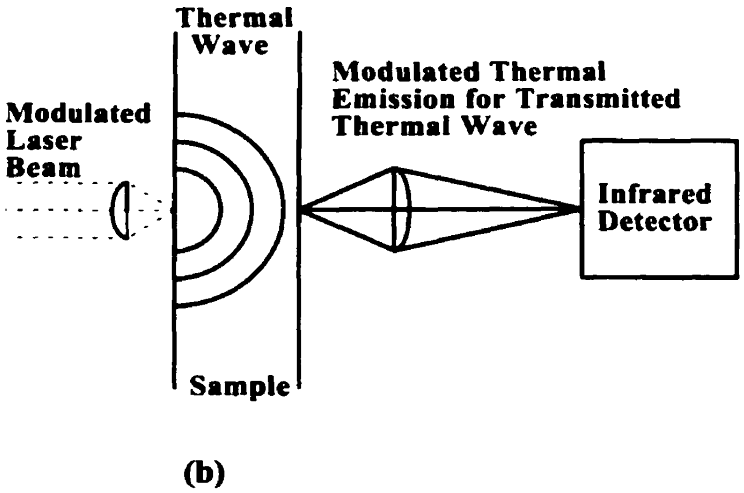

Figure 4.1 (a) Front surface (Backpropagation/Reflection) arrangement. (b) Rear surface (transmission) detection.

4.2.2 Experimental System

The depth profilometric application is a one-dimensional problem and therefore the experimental setup has a low spatial resolution. To maintain the one-dimensional heat diffusion formalism assumed in the theory, the pump beam spot size is made much larger than the maximum profile depth. The experimental apparatus is shown in Figure 4.2. A 514.5nm wavelength continuous-wave (cw) Innova Ar^+ laser from Coherent is modulated and then focused onto a sample, to a broad spot size of 10mm diameter, at an output power of 1W. To achieve the broad beam an optical diffuser, which is a 5mm thick polymeric substrate, is placed in the path of the beam and the scattered light is collimated with a lens onto the surface of the sample. The modulation is performed by an external Acousto-Optic Modulator (AOM) (ISOMET 1201E-1). The blackbody radiation from the optically excited sample is collected and collimated by two silver-coated, off-axis paraboloidal mirrors and then focused onto a liquid nitrogen cooled HgCdTe (Mercury-Cadmium-Telluride) detector (EG&G Judson Model J15D12-M204-S01M). The heated area of the sample is at the focal point of the one mirror positioned near the sample, and the detector is at the focal point of the other mirror. The HgCdTe detector is a photoconductive element that undergoes a change in resistance proportional to the intensity of the incident infrared radiation. It has an active square size of 1mm x 1mm and a bandwidth of 2-12μm. Since the efficiency of the detector increases with decreasing temperature, the detector is operated at a cryogenic temperature of 77^0 K [77]. An Anti-Reflecting (AR) coated germanium window with a transmission bandwidth of 2-14μm is mounted in front of the detector to block any visible radiation from the pump laser. Prior to being sent to the digital lock-in amplifier (Stanford Research System Model SR850) [78], the photothermal-radiometric signal is amplified by a preamplifier (Analog Modulus 350-3A), especially designed for operation with the HgCdTe detector. The low noise preamplifier ensures a proper performance for subsequent signal processing with a lock-in amplifier. The lock-in amplifier, which is interfaced with a personal computer, receives the pre-amplifier output and rejects all stray signals except those that have the same modulation frequency as the excitation beam. This process of data acquisition, storage, and scanning is fully automated.

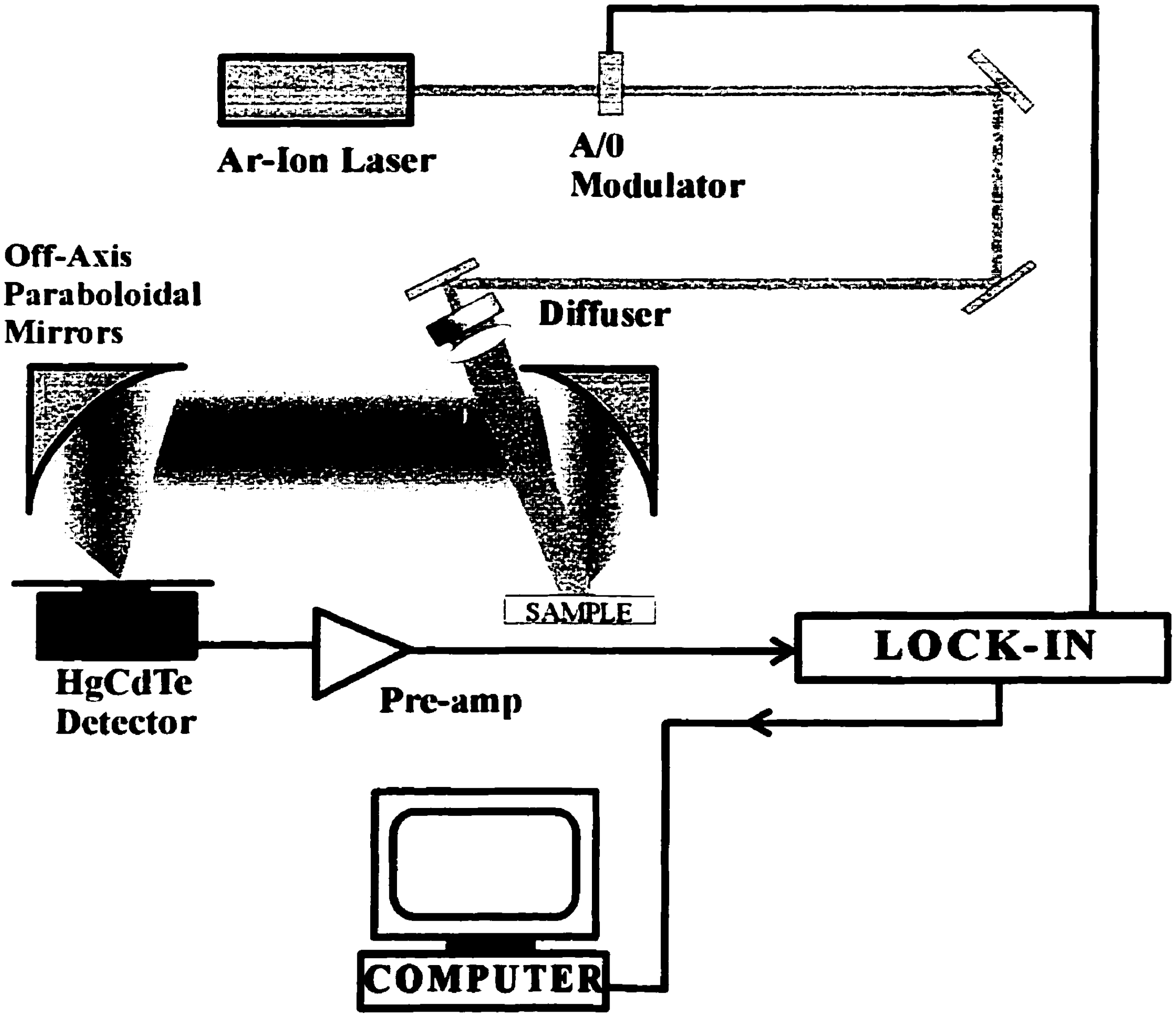

Figure 4.2 Frequency-domain photothermal radiometric instrumentation.

4.2.3 Experimental System: Detailed Procedure

For all the experiments, a cw Argon-ion Laser model 100-15 by Coherent was used, which operates in the 333.6-528.7nm band, and has an all-lines power output of 15 Watts. The unit is comprised of three major functional units: the laser head, the plasma tube within the laser head, and the power supply. The laser was configured to emit at 514.5nm, and was found to have a maximum optical output of 10 Watts at this wavelength. The intensity has a Gaussian distribution with a 1/e radius of 0.87mm. Before the laser was sent to the acousto-optic modulator, it was collimated by lenses to a Gaussian distribution with 1/e radius of 0.262mm. The collimating lens setup is shown in Figure 4.3. The beam profile was measured with a photodiode, and is shown in Figure 4.4, which confirms a good Gaussian profile.

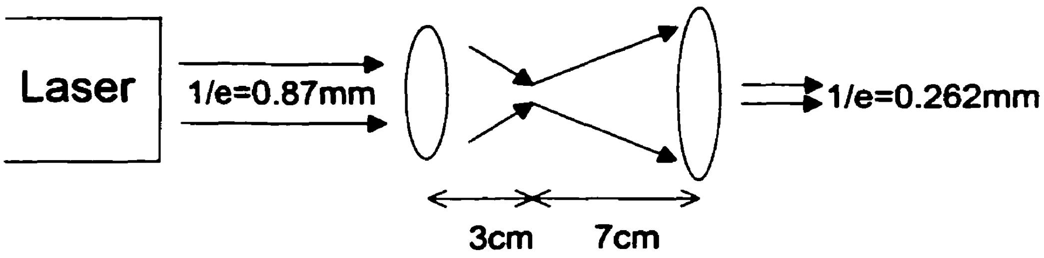

Figure 4.3 Laser beam collimating lens setup.

After the beam was collimated, it was directed to the aperture of an Isomet AOM (Model 1211). The AOM is a device that modulates the intensity of the incident beam by means of an RF signal at a given center frequency as shown in Figure 4.5. A digital (on-off) or analog (video) modulation can be produced, depending on the type of driver selected. In this assembly an analog Isomet driver (Model 223A-1) was used which accepted a sinusoidal wave from the internal function generator of the lock-in amplifier. This provided an amplitude-modulated RF output to the acousto-optic modulator at the particular frequency. The process of frequency scanning and data acquisition was then automated. The AOM was mounted on a translating vertical stage and a rotating micrometer stage for accurate adjustment. Beyond the exit of the modulator and after traveling for 20cm, the higher orders (I_2, I_3,...) were separated enough so that the preferred modulating first order beam (I_1) was chosen by blocking all the other beam orders with an iris.

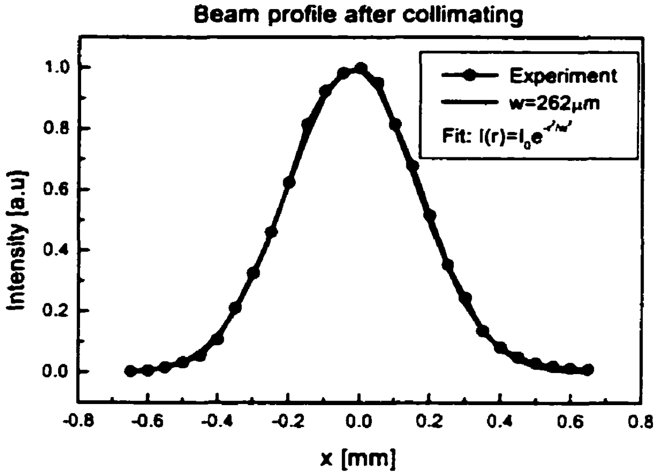

Figure 4.4 Beam profile after collimating, as measured with a photodiode.

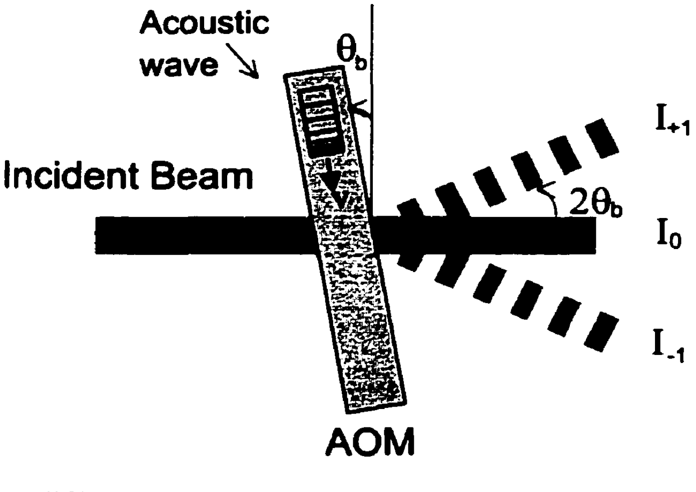

Figure 4.5 Laser beam diffracted paths from the AOM.

Frequency scans were then performed in the range of 0.5Hz -100kHz. The experiments were performed in two ranges: a) 0.5Hz-1kHz with broad 10mm diameter beam and b) 500Hz-100kHz with bare 2mm diameter beam. The data in the frequency range 500-1000Hz overlapped. This ensured that the thermal diffusion length was much smaller than the size of the beam and thus the signal remained one-dimensional. The reason for such an operation was that the SNR would increase at the higher frequency range since the power density [W/m^2] (Power/ beam cross-sectional area) with the 2mm beam was higher. The experimental surface temperature response on the sample was normalized by the surface temperature response of a reference sample (Zr alloy). This gave, for each frequency, an amplitude ratio and phase difference. The normalizing procedure was necessary to correct all instrumental frequency dependencies [36]. One instrumental frequency dependence arises from the response of the infrared detector. The responsivity and noise frequency dependence of the detector are shown in Figure 4.6. The responsivity of this detector is flat at the frequency region observed. When the frequency is below 1kHz both the sample and reference are affected by the 1/*f* noise frequency response of the detector. As a result, the normalization procedure amplifies the noise of the data.

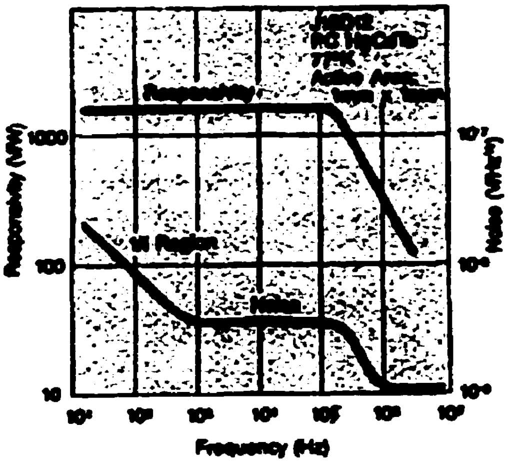

Figure 4.6 HgCdTe responsivity and noise frequency dependence [77].

4.2.4 Experimental Dimensionality

Depth profilometry theory assumes a one-dimensional heat diffusion formalism, which is difficult to achieve experimentally. At high frequencies, the penetration depth is close to the surface so lateral heat diffusion is negligible. However, at low frequencies, the thermal wave penetrates deep into the material and lateral heat diffusion is pronounced. To ensure one-dimensionality, the size of the beam must be much larger than the deepest penetration. Not only is the beam an important consideration here, but also the beam shape. The laser source has a Gaussian profile, an assumption not included in the theory. Experimentally a "top hat" distribution, which is a flat distribution of the beam, is needed in order to more closely satisfy the theoretical assumptions. To alleviate the three dimensionality introduced by the Gaussian distribution, a thick diffuser with the lens is placed in the path of the beam. This diffuses the light in order to redistribute the Gaussian distribution and redirect it into a broad distribution. By this process, the Gaussian profile is greatly reduced. The three dimensionality effects are drastically diminished but not eliminated as can be seen in Figure 4.7, which shows the response of a Zr reference sample for one bare and two diffused beams. As the beam is increasingly diffused both the amplitude and phase graphs approach one-dimensional theory. The response of a one-dimensional semi-infinite sample is derived in equation (2.9), where the amplitude is inversely proportional to the square-root of frequency and the phase is constant at -45°. Figure 4.7 presents unnormalized data, which explains the deviation from the theory at high frequencies. At low frequencies, the three-dimensionality effects are, as expected, more pronounced. Some of the deviation that exists relates to the AC coupled response of the infrared detector, which adds to the positive phase shift in the low frequency. This would be canceled by the normalizing procedure. To correct for the actual three-dimensionalities of the system, a known homogeneous sample with 2μm roughness is normalized with the reference Zr alloy sample, which is then fitted to the three-dimensional homogeneous layer theory derived in equation (2.44). The infinite integration was performed numerically by a routine written in C^{++} [74]. Figure 4.8 shows the normalized experimental data of a homogeneous steel with roughness and the expected one-dimensional response of the system. At low frequency there is an approximately 2° deviation from the one-dimensional theory. The deviation is due to the fact that below 10Hz lateral diffusion is not negligible. The three-dimensionality is not only a function of the beam, but also of the thermophysical properties of the sample and reference. With all the parameters known, a three-dimensional theory, equation (2.44), is fitted to the experimental data, and as seen in Figure 4.8, an excellent agreement between theory and experiment is obtained. The difference between the one-dimensional and three-dimensional theory is then included in the instrumental data, and all the experiments that follow are corrected. Also, in this data the 1/f noise dependence of the instrument is evident below 10Hz where the SNR decreases.

4.3 Experimental Samples and Heating Treatment

To understand the mechanism by which the thermal diffusivity profile in hardened steels develops, experimental samples were prepared for two heat treatments: the case hardening process of carburizing and quenching. In a previous study [57], only the quenching process was studied and the mechanism of the thermal diffusivity profile was not properly explained. In this work a hypothesis was made that the profile is formed at the carburizing stage. To test this hypothesis, the same set of samples were first studied after carburizing and then after quenching. Furthermore, in a laboratory study, neglecting surface roughness does not appear to be a severe limitation because rough samples can be easily polished. However, as an on-line industrial application, this technique would be prohibitively time consuming. It is thus, of great interest to incorporate the effects of roughness on the forward experimental data.

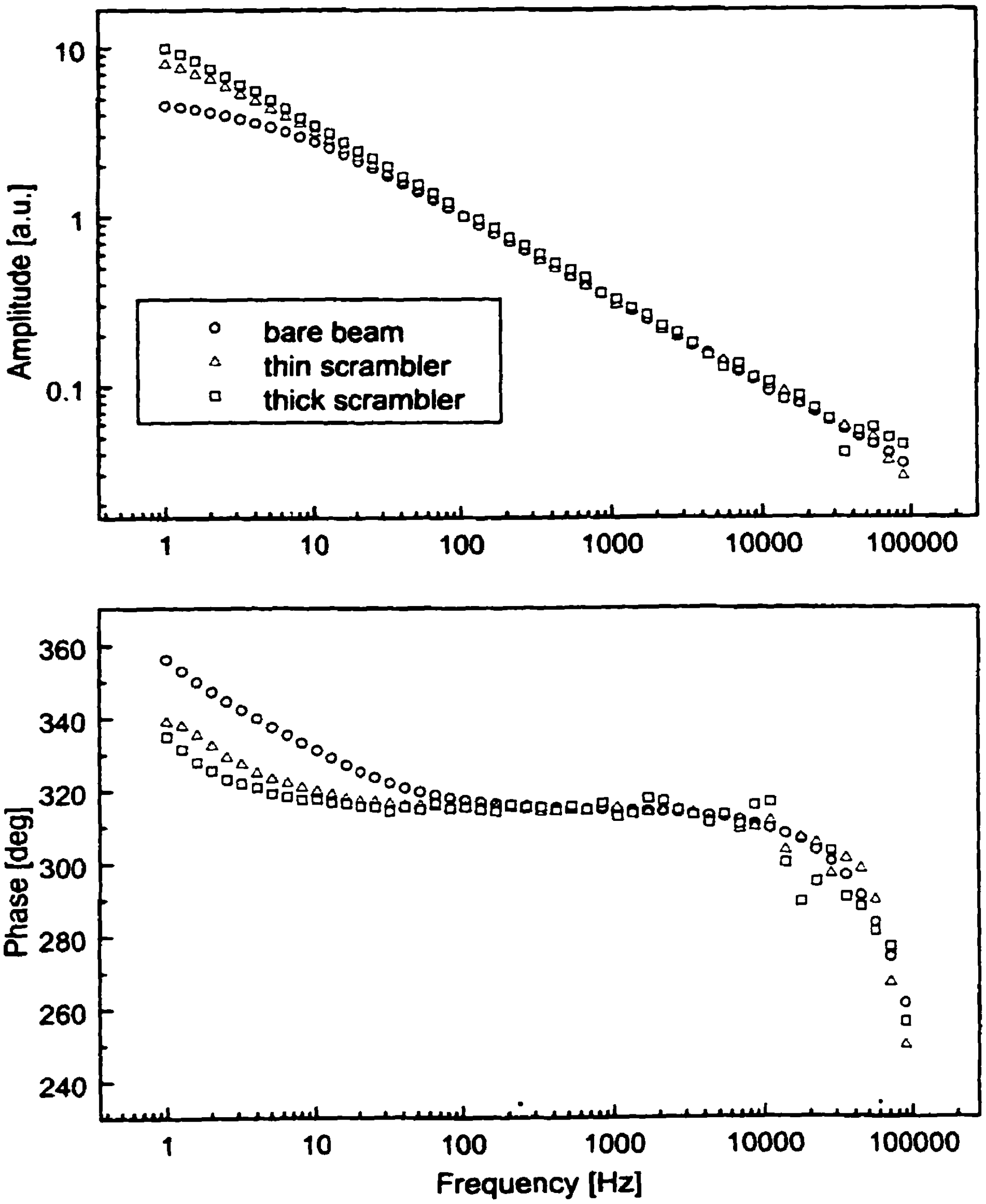

Figure 4.7 Zr alloy experimental reference. For clarity only 50% of the data are shown.

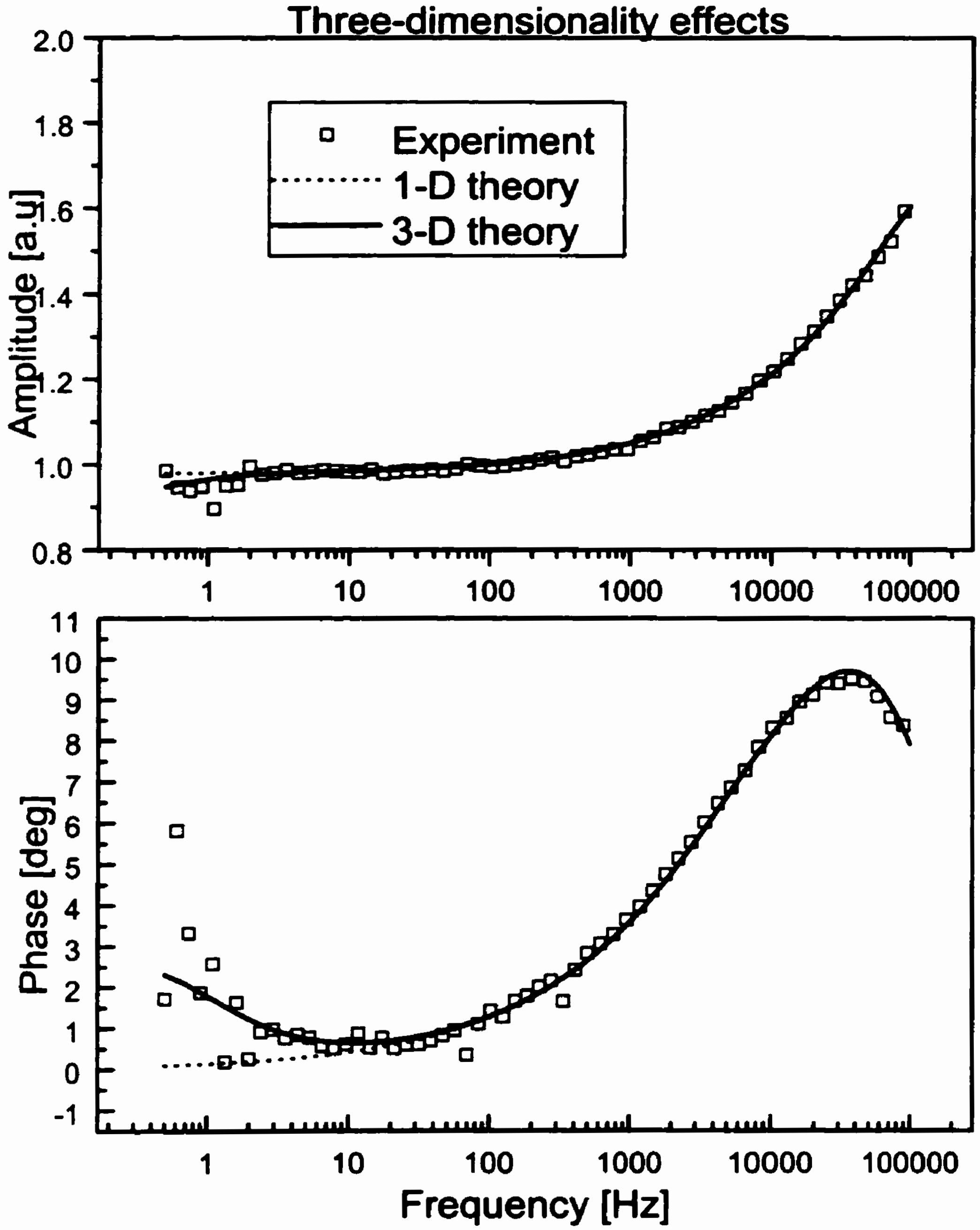

Figure 4.8 Frequency response of experimental data with roughness with one-dimensional and three dimensional theoretical fits. For clarity only 50% of the experimental data are shown.

With these goals, a sample matrix was constructed as a function of roughness and case hardness depth. The sample matrix is shown in Table 4.1, and for each possible case three samples are studied for statistical purposes. The samples used are 1cm thick, and are cut from the same slab of AISI 8620 steel alloy, which is a low carbon steel (0.25%C). The roughness of samples was prepared with a 200-grit silicon carbide (SiC) grinding-paper for samples 11-19, and with a 600-grit SiC grinding-paper for samples 21-29. Samples 1,10 and 7 were prepared with a 1μm polish. The bulk thermal diffusivity of the AISI 8620 steel was measured by photothermal radiometry in transmission [79] for three disks of 850μm, 500μm and 250μm. The average value obtained for thermal diffusivity is $0.125 cm^2/s$ which is within $0.005 cm^2/s$ of the documented value that exists for a similar low carbon steel [80].

Case hardness depth	0.02"	0.04"	0.06"	Photothermal test
200 grit (~5μm)	**sample 11** **sample 12** **sample 13**	**sample 14** **sample 15** **sample 16**	**sample 17** **sample 18** **sample 19**	**sample 32**
600 grit (~2.5μm)	**sample 21** **sample 22** **sample 23**	**sample 24** **sample 25** **sample 26**	**sample 27** **sample 28** **sample 29**	**sample 33**
Mirror Polish	**sample 1**	**sample 10**	**sample 7**	**sample 31**
Hardness test	**sample 34**	**sample 35**	**sample 36**	

Table 4.1 AISI 8620 steel sample matrix

The samples were first carburized, and then quenched at three case depths. The case depth is defined by 0.25% C on the carbon profile, as shown in Figure 4.9. The carbon profile curve is a preprocess factory estimation of heating process that will occur. Carbon is the principal hardening element in all steel. There are several kinds of carbon steel, classified by the quantity of carbon they contain and their mechanical properties. By composition, steels are classified as low carbon (<0.2%C), medium carbon (0.2-0.5%C) and high-carbon (>0.5%C). Figure 4.10 shows a simplified portion of the iron-carbon phase diagram [81]. Pure iron exists in two crystal forms below its melting point. One is the body-centered cubic (BCC), which is the stable form in room temperature, and is known as α-ferrite in the low temperature range, and δ-ferrite in the high temperature range. The other crystal form is the face-centered cubic (FCC) form known as austenite or γ-iron. Iron is uselessly soft without carbon. Carbon profoundly changes the phase relationships, microstructure and properties in steels [81]. At the eutectoid point D, austenite, ferrite and cementite (iron carbide-Fe_3C) all exist in equilibrium. Carburizing is the process by which the carbon concentration of a ferrous alloy is increased by diffusion. In this heat treatment process (approximately equilibrium condition), pearlite formation is accomplished by carbon diffusion. This is a time-dependent process where the carbon atoms diffuse away from regions that become ferrite to regions that become cementite. Both components grow in layers to form the lamellar structure of pearlite as carbon continues to be rejected by ferrite. A strong alloy (ferrite+cementite) results from this process. Quenching heat treatment is the rapid cooling process after carburizing that produces the highest hardness in steels. This heating treatment results in a martensite structure which is not present in the phase-diagram because it is formed under strictly non-equilibrium conditions. With quenching carbon diffusion is prevented, and thus the carbon remains fixed in a lattice structure, setting up intense local lattice strains that block movement of dislocations. As a result, the structure is hard and extremely strong.

After heating treatment the test samples were cross-sectioned and polished to observe the microstructure. For maximum contrast in developing ferrite grain boundaries in carburized and quenched steels, the samples were etched in 2% Nital (2ml of HNO_3 in 100ml of alcohol). An optical microscope image (X80) of the pearlite to ferrite gradient (1mm deep) for the deepest carburized depth (0.06") is shown in Figure 4.11. Under the optical microscope the pearlite structure has an iridescent appearance. Scanning electron microscope (SEM) pictures at X300 magnification are shown for different depths of the sample in Figure 4.12. Close to the surface the pearlite alloy exists (Figure 4.12a). Figure 4.12b shows the gradual interface between the pearlite and the original ferritic structure of AISI 8620 steel, and Figure 4.12c is at the center of the sample where the original ferritic form of the sample is maintained. In Figure 4.13 the martensite microstructure under the SEM for a) X1500 and b) X300 magnification is shown. Martensite has a needle-like structure that is formed by carbon being trapped in the iron crystal lattice. The gradient of the martensite is observed (Figure 4.14) under an optical microscope with the structure showing high carbon martensite to low carbon martensite. For a sample of this thickness (1cm) the whole structure is changed to martensite and therefore the bulk of the sample has a different structure than that of untreated and carburized steel.

Since microhardness testing is a time consuming and costly process, there is a demand for non-destructive testing in the heat treating industry. A photothermal non-destructive method which can monitor hardness (indirectly), would be an important achievement for the industry. Figure 4.15 shows the hardness profile for the carburized and quenched microhardness test of samples 34, 35 and 36 (Table 4.1). The carburized slow cool samples show a low and mild hardness profile, whereas after quenching the profile becomes harder and sharper. The error margin for these microhardness tests is between ±10HV for 300HV and ±20HV for 700HV with the error bars for each microhardness test shown in Figure 4.15. For the sake of clarity, in Figure 4.15, the last measured value for carburizing is not shown. This value is 193±7HV at 3810μm. The heating processes and microhardness tests were performed by B&W Heat Treating Ltd. (Kitchener, Ontario). Experimental frequency scans were performed on the same samples for three consecutive processes: first, the rough untreated process, second, the carburizing process, and finally, the quenching process.

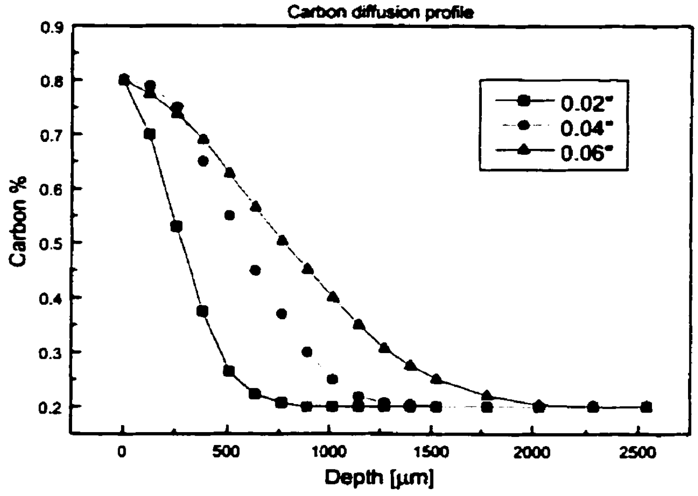

Figure 4.9 Carbon profile for case depths 0.02", 0.04" and 0.06".

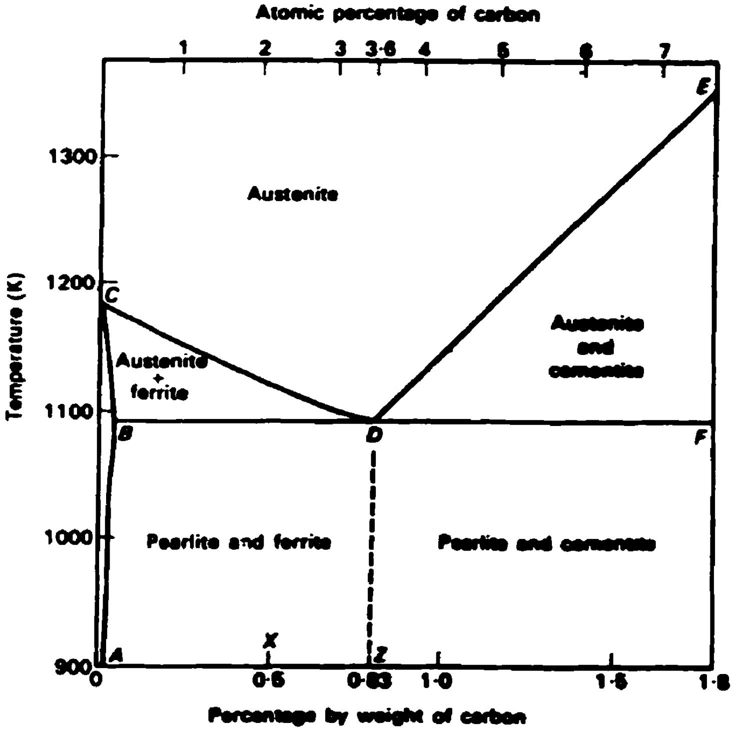

Figure 4.10 Simplified portion of the iron-carbon phase diagram [81].

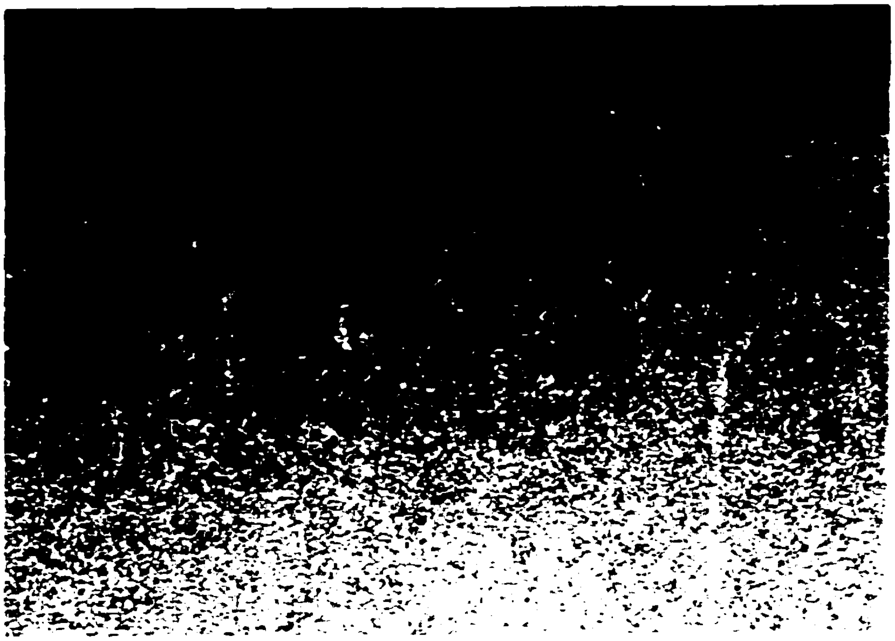

Figure 4.11 Optical microscope image; magnification X80; 1mm depth of pearlite to ferrite structure.

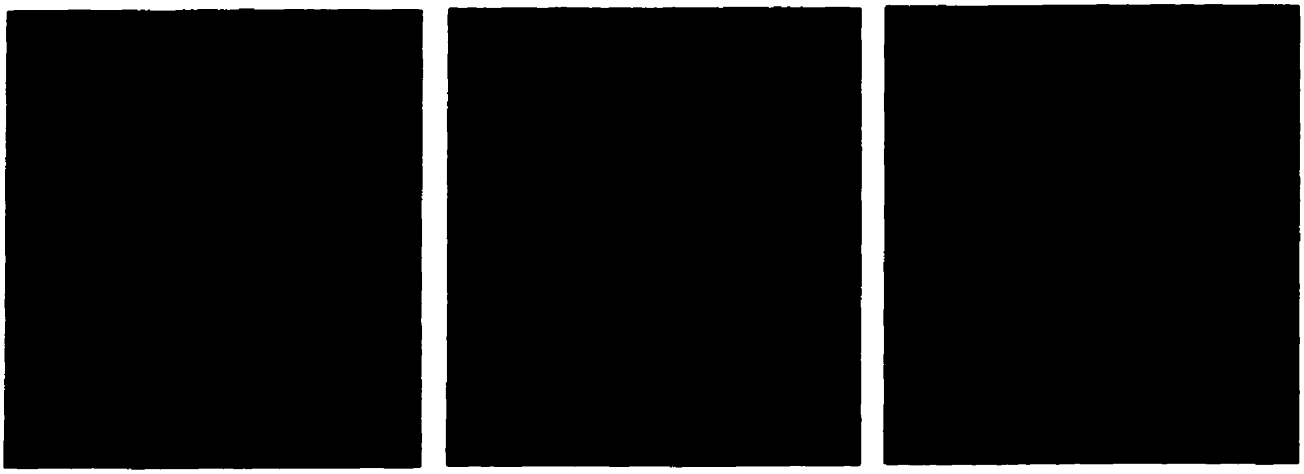

(a) (b) (c)

Figure 4.12 Microstructure of pearlite gradient; SEM magnification X300; a) pearlite; b)pearlite to ferrite; c) ferrite.

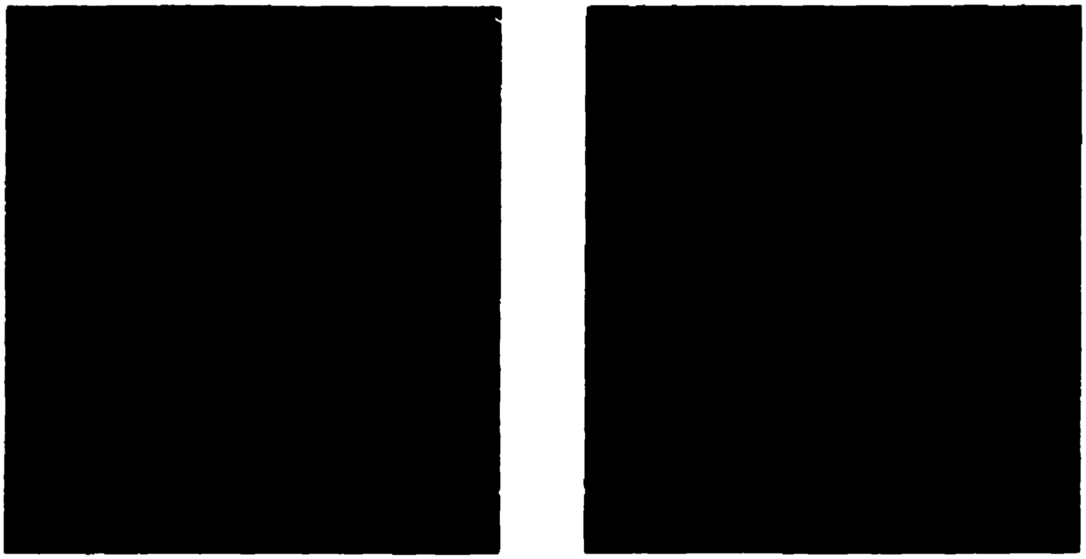

(a) (b)

Figure 4.13 Microstructure of martensite formed by quenching; SEM magnification a) X1500; b) X300.

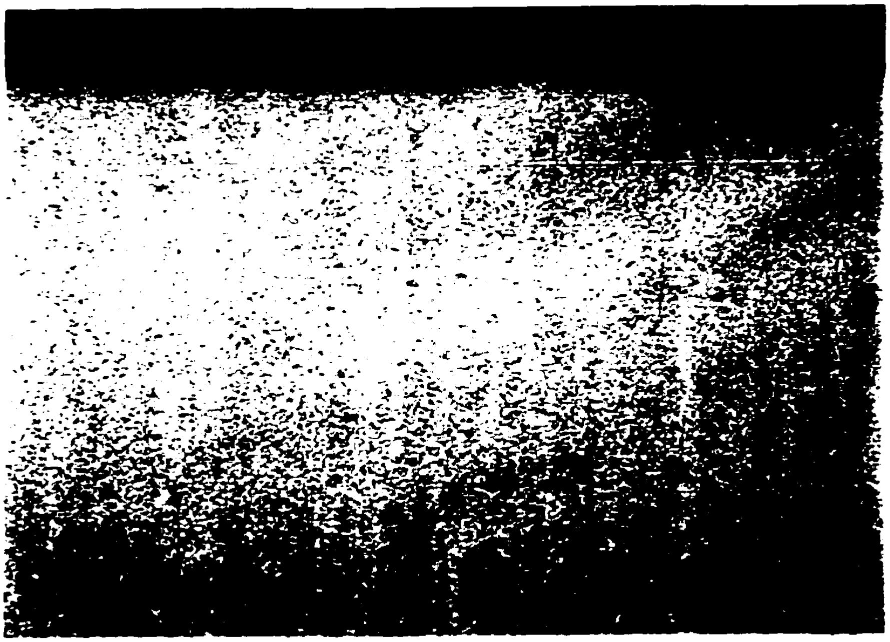

Figure 4.14 Optical microscope image (X80) of 1mm deep martensite gradient; high carbon martensite near surface; low carbon martensite in the bulk.

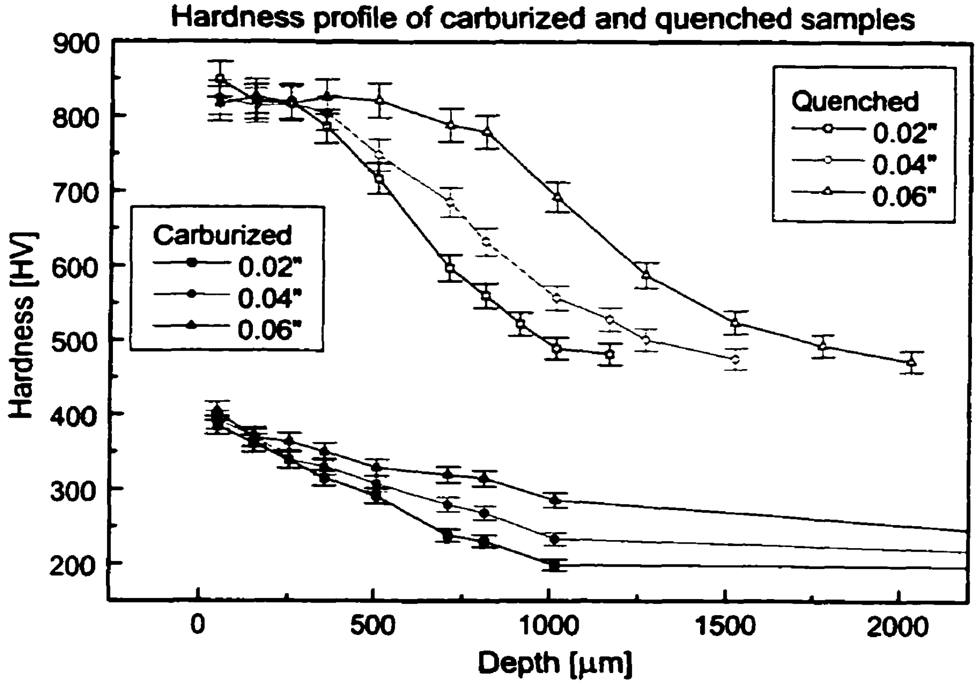

Figure 4.15 Hardness profile for carburized and quenched process of case depths 0.02", 0.04" and 0.06" (performed by B&W Heat Treating Ltd., Kitchener, Ontario).

4.4 Forward Experimental Data and Discussion

4.4.1 Untreated Experimental Data

Figures 4.16 and 4.17 show the normalized frequency response (amplitude and phase) of the untreated 200 and 600 grit samples, respectively. Roughness affects both the amplitude and phase response of a sample throughout the entire frequency spectrum, causing peaks in both the amplitude and phase data at different frequencies. This response is a notable deviation from the response of a homogeneous sample, which exhibits a constant normalized amplitude and phase of 1 a.u. and 0 degrees, respectively. At high frequencies, the penetration depth of the signal is shallow, and therefore information about the surface can be obtained. The surface thermal effusivity of the sample can be obtained by theoretically fitting the experimental response to a homogeneous layer (roughness layer) with a semi-inifinite homogeneous substrate to the model derived in equation (2.43). The effusivity, $e=(k\rho c)^{1/2}$, near the surface is the relevant thermal parameter in time-dependent surface-heating processes, rather than the thermal diffusivity, $\alpha=k/\rho c$, which governs the propagation inside the solid [82]. The thermal conductivity, k, mass density, ρ, and the specific heat capacity, c, can be measured separately for the bulk material. The homogeneous substrate was the same for all samples since the samples were obtained from the same steel rod. The only unknowns in equation (2.43) are the thermal diffusivity and conductivity, which when combined can be represented by the thermal effusivity of the rough layer. The roughness thickness, d, of each sample was measured independently with a surfometer (Series 400; Precision Devices, Milan, MI) of a 0.01μm total system resolution. The instrument measures over an evaluation length, which is the length over which the surface parameters are evaluated. The evaluation length (10mm) for each measurement consisted of five sampling lengths, where the sampling length is defined as the nominal wavelength used for separating roughness and waviness. For each measurement the following three surface parameters were documented: 1) roughness average, *R*a, 2) maximum height of the profile, *R*t, and 3) average maximum height of the profile, *R*z. *R*a is the arithmetic average of the absolute values of the profile heights over the evaluation length, *R*t is the vertical distance between the highest and lowest points of the profile within the evaluation length, and *R*z is the average of the successive values of *R*ti (*R*t of each sampling length) calculated over the evaluation length. The measurements were repeated at three independent positions on the surface of the sample, and the final value of each surface parameter was obtained as an average of the three measurements. For theoretical fitting the average of three independent *R*z values, $\mathrm{avg}_3(Rz)$, was used as the roughness thickness, *d*, in equation (2.43). This parameter was chosen as the effective thickness that generates the photothermal signal that can be modeled as a homogeneous layer on a semi-infinite substrate. In Table 4.2 the roughness thickness, d=avg$_3$(Rz) is documented for each sample. The average of the three independent values of *R*a, avg$_3$(*R*a), is also included in parenthesis.

Using the roughness thickness as a known parameter for each sample along with the bulk thermal properties, theoretical fitting was performed using equation (2.43) on all the samples. The actual thermal effusivity of the rough layer, can be seen in Table 4.2 for each untreated sample. It is found that the surface roughness effusivity is of lower thermal effusivity than the bulk, which is consistent with previous findings by Bein et al. [82]. The bulk thermal effusivity of the AISI 8620 steel is 13100 Ws$^{1/2}$/m^{2}K. The average surface thermal effusivity for the 600 grit (~2.5μm) samples was found to be 4808 Ws$^{1/2}$/m^{2}K and for the 200 grit (~5μm) was 2949 Ws$^{1/2}$/m^{2}K (Table 4.3). It was therefore concluded that as roughness increases the thermal effusivity of the surface decreases. Qualitatively, this can be understood phenomenologically by considering that roughness consists ideally of a series of pyramidal (or conical or triangular fin-like) structures of decreasing spatial extent away from the baseline [83]. The temperature rise due to optical absorption and thermal conversion inside these material shapes will be progressively higher closer to the apex of the pyramids [83], i.e with increasing modulation frequency or decreasing equivalent-thickness overlayer. The excess apex temperature will decrease the material thermophysical properties, leading to an increase in the experimental phase. In Appendix A-1, Scanning Electron Microscope (SEM) pictures of the cross-section of the untreated photothermal test samples 31, 33 and 32 (Table 4.1) are presented for magnifications of X300 and X1500, respectively. The roughness thickness for each sample is verified with the surformeter measured values. The roughest sample exhibits the strongest peaks and valleys on the surface. As seen in Figures 4.16 and 4.17, thermally, each roughness level is related to a center-frequency, f_c (maximum of phase) which shifts to a higher frequency as roughness decreases. For the 200 grit (~5μm) samples, $f_c \simeq 5$kHz, and for the lower roughness of 600 grit (~2.5μm), $f_c \simeq 25$kHz. The amplitude typically exhibits its own center-frequency, and for the 200 grit (~5μm) samples, $f_c = 50$kHz, and for the 600 grit (~2.5μm), $f_c > 100$kHz.

200 grit d=$\text{avg}_3(Ra)$ ($\text{avg}_3(Ra)$)	**Effusivity [$Ws^{1/2}/m^2K$]**			600 grit d=$\text{avg}_3(Ra)$ ($\text{avg}_3(Ra)$)	**Effusivity [$Ws^{1/2}/m^2K$]**		
	Untreat actual	Carburize effective	Quench effective		Untreat actual	Carburize effective	Quench effective
11 d=5.1μm (0.85μm)	3381	6483	2691	**21** d=2.3μm (0.33μm)	4761	6198	3298
12 d=5μm (0.83μm)	3381	6514	2937	**22** d=2.5μm (0.35μm)	4942	6126	3744
13 d=5μm (0.82μm)	2977	6419	3000	**23** d=2.6μm (0.35μm)	4659	6609	3995
14 d=5μm (0.83μm)	2667	4775	2307	**24** d=2.6μm (0.37μm)	4989	4347	4472
15 d=5μm (0.84μm)	2605	5774	2569	**25** d=2.6μm (0.35μm)	4553	3783	3479
16 d=5μm (0.83μm)	2754	4996	2384	**26** d=2.5μm (0.34μm)	4863	4648	3323
17 d=5.1μm (0.84μm)	2822	5693	2452	**27** d=2.5μm (0.33μm)	4855	5915	4165
18 d=4.7μm (0.78μm)	3408	5515	2727	**28** d=2.5μm (0.36μm)	4839	5989	3735
19 d=4.8μm (0.80μm)	2829	4884	2616	**29** d=2.4μm (0.33μm)	4808	5470	3465

Table 4.2 Rough layer effusivity values for all samples under all processes.

200 grit samples (~5μm)	Average Effusivity [Ws$^{1/2}$/m^{2}K]			600 grit samples (~2.5μm)	Average Effusivity [Ws$^{1/2}$/m^{2}K]		
	Untreated actual	Carburize effective	Quench effective		Untreated actual	Carburize effective	Quench effective
0.02"	-	6472	2876	**0.02"**	-	6311	3679
0.04"	-	5182	2420	**0.04"**	-	4260	3758
0.06"	-	5364	2598	**0.06"**	-	5791	3788
All	2949	-	-	All	4808	-	-

Table 4.3 Rough layer average effusivity values in terms of case depth samples.

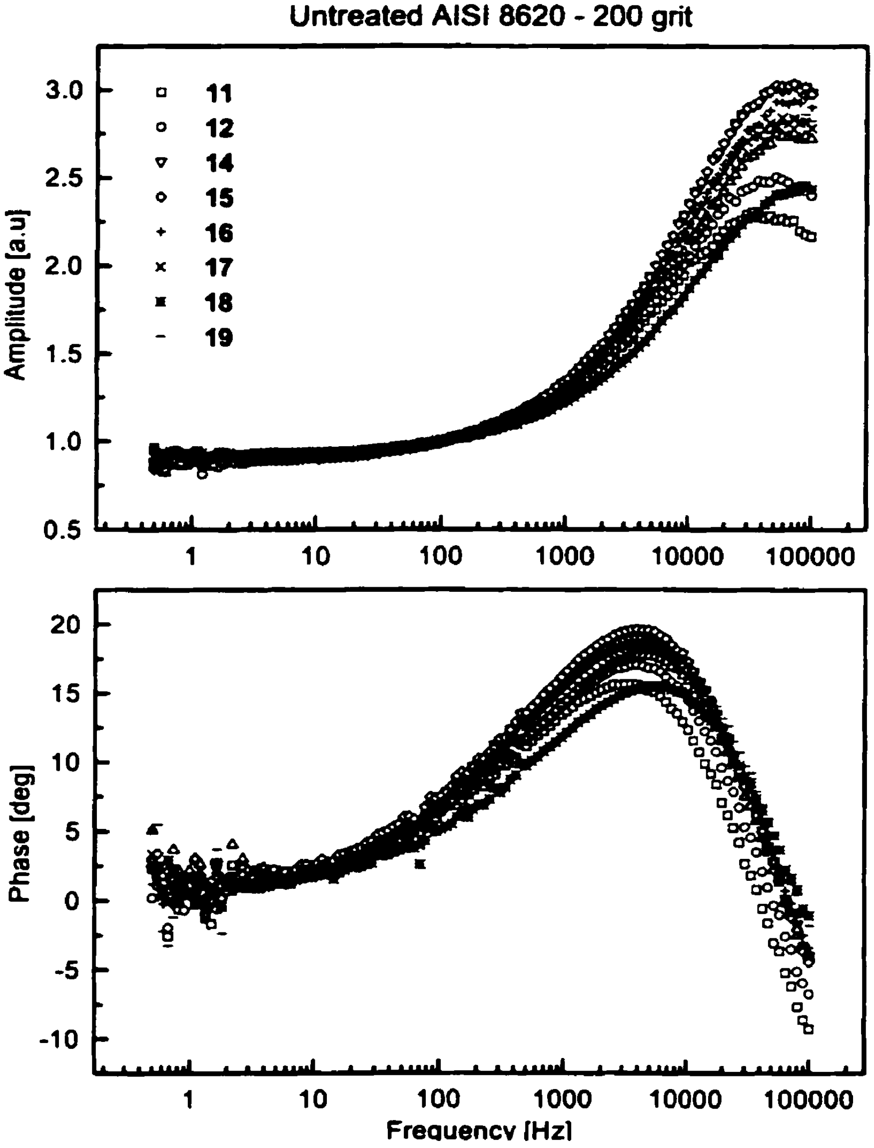

Figure 4.16 Frequency scans (amplitude and phase) of untreated 200 grit samples.

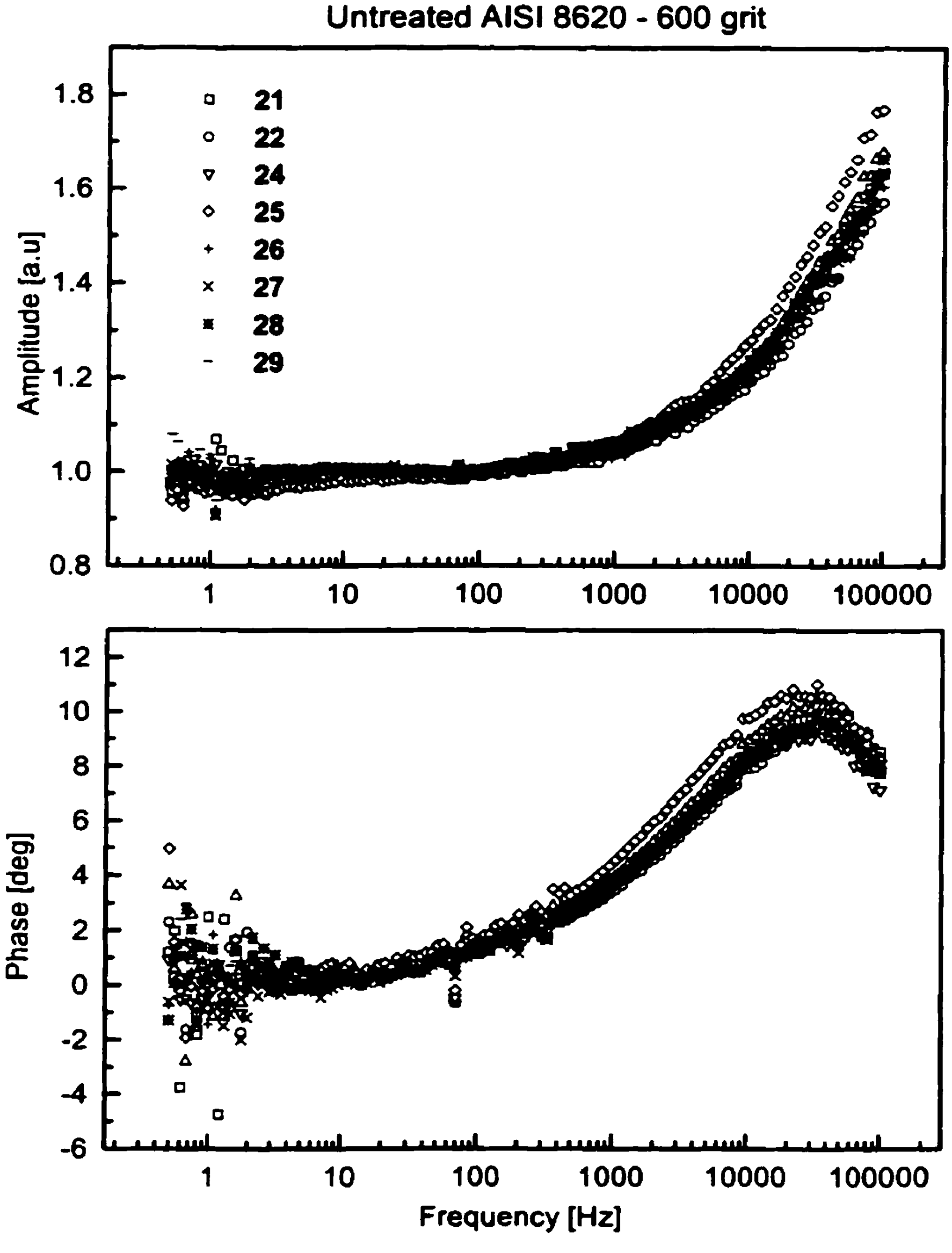

Figure 4.17 Frequency scans (amplitude and phase) of untreated 600 grit samples.

4.4.2 Carburized Experimental Data

Frequency scans (amplitude and phase) of the same range were performed on all carburized samples, as shown in Figures 4.18 and 4.19 for the 200 and 600 grit, respectively. Figures 4.20 and 4.21 are the smoothed data to be used in Chapter 5 for the reconstruction process for the 200 and 600 grit, respectively. Although the reconstruction method proved to work reasonably with noisy data [36], smoothed data was chosen in this work so as to reduce any uncertainties associated with noise. Upon investigation, it was found that the best smoothing of experimental data is performed using a 7th order polynomial fit. In all figures, the experimental data is color coded based on case depth; 0.02" samples are black, 0.04" samples are red, and the 0.06" depth samples are blue. When the carburized data is compared to the untreated data, it is observed that the surface thermal effusivity of these samples has increased. At the same time the Full-Width-Half-Maximum (FWHM) of the high frequency response is narrower, supporting an inhomogeneous behavior for the roughness layer. The rough layer thermal effusivity values for these samples are documented in Table 4.2. In Table 4.3 and the average rough layer thermal diffusivity per case depth is calculated. The effusivity values are effective values since they were obtained by fitting the phase maximum to the homogeneous layer with homogeneous semi-infinite substrate, i.e., equation (2.43). The thermal properties of the samples are related to the case depth and thus the thermal effusivity behaves accordingly. Overall the surface thermal effusivity of the 0.02" case depth is higher than that of the 0.04" and 0.06" case depth samples. The carburizing process has changed the surface and the most dramatic change is seen in samples 24, 25 and 26 (Figure 4.19). These samples behave like the rougher samples 14, 15 and 16 (Figure 4.18). All samples were re-measured with the surformeter and the roughness thickness was found to be approximately the same within a tolerance of $\pm 0.1 \mu m$. To investigate the effects of carburizing on the surface further, the samples were observed under Scanning Electron Microscope (SEM). In Appendix A-2 and A-3 the surfaces (top view) of the untreated photothermal test samples and the carburized samples are shown for magnifications X300 and X1500, respectively. The samples are shown in the form of a matrix with each column representing a distinct roughness thickness: ~0.1μm(polished), ~2.5μm and ~5μm, sequentially. Each row represents a unique treatment of the samples: untreated, 0.02", 0.04" and 0.06" carburizing depth, sequentially. Sample 31 is the untreated polished sample and samples 1, 10 and 7 are the polished samples that were carburized with 0.02", 0.04" and 0.06" case depth, respectively. As the case depth increases, microcracks and clusters that form at the surface increase. This is consistent with the fact that the deepest case depth has endured the longest oven time. The porosity of these samples has also increased as is more evident in Appendix A-3, where the X1500 magnification is shown. Similarly, sample 33 (2.5μm) is compared with same roughness carburized-samples 21, 24 and 27 of case depth 0.02", 0.04" and 0.06", respectively, and sample 32 (5μm) is compared with the same roughness carburized-samples 11, 14 and 17 of case depth 0.02", 0.04" and 0.06", respectively. The surface modifications should be similar to that of samples 1, 10 and 7 since they have endured the same process. Although more difficult to see, one observation is that the roughness seems to be more closely packed with valleys of clusters. On sample 24, which is one of the samples that behave differently, there are traces of elements shown as large white spheres, as seen in Appendix A-3. This may be the reason the thermal properties of the surface (lower thermal diffusivity) have changed so drastically. Both the photothermal signal and the SEM pictures support a change in the surface structure occurring with the carburizing process.

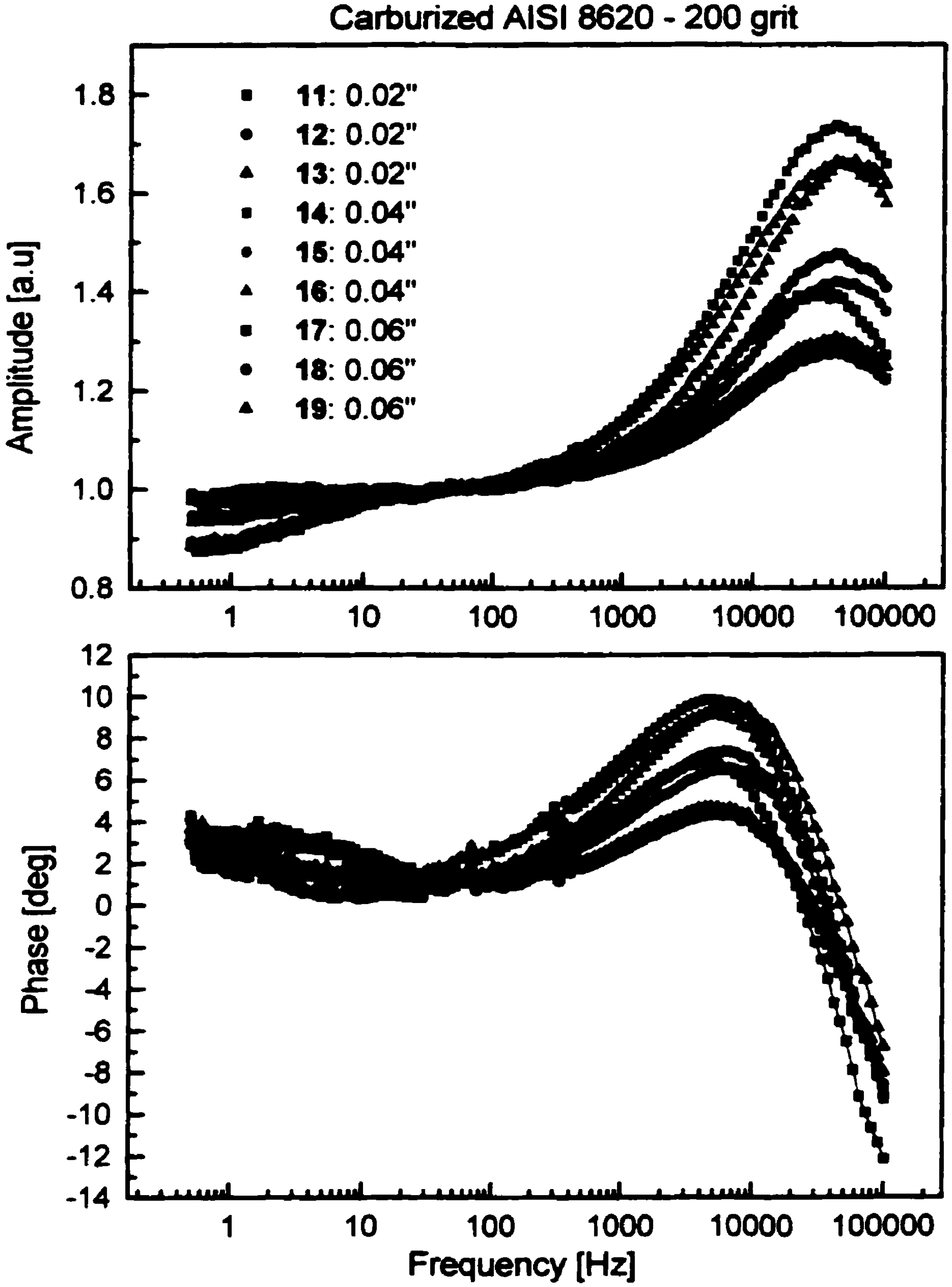

Figure 4.18 Frequency scans (amplitude and phase) of carburized 200 grit samples.

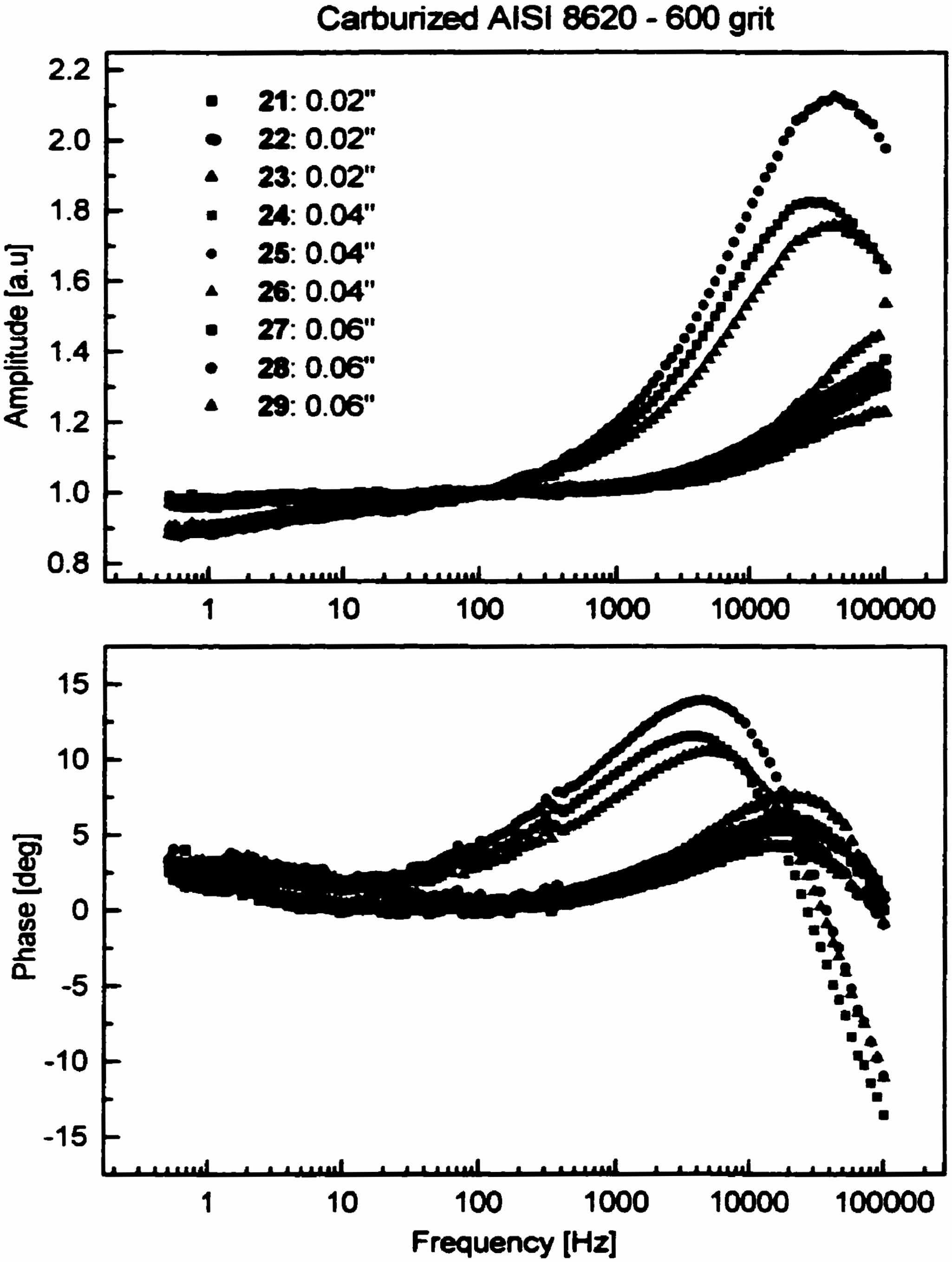

Figure 4.19 Frequency scans (amplitude and phase) of carburized 600 grit samples.

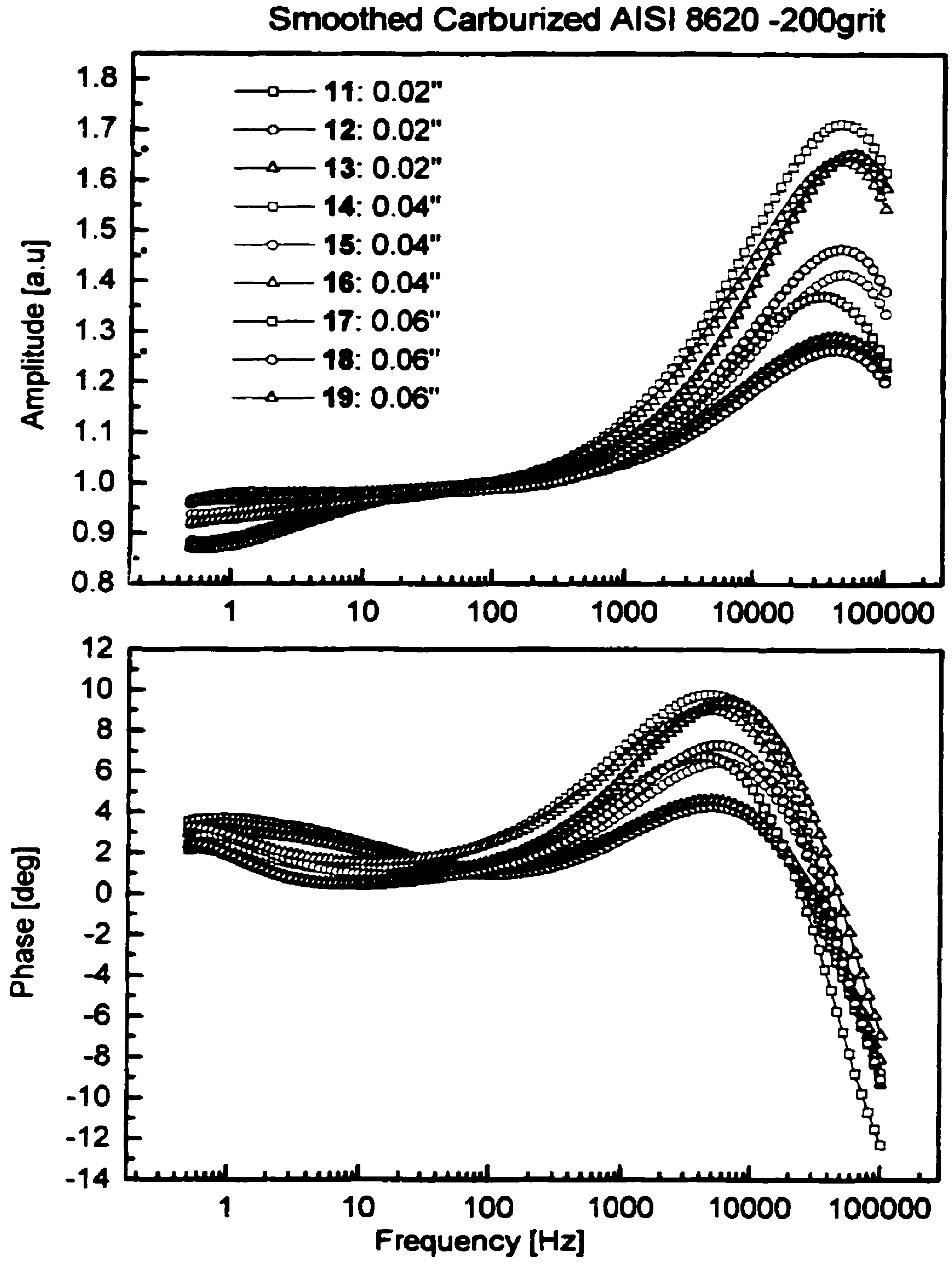

Figure 4.20 Smoothed data for carburized 200 grit samples.

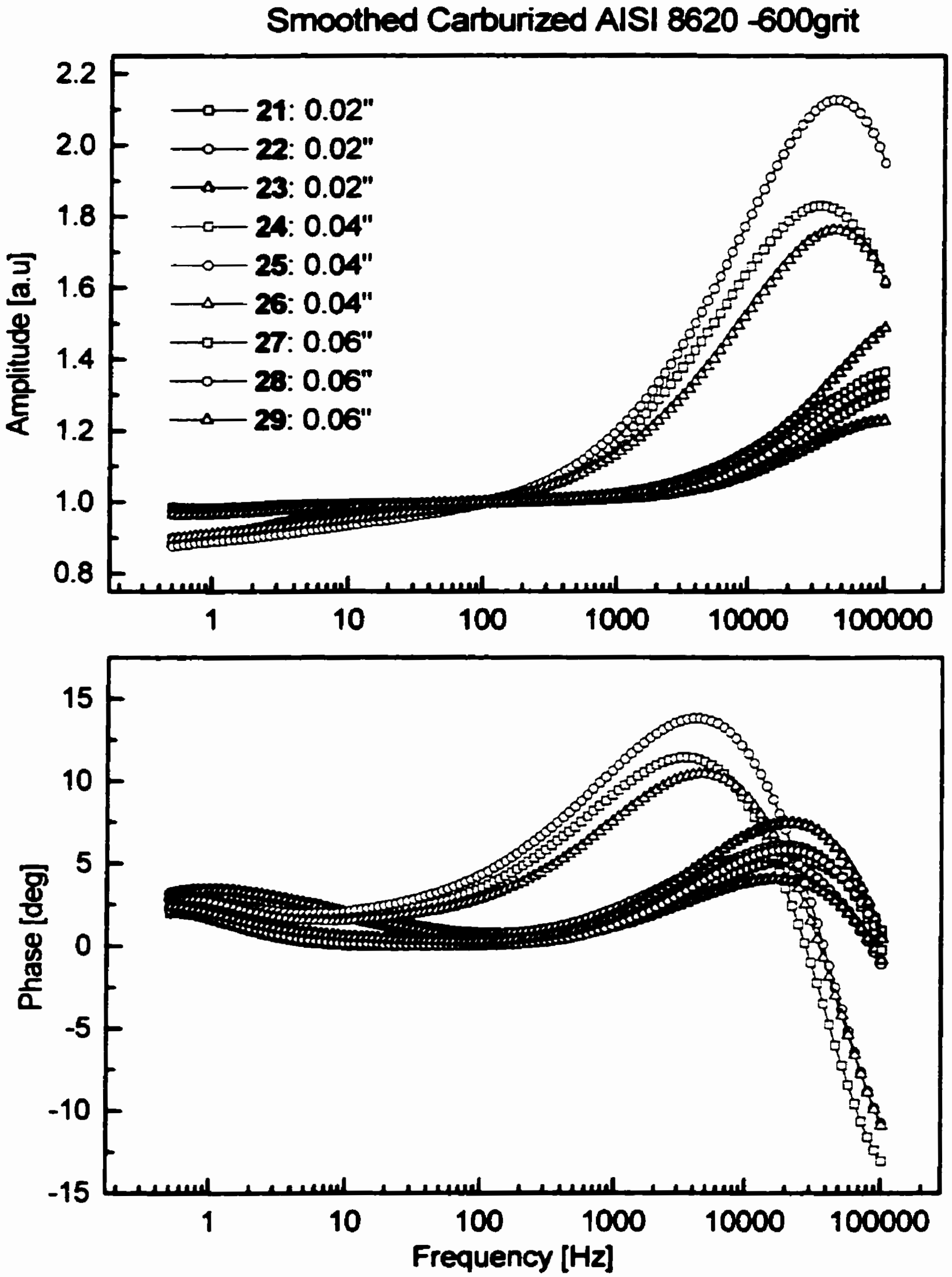

Figure 4.21 Smoothed data for carburized 600 grit samples.

4.4.3 Quenched Experimental Data

After the carburizing slow cool process, the samples were sent back to the factory for oil quenching. The photothermal signals for the 200 and 600 grit samples were then taken for these samples as shown in Figures 4.22 and 4.23, respectively. Figures 4.24 and 4.25 are the respective smoothed data to be used in Chapter 5 for reconstructions. In general, the low frequency inhomogeneous region resembles the response from the carburized data. In Figure 4.26 the untreated, carburizing and quenched frequency response of sample 11 (200 grit) are plotted for comparison. The roughness response of the quenched process has changed to resemble the response from the untreated samples at high frequency. At low frequency the data converges to that of the carburizing response. The same was re-plotted in Figure 4.27 for sample 21 (600 grit) where at low frequencies the response of quenching and carburizing processes approach each other. At high frequency, the quenched samples behave in a rougher manner than the untreated samples but are still within closer agreement as compared to the carburized response. For the quenched samples, the thermal effusivity of the rough surface for each sample is documented in Table 4.2, with the averages shown in Table 4.3. The thermal effusivity for the 200 grit is of the same order as that of the untreated steel samples. On an average, the surface thermal effusivity of the 600 grit quenched samples is lower than that of the originally untreated samples. This is consistent with Figure 4.27 where the maximum phase is the highest for quenching. The FWHM of the roughness has increased and the layer behaves in a more homogeneous manner. Samples 24, 25 and 26 again behave differently. This implies that the different behavior occurred at the carburizing stage. The samples were examined under the SEM and Appendix A-4 and A-5 show the pictures for the X300 and X1500 magnifications, respectively. The samples are shown in the form of a matrix with each column representing a distinct roughness thickness:

~0.1µm(polished), ~2.5µm and ~5µm, sequentially. Each row represents a unique treatment of the samples: untreated, 0.02", 0.04" and 0.06" carburizing depth, sequentially. Sample 24, as seen in Appendix A-5, again shows traces of white spheres. The mirror surface samples (1,11,7) of the quenched samples, look spatially similar to the carburized equivalent samples (A-3). The exception is that the quenched surfaces maintain better uniformity throughout the sample surface area.

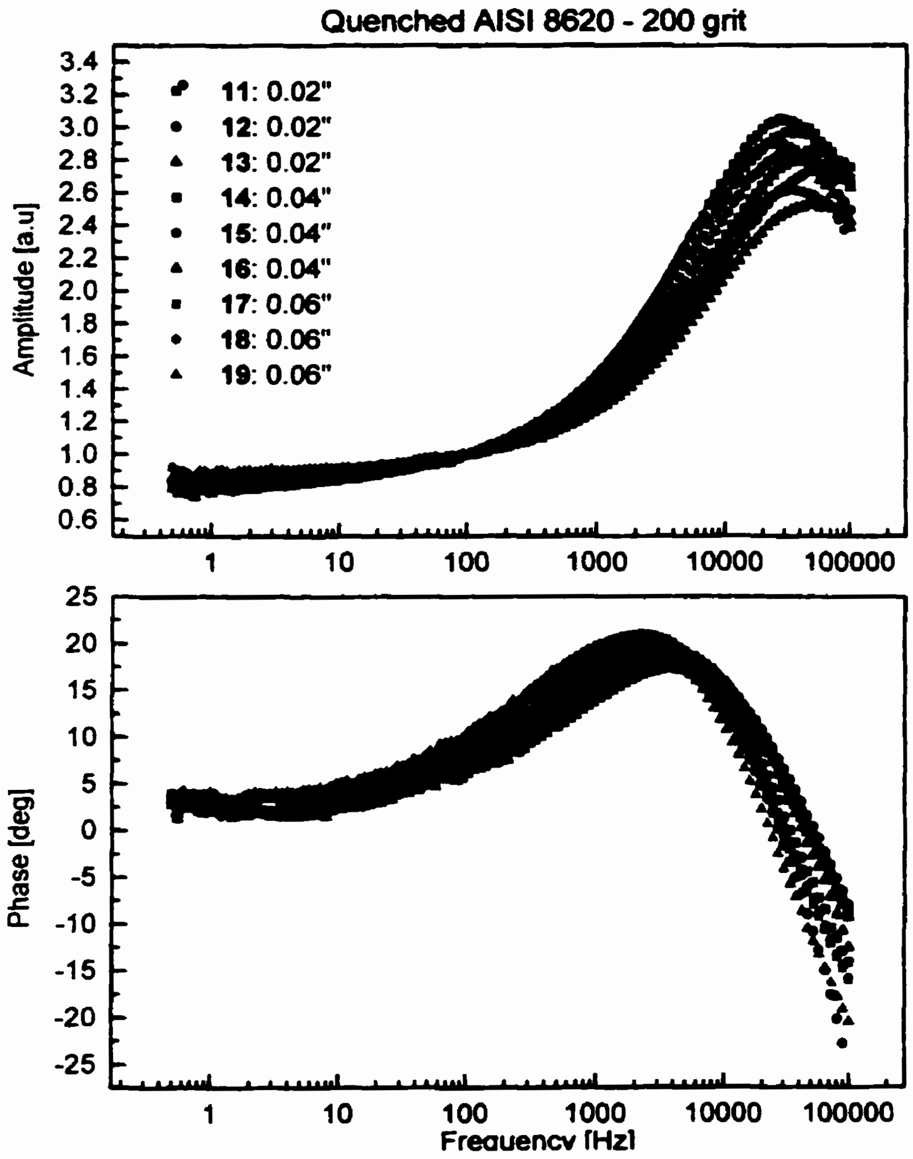

Figure 4.22 Frequency scans (amplitude and phase) of quenched 200 grit samples.

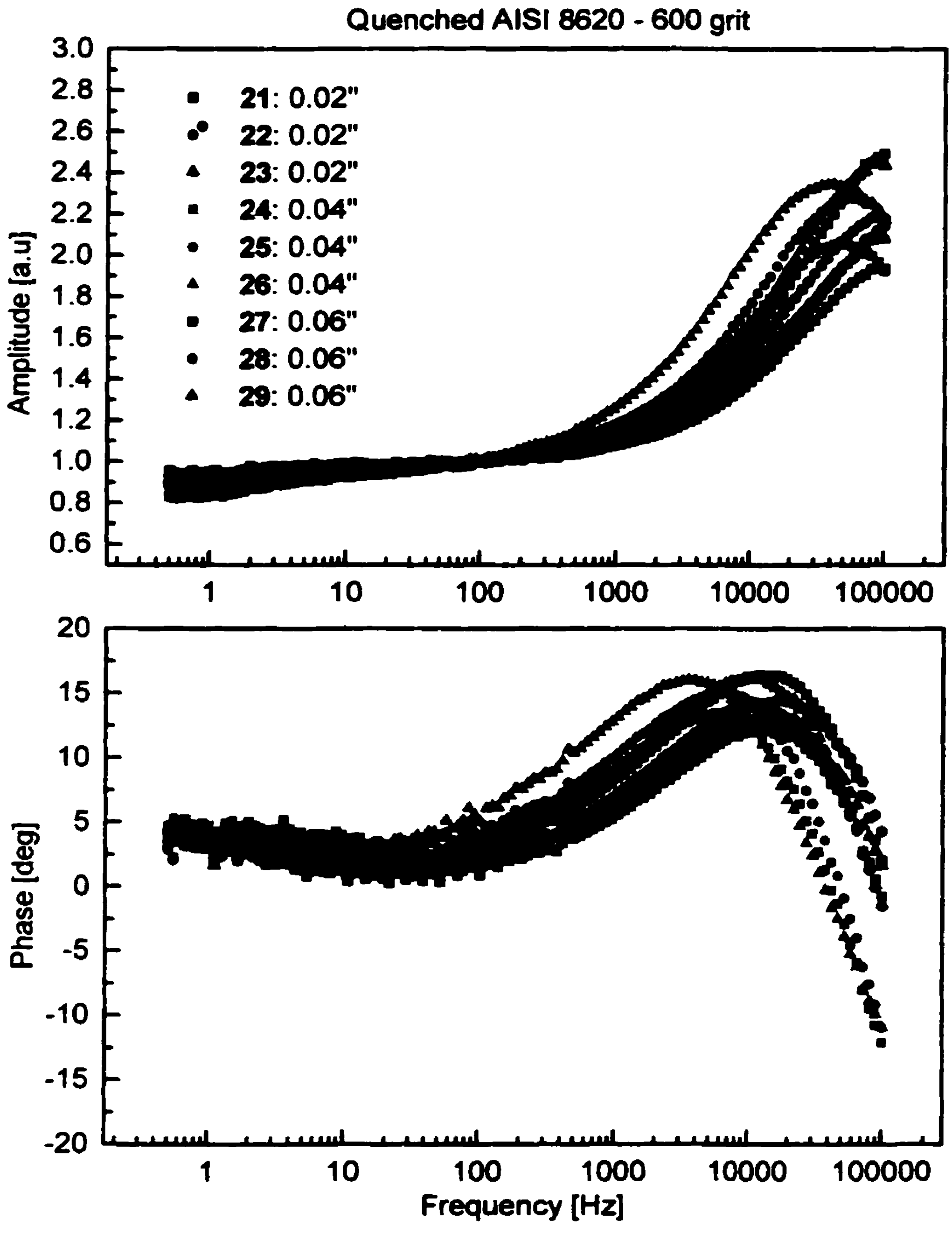

Figure 4.23 Frequency scans (amplitude and phase) of quenched 600 grit samples.

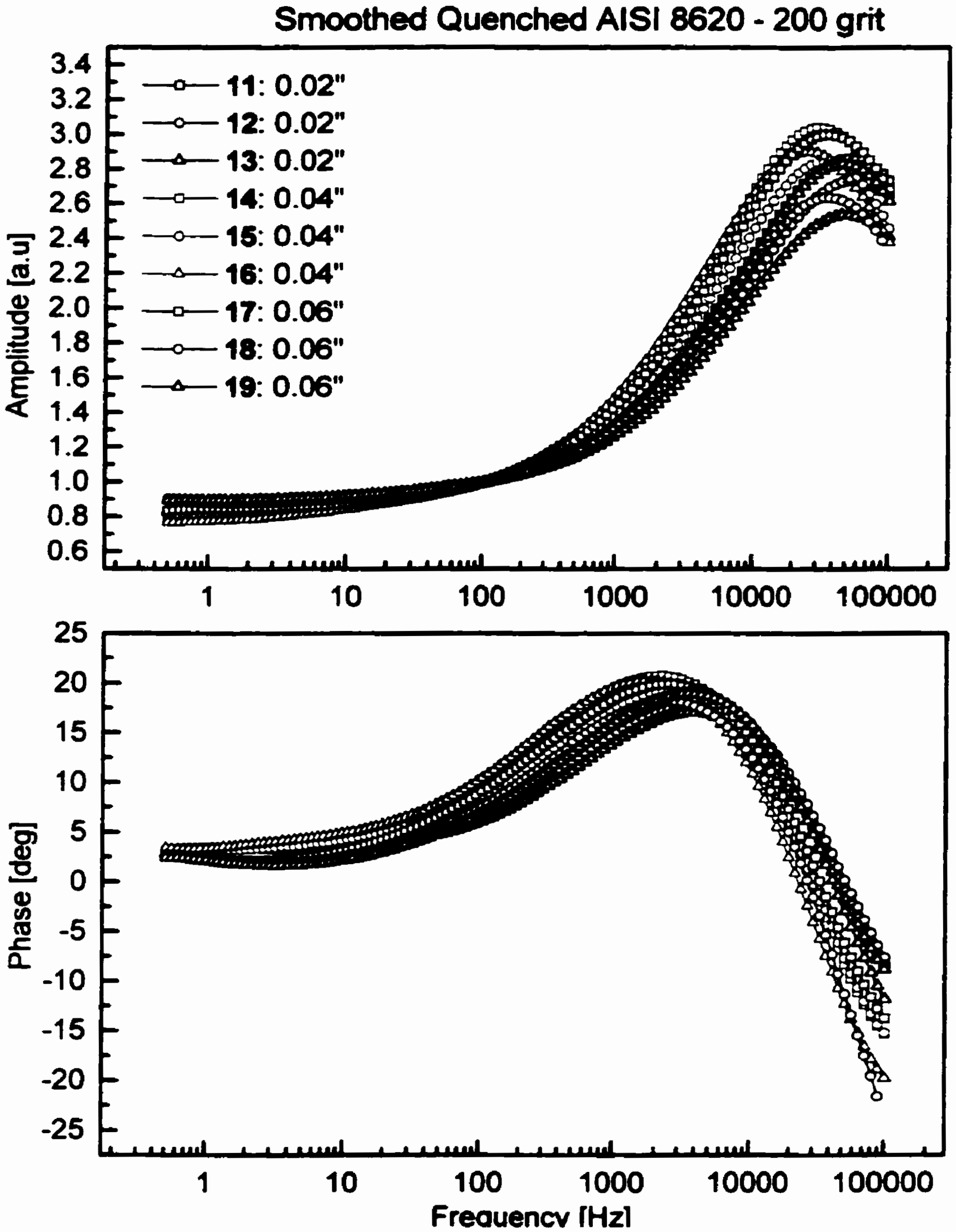

Figure 4.24 Smoothed data for quenched 200 grit samples.

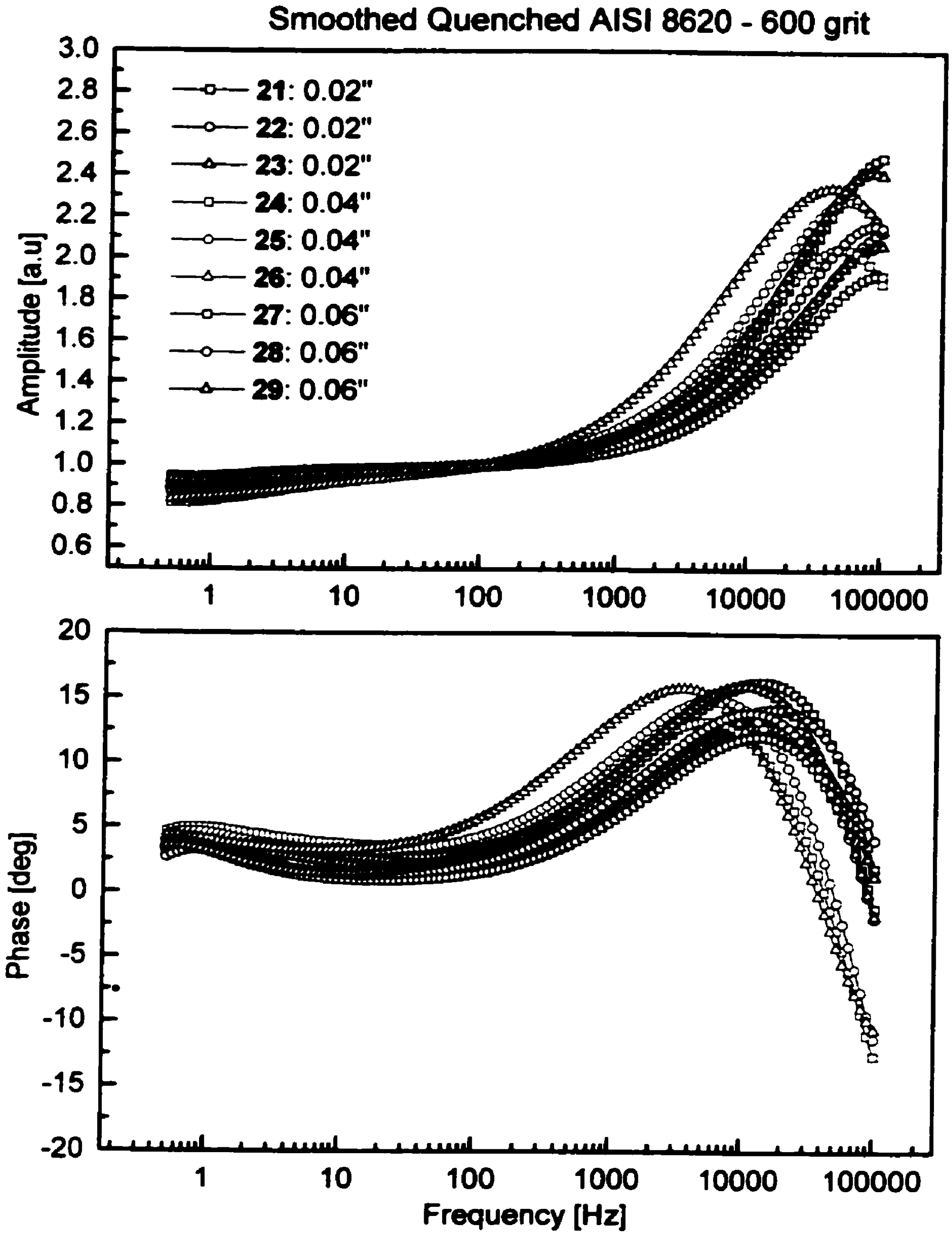

Figure 4.25 Smoothed data for quenched 600 grit samples.

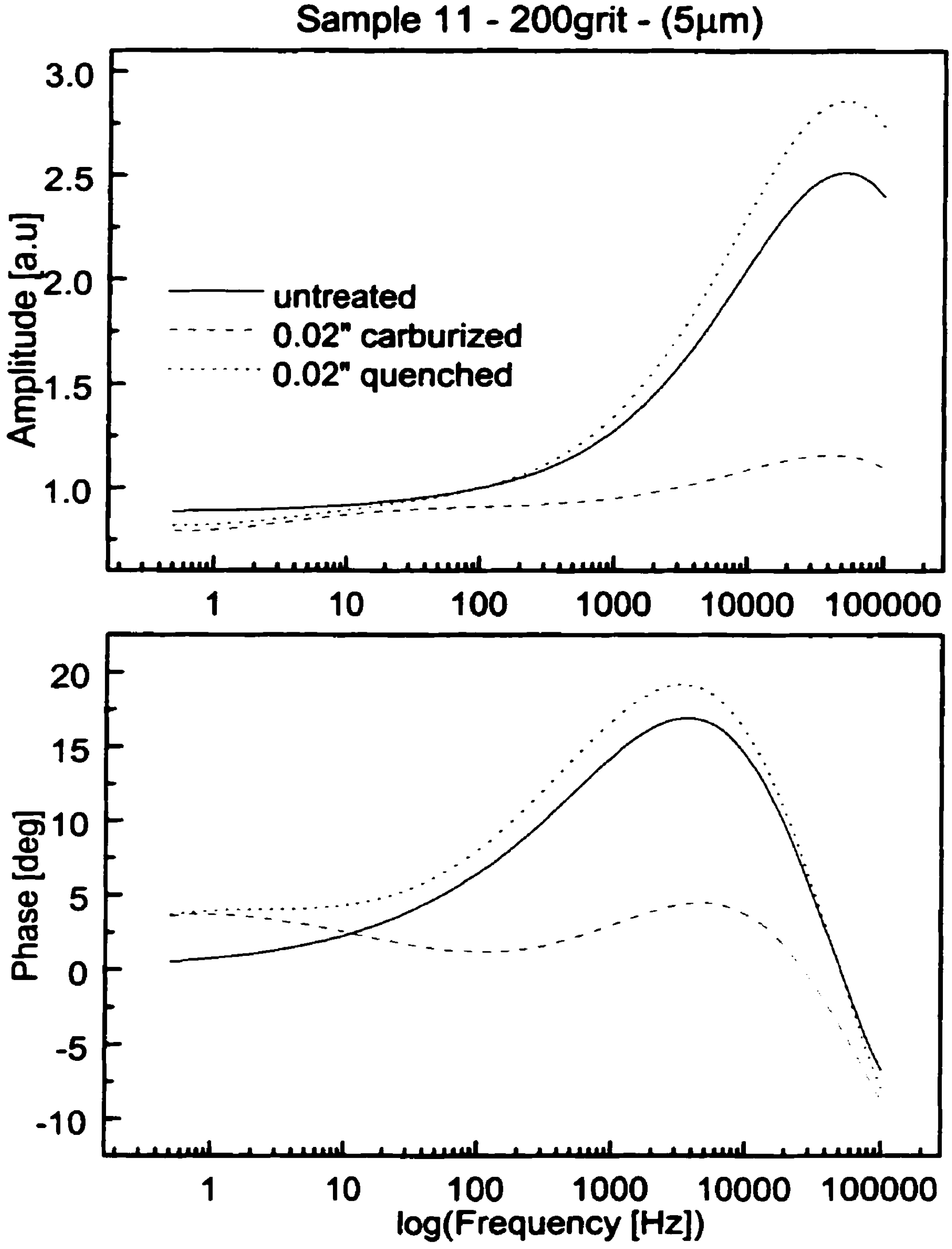

Figure 4.26 Frequency scan of Sample 11 (200 grit) for untreated (solid), carburized (dash) and quenched (dot) process.

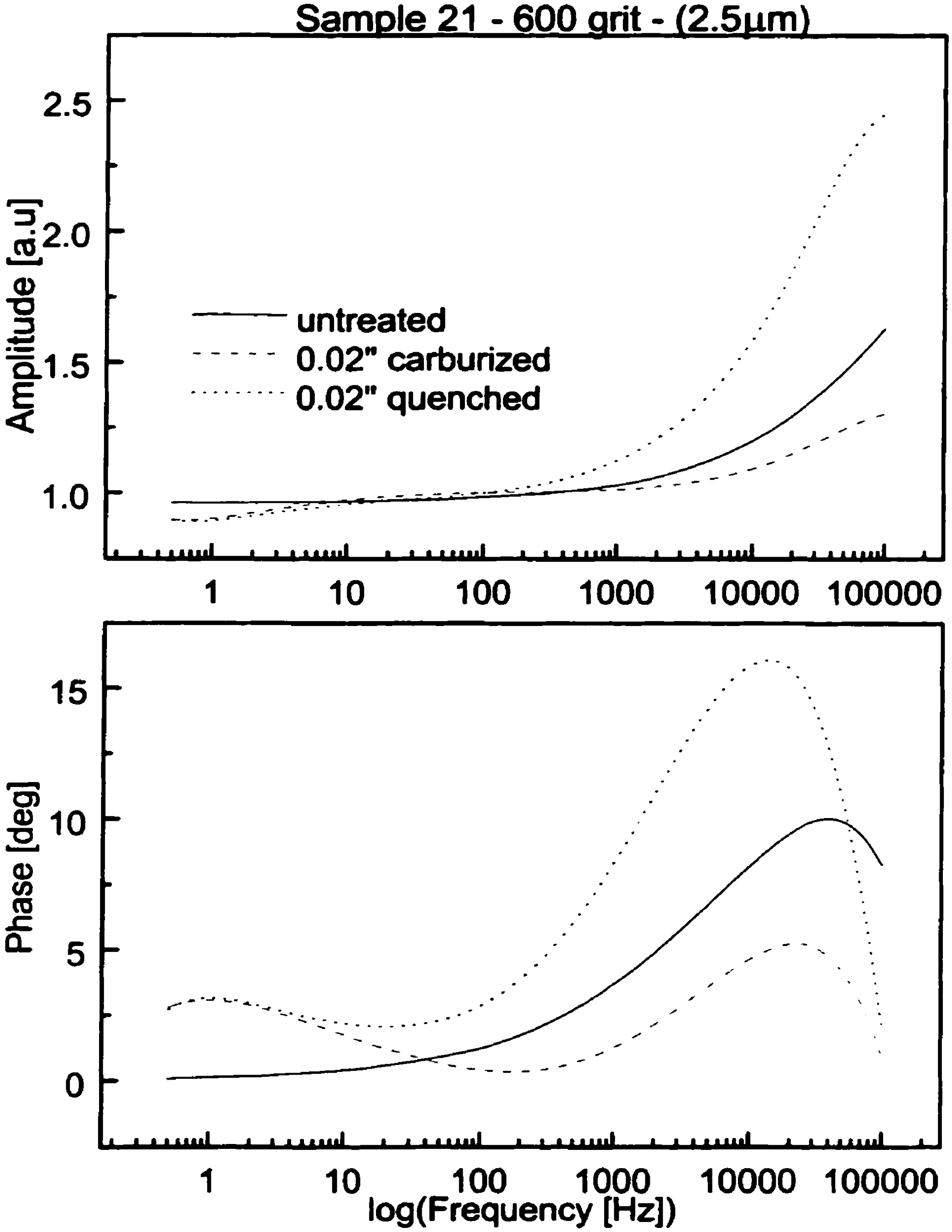

Figure 4.27 Frequency scan of Sample 21 (600 grit) for untreated (solid), carburized (dash) and quenched (dot) process

4.4.4 Bulk Thermal Diffusivity

Before the reconstruction process can take place on all the experimental data, the bulk thermal diffusivity is needed as additional information. The bulk thermal diffusivity for each cross-section of untreated, carburized and quenched data was measured using a high-resolution photothermal radiometric experimental set-up (which is described in Chapter 7) with a 27μm beam spot size. This is a three-dimensional method that enables the measurement of thermal diffusivity in reflection. The theoretical formulation of the experiments was developed in Chapter 2, and is represented by equation (2.44). The only unknown parameter in this equation is the thermal diffusivity (the thermal conductivity is k=46.6W/mK).

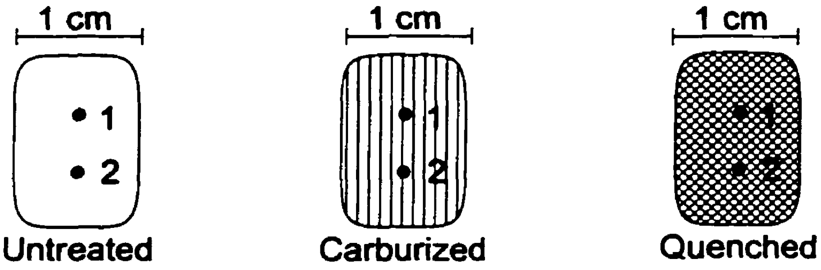

Figure 4.28 Frequency scan position for each sample of untreated, carburized and quenched category.

To increase the confidence of the results, two measurements were taken for each cross-section, as indicated in Figure 4.28. In Figure 4.29, the phase was chosen out of convenience for implementing the respective error bars for each sample. The black line represents the untreated steel, the blue line the carburized steel, and the red line is the quenched steel. The frequency response is normalized with respect to an instrumental function obtained though a Zr alloy of known thermal parameters. By fitting the Zr alloy to the theoretical response (equation 2.44) and obtaining the difference (small variations), the instrumental function was constructed. The theoretical fittings, equation (2.44), for both amplitude and phase of the normalized experimental data for the bulk untreated, carburized and quenched samples are shown in Figure 4.30. It is found that the untreated and carburized steels have the same thermal diffusivity of $\alpha=12.5\times10^{-6}m^2/s$ whereas the quenched steel has a lower thermal diffusivity of $\alpha=10.5\times10^{-6}m^2/s$. The untreated and carburized steels have the same ferritic microstructure whereas the quenched steel has a martensite structure in the bulk.

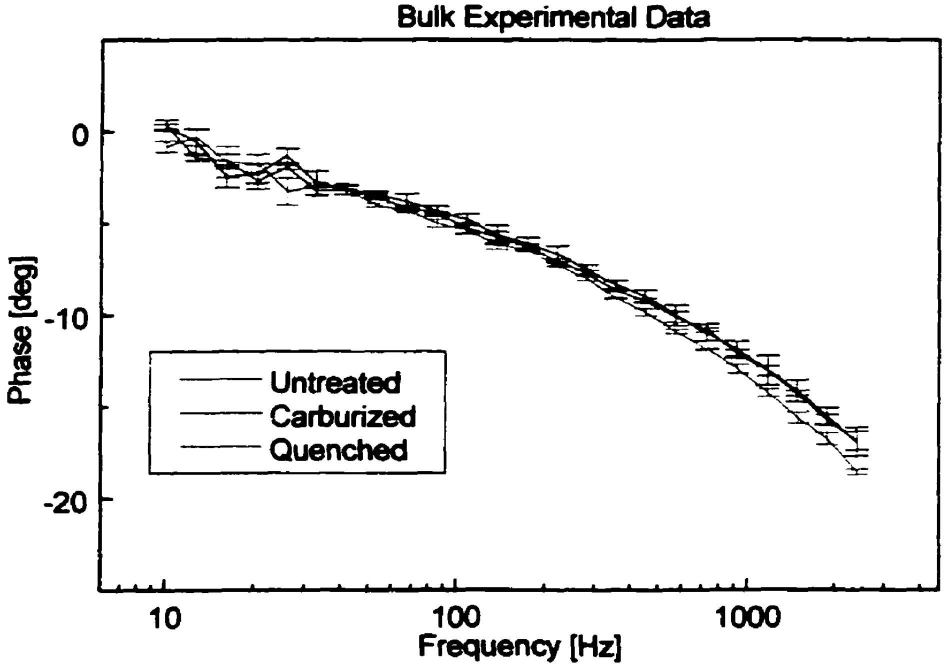

Figure 4.29 Three-dimensional experimental phase data of untreated (black), carburized (blue) and quenched (red) steel.

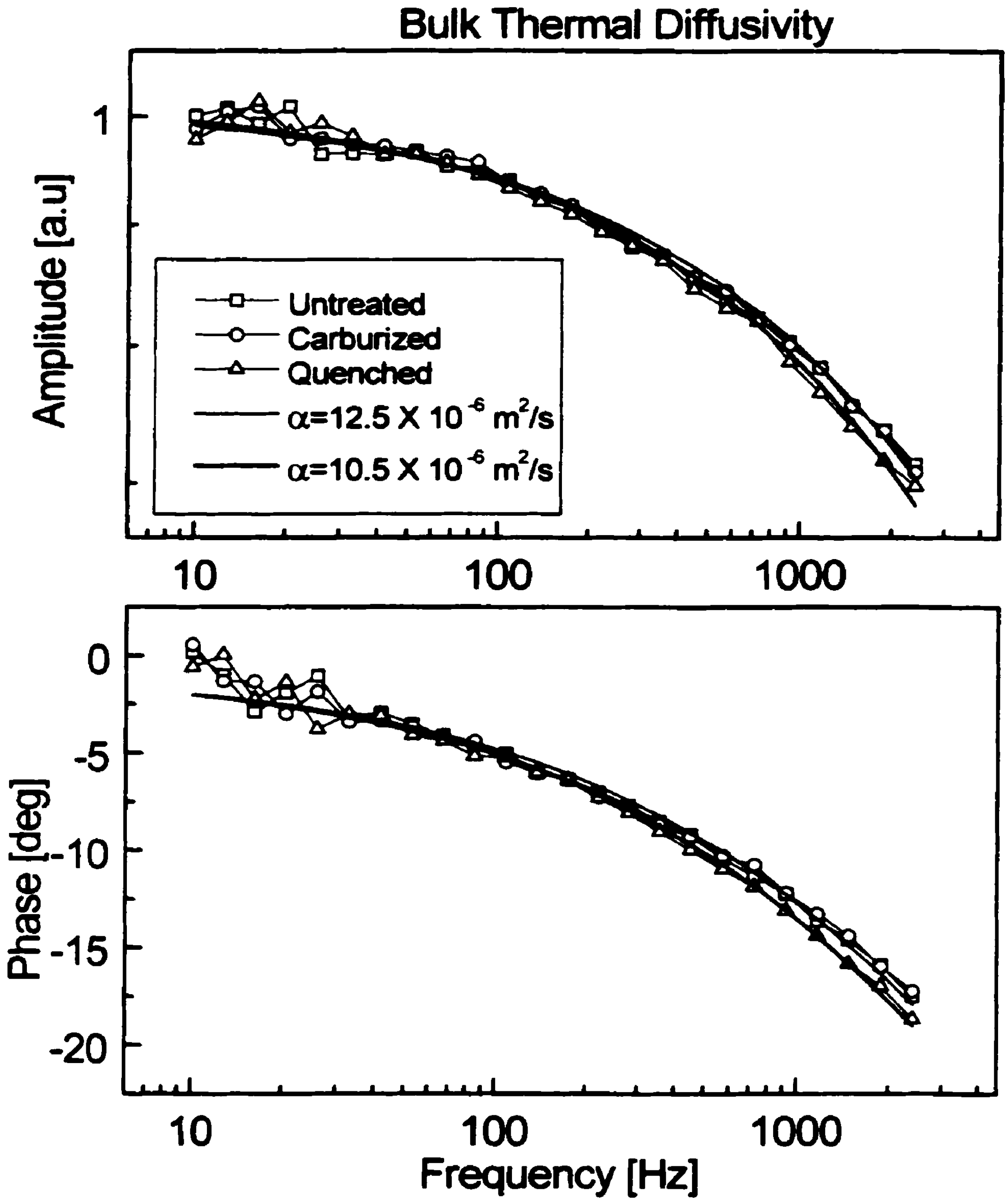

Figure 4.30 Three-dimensional experimental phase data with theoretical fitting; untreated (square), carburized (circle) and quenched (triangle) steel; theory $\alpha = 12.5 \times 10^{-6} m^2/s$ (red); theory $\alpha = 10.5 \times 10^{-6} m^2/s$ (blue).

Chapter 5

Depth Profilometric Inversions and Discussion

5.1 Introduction

In this chapter, the depth profilometric reconstructions from the experimental data presented in Chapter 4 are shown. The reconstructions are produced using the theoretical and numerical methodologies developed in Chapters 2 and 3, respectively. In Section 5.2, the effects of roughness are investigated and incorporated into the experimental data. A novel heuristic approach for accounting for the effects of roughness in experimental data is developed. The final reconstruction for both carburized and quenched data is outlined in Section 5.3. Finally, the conclusions and limitations of the method are discussed in Section 5.4.

5.2 Depth Profilometic Reconstructions of Rough Steels

Modeling roughness is a non-trivial problem. In most photothermal applications, the surface of the sample is polished so that roughness effects can be neglected. The use of a polished sample can introduce errors in the results if a careful examination is not performed. Polished samples also need a high incident power for a high SNR since most of the incident energy is reflected. The mirror surface can be seen as a thermal barrier to the substrate. Also, when normalizing with the instrumental function, great care must be taken so that the size of the Gaussian laser beam would be the same. With a mirror surface, the laser beam shape is imprinted on the surface and any inhomogeneities that may exist become more pronounced. A rough surface tends to act as a scrambler resulting in a quasi-uniformity of intensity over the illuminated surface. With careful experimentation, polishing can work in laboratory conditions but it can be costly and time consuming for industrial applications. Thus, a method of "eliminating" roughness theoretically/numerically can be advantageous. Roughness effects on the photothermal signal have been reported by Bein et al. [82]. They have modeled roughness as a three-layer model and have found that the rough surface has a low thermal effusivity, the intermediate porous layer has an increased thermal effusivity and, finally, the bulk has the highest thermal effusivity. This is consistent with this work (Section 4.4.1), where the rough surface was found to have a lower thermal effusivity (5μm:~5000$Ws^{1/2}/m^2K$, 2.5μm:~3000$Ws^{1/2}/m^2K$) than the bulk (~13000 $Ws^{1/2}/m^2K$). It was also found that the rough-layer thermal effusivity decreases, with increasing roughness.

Roughness effects became visible at high frequency, appearing as a peak in the phase data, affecting the signal beyond the roughness depth and thus is necessary to treat. In modeling roughness, one option is to use a finite thickness layer theory (Chapter 2) for depth reconstruction in order to obtain a reliable profile beyond the depth of the roughness. A second option is to account for roughness in the experimental data by considering roughness as a random processes.

5.2.1 Depth Profiles of Rough Untreated AISI 8620 Steels

The first method developed for treating roughness was based on the theoretical model developed in Chapter 2 of the geometry shown in Figure 2.1 (*d*= roughness thickness). As outlined in Section 3.4, the bulk thermal diffusivity is needed *a priori* for the reconstruction method. In Section 4.4.4, the bulk thermal diffusivity was measured as α_∞=12.5x10^{-6}m^2/s. Reconstructions are performed using the independent measurement of the bulk thermal diffusivity and roughness thickness (600 and 200 grit) of the untreated AISI 8620 samples. The numerical procedure is based on reconstructing from the high frequency end by fitting α_0 at each virtual slice (Figure 3.1). With this method, the effect of surface roughness is greatly reduced from the system. For the samples in question, the input parameters for the equivalent roughness layer were thermal diffusivity α_d, thermal conductivity k_d, and independently measured roughness thickness (*d*=2.3μm). For the 600 grit the input parameters were α_d=4.5x10^{-6}m^2/s, k_d=10.1W/mK and roughness thickness *d*=2.3μm. For the 200 grit the input parameters were α_d=2.2x10^{-6}m^2/s, k_d=4.6W/mK and roughness thickness *d*=5μm. It is observed that as roughness increases the thermal effusivity of the surface decreases (Table 4.2). The smoothed experimental data with the theoretical fit, which assumes one homogeneous layer (roughness) with a homogeneous substrate, are shown in Figure 5.1. The forward theoretical fit is in agreement with the experimental data. Small discrepancies exist at the high frequency end where the roughness is more difficult to model. In Figure 5.2, the experimental data were numerically inverted to obtain the corresponding thermal diffusivity profile.

The roughness layer, which is assumed to be homogeneous with low thermal parameters, is theoretically eliminated. Thus, the reconstruction shown in Figure 5.2 commences below the roughness layer. It is seen from the reconstruction that the thermophysical properties are disturbed up to about 50μm and 400μm for the 2.5μm and 5μm roughness, respectively. Beyond these depths, the bulk material is undisturbed and approaches the experimentally independently measured value of $\alpha=12.5\times10^{-6}m^2/s$. The near surface fluctuation can be attributed to the approximate modeling of roughness as a homogeneous layer. Another reason can be the violation at the high frequency *increments* of the requirement for nonsteep local variations of the effusivity (equation 2.28). Since rough profiles have steep variations at high frequency, a very large number of modulating frequencies is needed to satisfy the nonsteep local variation assumption. For low roughness materials, the perturbation can be neglected since hardness measurements are usually of interest above 50μm. Such a reconstruction can serve as a guide to determine the extent to which roughness influences a specific profile. As roughness increases, the reconstruction becomes less reliable. There are two reasons for this: (1) the forward model is not represented adequately in the higher frequency spectrum where the randomness of roughness is more evident, and (2) the inverse problem becomes more ill-posed, since more variables (effective roughness properties) are introduced. Overall, reconstructing in this manner (homogeneous layer assumption) can only be satisfactory for low roughness materials.

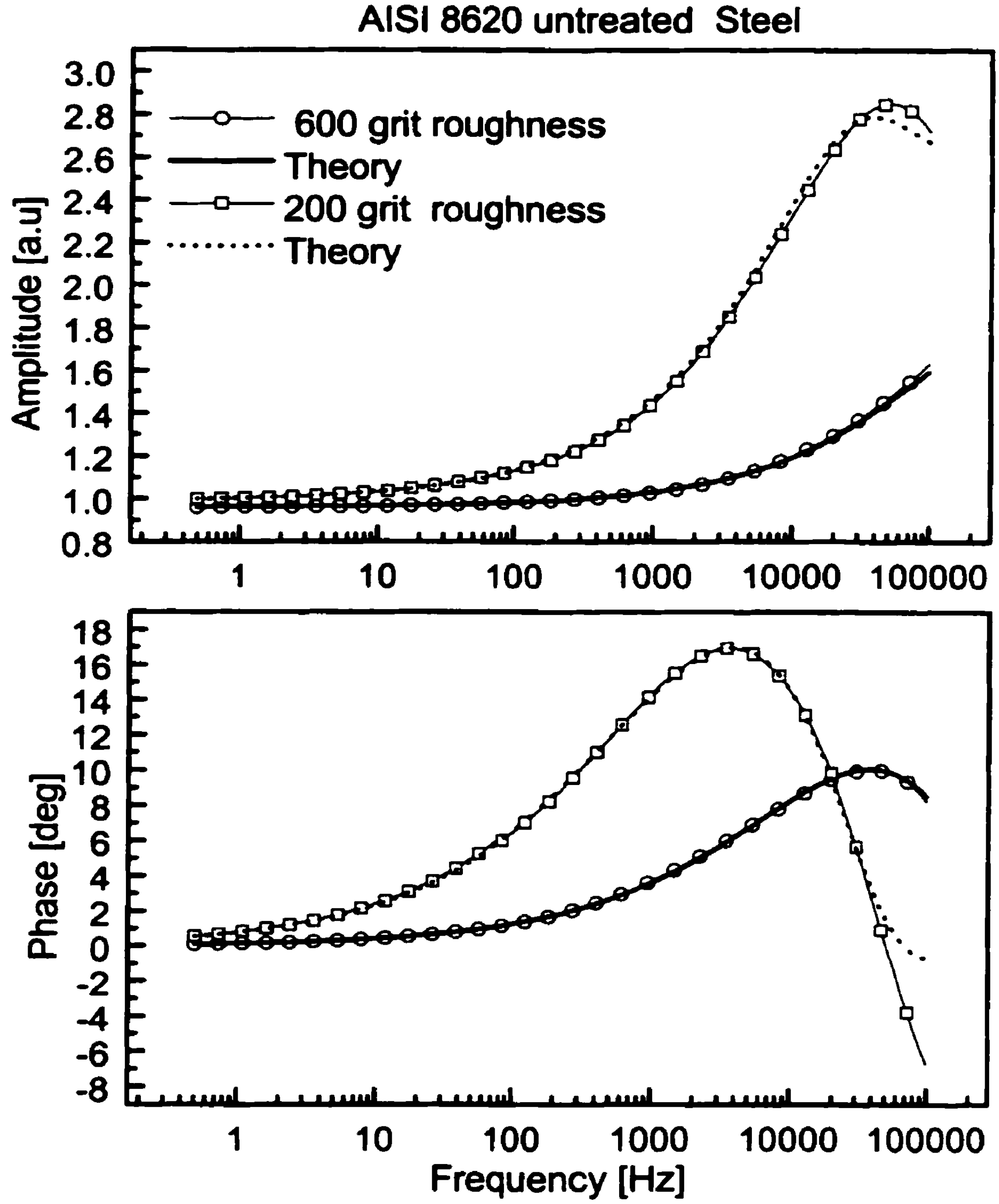

Figure 5.1 Experimental and theoretical forward fit of 200 and 600 grit samples. For clarity only 25% of the experimental data is shown.

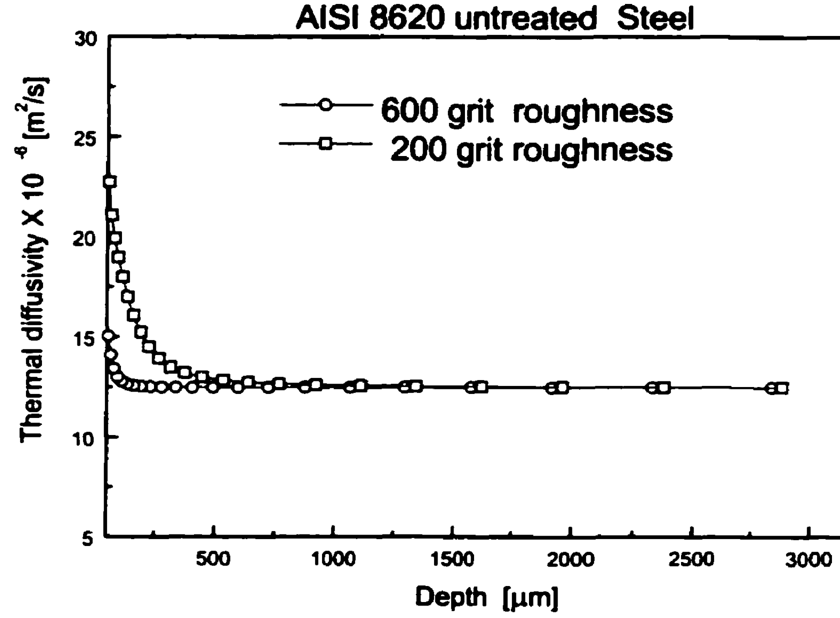

Figure 5.2 Reconstruction of 200 and 600 grit untreated samples. For clarity only 25% of the data is shown.

5.2.2 Random-Spatial-Variable Approach to Eliminate Roughness from Experimental Data

The one-layer theoretical model above treats roughness as a homogeneous layer over an inhomogeneous substrate and, with a low-level roughness, the results are satisfactory as seen in Figure 5.2. This theoretical model is, however, too simplistic. As the level (thickness) of roughness increases, the thermal wave spectrum becomes more complicated, especially at high frequencies, resulting in an erroneous thermal diffusivity profile. In this part of the work, a new approach is adopted and tested for various levels of roughness and inhomogeneity. By using the concept that random roughness is equivalent to white (Gaussian) noise in the spatial depth coordinate, the effects of inhomogeneity and roughness can be deconvolved. The theoretical simulations show great promise and, therefore, the method has been implemented to reconstruct experimental data. In a frequency domain method, both the roughness and the inhomogeneity are observed throughout the frequency spectrum. A simple approach for deconvolving roughness from inhomogeneity would not be valid since this is a non-linear system. The roughness method is based on recognizing distinct features (phase maxima) from the frequency spectrum. Since roughness is associated with the surface of a sample, the effects are strongest at high frequencies, whereas low frequencies are substantially related to substrate inhogeneities. The objective of the method is to deconvolve the roughness spectrum from the underlying profile (homogeneous or inhomogeneous). To demonstrate the method, simulations of a semi-infinite inhomogeneous profile, equation (2.42), using a single profile of equation (2.32) are performed with different roughness thicknesses. Three cases *A*, *B* and *C* with roughness 1.6μm, 7μm and 10μm, respectively, are examined. Table 5.1 displays the thermal parameters used for each *case*, modeled for four thermal geometries (referred to as *curves*). Curve 1 is the response of an inhomogeneous sample with roughness. Curve 2 is the inhomogeneous field with no roughness. Curve 3 is the homogeneous field with roughness and Curve 4 is an effective homogeneous field fitted to the high frequency of Curve 1.

Figure 5.3 shows the amplitude and phase of Case *A* with the parameters displayed in Table 5.1. Curve 1 shows the response of an inhomogeneous sample with roughness d=1.6μm and Curve 2 is the inhomogeneous field with d=0μm. Curve 2 represents the ideal experimental situation where no roughness effects are present (i.e., polished surface). Curve 3 is the homogeneous field with roughness (i.e., untreated samples). Curves 2 and 3 are the individual responses forming the inhomogeneity and roughness. The objective of the method is to retrieve Curve 2 from Curve 1 by eliminating roughness. A theoretical fitting (equation 2.42) of a homogeneous substrate with roughness is made to the higher frequency end of Curve 1. This is the region that is associated with the roughness. The input parameters of this Curve 4 are the same as the ones used for Curve 3, except that an effective thermal conductivity is used for the roughness layer. With this operation, the high frequency response of Curve 1 is fitted. Using a simple normalizing procedure of the total field Curve 1 and 4, the sought inhomogeneity is obtained as

$$T_{final(E)}(0,\omega) = \frac{\text{Curve 1}}{\text{Curve 4}} = \frac{|M_{total}(\omega)|e^{i\Delta\phi_{total}(\omega)}}{|M_{eff}(\omega)|e^{i\Delta\phi_{eff}(\omega)}} = \left|\frac{M_{total}(\omega)}{M_{eff}(\omega)}\right| e^{i[\Delta\phi_{total}(\omega)-\Delta\phi_{eff}(\omega)]}, \quad (5.1)$$

where each temperature distribution is defined in equation (2.42). The result of equation (5.1) is Curve 5. Comparing Curve 5 with Curve 2, in Figure 5.3, the two results are found to be in excellent agreement. Operation (5.1) can thus be used as a tool for obtaining the inhomogeneity from a rough sample. The method is then tested for a higher level of roughness. Figure 5.4 shows Case *B* where the roughness thickness is d=7μm. Apart from the roughness thickness the thermal properties are identical to Case 1 as seen in Table 5.1. The final result (Curve 5) is in agreement with the expected theoretical value (Curve 2) although there are small deviations at the low frequency end. The important observation is that the effective thermal properties of Curve 4 for Cases *B* and *A* are identical. A more complicated situation, Case *C*, is then examined where the amplitude and phase do not show any characteristic maximum from which the inhomogeities can be inferred (Figure 5.5). The knowledge that the same inhomogeneities affect the roughness spectrum in a similar manner is used in this case. Curve 4 is constructed using the same effective properties as in Cases *A* and *B*. The thermal values for each curve of Case *C* are shown in Table 5.1. For this case, the deviations of Curve 5 from the theoretical value of Curve 2 are more pronounced as compared to Cases *A* and *B*, but are still within satisfactory boundaries.

Thermal Properties	**Case A**	**Case B**	**Case C**
Curve 1: Total field: Inhomogeneous with roughness	α_L=6.15x10^{-6}m^2/s α_0=4.0x10^{-6}m^2/s q=2x10^3 m^{-1} α_d=2.1x10^{-6}m^2/s k_d=4.8W/mk **d=1.6μm**	α_L=6.15x10^{-6}m^2/s α_0=4.0x10^{-6}m^2/s q=2x10^3 m^{-1} α_d=2.1x10^{-6}m^2/s k_d=4.8W/mk **d=7μm**	α_L=6.15x10^{-6}m^2/s α_0=4.0x10^{-6}m^2/s q=2x10^3 m^{-1} α_d=2.1x10^{-6}m^2/s k_d=4.8W/mk **d=13μm**
Curve 2: Inhomogeneous with no roughness	α_L=6.15x10^{-6}m^2/s α_0=4.0x10^{-6}m^2/s q=2x10^3 m^{-1} d=0μm	α_L=6.15x10^{-6}m^2/s α_0=4.0x10^{-6}m^2/s q=2x10^3 m^{-1} d=0μm	α_L=6.15x10^{-6}m^2/s α_0=4.0x10^{-6}m^2/s q=2x10^3 m^{-1} d=0μm
Curve 3: Homogeneous with roughness	α_L=6.15x10^{-6}m^2/s α_0=6.15x10^{-6}m^2/s α_d=2.1x10^{-6}m^2/s k_d=4.8W/mk **d=1.6μm**	α_L=6.15x10^{-6}m^2/s α_0=6.15x10^{-6}m^2/s α_d=2.1x10^{-6}m^2/s k_d=4.8W/mk **d=7μm**	α_L=6.15x10^{-6}m^2/s α_0=6.15x10^{-6}m^2/s α_d=2.1x10^{-6}m^2/s k_d=4.8W/mk **d=13μm**
Curve 4: Homogeneous with effective roughness	**k_{eff}=5.96W/mK**	**k_{eff}=5.96W/mK**	**k_{eff}=5.96W/mK**

Table 5.1 Thermal properties of simulations shown in Figures 5.3-5.5.

Gaussian Fit	**sample 22**		**sample 12**	
	Amplitude	Phase	Amplitude	Phase
M_0 or $\Delta\Phi_0$	0.98	0.08	0.98	0.11
log(ω_{c1})	4.89	4.61	4.81	4.96
log(W_1)	3.69	2.03	0.81	2.28
A_1	0.29	21.29	0.12	41.86
log(ω_{c2})	5.06	8.47	4.34	5.81
W_2	1.51	3.09	1.32	2.03
A_2	0.54	-429.12	0.29	-82.02
log(ω_{c3})	-	-	3.38	-
log(W_3)	-	-	2.47	-
A_3	-	-	0.13	-

Table 5.2 Gaussian fit parameters of experimental data shown in Figures 5.6 and 5.7.

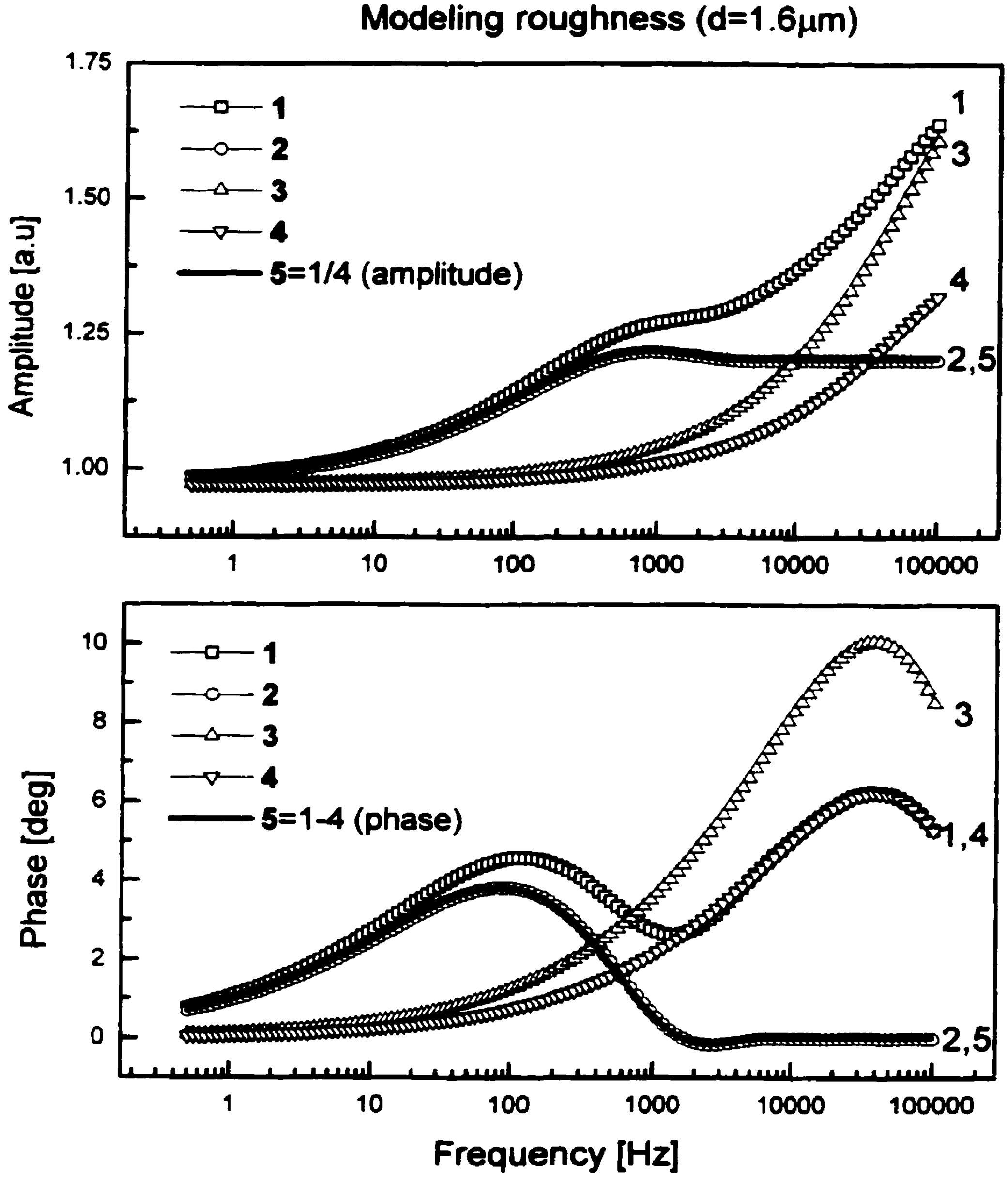

Figure 5.3 Simulation of roughness elimination method with 1.6μm roughness thickness.

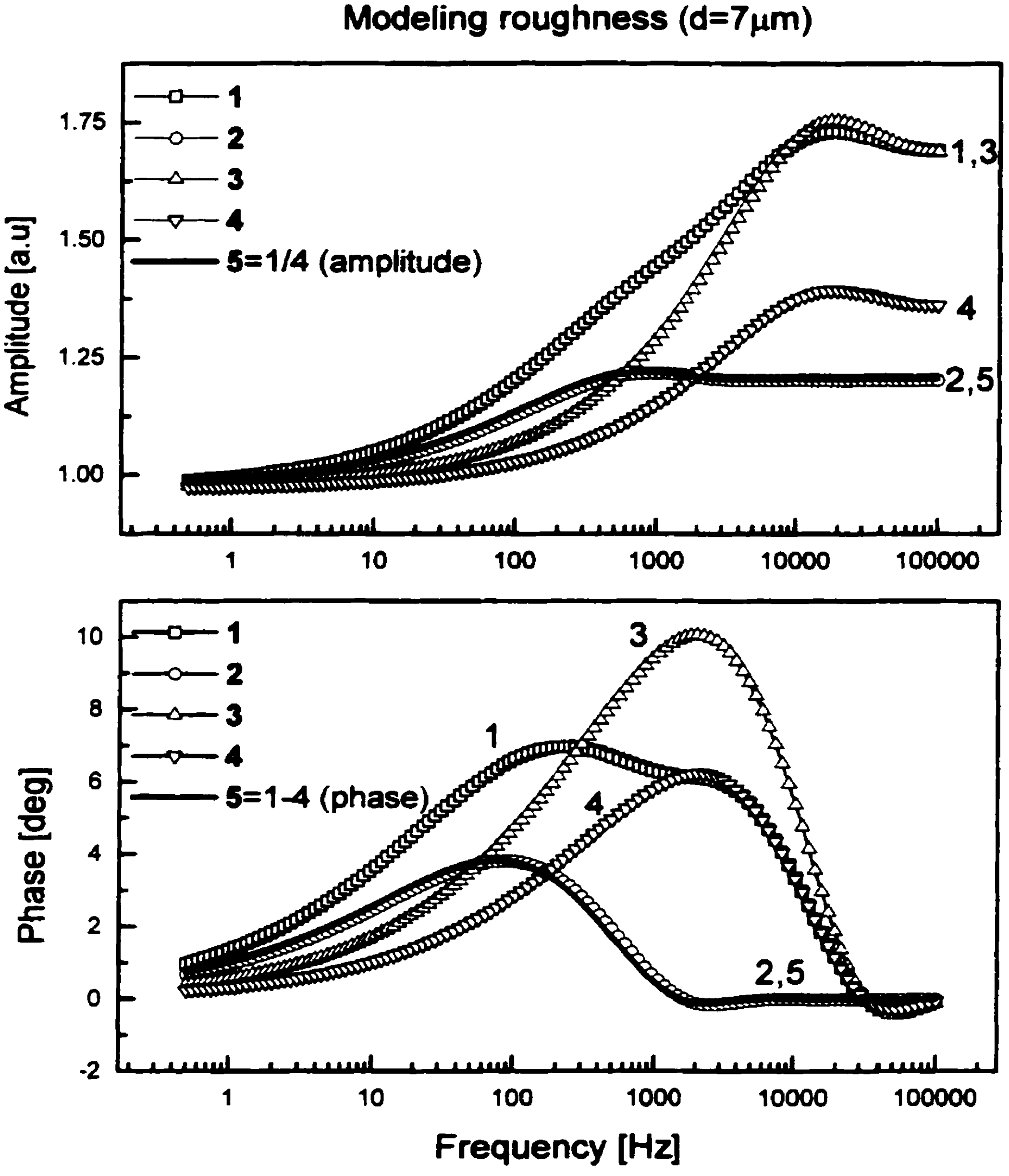

Figure 5.4 Simulation of roughness elimination method with 7μm roughness thickness.

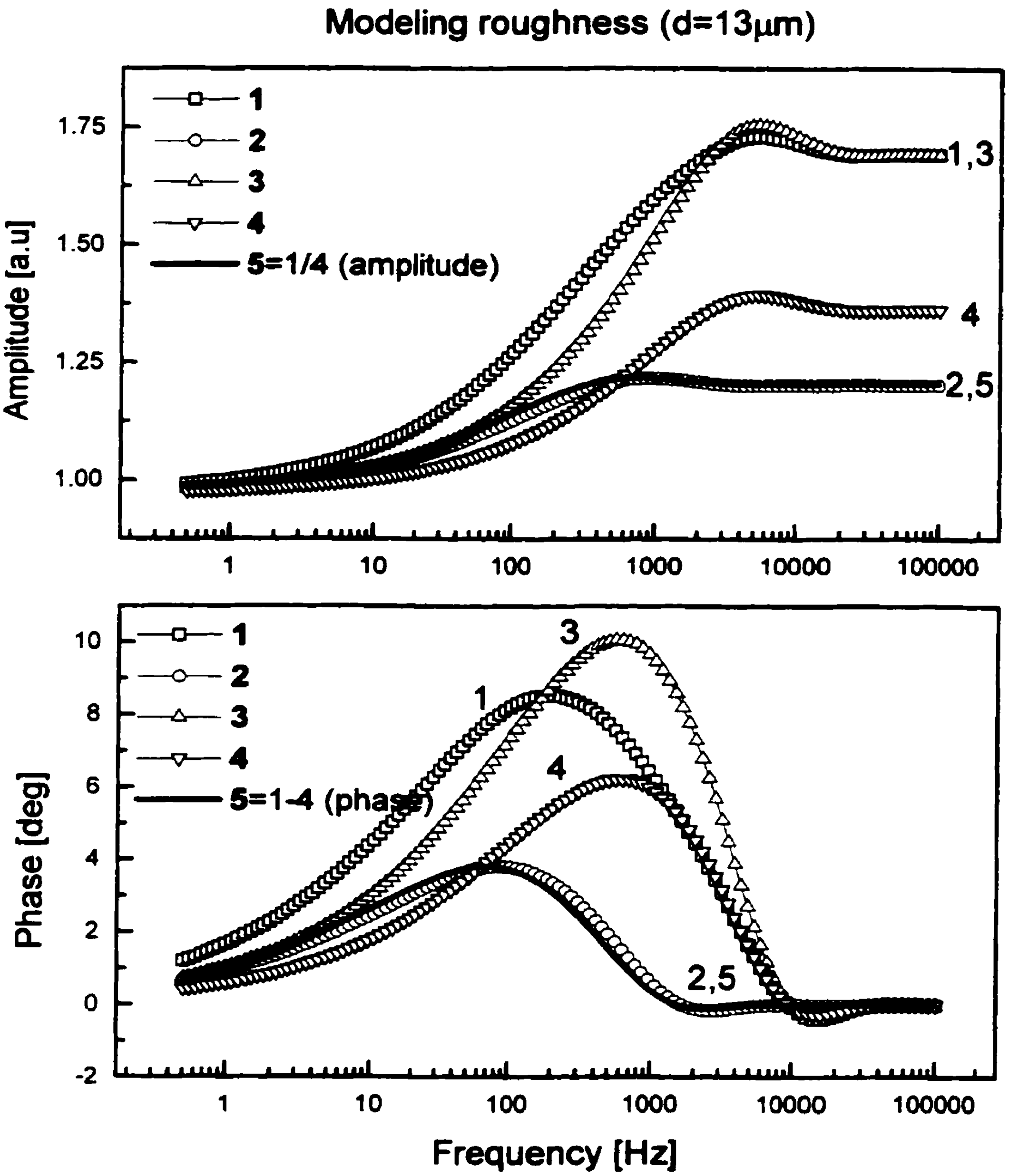

Figure 5.5 Simulation of roughness elimination method with 13μm roughness thickness.

Although the above method proves to be very effective in a theoretical application of an inhomogeneous substrate with a rough layer, a more general expression (not based on the theoretical model) for modeling the roughness can be obtained. Since roughness can be viewed as a random spatial-variable effect, a white Gaussian noise is fitted to the effective frequency-domain roughness profile (Curve 4), based on the theoretically expected Gaussian-to-Gaussian Fourier transformation. Through a spatial Fourier transformation, it is expected that the roughness spatial Gaussian profile will also be mapped as a Gaussian distribution in the frequency coordinate. By extension, there can be a linear superposition of several such Gaussian functions, if there are multiple characteristic roughness scales associated with a particular surface. The field thus created a non-symmetrical field and, therefore, the expressions for amplitude and phase, respectively, are as follows

$$M_{eff}(\omega_0) = M_0 + \sqrt{\frac{2}{\pi}} \sum_{i=2}^{N} \frac{A_{1i}}{W_{1i}} e^{-\frac{(\omega_{10} - \log(\omega_{1ci}))^2}{W_{1i}^2}} \tag{5.2}$$

$$\Delta\Phi_{eff}(\omega_0) = \Delta\Phi_0 + \sqrt{\frac{2}{\pi}} \sum_{i=2}^{N} \frac{A_{2i}}{W_{2i}} e^{-\frac{(\omega_{20} - \log(\omega_{2ci}))^2}{W_{2i}^2}} , \tag{5.3}$$

where M_0 and $\Delta\Phi_0$ are the amplitude and phase offsets, respectively, W is the full width, A is the area and ω_c is the center-frequency of the Gaussian function. N is the upper number of characteristic roughness lengths anticipated. The summation of Gaussians is greater than one ($N \geq 1$) so as to account for the asymmetry of the field. The offset values can be derived by using the first point of theoretical fit of the effective roughness (Curve 4). This can serve as a guide to the level at which the Gaussian function will saturate, and is an approximation. The approximate offset values are "1" for amplitude and "0" for phase. Hence, in order to retrieve and eliminate roughness from the experimental data, a Gaussian fit to the high frequency end (roughness) is made based on equations (5.2) and (5.3). Figure 5.6 shows the elimination of roughness from experimental data. The sample has a roughness of 2.5μm (Sample 22) on an inhomogeneous substrate. The profile needed to perform such an operation on these data is a double Gaussian function whose parameters can be found in Table 5.2. Figure 5.7 shows the method of elimination on rougher data (*d*=5μm) with an inhomogeneous substrate. Although the phase roughness is fitted to a double Gaussian function as above, the amplitude for this data requires a summation of three Gaussians to perform the operation. A double Gaussian function would have fitted the data, but the higher frequencies would have suffered from deviations from the experimental data. The parameters for the Gaussians can be found in Table 5.2.

5.2.3 Interpretation of the Roughness Elimination Method

In the above section, roughness was eliminated by fitting a Gaussian distribution to it. In this section, a physical explanation is attempted. An analogy of the method can be made with astrophysics where Gaussian distributions are fitted to each spectrum response to find the temperature of the planet observed. When fitting the summation of Gaussians to the roughness, each Gaussian function is associated with a different frequency constant. This can be explained by viewing roughness as layers over layers as seen in Figure 5.8. Each level of roughness is associated with a characteristic frequency whose randomness can be represented as a Gaussian distribution. The roughness is thus modeled as white noise of random spatial distribution in the frequency domain. In the future, the random distribution of spatial roughness diffusion can perhaps be modeled using "fractal" analysis which was introduced to explain diffusion processes in the micron or submicron scale [84].

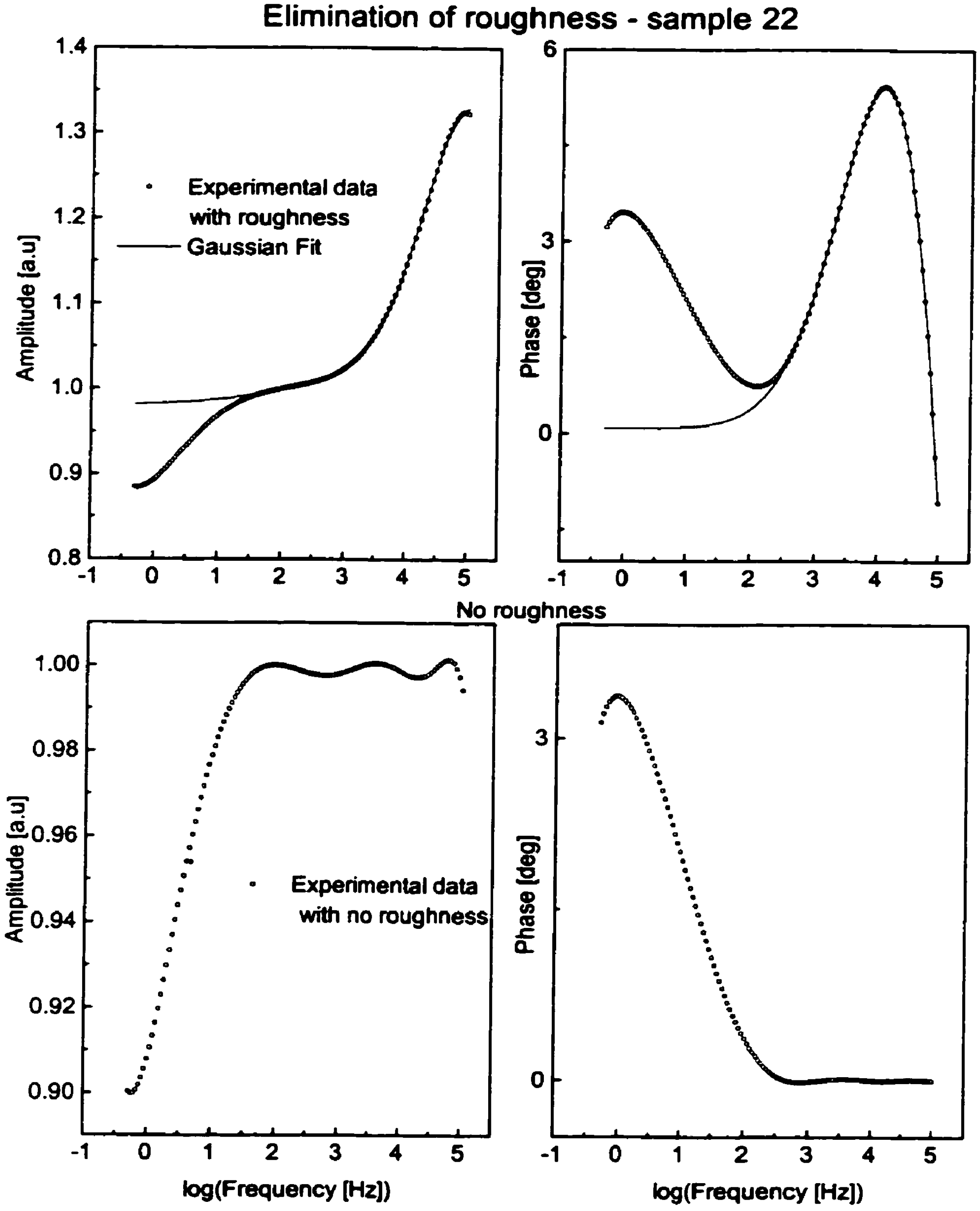

Figure 5.6 Result of computational elimination from experimental data of 2.5μm thickness roughness.

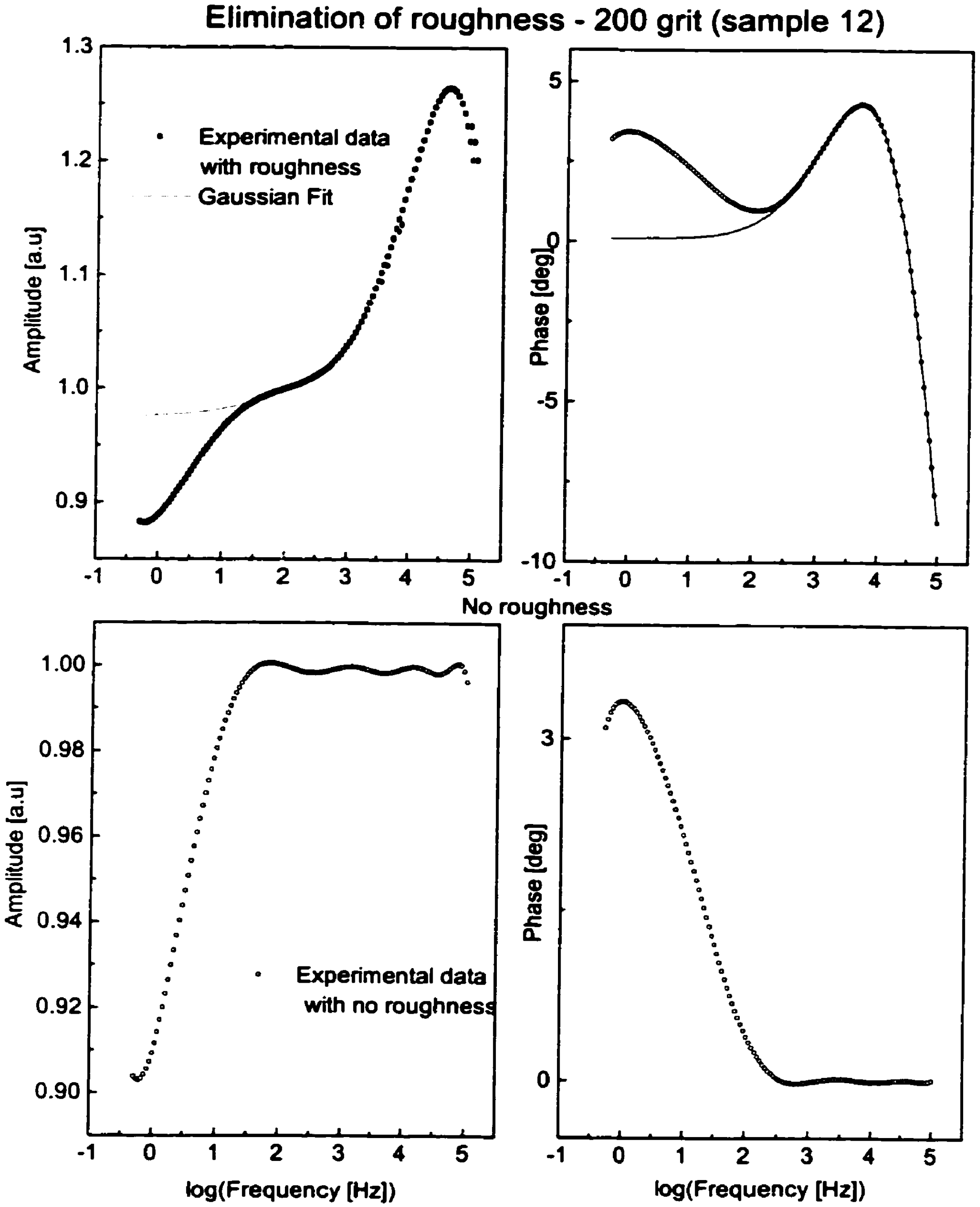

Figure 5.7 Result of computational elimination from experimental data of 5μm thickness roughness.

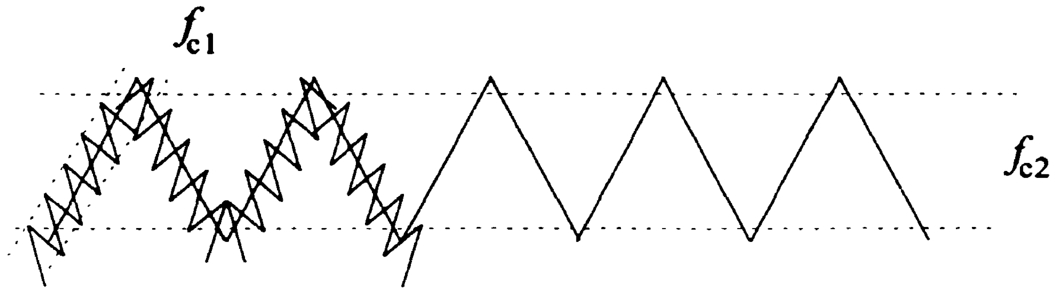

Figure 5.8 Multiple (two shown) layers of roughness with multiple (two shown) frequency centers.

5.3 Depth Profiles of Carburized AISI 8620 Steels with a Rough Layer

Roughness elimination is performed on all the carburized and quenched data. The success of the method is clearly seen when two different levels of roughness result in the same inhomogeneous experimental response.

5.3.1 Carburized Samples

Using the Gaussian elimination method, the roughness effects were eliminated from all smoothed experimental data of Figures 4.20 and 4.21 for the 200 and 600 grit, respectively, as shown in Figure 5.9. The solid symbols correspond to 200 grit roughness, whereas the open symbols correspond to 600 grit roughness. The black, red and blue curves correspond to 0.02", 0.04" and 0.06" case depth, respectively. After eliminating roughness, the underlying profiles for both roughness depths are superimposed over each other (solid black with open black, solid red with open red, and solid blue with open blue). This is an indication of the satisfactory performance of the roughness elimination method. With knowledge of the bulk thermal diffusivity of carburized samples, as measured in Section 4.4.4, reconstructions are performed for all experimental data, using the method outlined in Chapter 3. The bulk thermal diffusivity serves as a guide for finding the initial guess for (α_0, q). The reconstructions for all samples are shown in Figure 5.10. In order to develop a statistical boundary for the reconstructions, the experimental data were averaged as per hardness case depth (0.02",0.04" and 0.06"). Figure 5.11 shows the average curves with their respective error bars. The variations between experiments are due to sample variation rather than due to poor experimental reproducibility. The experimental reproducibility is in fact better than 1% for frequencies higher than 10Hz, and on the order of 2% to 5% for the lower frequency regime. The same data are presented on 1/sqrt(*f*) axis (Figure 5.12) showing the relative rate of change of signal with depth since the depth of propagation is proportional to 1/sqrt(*f*). The reconstruction of the average experimental curve is performed and the resulting reconstructions are shown in Figure 5.13. To ensure the validity of reconstructing the average experimental data, the average of all the reconstructions performed per case depth is shown on the same graph. At shallow depths, there is an agreement between the average reconstruction and the mean of reconstructions. As the depth increases the deviation of the two methods increases but it is still within 0.3% variation. In this way, a standardized instrumental methodology can be developed where, first multiple positions on the sample can be monitored, and then, the average of experimental data can be reconstructed. The thermal diffusivity reconstruction of the average is compared to the conventional microhardness test as seen in Figure 5.14. The depth profiles of the hardened samples exhibit an anti-correlation between thermal diffusivity and hardness. A good one-to-one correlation between hardness and thermal diffusivity is present, although the curves are not a mirror image of each other. The anti-correlation relationship is consistent with earlier works [46,59]. The reconstruction is shown up to a 1mm depth, which is the region where the carburized hardness profile is available. Both the hardness and thermal diffusivity profiles have not yet saturated to the bulk value.

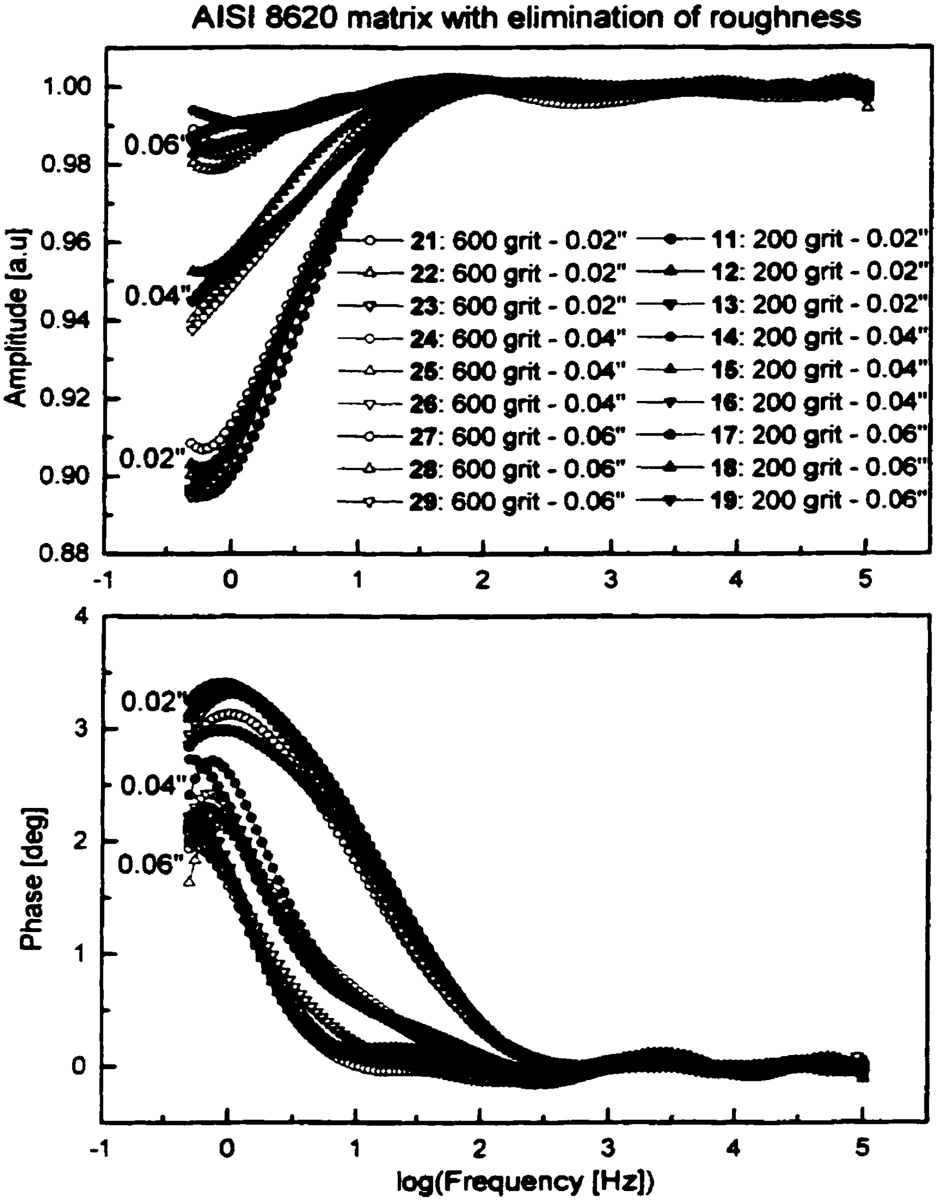

Figure 5.9 Carburized experimental data after elimination of roughness for 0.02" (black), 0.04" (red) and 0.06" (blue) case depth with 600 grit (open symbols) and 200 grit (solid symbols) roughness.

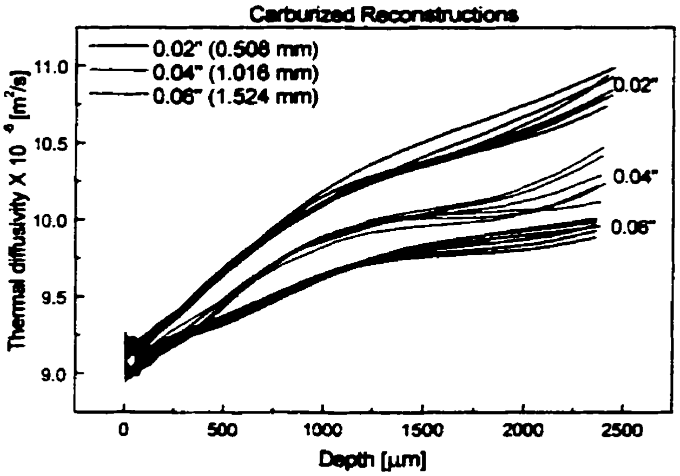

Figure 5.10 Reconstructions of all data in Figure 5.9 for 0.02" (black), 0.04" (red) and 0.06" (blue) case depth.

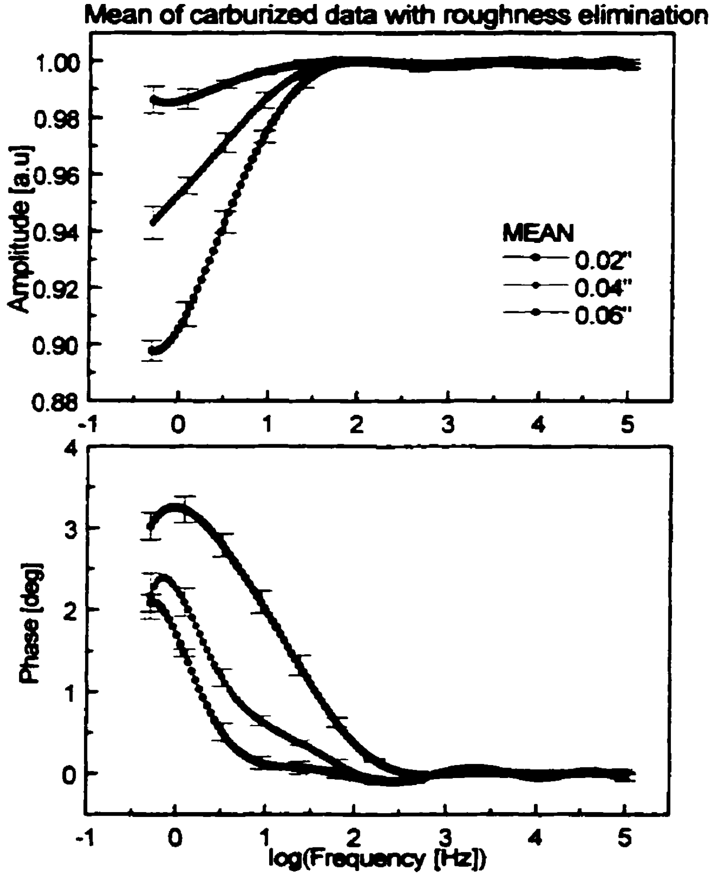

Figure 5.11 Average forward experimental data of Figure 5.9 for 0.02" (black), 0.04" (red) and 0.06" (blue) case depth.

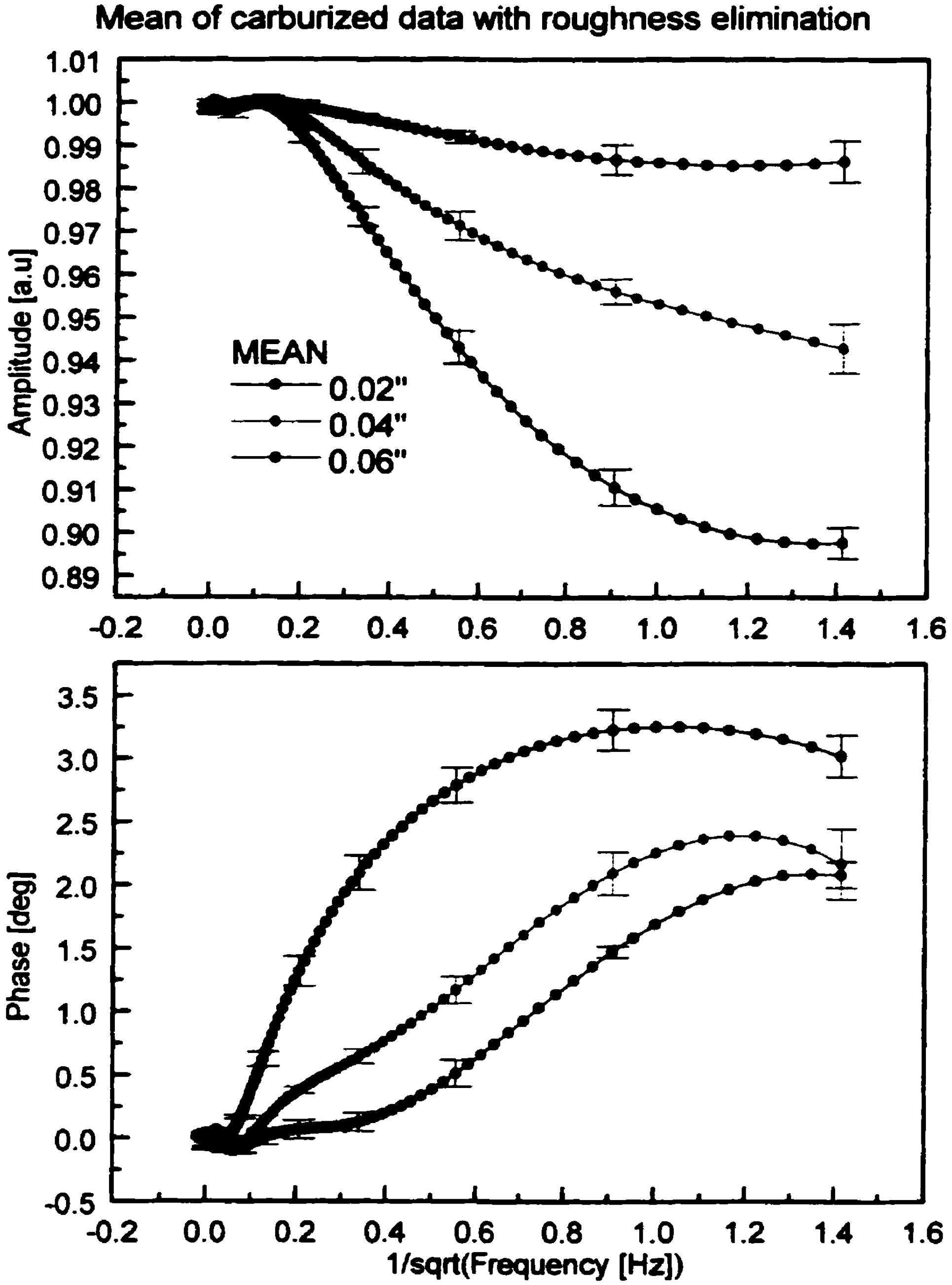

Figure 5.12 Average data versus 1/sqrt(frequency) for 0.02" (black), 0.04" (red) and 0.06" (blue) case depth.

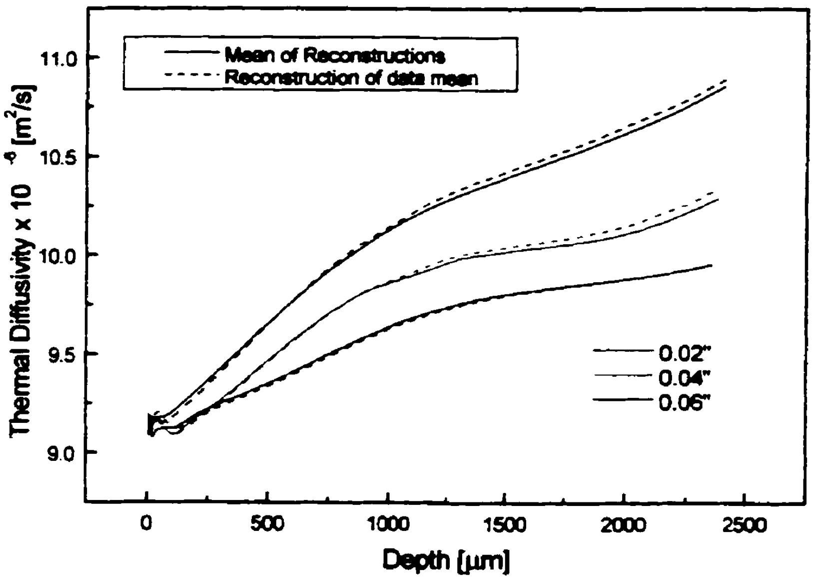

Figure 5.13 Comparison between carburized data mean of reconstructions (solid) and reconstruction of data mean for 0.02" (black), 0.04" (red) and 0.06" (blue) case depth.

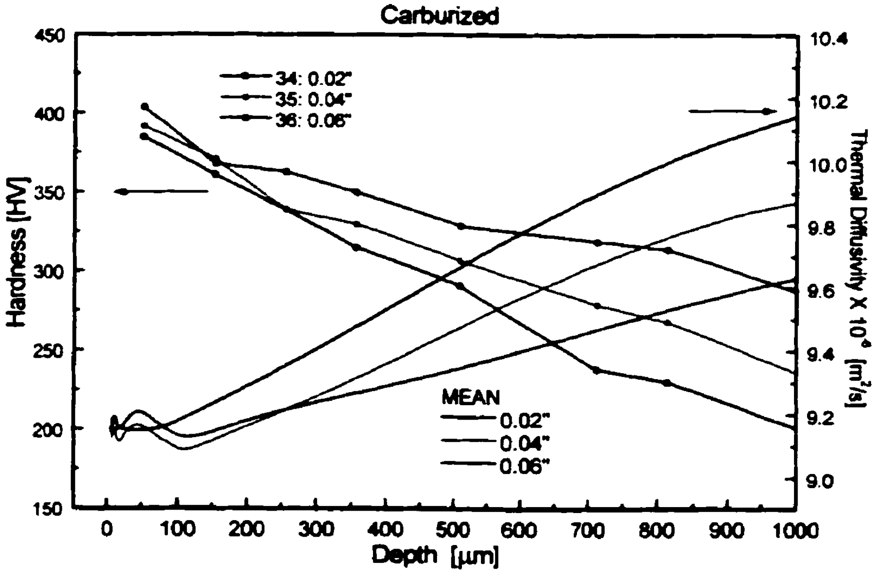

Figure 5.14 Hardness and thermal diffusivity profile for carburized data; 0.02" (black), 0.04" (red) and 0.06" (blue) case depth.

5.3.2 Quenched Samples

After carburizing, the same samples were oil quenched and the frequency response was repeated. Gaussian roughness elimination was again performed on these data as shown in Figure 5.15, where roughness was eliminated from all smoothed experimental data in Figures 4.24 and 4.25 for the 200 and 600 grit, respectively. The solid symbols correspond to 200 grit roughness whereas the open symbols correspond to 600 grit roughness. The black, red, blue curves correspond to 0.02", 0.04" and 0.06" case depth, respectively. After eliminating roughness, the underlying profiles for each respective roughness depth were superimposed over each other (solid black with open black, solid red with open red and solid blue with open blue). The averages of these data were taken (Figure 5.16), and the reconstruction for each depth (Figure 5.17) was compared to the microhardness test, where once again an anti-correlation was noted. As the depth increases, the one-to-one anti-correlation between microhardness and thermal diffusivity decreases. Beyond 2mm, the hardness profiles approach the bulk value but the diffusivity profiles do not yet saturate to the bulk thermal diffusivity. This could be due to the high sensitivity of photothermal methods detecting actual small variations before reaching the bulk value (5mm for this case). The exact mechanism of the thermal diffusivity versus the microstructure is discussed in the following section.

5.3.3 Sample Correlation

An important aspect of the reconstruction procedure is the understanding of the driving forces for the anti-correlation between thermal diffusivity and hardness. In this thesis, the samples underwent two major heat treating processes of carburizing and quenching. A comparison between the two treatments can assist in the data interpretation. The experimental data for both the carburizing and quenching process are shown Figure 5.18. The experimental data between the carburizing and quenching process show small variations suggesting that there are no major differences in terms of the relative thermal diffusivity depth profiles. It must, however, be noted that the bulk thermal diffusivity for these samples is different and, thus, the absolute reconstruction was at different saturation levels, as outlined in Section 3.4. The back-propagation one-dimensional experiment only provides information about the *relative* thermal diffusivity of a material. The bulk thermal diffusivity is measured independently. Figure 5.19 compares the reconstructions of both the carburized and quenched data and, although they are at different levels, the depth profile (as indicated by shape) in each reconstruction is similar. The quenched data reconstructions are of lower thermal diffusivity value since the quenched bulk thermal diffusivity value is lower than the carburized one. The result was obtained from the forward measurement of the bulk thermal diffusivity for the quenched versus carburized sample (Section 4.4.4). At the bulk value the same carbon content exists but the carburized samples have a ferritic structure whereas the quenched samples have a martensite structure. This leads to the conclusion that the microstructure dominates the absolute value of thermal diffusivity. The diffusivity shape similarity between the carburized and quenched reconstructions can be related to their common carbon profile (Figure 4.9). Thus, it can be concluded that the shape of the thermal diffusivity profile is dominated by carbon diffusion.

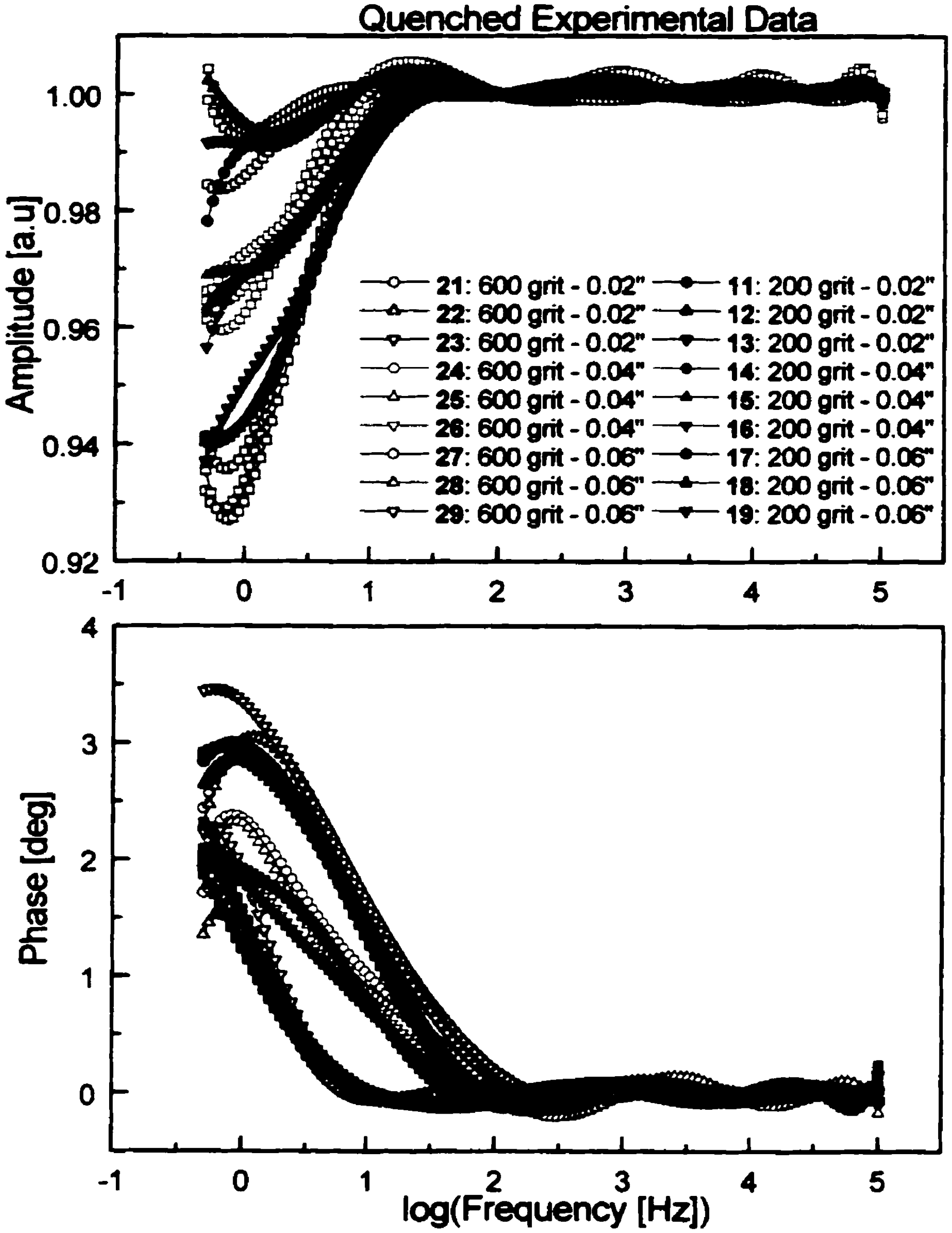

Figure 5.15 Quenched experimental data after elimination of roughness for 0.02" (black), 0.04" (red) and 0.06" (blue) case depth with 600 grit (open symbols) and 200 grit (solid symbols) roughness.

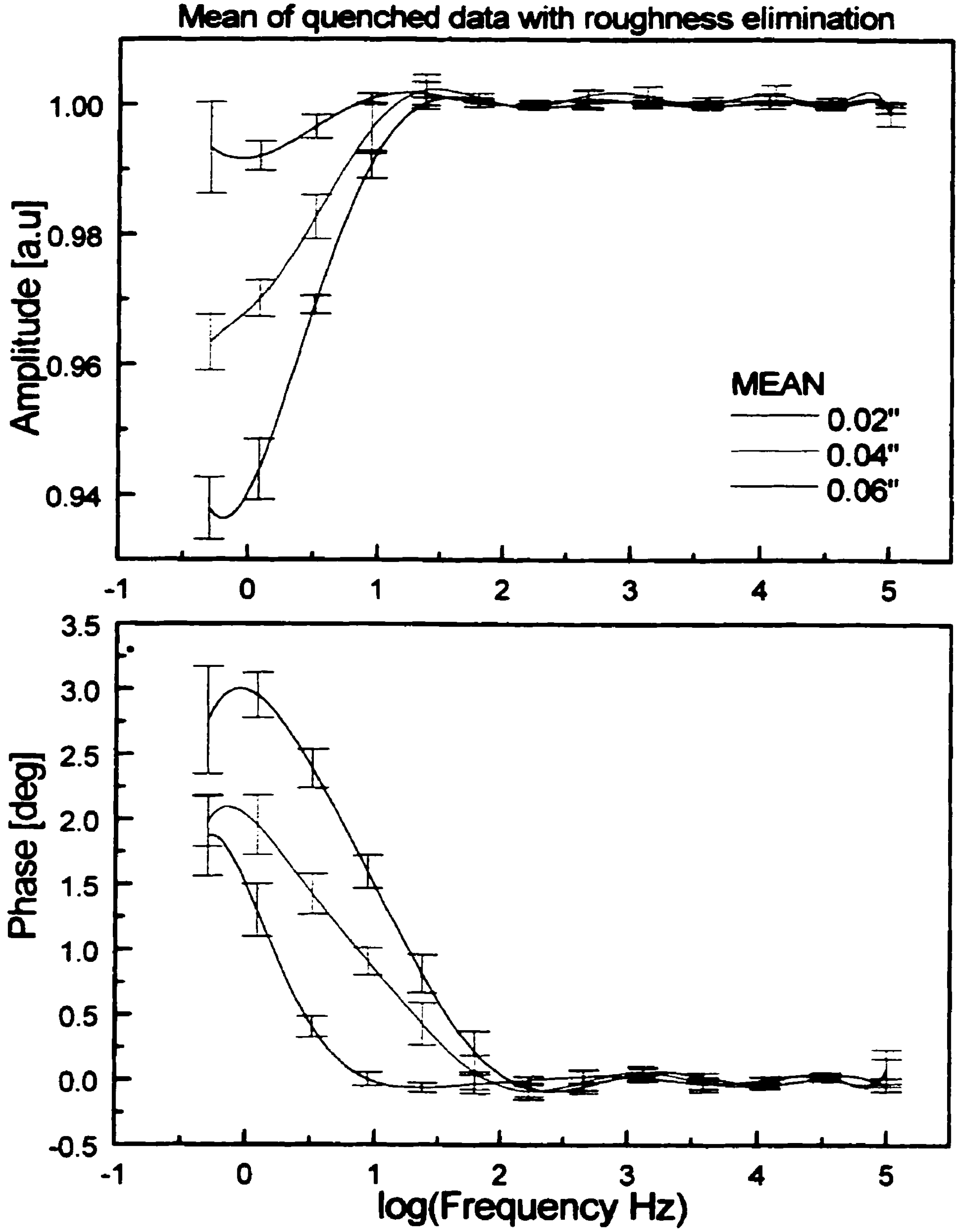

Figure 5.16 Average forward experimental data of Figure 5.15 for 0.02" (black), 0.04" (red) and 0.06" (blue) case depth.

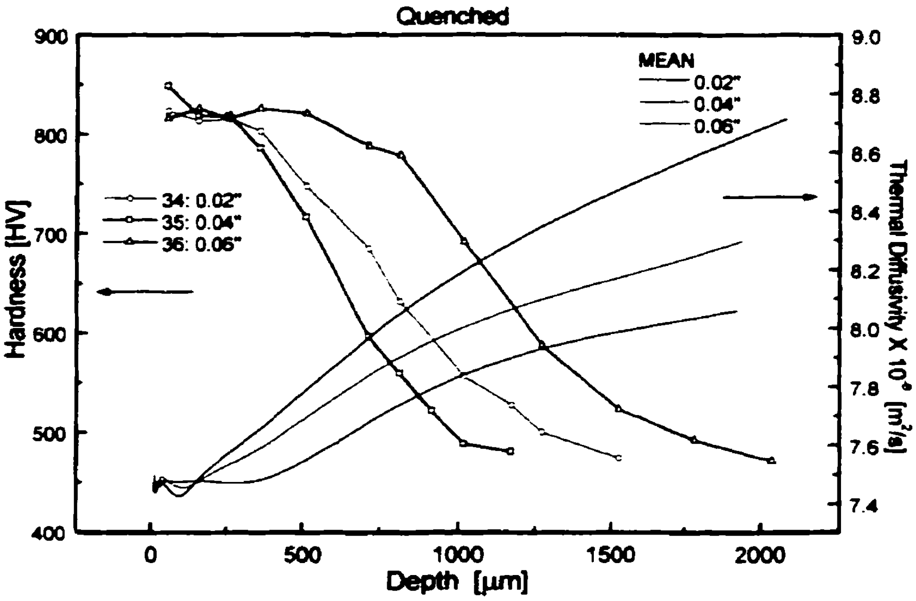

Figure 5.17 Hardness and thermal diffusivity profile for quenched data; 0.02" (black), 0.04" (red) and 0.06" (blue) case depth.

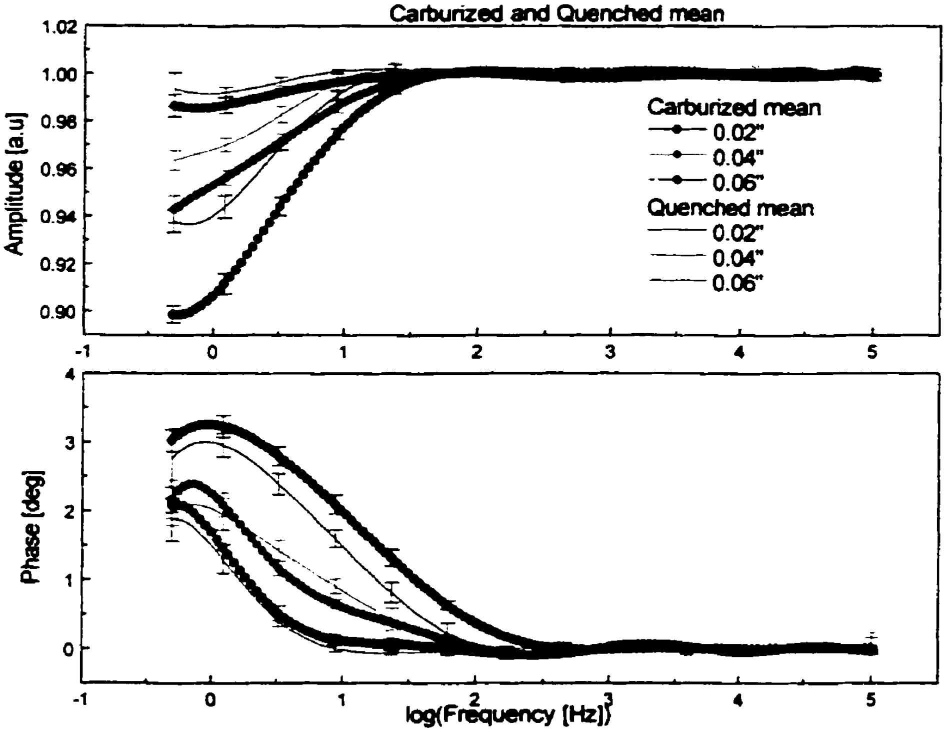

Figure 5.18 Average forward carburized (dots) and quenched (solid line) experimental data for 0.02" (black), 0.04" (red) and 0.06" (blue) case depth.

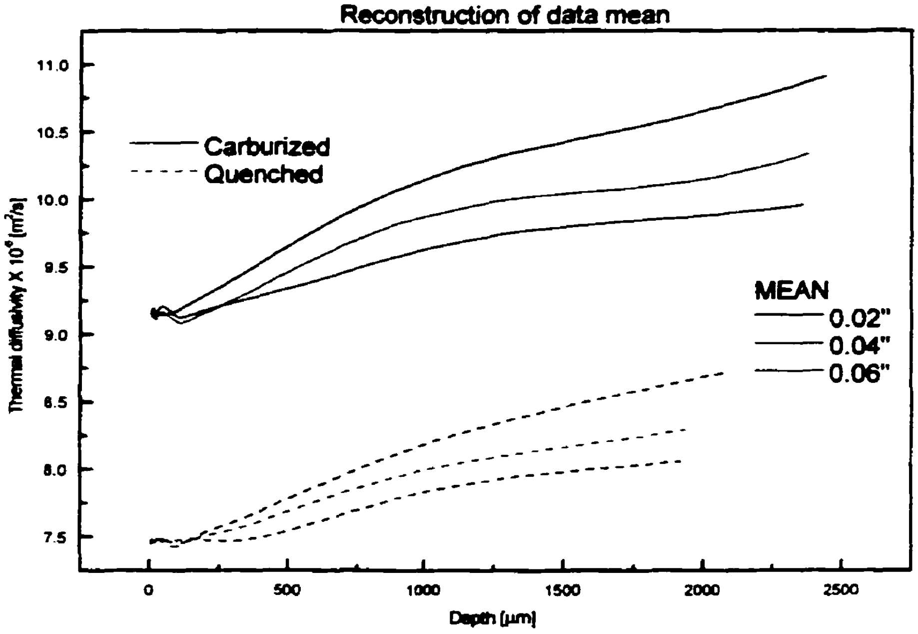

Figure 5.19 Average reconstructions of carburized (solid) and quenched (dash) data for 0.02" (black), 0.04" (red) and 0.06" (blue) case depth.

5.4 Conclusions

Thermal wave depth profilometry can be an invaluable analytical technique for understanding the effect surface treatment processes such as case hardening of metals. In this work, AISI 8620 type steels were subject to common industrial heat treatments like carburizing and quenching. A complete experimental and theoretical/computational analysis was performed to generate thermal diffusivity profiles. A novel approach of treating roughness as spatial (depth-coordinate) white noise was introduced. This method led to a Gaussian roughness profile in the frequency domain and helped establish a procedure for eliminating the effects of this layer from the frequency response of the inhomogeneous substrate. The Gaussian elimination of roughness proves to be an important method of improving the experimental data and achieving thermal diffusivity reconstructions of non-homogeneous underlayers. This method can thus be of great interest in other photothermal applications where roughness can be an undesirable parameter. In fact, it has been recently applied in the Photothermal Laboratory of the University of Toronto with success to thermal spray coatings.

The current methods used to characterize case hardening are destructive and, therefore, success in developing a correlation (anti-correlation) between hardness and thermal diffusivity profiles implies a significant contribution to the steel industry. A near anticorrelation between the thermal diffusivity profile of a hardened surface and its microhardness is found in this thesis. The study of the two processes of carburizing and quenching concluded that the shape of the thermal diffusivity profile is dominated by carbon diffusion whereas the absolute thermal diffusivity depth profile is dominated by microstructural changes. Obtaining the carbon diffusion can be significant to the steel industry since, in the heating process, the carbon content is not a measured output but only an estimated input. Care must be taken to measure the correct bulk thermal diffusivity which is used *a priori* otherwise the shape of the profile would be correct but the absolute thermal diffusivity depth profile would be incorrect.

Chapter 6

Forward Process: Thermal Wave Diffraction Theory

6.1 Introduction

In the next chapters (Chapter 6-9), the three-dimensional inverse problem of Thermal wave Slice Diffraction Tomography (TSDT) is studied. TSDT is a method for retrieving sub-surface thermal defects.

In this chapter, the mathematical theory of the thermal wave propagation process will be developed utilizing thermal wave diffraction [66], and will be called the *forward process*. The mathematical formulation of thermal wave propagation will be presented as an integral solution for the Helmholtz equation. Approximations of the integral solution will be established in the limit of a perturbative first Born (or Rytov) approximation.

6.2 General Form of the Thermal Wave Equation

Upon a harmonic optical excitation of the boundary S enclosing some inhomogeneous region in space, R, and having functional form [66],

$$I(\boldsymbol{r}, t) = I_0(\boldsymbol{r}) \exp(-i\omega t) \tag{6.1}$$

where I is the incident optical irradiance on S and $\omega=2\pi f$ is the optical beam intensity modulation angular frequency, the resulting photothermal wavefield in R can be described fully by the equation [5,66],

$$\nabla K(\boldsymbol{r}) \bullet \nabla T(\boldsymbol{r}) + K(\boldsymbol{r})\nabla^2 T(\boldsymbol{r}) - i\omega\rho(\boldsymbol{r})c(\boldsymbol{r})T(\boldsymbol{r}) = 0 \tag{6.2}$$

where $K(\mathbf{r})$, $\rho(\mathbf{r})$, $c(\mathbf{r})$ are the coordinate-dependent thermal conductivity, density and specific heat of the matter in R, at location $\mathbf{r}$ from a suitably chosen origin. $T(\mathbf{r})$ is the spatial part of the modulated temperature field,

$$\Theta(\boldsymbol{r}, t) = T(\boldsymbol{r})\exp(i\omega t) \tag{6.3}$$

Equation (6.2) may be written in the following form

$$\nabla^2 T(\boldsymbol{r}) - i\left(\frac{\omega}{\alpha(\boldsymbol{r})}\right)T(\boldsymbol{r}) = -\left(\frac{\nabla K(\boldsymbol{r})}{K(\boldsymbol{r})}\right) \bullet \nabla T(\boldsymbol{r}) \tag{6.4}$$

where

$$\alpha(\boldsymbol{r}) \equiv \frac{K(\boldsymbol{r})}{\rho(\boldsymbol{r})c(\boldsymbol{r})} \tag{6.5}$$

is the local thermal diffusivity. In the case where the thermal conductivity of the matter in R does not vary drastically with position, so that the fractional change of $K(\mathbf{r})$ in one local thermal wavelength, $\lambda_t({}_r;\omega)=2\pi(\alpha(\mathbf{r})/\omega)^{1/2}$, is small, the right hand side of equation (6.4) may be neglected, which then yields the Helmholtz pseudowave equation [5,66]

$$(\nabla^2 - \tilde{q}^2(\boldsymbol{r}))T(\boldsymbol{r}) = 0 \tag{6.6}$$

where

$$\tilde{q}(\boldsymbol{r}) = (1+i)\left[\frac{\omega}{2a(\boldsymbol{r})}\right]^{1/2} \tag{6.7}$$

is the complex thermal wavenumber. Letting the thermal diffusivity of the assumed homogeneous medium surrounding the object region R be α_0, equation (6.6) may be replaced by a modified Helmholtz pseudowave equation [66]:

$$(\nabla^2 - \tilde{q}_0^2)T(\boldsymbol{r}) = F(\boldsymbol{r})T(\boldsymbol{r}) \tag{6.8a}$$

where

$$F(r) = \begin{cases} 0 & \boldsymbol{r} \notin R \\ \tilde{q}_0^2(n^2(\boldsymbol{r}) - 1) & \boldsymbol{r} \in R \end{cases} \tag{6.8b}$$

and

$$\tilde{q}_0 = (1+i)\left(\frac{\omega}{2a_0}\right)^{1/2} \equiv q_0 e^{i\pi/4} \tag{6.8c}$$

and

$$n(\boldsymbol{r}) \equiv \sqrt{\frac{a_0}{a(\boldsymbol{r})}} \tag{6.8d}$$

$n(\mathbf{r})$ is a measure of the variation of the thermal diffusivity values in the scattering object R from that of the surrounding (reference) region R_0. The ratio in equation (6.8d) has been symbolized by $n(\mathbf{r})$ deliberately, to suggest the analogy of this parameter to the effects of variations in the refractive index in conventional optical propagating fields [66]. The effect of the inhomogeneities of object region R appear as a source function in the right side of equation (6.8a) even though a new source was not introduced in the wave field. This is in agreement with the fact that inhomogeneities are sources of the scattered fields. $F(\mathbf{r})$ is the object function and it represents the inhomogeneities of scattering object region R. The object function $F(\mathbf{r})$ is zero at every point outside region R and has a non-zero value that represents the ratio of thermal diffusivities inside region R. If the inhomogeneous region R is removed from boundary S, then $F(\mathbf{r})$ will be zero everywhere and thus the medium in boundary S would be totally homogeneous. With this in mind, equation (6.8a) represents an inhomogeneous wave equation, and if the right hand side of equation (6.8a) is identically zero, it represents a homogeneous wave equation.

The full solution of equation (6.8a) satisfies, in three dimensions [85,86,71],

$$T(\boldsymbol{r}) = \int\int\int_{R} G_0(\boldsymbol{r}/\boldsymbol{r}_0)F(\boldsymbol{r}_0)T(\boldsymbol{r}_0)d^3\boldsymbol{r}_0 + \int\int_{\partial R}[G_0(\boldsymbol{r}/\boldsymbol{r}_0)\frac{\partial T}{\partial \boldsymbol{n}_r}(\boldsymbol{r}_0) - T(\boldsymbol{r}_0)\frac{\partial G_0}{\partial \boldsymbol{n}_r}]d\boldsymbol{r}_0. \qquad (6.9)$$

The integration is carried over spatial object region R and boundary ∂R. Also, $\mathbf{n}_r$ is the normal outward unit vector to ∂R. Region R is a cross-sectional slice in two-dimensional space [66], and is of constant thickness. $T(\mathbf{r})$ is the total thermal wave field; $\mathbf{r}$ and $\mathbf{r}_0$ are the coordinates of the observation point and the source point, with respect to the origin; $G_0(\mathbf{r}/\mathbf{r}_0)$ is the Green function, which will be discussed in more detail in a further section. In equation (6.9) the surface integral yields the bulk field (homogeneous), and the volume integral contains the scatterers. Thus, the integral equation (6.9) can be re-written in the following form, where the total surface integral is represented by the homogeneous field, $T_i(\mathbf{r})$,

$$T(\boldsymbol{r}) = T_i(\boldsymbol{r}) + \int\int\int_R G_0(\boldsymbol{r}/\boldsymbol{r}_0)F(\boldsymbol{r}_0)T(\boldsymbol{r}_0)d^3\boldsymbol{r}_0. \tag{6.10}$$

The total thermal wave field, $T(\mathbf{r})$, can be expressed as the sum of the incident (homogeneous) field, $T_i(\mathbf{r})$, and of the scattered field, $T_s(\mathbf{r})$, as follows:

$$T(\boldsymbol{r}) = T_i(\boldsymbol{r}) + T_s(\boldsymbol{r}). \tag{6.11}$$

Thus, from equations (6.10) and (6.11), one obtains the following expression for the scattered field,

$$T_s(\boldsymbol{r}) = \int\int\int_R G_0(\boldsymbol{r}/\boldsymbol{r}_0)F(\boldsymbol{r}_0)T(\boldsymbol{r}_0)d^3\boldsymbol{r}_0 \tag{6.12}$$

This is the final integral equation needed for solving the inverse problem. If the thermal wave source, $\boldsymbol{r}_0$, and/or observation point, $\boldsymbol{r}$, are not infinitesimally close to the boundary, S, which encloses the spatial region, R, then [85],

$$G_0(\boldsymbol{r}/\boldsymbol{r}_0) = G_0(\boldsymbol{r} - \boldsymbol{r}_0). \tag{6.13}$$

If not the case, then there will be $\boldsymbol{r}$ and $\boldsymbol{r}_0$ dependent components to G, but not in the $\boldsymbol{r}$-$\boldsymbol{r}_0$ form only.

6.3 Geometry for TSDT with Backpropagation and Transmission Detection

Thermal Wave Slice Diffraction Tomography can be evaluated in either backpropagation or transmission mode. The thermal wave field is excited with a laser beam, and the thermal wave field characteristics (amplitude and phase) are measured with a photothermal detector along the detection line. Backpropagation mode is met when the thermal excitation (at y=0) and the detection (at y=0) occur on the same side of the cross-section, whereas transmission is met when the thermal excitation (at y=0) and the detection (at $y=y_f$) occur on opposite sides, figure 6.1.

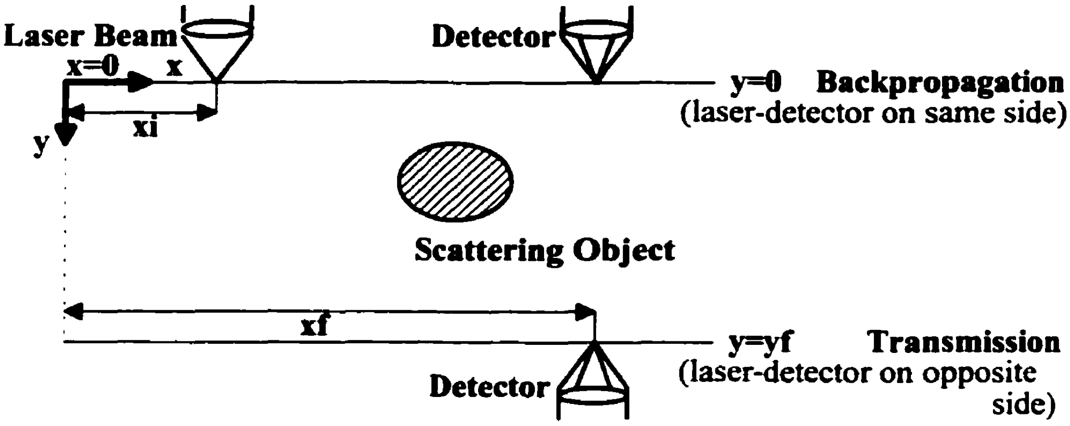

Figure 6.1 Geometry for TSDT amenable to backpropagation and transmission detection.

Region R in equation (6.12) is a slice in two-dimensional space, and it is assumed to be rectangular, with the thermal excitation on one side of the region (y=0), as in Figure 6.1. The rectangular region is then

$$R = \{(x,y)|x_i \leq x \leq x_f; 0 \leq y \leq y_f\}. \qquad (6.14)$$

If the thermal wave field in backpropagation $T(x,y=0)$ is measured, then from equation (6.12), the scattered field is

$$T_s(x,0) = \int_{x_i}^{x_f} \int_{0}^{y_f} G_0[r(x,0)|r_0(\xi,\eta)]F[r_0(\xi,\eta)]T[r_0(\xi,\eta)]d\xi d\eta \tag{6.15a}$$

where ξ and η are the integration dummy variables. Similarly, if the thermal wave field in transmission, $T(x,y=y_f)$, is measured, then the scattered field is

$$T_s(x,y_f) = \int_{x_i}^{x_f} \int_{0}^{y_f} G_0[r(x,y_f)|r_0(\xi,\eta)]F[r_0(\xi,\eta)]T[r_0(\xi,\eta)]d\xi d\eta. \tag{6.15b}$$

6.4 Approximations to the Wave Equation

Equation (6.12) is a Fredholm equation of the first kind and can not be solved directly. A solution can be written using either the Born or the Rytov approximation. These approximations are valid under different conditions, but the forms of the resulting solutions are quite similar [67].

6.4.1 The First Born Approximation

When the object is weakly inhomogeneous, the scattered field is weak and much smaller than the total field, $T_s(\mathbf{r}) \ll T(\mathbf{r})$. With equation (6.11), the scattered field in equation (6.12), can be written as

$$T_s(\boldsymbol{r}) = \int\int\int_R G_0(\boldsymbol{r}/\boldsymbol{r}_0)F(\boldsymbol{r}_0)T_i(\boldsymbol{r}_0)d^3\boldsymbol{r}_0 + \int\int\int_R G_0(\boldsymbol{r}/\boldsymbol{r}_0)F(\boldsymbol{r}_0)T_s(\boldsymbol{r}_0)d^3\boldsymbol{r}_0. \tag{6.16}$$

If the scattered field is small, compared to the total field, the effects of the second integral can be considered a small perturbation and thus ignored, leading to the approximation [67],

$$T_s(\boldsymbol{r}) \cong T_{Born}(\boldsymbol{r}) = \int\int\int_R G_0(\boldsymbol{r} - \boldsymbol{r}_0)F(\boldsymbol{r}_0)T_i(\boldsymbol{r}_0)d^3\boldsymbol{r}_0. \tag{6.17}$$

6.4.2 The First Rytov Approximation

An alternative to the scattered field is the Rytov approximation, which is valid under slightly different restrictions. Let the total field be represented as a complex phase [67]

$$T(\boldsymbol{r}) = \exp(\Psi(\boldsymbol{r})). \tag{6.18}$$

Substituting equation (6.18) into equation (6.8a), the following is obtained,

$$(\nabla\Psi(\boldsymbol{r}))^2 + \nabla^2\Psi(\boldsymbol{r}) + \tilde{k}_0^2 = -F(\boldsymbol{r}). \tag{6.19}$$

The total complex phase can be expressed as the sum of the incident and the scattered phase [67],

$$\Psi(\boldsymbol{r}) = \Psi_i(\boldsymbol{r}) + \Psi_s(\boldsymbol{r}). \tag{6.20}$$

The solution to equation (6.16) using (6.17) is then [67],

$$\Psi_s(\boldsymbol{r}) = \Psi_{rytov} = \frac{1}{T_i(\boldsymbol{r})} \iint\limits_{A_0} F(\boldsymbol{r}_0) T_i(\boldsymbol{r}_0) G_0(\boldsymbol{r} - \boldsymbol{r}_0) dA_0. \tag{6.21}$$

The Rytov approximation is valid when the phase change over a single wavelength is small. For very small objects and perturbations it can be proven mathematically that the Rytov solution is approximately equal to the Born solution [67].

6.5 Three-Dimensional Thermal Wave Green Function

Scatterer detection methodologies using propagating fields (e.g., acoustic, electromagnetic, optical, microwave) can be best quantified using Green function techniques [71]. If $G(\mathbf{r}/\mathbf{r}_0)$ is the field at the observer's point $\mathbf{r}$, caused by a unit point source at the source point $\mathbf{r}_0$, then the field at $\mathbf{r}$, caused by a source distribution $\rho(\mathbf{r}_0)$, is the integral of $G(\mathbf{r}/\mathbf{r}_0)\rho(\mathbf{r}_0)$ over the whole range of $\mathbf{r}_0$ occupied by the source [85]. The Green function, therefore, represents the field response resulting from a single point scatterer, so the scattered field can be expressed by a summation or integration over all individual scatterers. Boundary conditions are satisfied in the same way. The field at the boundary value is zero at every point except for surface point, $\boldsymbol{r}_0^s$. The boundary conditions on a surface can be thought of as being equivalent to source distributions on the surface [85].

6.5.1 Semi-Infinite Geometry

If the thermal wave flux is prescribed at the interface, z=0, the Green function must satisfy the homogeneous Neumann boundary condition at the source coordinate, z_0=0,

$$\nabla_0 G_0(\boldsymbol{r}-\boldsymbol{r}_0|\boldsymbol{r}-\boldsymbol{r}_0' \;,\omega)|_{z_0=0} = 0. \tag{6.22}$$

∇_0 indicates the normal derivative of G_0 along the normal source coordinate, z_0, at the interface. The coordinate, z_0, coincides with the direction normal to the dividing interface. From analogy to the infinite-domain Green function [11],

$$G_0(\boldsymbol{r}-\boldsymbol{r}_0,\omega) = \frac{e^{-q(\omega)|\boldsymbol{r}-\boldsymbol{r}_0|}}{4\pi a|\boldsymbol{r}-\boldsymbol{r}_0|}; \tag{6.23}$$

an impulsive image must be placed at $\mathbf{r}_0$ such that the thermal wave fluxes cancel out at the interface; $q(\omega)$ is the thermal wave number, equation (1.3a). The appropriate combination is [71],

$$G_0(\boldsymbol{r}-\boldsymbol{r}_0|\boldsymbol{r}-\boldsymbol{r}_0',\omega) = \frac{1}{4\pi a}\left(\frac{e^{-q(\omega)|\boldsymbol{r}-\boldsymbol{r}_0|}}{|\boldsymbol{r}-\boldsymbol{r}_0|} + \frac{e^{-q(\omega)|\boldsymbol{r}-\boldsymbol{r}_0'|}}{|\boldsymbol{r}-\boldsymbol{r}_0'|}\right), \tag{6.24}$$

corresponding to the situation shown in Figure 6.2. In terms of the coordinate system of Figure 6.2,

$$|\boldsymbol{r}-\boldsymbol{r}_0| = \sqrt{(x-x_0)^2+(y-y_0)^2+(z-z_0)^2} \equiv R_0 \tag{6.25a}$$

and

$$|\boldsymbol{r}-\boldsymbol{r}_0'| = \sqrt{(x-x_0)^2+(y-y_0)^2+(z+z_0)^2} \equiv R_0'. \tag{6.25b}$$

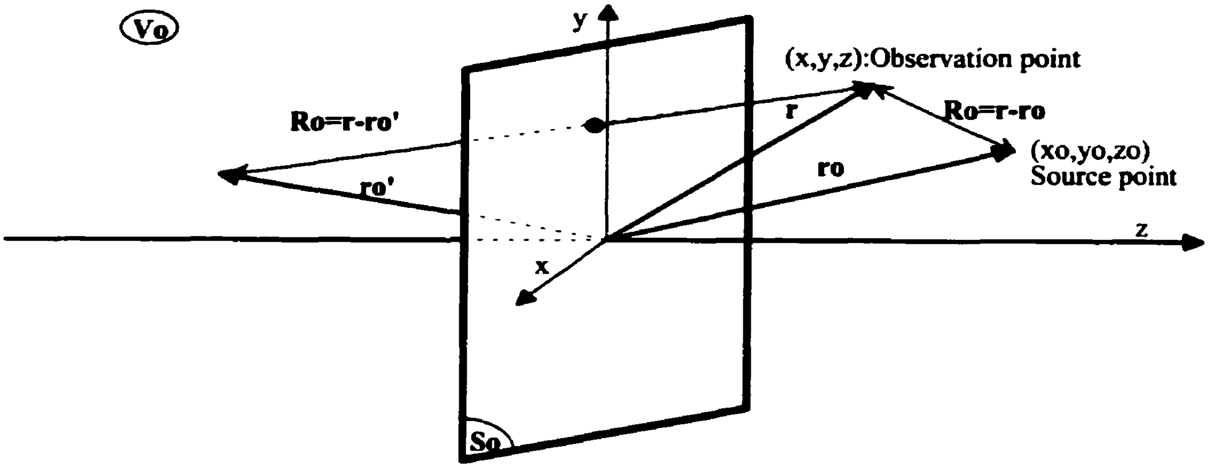

Figure 6.2 Coordinate system for three dimensional geometry.

6.5.2 Finite Geometry

For a finite geometry, the method of images can be used to accommodate plane bounding surfaces at z=0,L. Satisfying the Neumann boundary conditions at z=0,L, the resulting Green function is [11],

$$G_0(\boldsymbol{r}-\boldsymbol{r}_0|\boldsymbol{r}-\boldsymbol{r}_0',\omega)=\frac{1}{4\pi a}\sum_{n=-\infty}^{\infty}\left(\frac{e^{-q(\omega)|\boldsymbol{r}-\boldsymbol{r}_{0n}|}}{|\boldsymbol{r}-\boldsymbol{r}_{0n}|}+\frac{e^{-q(\omega)|\boldsymbol{r}-\boldsymbol{r}_{0n}'|}}{|\boldsymbol{r}-\boldsymbol{r}_{0n}'|}\right) \tag{6.26}$$

where,

$$|\boldsymbol{r}-\boldsymbol{r}_{0n}|=\sqrt{(x-x_0)^2+(y-y_0)^2+(z-(2nL+z_0))^2} \tag{6.25c}$$

and

$$|\boldsymbol{r}-\boldsymbol{r}_{0n}'|=\sqrt{(x-x_0)^2+(y-y_0)^2+(z-(2nL-z_0))^2} \tag{6.25d}$$

6.6 Homogeneous Temperature Field

The solution to the homogeneous thermal wave equation is [71],

$$\theta(\boldsymbol{r},\omega) = a \iint_{S_0} [G_0(\boldsymbol{r}-\boldsymbol{r}_0^s,\omega)\nabla_0\theta(\boldsymbol{r}_0^s,\omega) - \theta(\boldsymbol{r}_0^s,\omega)\nabla_0 G_0(\boldsymbol{r}-\boldsymbol{r}_0^s,\omega)]dS_0 \tag{6.27}$$

where S_0 is the surface surrounding the source volume V_0; r_0^s is a coordinate point on S_0. The thermal diffusivity, α, and thermal conductivity, *k*, are assumed to be constant throughout V_0. Equation (6.27) is equivalent to equation (6.9) without any volume sources.

Thermal wave flux, ϕ, is prescribed over the interface plane, z_0=0,

$$\phi(\boldsymbol{r}_s,t) = \phi_0 e^{-r_s^2/w^2} e^{i\omega t} \tag{6.28}$$

generated by a Gaussian laser beam of spot size, *w*, Figure 6.3.

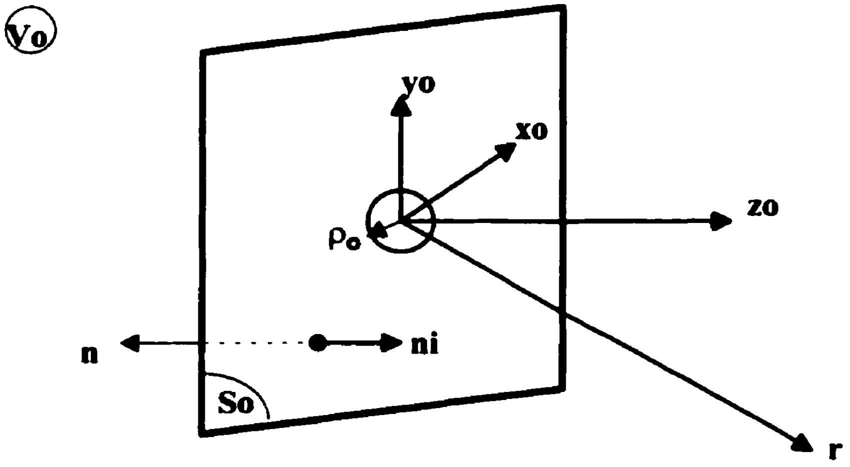

Figure 6.3 Semi-inifinite geometry for calculation of semi-inifinite thermal wave field generated by a Gaussian laser beam totally absorbed at the surface plane z_0=0.

6.6.1 Semi-Infinite Geometry

The Green function must satisfy the homogeneous Neumann boundary conditions on the source plane, $z_0=0$, and is given by equation (6.24). For the homogeneous case, no volume sources exist in the half-space (x_0,y_0,z_0), as in Figure 6.2. Therefore, from equation (6.27), the thermal wave field becomes [71],

$$\theta(\boldsymbol{r},\omega) = a \iint\limits_{S_0} G_0(\boldsymbol{r}-\boldsymbol{r}_0^s|\boldsymbol{r}-\boldsymbol{r}_0'^s,\omega)\nabla_0\theta(\boldsymbol{r}_0^s,\omega)\cdot d\boldsymbol{S}_0 \tag{6.29}$$

where dS_0 must be replaced by $d\boldsymbol{S}_i = \hat{\boldsymbol{n}}_i dx_0 dy_0$ pointing in the direction inside the half-space, V_0, to indicate the inflow of thermal energy. The surface, S_0, is the plane, $z_0=0$. Furthermore,

$$\nabla_0 = \hat{n}_0\frac{\partial}{\partial z_0} = -n_i\frac{\partial}{\partial z_0}, \tag{6.30}$$

so that, from the definition of thermal flux,

$$\begin{aligned}\phi(\boldsymbol{r}_s,t) = \phi(x_0,y_0,0;t) &= -k\frac{\partial}{\partial z_0}\theta(x_0,y_0,z_0;t)|_{z_0=0} \\ &= \phi_0 e^{i\omega t}\exp\left(-\frac{(x_0^2+y_0^2)}{w^2}\right)\end{aligned} \tag{6.31}$$

$$\nabla_0\theta(\boldsymbol{r}_0^s,\omega) = \hat{\boldsymbol{n}}_i\left(\frac{\phi_0}{k}\right)e^{i\omega_0 t}\exp\left(-\frac{(x_0^2+y_0^2)}{w^2}\right) \tag{6.32}$$

Combining equations (6.24), (6.29) and (6.32), the spectrum of the thermal wave field in the form of an integral over the bounding interface, $S_0(x_0,y_0)$ [71], is

$$\theta(\boldsymbol{r},\omega)=\frac{2\phi_0}{\pi k}e^{i\omega_0 t}\iint_{-\infty}^{\infty}\frac{dx_0dy_0}{R}\exp\left(-\frac{(x_0^2+y_0^2)}{w^2}-q(\omega)R\right), \tag{6.33}$$

where, at $z_0=0$,

$$R=|\boldsymbol{r}-\boldsymbol{r}_0|=|\boldsymbol{r}-\boldsymbol{r}'_0|=\sqrt{(x-x_0)^2+(y-y_0)^2+z^2}\,. \tag{6.34}$$

After some manipulation and a change of variables of equation (6.33), the thermal wave field of a semi-infinite geometry with a thermal wave flux prescribed over the surface becomes [71],

$$\theta(r,\omega)=\frac{2\phi_0}{\pi k}e^{i\omega_0 t}\exp\left(-\frac{(x^2+y^2)}{w^2}\right)J_3(x,y,z) \tag{6.35}$$

with,

$$J_3(x,y,z)=2\pi\int_0^{\infty}\frac{\rho}{\sqrt{\rho^2+z^2}}\exp\left(-\tfrac{\rho^2}{w^2}-q(\omega)\sqrt{\rho^2+z^2}\right)\boldsymbol{I}_0\left(\tfrac{2\rho}{w^2}\sqrt{x^2+y^2}\right)d\rho. \tag{6.36}$$

I_0 is the modified Bessel function of order zero. The thermal wave field represented by equations (6.35) and (6.36) can be evaluated numerically using the polynomial approximation for $I_0(x)$

given in [87, entries 9.8.1-9.8.4]. Integral J_3 has a removable singularity at z=0, which makes it very attractive for programming. At z=0, J_3 becomes,

$$J_3(x,y,0) = 2\pi \int_0^{\infty} \exp\left(\tfrac{\rho^2}{w^2} - q(\omega)\rho\right) I_0\left(\tfrac{2\rho}{w^2}\sqrt{x^2+y^2}\right) d\rho. \tag{6.37}$$

6.6.2 Finite Geometry

In the finite region, z_0=0,L, the thermal wave flux is prescribed over the interface plane, z_0=0, generated by a Gaussian laser beam of spot size, *w*, given by equation (6.28). The thermal-wave field is given by equation (6.29), with the thermal wave flux being approximately zero at z_0=L. The relevant Green function is now equation (6.26), satisfying the homogeneous Neumann conditions at the two interface planes. Equation (6.29) becomes [71],

$$\theta(\boldsymbol{r},\omega) = -\frac{1}{4\pi}\left[-\tfrac{\partial}{\partial z_0}\theta(x_0,y_0,z_0;\omega)|_{z_0=0}\right] \sum_{n=-\infty}^{\infty}\left(\frac{e^{-q(\omega)|\boldsymbol{r}-\boldsymbol{r}_{0n}|}}{|\boldsymbol{r}-\boldsymbol{r}_{0n}|} + \frac{e^{-q(\omega)|\boldsymbol{r}-\boldsymbol{r}'_{0n}|}}{|\boldsymbol{r}-\boldsymbol{r}'_{0n}|}\right) \tag{6.38}$$

where $\partial\theta/\partial z_0$ is given by equation (6.31). Defining the integrals

$$J_4^{(n)}(x,y,A_n) = 2\pi \int_0^{\infty} \frac{\rho}{\sqrt{\rho^2+A_n^2}} \exp\left(-\tfrac{\rho^2}{w^2} - q(\omega)\sqrt{\rho^2+A_n^2}\right) I_0\left(\tfrac{2\rho}{w^2}\sqrt{x^2+y^2}\right) \tag{6.39}$$

and splitting up the summation in equation (6.38) results in the expression

$$\theta(\mathbf{r},\omega)=\frac{2\phi_0}{\pi k}e^{i\omega_0 t}e^{\left(-\frac{x^2+y^2}{w^2}\right)}J_3(x,y,z)+\sum_{n=1}^{\infty}[J_4^{(n)}(x,y,2nL-z)+J_4^{(n)}(x,y,2nL+z)\}]. \tag{6.40}$$

The backpropagation thermal wave field becomes

$$T(x,y,0;\omega_0)=\frac{2\phi_0}{\pi k}\exp\left(-\frac{x^2+y^2}{w^2}\right)[J_3(x,y,0)+\sum_{n=1}^{\infty}\{J_4^{(n)}(x,y,0)+J_4^{(n)}(x,y,2nL)\}], \tag{6.41a}$$

and the transmitted thermal wave field becomes

$$T(x,y,L;\omega_0)=\tfrac{2\phi_0}{\pi k}\exp\left(-\tfrac{x^2+y^2}{w^2}\right)\begin{pmatrix} J_3(x,y,L)+\sum\limits_{n=1}^{\infty}\{J_4^{(n)}(x,y,(2n+1)L) \\ +J_4^{(n)}(x,y,(2n-1)L)\} \end{pmatrix}. \tag{6.41b}$$

Chapter 7

Inverse Process: TSDT Numerical Method

7.1 Introduction

The thermal wave diffraction problem leads to a so-called discrete ill-posed problem when solved numerically. By a discrete ill-posed problem it is meant that in either a square or an overdetermined system of linear algebraic equations (i.e., $\mathbf{Ax}=\mathbf{b}$ or min $\|\mathbf{Ax}-\mathbf{b}\|_2$) the coefficient matrix, **A**, is ill-conditioned, in a way that its singular values decay rapidly to zero [88]. In an ill-conditioned problem, small perturbations in the data cause large perturbations in the solution [89]. These types of problems are intrinsically difficult to solve, and, indeed, the standard methods in numerical linear algebra, such as LU- or QR- factorizations, cannot be used. Instead, a regularization method can be applied to stabilize the problem. In this work, the Tikhonov regularization method is used.

In this chapter the discretization (Section 7.2) of the theoretical formulation of Chapter 6 and numerical solution of the inverse problem (Section 7.3) is presented. In Section 7.4, the definition of an ill-posed problem is given, along with the regularization method used, necessary for solution. The optimization method used for the ill-posed problem is also explained in this section. Finally, in Section 7.5 the numerical procedure used to solve the infinite integrals of the homogeneous field is outlined.

7.2 Discretization of Equations

The sample region is divided into n intervals, and the rectangular region

$$R = \{(x,y) |\, x_i \le x \le x_f; 0 \le y \le y_f\}, \tag{7.1}$$

is divided into n^2 cells. Since, equations (6.15a) and (6.15b) are double integrals, the choice of n^2 points at the boundary is essential to obtain a square matrix [69].

For $1 \le j \le n^2$, equation (6.15b) assumes the following form,

$$T_s(j\Delta x, y_f) = \int_{x_i}^{x_f}\int_{0}^{y_f} G_0[r(j\Delta x, y_f)|r_0(\xi,\eta)]F[r_0(\xi,\eta)]T[r_0(\xi,\eta)]d\xi d\eta \tag{7.2}$$

and equation (6.15a) can be written in similar form, with $y_f=0$. To obtain the discretized form of equation (7.2), the grid points in R, $(k\Delta\xi, l\Delta\eta)$, are ordered in the following matrix order, m(k,l) [68],

$$\begin{pmatrix} 1 & 2 & 6 & 7 & 15 & 16 & . \\ 3 & 5 & 8 & 14 & 17 & . & . \\ 4 & 9 & 13 & .18 & . & . & . \\ 10 & 12 & 19 & . & . & . & . \\ 11 & 20 & . & . & . & . & . \\ 21 & . & . & . & . & . & . \\ . & . & . & . & . & . & . \end{pmatrix}. \tag{7.3}$$

The type of ordering in matrix (7.3) is general and it does not depend on the matrix dimensions. In addition, it is not difficult for numerical programming. Discretizing equation (7.2) by the rectangular rule [90],

$$T_s(k\Delta x, y_f) = \sum_{m=1}^{n^2} G_0(|r_k - r_{0m}|)F(r_{0m})T(r_{0m}), \tag{7.4}$$

where

$$r_{0m} = r_{0m(i,j)} = \ < (i\Delta\xi)^2, (j\Delta\eta)^2 >. \tag{7.5}$$

In addition, the scattered field in the entire cross-sectional region, R, for $0 \leq k.l \leq n$, can be calculated by [69],

$$T_s(k\Delta x, l\Delta y) = \sum_{i=1}^{n}\sum_{j=1}^{n} G_0(|r_{k,l} - r_{0m(i,j)}|)F(r_{0m(i,j)})T(r_{0m(i,j)}). \tag{7.6}$$

The complete solution to the inverse problem, with the final goal of retrieving the behavior of the object function, F, can be accomplished with the following arrangement of equations. Experimentally, the total transmitted or backpropagated field is measured. The measurement provides the amplitude, $|T|$, and phase, v, of the field, and, thus, the total field can be expressed in the following complex form,

$$T = |T|\exp(iv). \tag{7.7}$$

Using equation (6.11) with the theoretically calculated incident field, equation (6.41), the scattered field at the transmitted or backpropagated surface is computed. With a theoretically known complex Green function given by equation (6.26), the complex valued linear system (7.4) is solved for the multiplicity, *FT*, of the object function and the complex temperature field, *T*. Therefore, the scattered field in the entire region, R, can, then, be calculated with the complex valued linear system (7.6). The total field is computed with equation (6.11), and which is used in equation (7.4) to solve for the object function, *F*. The solution of the complex linear system (7.4) is a complex function whose real part is the required object function, *F*, and whose imaginary part is theoretically zero [69]. Numerically, it is not exactly zero, and its value may serve as a measure for successful reconstruction [69]. The computational flowchart of the full solution is shown in Table 7.1.

Although it is entirely possible to solve the inverse problem exactly by following the flowchart in Table 7.1, in this work the first Born approximation, equation (6.17) - Table 7.2, is adopted. Namely, in equation (7.2), $T_i(r)$ is used instead of $T(r)$. Again, using equation (6.11), with the theoretically calculated incident field, equation (6.41), the scattered field at the transmitted or backpropagated surface is computed. The object function, $F(r_0)$, is directly computed with the complex linear system (7.4) by replacing T with T_i. The computational flowchart of the approximate solution of the inverse problem for the object function is shown in Table 7.6. The use of the Born approximation simplifies large scale computation and saves computer time.

Known Input Fields	Equation #	Computed Field
$T(k\Delta x, y_f/0)$ -Experimental $T_i(k\Delta x, y_f/0)$ -Theoretical	$\longrightarrow$ (6.11) $\longrightarrow$	$T_s(k\Delta x, y_f/0)$
$T_s(k\Delta x, y_f/0)$ -Computational $G_0(\lvert\mathbf{r}-\mathbf{r}_0\rvert)$ -Theoretical	$\longrightarrow$ (7.4) $\longrightarrow$	$F(\mathbf{r}_0)T(\mathbf{r}_0)$
$F(\mathbf{r}_0)T(\mathbf{r}_0)$ -Computational $G_0(\lvert\mathbf{r}-\mathbf{r}_0\rvert)$ -Theoretical	$\longrightarrow$ (7.6) $\longrightarrow$	$T_s(k\Delta x, l\Delta y)$
$T_s(k\Delta x, l\Delta y)$ -Computational $T_i(\mathbf{r}_0)$ -Theoretical	$\longrightarrow$ (6.11) $\longrightarrow$	$T(\mathbf{r}_0)$
$T(\mathbf{r}_0)$ -Computational $G_0(\lvert\mathbf{r}-\mathbf{r}_0\rvert)$ -Theoretical $T_s(k\Delta x, y_f/0)$ -Computational	$\longrightarrow$ (7.4) $\longrightarrow$	$F(\mathbf{r}_0)$

Table 7.1 Computational flowchart for the calculation of the object function $F(\mathbf{r}_0)$ ($y_f/0$ indicates transmitted/backpropagated thermal wave detection).

Known Input Fields	Equation #	Computed Field
$T(k\Delta x, y_f/0)$ -Experimental $T_i(k\Delta x, y_f/0)$ -Theoretical	$\longrightarrow$ (6.11) $\longrightarrow$	$T_s(k\Delta x, y_f/0)$
$T_i(\mathbf{r}_0)$ -Theoretical $G_0(\lvert\mathbf{r}-\mathbf{r}_0\rvert)$ -Theoretical $T_s(k\Delta x, y_f/0)$ -Computational	$\longrightarrow$ (7.4) $\longrightarrow$	$F(\mathbf{r}_0)$

Table 7.2 Computational flowchart for the calculation of the object function $F(\mathbf{r}_0)$ by means of the Born approximation ($y_f/0$ indicates transmitted/backpropagated thermal wave detection).

7.3 Matrix Formalization of Linear System

The main objective is to solve the complex linear system (7.4) for the object function $F(\mathbf{r})$. This can be achieved by expressing the linear system in terms of linear algebra. Let **L** be the following complex matrix,

$$L_{km} = G_0(|r_k - r_{0m(i,j)}|). \tag{7.8}$$

When calculating the solution of equation (6.11), instead of the rectangular rule for integration, the trapezoidal rule for integration is used for even values of n, and Simpson's rule for integration is used for odd values of n [90]. The trapezoidal rule is a second-order method, and is more accurate than the rectangular rule which is a first-order method. Simpson's rule is a fourth-order method [91]. Because of its higher accuracy level, Simpson's rule is used whenever possible. Furthermore, an n^2 x n^2 system of linear equations can be defined as follows,

$$Af = t, \tag{7.9}$$

where $\mathbf{A}=\mathbf{D}_{\mathrm{km}}\mathbf{L}_{\mathrm{km}}$, $\mathbf{D}_{\mathrm{km}}$ is the constant matrix that applies either trapezoidal or Simpson's rule of integration, $\mathbf{f}=FT$, and $\mathbf{t}=T_s$. Let **f** represent the solution of matrix system (7.9). The matrix system is solved for FT and, after deducing T from equations (7.6) and (6.11), a new linear system is defined with $\mathbf{f}=F$ and $\mathbf{A}=\mathbf{D}_{\mathrm{km}}\mathbf{L}_{\mathrm{km}}T$. Thus, the final solution can be reached. When the Born approximation is used, $\mathbf{f}=F$ and $\mathbf{A}=\mathbf{D}_{\mathrm{km}}\mathbf{L}_{\mathrm{km}}T_i$.

7.4 Ill- Conditioning and Tikhonov Regularization Method

From a computational point of view, the main problem with this linear system is that the matrix G_{0T_i} is often almost singular [68]. The accuracy of the solution is substantially influenced by the conditioning of the given system of equations. Discrete ill-posed problems are analyzed and solved by numerical techniques. The rapid development of computer engineering, the introduction of mathematical methods to new fields of science and technology, and the widespread use of computers have brought computing mathematics to a point of intensive development of theory and methods for solving ill-posed problems [89]. The general theory and methods for solving ill-posed problems were initiated by the work of Tikhonov (1943) [89,93]. From Tikhonov and other prominent mathematicians, a number of vital and interesting results have been obtained in the theory of ill-posed problems, to date.

7.4.1 Ill-Posed Problems

The ill-conditioning of a matrix can be defined by the condition number,

$$\mathrm{cond}(A) = \|A\| \; \|A^{-1}\|, \tag{7.10}$$

where $\|A\|$ denotes a given matricial norm. A linear system for which $\mathrm{cond}(A) \cong 1$ is called *well conditioned*; a linear system for which $\mathrm{cond}(A) >> 1$ is called *ill-conditioned* [92]. Namely, a system is said to be ill-conditioned if a relatively small change in one of the coefficients results in a relatively large change in the solution. If there are elements in the inverse $\mathbf{A}^{-1}$ of the matrix that are several orders of magnitude larger than those in original matrix **A**, then the matrix is probably ill-conditioned. Formally speaking, an inverse problem is ill-posed (ill-conditioned) if one of the criteria, introduced by Hadamard [94], of existence, uniqueness and stability is violated. Let **Ax=b** be an algebraic problem, equivalent to system (7.9), with **A** being ill-conditioned. For existence to be fulfilled there must exist a solution **x** for any **b**. A way of overcoming this criterion is to calculate a function $\mathbf{x}_\sigma$ that minimizes the distance between **Ax** and **b** [95],

$$\min \|\mathbf{b}-\mathbf{A}\mathbf{x}\| = \|\mathbf{b}-\mathbf{A}\mathbf{x}_\sigma\|. \tag{7.11}$$

Uniqueness is fulfilled if there exists one and only one solution **x** for any **b**. In order to overcome the uniqueness criterion, information from the experimental nature of the problem can be used *a posteriori* for selecting the inverse solution. Finally, stability occurs when the solution **x** is continuously dependent on **b**. Lack of stability means that two numbers η and $\varepsilon(\eta)$ do not exist so that [95], if

$$\|\mathbf{b}_2-\mathbf{b}_1\| \le \eta \tag{7.12}$$

it follows that

$$\|\mathbf{x}_2-\mathbf{x}_1\| \le \varepsilon(\eta), \tag{7.13}$$

independently of the choice of $\mathbf{x}_1$ and $\mathbf{x}_2$. The stability of the linear system is obtained by forcing the validity of $\varepsilon(\eta) \rightarrow 0$ for $\eta \rightarrow 0$. Numerical methods for treating discrete ill-posed problems seek to overcome the problems associated with a large condition number by replacing the problem with a "nearby" well-conditioned problem whose solution approximates the required solution. Such methods are called *regularization methods*, and they include a so-called regularization parameter, σ, which controls the degree of smoothing or regularization applied to the problem [96]. There are different methods of regularization such as truncated Singular-Value Decomposition (SVD), Tikhonov regularization, and maximum-entropy. These methods are the subject of many publications [97].

7.4.2 Tikhonov Regularization Method

To solve the ill-posed problem in equation (7.9), Tikhonov's regularization method is used. Let **Ax=b** be an algebraic problem, equivalent to system (7.9), with **A** being ill-conditioned. The regularized solution, $\mathbf{x}_\sigma$, as proposed by Tikhonov is [93],

$$\boldsymbol{x}_\sigma = \min\{\|\boldsymbol{A}\boldsymbol{x}-\boldsymbol{b}\|_2 + \sigma\|\boldsymbol{L}(\boldsymbol{x}-\boldsymbol{x}_0)\|_2\} \tag{7.14}$$

where $\mathbf{x}_0$ is an initial estimate of the solution, and matrix **L** is either the identity matrix **I** or a discrete approximation to a derivative operator. The regularization parameter, σ, controls the weight given to minimization of the side constraint, $\|\mathbf{L}(\mathbf{x}-\mathbf{x}_0)\|_2$, relative to minimization of the residual norm, $\|\mathbf{Ax}-\mathbf{b}\|_2$. For this work, no particular knowledge about the desired solution is available, so $\mathbf{x}_0=\mathbf{0}$ is used; also matrix **L** is set as the identity matrix, **I**. The solution reduces to minimizing the following function,

$$\Phi(x) = \|\boldsymbol{A}\boldsymbol{x}-\boldsymbol{b}\|_2 + \sigma\|\boldsymbol{x}\|_2, \tag{7.15}$$

where

$$\|x\|_2 = \sqrt{\sum_{i=1}^{n} |x_i|^2}\,. \tag{7.16}$$

Minimization of function, $\Phi(\mathbf{x})$, is equivalent to minimization of

$$\Psi(x) = \sum_{i=1}^{n}\left(\sum_{j=1}^{n} a_{ij}x_j - b_i\right)\left(\sum_{j=1}^{n} \bar{a}_{ij}\bar{x}_j - \bar{b}_i\right) + \sigma \sum_{i=1}^{n} x_i\bar{x}_i, \tag{7.17}$$

where bars indicate complex conjugation [69]. Differentiating with respect to the components of x, it is found that the minimum can be obtained as the solution of the linear system

$$(\sigma \boldsymbol{I} + \boldsymbol{A}^*\boldsymbol{A})\boldsymbol{x} = \boldsymbol{A}^*\boldsymbol{b}, \tag{7.18}$$

where asterix quantities denote adjoint matrices.

To solve the system (7.16), the Eispack library [98] is used to compute the eigenvalues and eigenvectors of matrix $\mathbf{M}=\sigma\mathbf{I}+\mathbf{A}^*\mathbf{A}$. Letting $\mathbf{V}$ be a matrix whose columns are the eigenvectors of $\mathbf{M}$, and $\mathbf{E}$ be a diagonal matrix of the corresponding eigenvalues,

$$\boldsymbol{M}^{-1} = \boldsymbol{V}\boldsymbol{E}^{-1}\boldsymbol{V}^*. \tag{7.19}$$

The elements of the diagonal matrix, $\mathbf{E}$, are greater or equal to regularization parameter, σ, and, therefore, as long as σ is kept within the computer accuracy, a good inversion can be obtained. The fundamental idea in Tikhonov regularization is to introduce a trade-off between the size of the residual norm $||\mathbf{Ax}-\mathbf{b}||_2$ and the side constraint $||\mathbf{x}||_2$ by choosing a suitable regularization parameter, σ, a satisfactory solution for which the two constraints must be balanced [99]. Too much regularization leaves out information actually available in **b** while too little regularization produces a solution dominated by errors. A method for choosing the optimal regularization parameter, and thus the optimal solution, is needed for the Tikhonov regularization. Many methods have been introduced for finding the optimum regularization parameter like the discrepancy principle, the quasi-optimality criterion, generalized cross-validation and L-curve criterion [96].

7.4.3 L-Curve Method

In this thesis, we adopt the L-curve method [96,100] for finding the optimal regularization parameter. The L-curve is *a posteriori* method based on plotting the side constraint $\|\mathbf{x}_\sigma\|_2$ of the solution versus the residual norm $\|\mathbf{Ax}-\mathbf{b}\|_2$ for a particular regularization parameter. A schematic of the L-curve is shown in Figure 7.1 and, as can be seen, the name "L-curve" is derived from the fact that the curve is L-shaped. The "corner" of the curve corresponds to a regularization parameter that is optimal [96].

The "flat" part of the L-curve is dominated by regularization errors occurring from oversmoothing and the "vertical" part is dominated by perturbation errors occurring from undersmoothing. Thus the corner of the L-curve corresponds to a solution in which there is a fair balance between the regularization and perturbation errors. A simple example to illustrate the behavior of the L-curve is shown below.

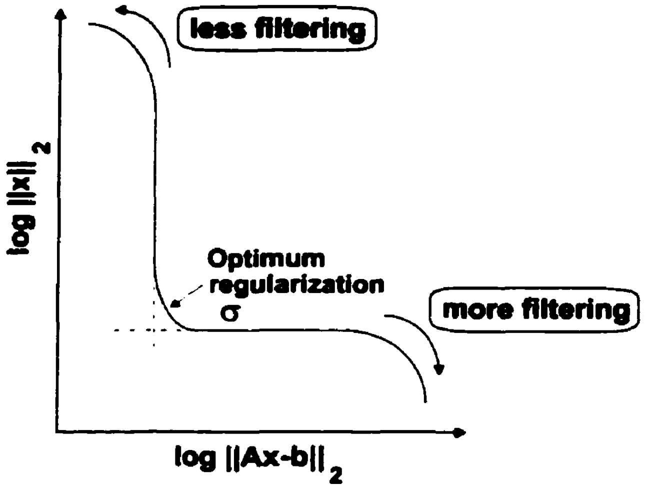

Figure 7.1 L-curve method: corner of curve corresponds to optimum regularization.

7.4.3 L-Curve Example

The definition of the L-curve example was taken from Hansen [99] and it was solved using numerical code developed as part of this work. The problem is based on considering the discrete ill-posed problem of a Fredholm integral equation of the first kind,

$$\int_a^b K(s,t)f(t)dt = g(s), \qquad c \le s \le d, \tag{7.20}$$

where K is the kernel, g is the observed quantity and f is the unknown solution. This is an example taken from image restoration [99] with,

$$K(s,t) = \left[(\cos s + \cos t)\left(\frac{\sin u}{u}\right)\right]^2, \tag{7.21}$$

$$u = \pi(\sin s + \sin t) \quad s,t \in [-\pi/2, \pi/2]. \tag{7.22}$$

$$f(t) = 2\exp(-6(t-0.8)^2) + \exp(-2(t+0.5)^2). \tag{7.23}$$

with *f(t)* being the exact solution. The problem was then discretized in the following matrix form,

$$\mathrm{A}\mathbf{x}_\sigma = \mathbf{b} + e \tag{7.24}$$

where $\mathbf{A} \equiv K(s,t)$, $\mathbf{b} \equiv g(s)$ and $\mathbf{x}_\sigma$ is the sought solution. e is perturbation noise introduced in the problem with a zero mean and a standard deviation of 1×10^{-4}. Equation (7.22) solved with Tikhonov regularization method is presented in Section 7.4.2. The side constraint $\|\mathbf{x}_\sigma\|_2$ of the solution was plotted versus the residual norm $\|\mathbf{A}\mathbf{x} - \mathbf{b}\|_2$ for particular regularization parameters as is seen in Figure 7.2. In this graph the corner of the L-curve corresponds to a regularization parameter, $\sigma = 2.3 \times 10^{-6}$. The exact solution of the problem as well as solutions corresponding to regularization parameters $\sigma = 4.3 \times 10^{-8}$, $\sigma = 2.3 \times 10^{-6}$ and $\sigma = 0.1$, are shown in Figure 7.3. The first solution of regularization parameter, $\sigma = 4.3 \times 10^{-8}$ is a solution which is from the "vertical" part of the L-curve and it is dominated by noise which distorts the maximums of the solution. This is an undersmooth solution influenced by the perturbation noise. The solution with a regularization parameter, $\sigma = 0.1$ is from the "flat" part of the L-curve and it is an oversmoothed solution which reduces the contrast of the maximum. The best solution is, indeed, the corner of the L-curve, regularization parameter, $\sigma = 2.3 \times 10^{-6}$, as shown in Figure 7.3.

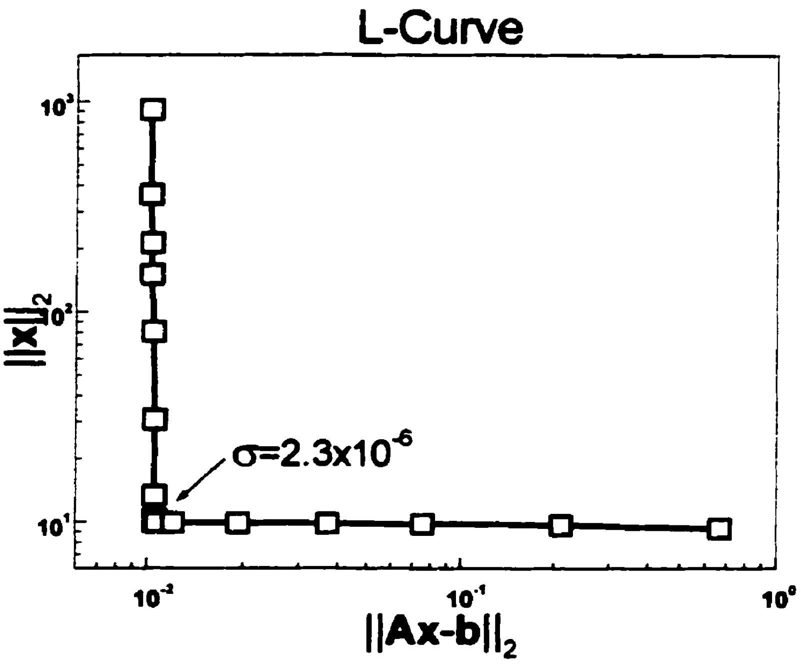

Figure 7.2 L-curve of inverse problem defined in equation 7.22.

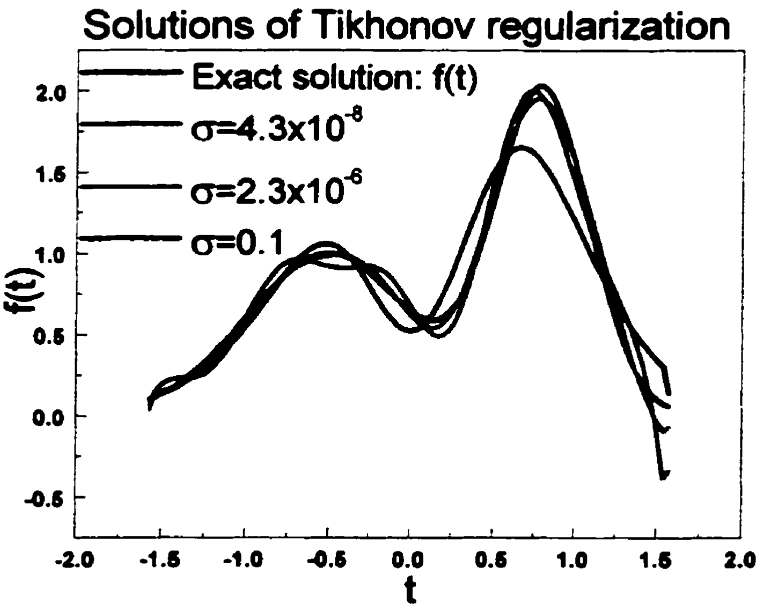

Figure 7.3 Inverse problem defined in equations (7.18)-(7.21): exact solution (black); $\sigma=4.3\times10^{-8}$ (green), $\sigma=2.3\times10^{-6}$ (red) and $\sigma=0.1$ (blue).

7.5 Amplitude and Phase of Homogeneous Field

For the homogeneous backpropagation or transmission thermal wave field, the amplitude and phase of the field were measured. Equations (6.41a) and (6.41b) were rewritten, for numerical ease, by separating the field into a real and an imaginary part,

$$\begin{matrix} Re[T(x,y,z;\omega_0)] \\ Im[T(x,y,z;\omega_0)] \end{matrix} = \begin{matrix} + \\ - \end{matrix} \frac{4\phi_0}{k}\exp(-\frac{x^2+y^2}{w^2})$$

$$\times\{\int_0^\infty \frac{e-\frac{\rho^2}{w^2}}{\sqrt{\rho^2+z^2}} e^{-a\sqrt{\rho^2+z^2}} I_0\left(\frac{2\rho}{w^2}\sqrt{x^2+y^2}\right)\rho d\rho \begin{matrix} \cos(a\sqrt{\rho^2+z^2}) \\ \sin(a\sqrt{\rho^2+z^2}) \end{matrix}$$

$$+\sum_{n=1}^\infty \int_0^\infty \frac{e^{-\frac{\rho^2}{w^2}}}{\sqrt{\rho^2+(2nL-z)^2}} e^{-a\sqrt{\rho^2+(2nL-z)^2}} I_0\left(\frac{2\rho}{w^2}\sqrt{x^2+y^2}\right)\rho d\rho \begin{matrix} \cos(a\sqrt{\rho^2+(2nL-z)^2}) \\ \sin(a\sqrt{\rho^2+(2nL-z)^2}) \end{matrix}$$

$$+\sum_{n=1}^\infty \int_0^\infty \frac{e^{-\frac{\rho^2}{w^2}}}{\sqrt{\rho^2+(2nL+z)^2}} e^{-a\sqrt{\rho^2+(2nL+z)^2}} I_0\left(\frac{2\rho}{w^2}\sqrt{x^2+y^2}\right)\rho d\rho \begin{matrix} \cos(a\sqrt{\rho^2+(2nL+z)^2}) \\ \sin(a\sqrt{\rho^2+(2nL+z)^2}) \end{matrix} \quad \}$$

(7.25)

where, a is the inverse of thermal diffusion length, $a=\sqrt{\frac{\pi f}{a_0}}$; and the other variables are as defined in Section 6.6. When z=0, the backpropagation homogeneous field is represented, when z=L, the transmission homogeneous field is represented. The amplitude of the field can then be calculated as,

$$|\theta(x,y,z;\omega_0)| = \sqrt{[Re\theta]^2+[Im\theta]^2}, \tag{7.26}$$

and, the phase of the field as,

$$\phi(x,y,z;\omega_0) = \tan^{-1}\left[\frac{Im\theta}{Re\theta}\right]. \tag{7.27}$$

For the backpropagation mode (z=0), the first integral of equation (7.25) has an analytically removable singularity at z=0, thus eliminating any numerical problems from the function to be integrated.

The Hankel integral of equation (7.25) is an improper integral i.e., its upper limit is infinite. It is assumed that the integral exists and approaches a finite value as the upper limit of integration approaches infinity. This assumption is based on the physical quantity represented by the integral. Equation (7.25) was calculated using the improper integral routine, *qromo* with *midpnt* taken from Numerical Recipes in Fortran [101]. The routine solves for smooth integrals with an upper limit to infinity using Romberg integration on a semi-open interval. In calculating improper integrals the convergence criterion must be carefully met. A convenient convergence approach for this integral is to replace the infinite upper limit with a finite value *b* and to evaluate the integral with increasing values of *b* until any further increase in *b* results in a negligible change in the integral. The downfall of this approach is that the value *b* is chosen according to the integrand behavior, which in turn depends on the input parameters. If the integrand is not tested for convergence each time an input parameter is changed, an error can occur. To avoid this rigorous procedure the additional routine *midinf* [101], which maps an infinite range of integration to a finite one using the identity

$$\int_{a}^{b} f(x)dx = \int_{1/b}^{1/a} \frac{1}{t^2} f\left(\frac{1}{t}\right)dt \tag{7.28}$$

is used. As a result, the Hankel integral is separated into two integrals,

$$\int_{0}^{\infty} f(x)dx = \int_{0}^{b} f(x)dx + \int_{1/1\times10^{30}}^{1/b} \frac{1}{t^2} f\left(\frac{1}{t}\right)dt \tag{7.29}$$

where the first integral is calculated using *midpnt* routine from 0 to b and the second integral is calculated using *midinf* routine from b to a large number (1×10^{30}). This type of methodology assures that the convergence criterion is reached every time, provided b is large enough so that the integrand begins to approach its asymptotic decrease.

The original numerical code to solve the system (7.18) was written in Fortran 77 for a Sun4 workstation by Offer Pade [68], and was later transferred to a Pentium II 266MHz CPU with 128Mb of RAM personal computer, where it was modified for a Microsoft Fortran Powerstation compiler [70]. In addition, the development of the homogeneous field and Green function presented in Chapter 6 was implemented in the program [70]. The L-curve method was implemented in the program by executing for a range of regularization parameters, plotting all the residuals and finally choosing the corner solution of the L-curve.

Chapter 8

Experimental System and Data: Tomographic microscope

8.1 Introduction

In this chapter, the experimental technique needed to acquire the scanned data for thermal wave tomograms is explored. The data is obtained at one cross-section from different laser and detector positions. Historically, the first detection method used to obtain tomographic slice data was photopyroelectric detection [62,63], which was limited to transmission measurements. A photothermal radiometric detection method then followed [70]. However, a main disadvantage was that a low resolution setup was used which resulted in image broadening [72]. To overcome this problem, a high-resolution photothermal setup for tomographic application was constructed in this thesis. The method is based on the photothermal radiometric detection outlined in Chapter 4, which has the flexibility for both backpropagation and transmission measurements. This is a non-contact method.

8.2 Experimental System: Short Description

The experimental setup for cross-sectional imaging via photothermal-radiometric detection is shown in Figure 8.1. A 514.5nm wavelength cw Innova Ar^+ laser from Coherent is modulated and then focused onto a sample to a spot size of approximately 27μm. The modulation is performed by an external Acousto-Optic modulator (AOM) (ISOMET 1201E-1).

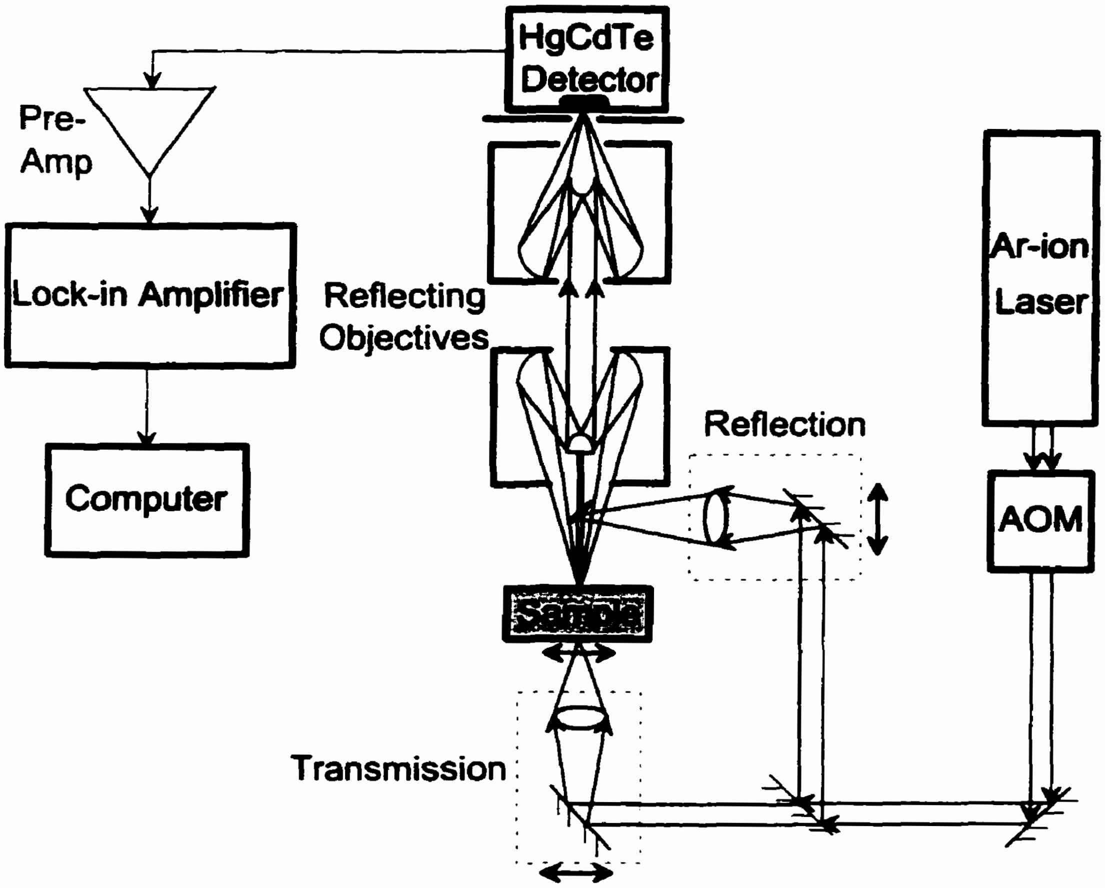

Figure 8.1 High resolution tomographic microscope experimental setup.

The blackbody radiation from the optically excited sample is collected and collimated by two axially aligned reflecting objectives [102]. It is then focused onto a liquid nitrogen cooled HgCdTe (Mercury-Cadmium-Telluride) detector (EG&G Judson Model J15D12-M204-S050U). The HgCdTe detector is a photoconductive element that undergoes a change in resistance proportional to the intensity of the incident infrared radiation. It has an active square size of 50μm x 50μm and a bandwidth of 2-12μm. The detector is operated at a cryogenic temperature of 77°K [77] since its efficiency increases with decreasing temperature. An A-R coated germanium window with a transmission bandwidth of 2-14μm is mounted in front of the detector to block any visible radiation from the pump laser. Before being sent to the digital lock-in amplifier (Stanford Research System Model SR850) [78], the photothermal-radiometric signal is amplified by a preamplifier (EG&G Judson Model PA-300) specifically designed for operation with the HgCdTe detector. The low noise preamplifier ensures a proper performance for subsequent signal processing with a lock-in amplifier. The lock-in amplifier, which is interfaced with a personal computer, receives the preamplifier output and rejects all stray signals except those that have the same modulation frequency as the excitation beam. This process of data acquisition, storage, and scanning is fully automated. The instrumentation has the ability to perform in either backpropagation or transmission mode by directing the laser beam to the front or rear surface of the sample using removable mirrors.

8.3 Experimental System: New Components Detailed Description

After modulation, the beam was directed towards a focusing lens through mirrors. Before entering the focusing lens the beam size was measured to be 0.78mm, 1/e radius. In this work, a diffraction-limited Gradium glass Plano-Convex lens (Newport Gradium™ GPX085 LR.14) with 60mm focal length and a 400-700nm anti-reflection coating was used. Gradium lenses utilize a unique optical glass where the refractive index varies along the optical axis providing a focusing power by eliminating spherical aberration and significantly reducing coma. Spherical aberration occurs when not all incoming rays focus on the focal point thus forming an image that is not sharp. Coma results when different parts of the lens surface exhibit different degrees of magnification. The lens was mounted on a 12.2mm travel XYZ miniature translation stage (Newport MS-500-XYZ). This mounting was ideal for precise centering of the Gradium lens. For accurate theoretical modeling the beam profile at the focal point was measured with a photodiode and the 1/e radius was found to be 27μm as shown in Figure 8.2. The results of the measurement were reconfirmed using a beam profilometer with a CCD camera. A good Gaussian profile was also obtained.

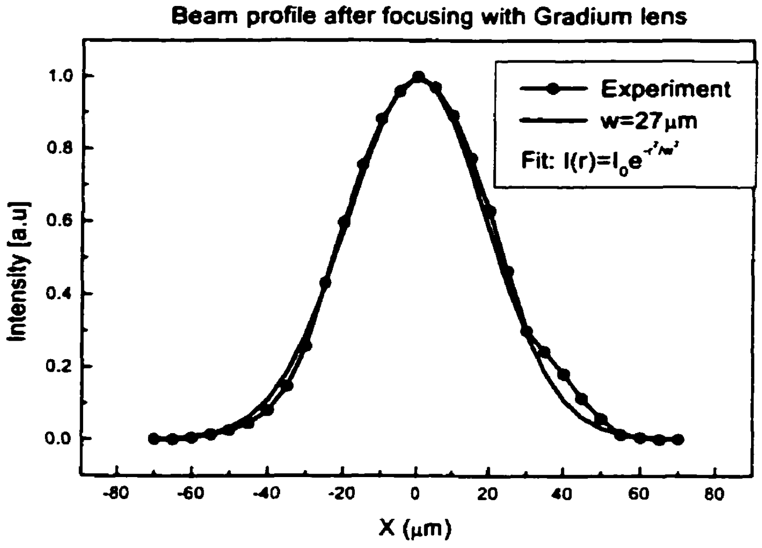

Figure 8.2 Beam profile after focusing, as measured with a photodiode.

The blackbody radiation from the optically excited sample is collected and collimated by two axially aligned reflecting objectives (Ealing: x36 0.5 N.A. 25-0522 and x15 0.28 N.A 24-0506). Reflecting microscope objectives are known for their unique optical properties. They are based on a two-mirror design; a small convex primary mirror and a larger concave secondary mirror (Figure 8.3). Because of the all-reflecting construction, the reflecting objectives are free of chromatic aberration. Spherical aberration, coma and astigmatism are corrected by choosing appropriate values for the mirror radii of curvature and their separation. Reflecting objectives have large Numerical Aperture (NA) for improved light gathering power and high throughput from the ultraviolet to the far infrared due to their all-reflective construction.

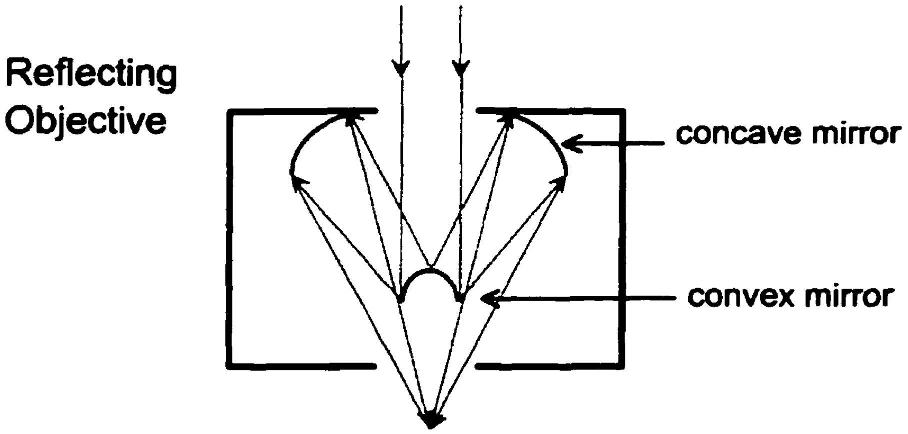

Figure 8.3 Reflecting objective schematic.

The radiometric signal was detected with an HgCdTe detector (EG & G Judson Model J15D12-M204-S050U), which is a photoconductive detector designed for operation in the 2-12μm wavelength range. The detector requires a low voltage noise preamplifier. An AC coupling capacitor blocks the DC bias voltage from the high gain preamplifier and prevents DC saturation. The preamplifier used (PA-300) was supplied with a bias resistor to provide optimum bias voltage to the detector. This preamplifier offers a low noise, adjustable gain, DC offset compensation and a linearizing network. A low noise digital lock-in amplifier (Stanford Research System Model SR850) [78] was used. The lock-in amplifier is interfaced with a personal computer and the data acquisition is automated. All the experimental system components were placed on a pneumatic table (Newport corporation) so that the system would be isolated by building vibrations.

8.4 Scanning System

In the experimental setup, both the modulated heating source and the detector are localized, and therefore can be scanned independently. For each laser position, data is collected at several detector positions along a straight line. This defines the cross-sectional plane (tomographic scan) to be imaged i.e., line PQ in Figure 8.4. The scan for the same cross-section is repeated for different laser positions. The experimental information is then used to reconstruct the respective cross sectional slice, using the method outlined in Chapter 7.

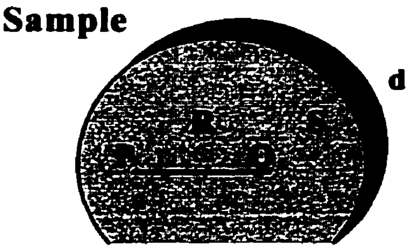

Figure 8.4 Line scan for cross-sectional imaging, of sample thickness d with subsurface defect.

In practice moving the sample becomes equivalent to moving the detector. For example, the transmission tomographic scan is performed by first positioning the laser and then moving the sample and laser together over the detector. Figure 8.5 illustrates a tomographic scan in transmission with three detection points and three laser positions, which ensures that the same cross-section is observed at all times. When detector and laser are aligned with each other the signal is the highest. For laser position 1, the maximum occurs at point 3, for laser position 2, the maximum occurs at point 2 and for laser position 3, the maximum occurs at point 1. These three scans construct the experimental tomographic scan. In backpropagation mode the tomographic scan is achieved by attaching a 45° mirror to the first reflective objective (Figure 8.6). The size of the mirror is limited by the dead optical field that the reflective objective produces. For this reason the dimensions of the mirror are 3mm×2mm, limiting the tomographic scan to 1.5mm

(3mm/2). Experimentally, this limit was found to be 0.7mm and thus tomographically only a maximum cross-section of 0.7mm can be investigated at a time.

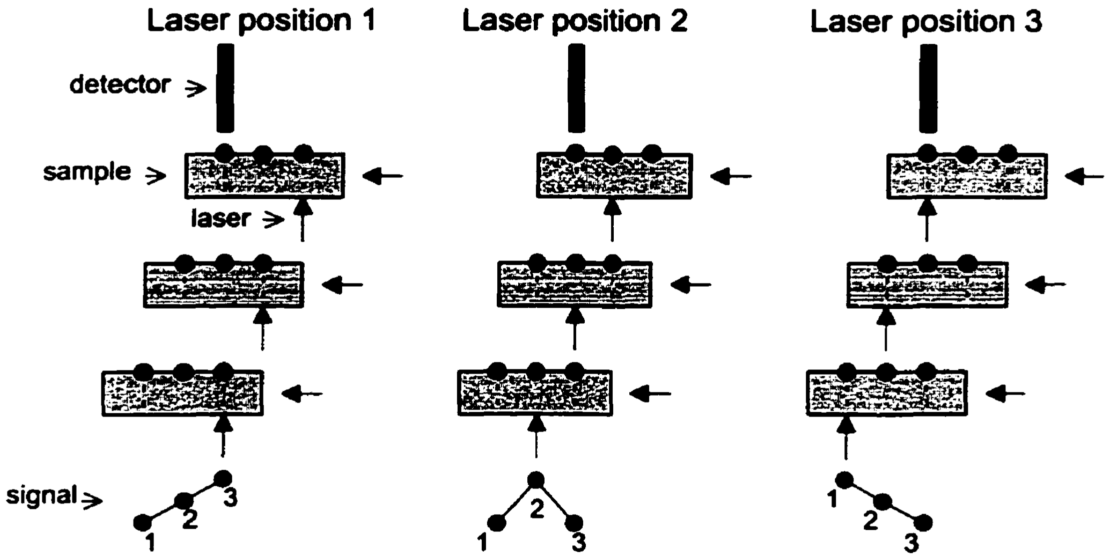

Figure 8.5 Method of tomographic scan.

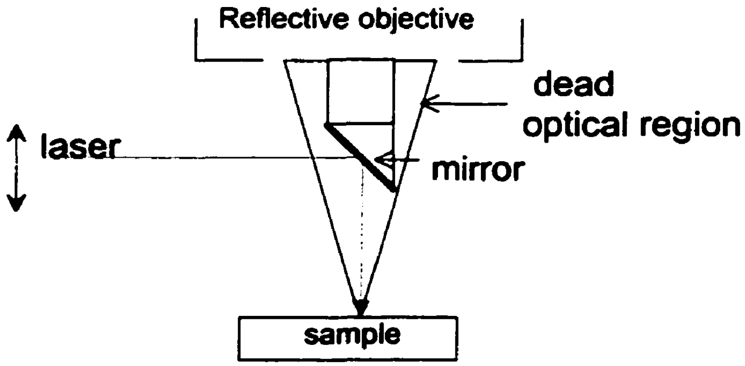

Figure 8.6 Part of backpropagation experimental setup.

8.5 Instrumental Performance and Image Resolution

As mentioned in the introduction, many factors can contribute to the resolution of a microscope. Apart from the extreme-near-field underlying physics of the thermal microscope, experimental factors like imperfections in lenses or mirrors, coarseness of the detector can lead to a lower resolution. With proper experimental design, the most significant limitation becomes the beam spot size which if not smaller than the defect, will cause the image to broaden [15].

In the previous tomographic work [72], the experimental setup was similar to the setup described in Chapter 4. The difference was that the beam spot size was focuced to about 50μm and the dimensions of the detector active area were 50μm x 50μm. The major disadvantage of the system was that the collected infrared radiation was focused to a spot size much larger (~70μm) than the detector active area. This not only led to a significant loss of signal but also made the detector size the limiting factor of the observed image area. When a detector with an active area of 1mm x 1mm was used, there was no signal loss, but a broader image was seen. This broadening, due to the detection size, is explored by using the new high-resolution experimental configuration for photothermal radiometric microscopy.

The radial temperature field (amplitude and phase) of a homogeneous mild steel in transmission, at constant frequency, for both the old (50μm detector, paraboloidal mirrors) and new (50μm detector, reflecting objectives) experimental setups, is shown in Figure 8.7. As expected, the field measured with the new experimental setup is narrower compared to that measured with the old experimental design. The theoretically calculated homogeneous field of a mild steel is in good agreement with the new experimental field.

The experiment was repeated in backpropagation using the high resolution experimental setup (Figure 8.8) and again the agreement between theory and experiment is obvious. This is an important achievement for TSDT since the method uses the theoretical calculation of the homogeneous temperature distribution. A small degree of broadening still exists at the edges of the radial scan. In a 0.5mm scan this broadening is greatly diminished. The limiting factor for the resolution of this microscope is the laser-beam size (w=27μm).

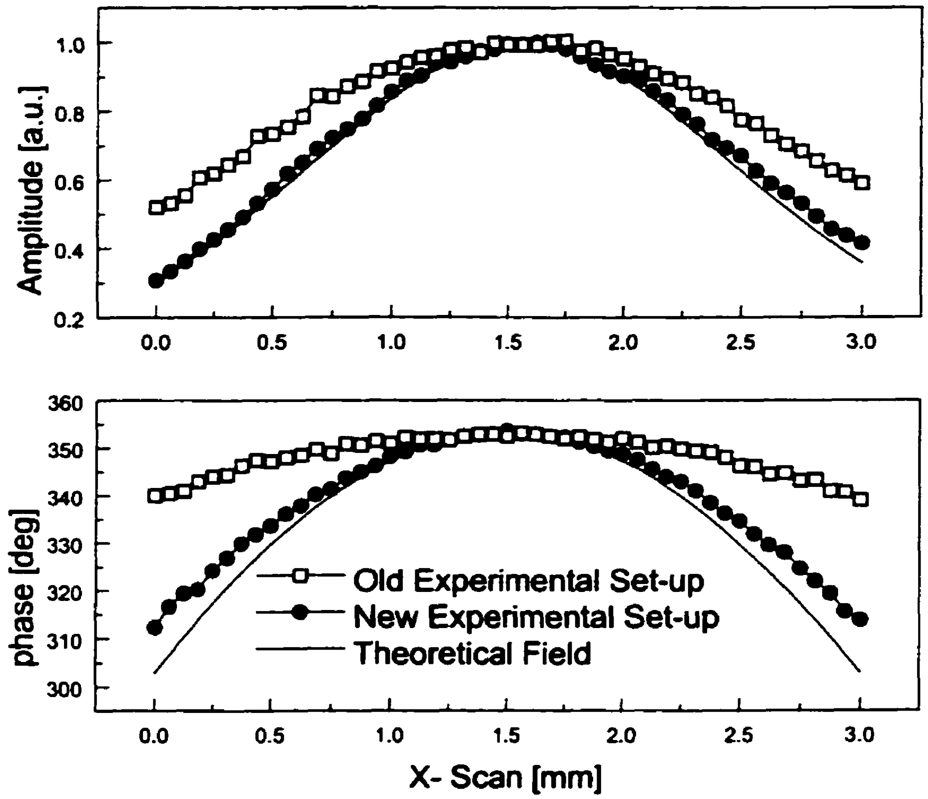

Figure 8.7 Transmission of homogeneous mild steel: theory (solid); old experimental setup (square); new experimental setup (circle).

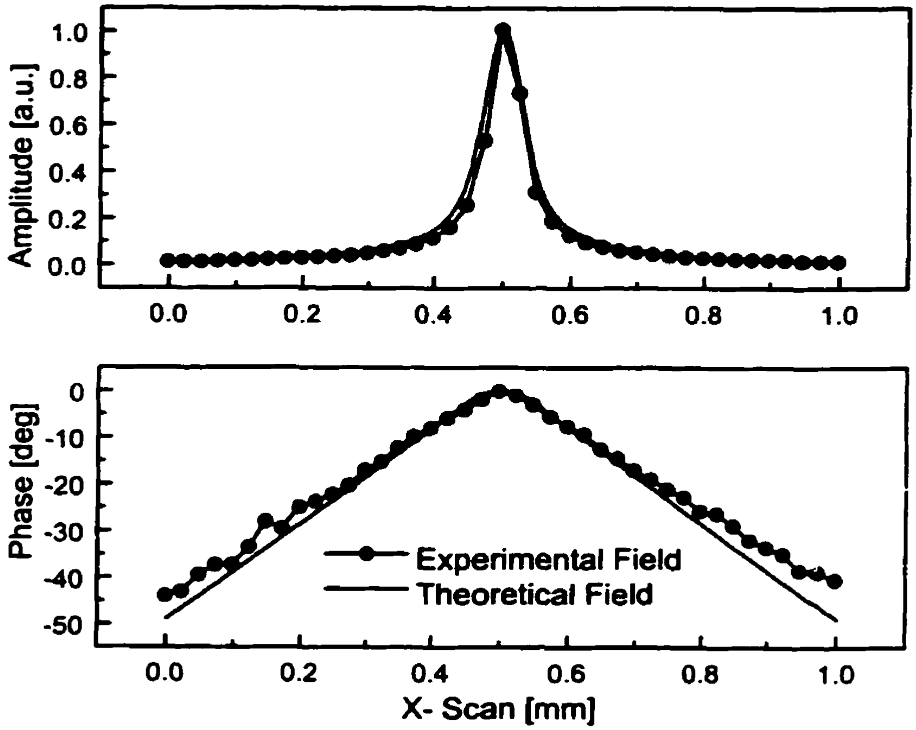

Figure 8.8 Backpropagation (reflection) of homogeneous mild steel: theory (solid); new experimental setup (circle)

8.6 Experimental Results

8.6.1 Thermal Wave Imaging

Before tomographic experiments were performed using the high-resolution experimental setup, thermal wave imaging was performed on a sample with an induced crack to test the performance of the radiometric microscope. The material investigation is a sintered reaction bonded Eaton E-process™ Silicon Nitride with an induced cone crack. This is a material that requires a low cost route to achieve commercial applications, thus information is required of the fatigue properties before widespread use materializes [103]. Spherical indenter geometry reproduces the loading that ceramics would have to endure in applications like roller bearings. In this investigation, Hertzian fatigue damage is studied using thermal wave imaging. Hertzian indentation produces a ring/cone crack combination below the indenter. A schematic of Hertzian indentation [104] and the corresponding ring/cone crack is shown on Figure 8.9 with P being the load of the indenter. "Ring" cracks refer to the partial or complete circular cracks around an indent visible on the surface. "Cone" cracks are subsurface extensions from the ring cracks that extend down into the material in a conical manner. The interest here is the subsurface conical crack since it is optically invisible. Figure 8.10 shows an optical image of the indentation with the surface ring crack illustrated with arrows. The specimen was exposed to a load of 2700N (600lbs) for 17000cycles. On the surface of the sample there is a ring contact scar 0.7mm in diameter from inducing the crack. An approximate 90° arc of a ring crack exists to the left of the contact scar.

Figure 8.11 shows thermal wave images of the sample at three modulation frequencies with three different methods of radiometric imaging. The region imaged corresponds to the optical area marked in Figure 8.10. The thermal images are presented in a matrix type order where the three rows correspond to a frequency of 500Hz, 175Hz and 73Hz, respectively and the three columns correspond to three types of imaging methods. Method 1 is the conventional method of moving the sample along the constant detector and laser location. Method 2 is based on mathematically offsetting the quadrature signal to enhance the contrast of the image as compared to the conventional image by:

$$V_{sig} = (Amplitude)\sin(phase - \theta_{offset}). \tag{8.1}$$

The method enhances the contrast of the images. Method 3 is based on separating the laser from the detector at a constant distance in the order of the object size (crack). This increases the contrast between the object and the background.

Varying the frequency determines the penetration depth of the thermal wave. The thermal diffusion length is a measure of the effective depth sampled and indicates that with decreasing frequency an increasing penetration is observed. The thermal response of this region is varied with modulation frequency. At 500Hz with a thermal diffusion length of 96μm the response is deeper than the surface. At 175Hz the thermal diffusion length is 162μm and at 73Hz the thermal diffusion length is 250μm. At 500Hz, Method 1 faintly shows some characteristics of a ring surface crack along y=0.1mm, Method 2 clearly shows a shadow at y=0.05mm, beyond the size of the ring crack which suggests deeper damage into the sample. In Method 3 the separation distance between the detector and the laser is 0.1mm and the ring crack is clearly defined with some subsurface defects at (0.05mm,0.75mm) coordinates. Looking deeper into the sample, at 175Hz Method 1 again shows some faint characteristics of a crack at y=0.1mm. By mathematically offsetting the sample (method 2) the shadow on the ring crack expands at y=0.05mm, which suggests that the defect is deeper into the sample. In Method 3 the damaged area at (0.05mm,0.75mm) coordinates, is more localized and is well-defined. Finally, at 73Hz, Method 1 again shows some faint subsurface damage at y=0.1mm. Method 2 does not show any clear extension of the crack. In Method 3 the shadow at (0.05mm,0.8mm) coordinates, expands further, which indicates that the crack extends as deep as the corresponding thermal diffusion length of 250μm. The conventional method of imaging is not as sensitive as the experimentally offsetting method. Thermal wave imaging provides the information about the existence and approximate depth of the crack (one thermal diffusion length). The depth of the defect can be easily determined by the offsetting imaging method (~250μm). Much of engineering science is concerned with the behavior of materials under stress as their performance under extreme conditions and subsequent failure analysis is essential for the continued development of both material and design criteria. The potential of thermal wave analysis therefore lies in its ability to image subsurface structures or defects in a nondestructive manner.

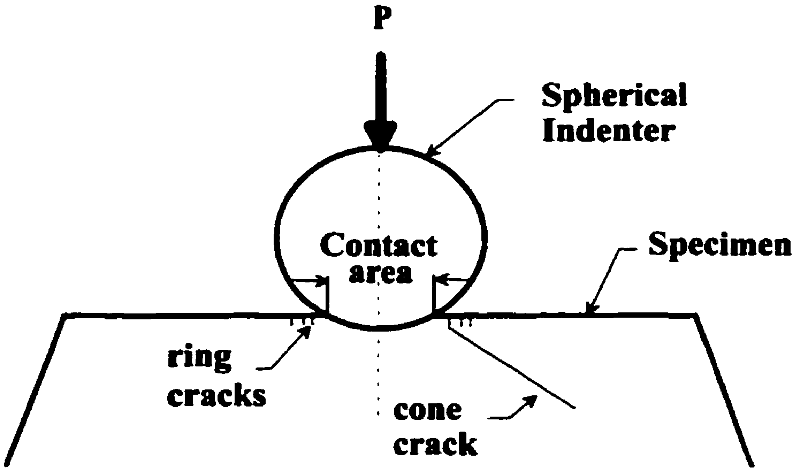

Figure 8.9 Hertizian indentation by spherical indenter with P load.

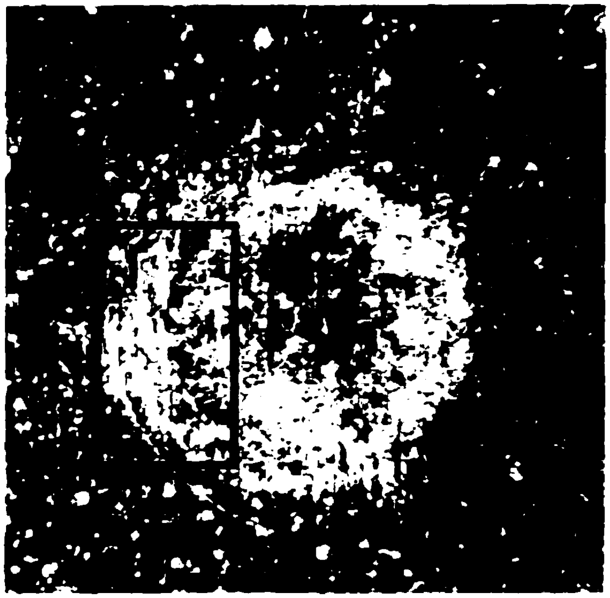

Figure 8.10 Optical image of specimen inflicted by Hertzian crack; magnification X50; ring crack illustrated with arrows. Solid line indicates the approximate area thermally imaged. The optical image provided by D. Rose of US Army TACOM.

8.6.2 Tomographic Experiments

Steel is a good thermal emitter and can be reasonably assumed homogeneous for testing the tomographic method. Two samples of mild steel type alloy with subsurface defects were used for the tomographic experiments. Sample 1 contained a subsurface hole of diameter 0.6mm located 0.1mm below the surface and had a thickness of 2mm. The sample geometry is shown in Figure 8.12, with line AB representing the cross-section scanned for the experiments. The thermal diffusivity of the sample was measured in transmission [79] and was found to be $\alpha=1.1\times10^{-5}m^2/s$. Since the experimental setup in backpropagation was limited by the tomographic range, a second steel sample (similar geometry as Sample 1) was customized to investigate the backpropagation experiments. Sample 2 had two 0.3mm diameter defects, 0.1mm and 0.2mm deep in the material, respectively. The thermal diffusivity of this steel material was measured in transmission [79] and was found to be $\alpha=1.55\times10^{-5}m^2/s$. Before any experiments were run, the linearity [43] of signal obtained from all samples was tested for different modulated laser powers showing that the detected signal is linearly proportional to the surface temperature excursion. For Sample 1 (Figure 8.13), the signal remains linear up to 0.4W laser power output. Therefore, the mild steel samples were safely run at 0.2W output power.

First, Sample 1 was tested in transmission at a modulation frequency of 11Hz with a thermal diffusion length, μ, of 0.56mm. The tomographic scan was taken along cross section AB (Figure 8.12). The defect imaged is 0.1mm from the front surface and 0.6mm in diameter. Figure 8.14 shows a conventional 2-D scan along the imaged line. A 2-D scan is achieved by scanning the laser and the detector together. This provides information about the defect's x-location. Both the amplitude and phase of the scan exhibit a minimum at the defect location. This behavior is due to the fact that the defect (air) is poor thermal conductor and thus the heat propagation is blocked in transmission. In general, the amplitude of the signal is influenced by surface blemishes and reflectance, whereas the phase is largely unaffected and truly represents sub-surface defects. From the 2-D scan data the defect is found to be at the center of the scan (x=1.5mm). Figure 8.15 is the amplitude and phase of the backpropagation tomographic scan with five laser positions along line AB (3mm) at 49 detector points. The five laser positions used were x_f=0.5, 1, 1.5, 2, 2.5mm. From the tomographic scan, the information given from a 2-D scan can also be obtained. In a tomographic scan, the maximum signal always occurs when the laser and detector are aligned with each other, and therefore, the maximum of each laser position scan can map the 2-D scan. This is the diagonal line (x=y) in the experimental data as seen in Figure 8.15 where a minimum is observed for both amplitude and phase equivalent to the 2-D scan.

Before the backpropagation tomographic experiments were performed on Sample 2, 2-D scans at different frequencies (40-1000Hz) were taken for the 0.1mm deep defect. This was performed so that the frequency with the best resolution would be selected for the tomographic scans. Figure 8.16 shows these experiments and the two frequencies chosen for the tomographic scans were 80Hz and 300Hz. In backpropagation a maximum is observed in the amplitude. Since the defect is a poor thermal conductor (air), heat diffusion is blocked by the boundary, which results in a larger amplitude signal. A thermal wave image (top view) was also performed on the sample so that the actual defect location and shape would be found. Figure 8.17 shows all channels (in-phase, quadrature, amplitude and phase) of the signal. This image also illustrates that thermal wave imaging is a 2-D projection of the probing area whereas tomography is a cross-sectional projection. The black line is the exact location where the tomographic scans were performed. The quadrature shows the highest fidelity regarding defect shape.

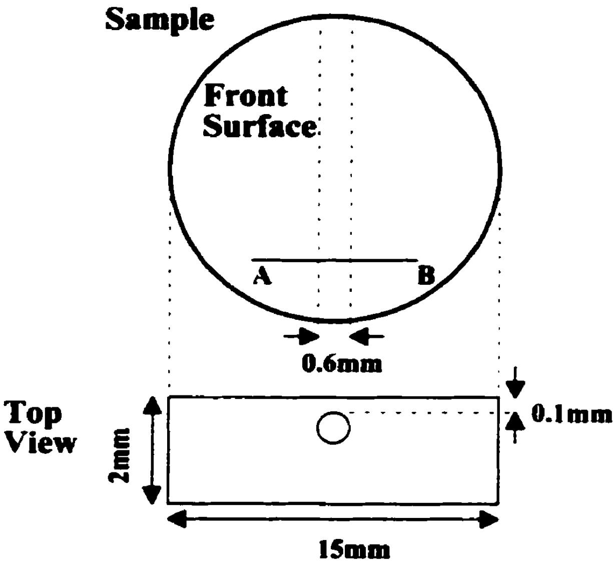

Figure 8.12 Sample 1 and 2 geometry. Dimensions shown for sample 1.

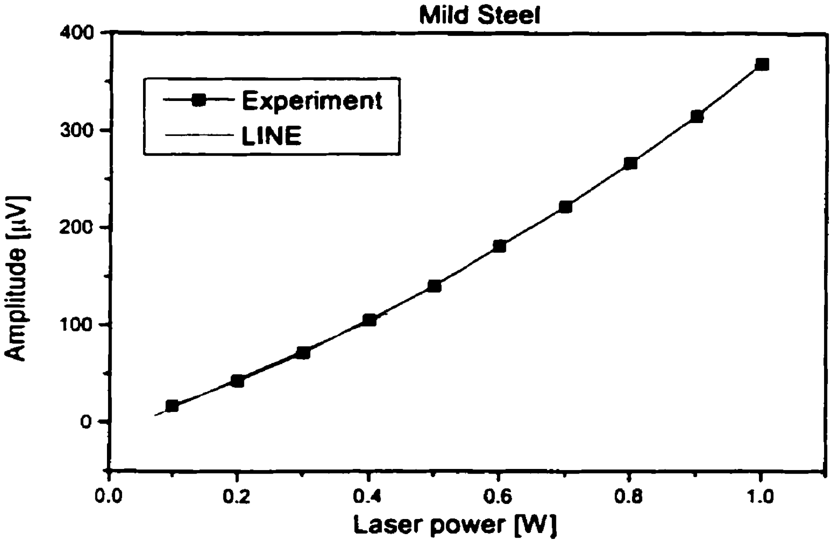

Figure 8.13 Output laser power vs signal amplitude for sample 1 (mild steel).

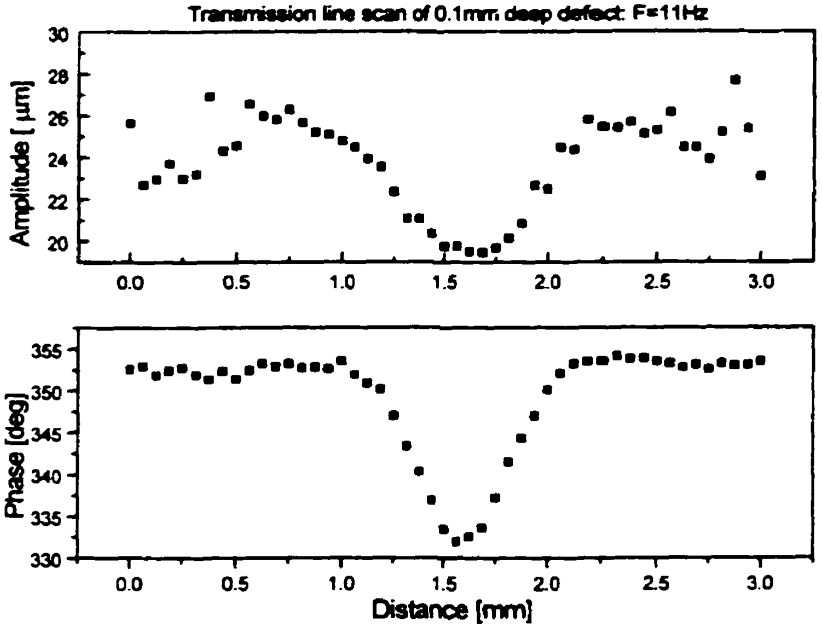

Figure 8.14 Amplitude and phase in transmission of the 2-D line scan.

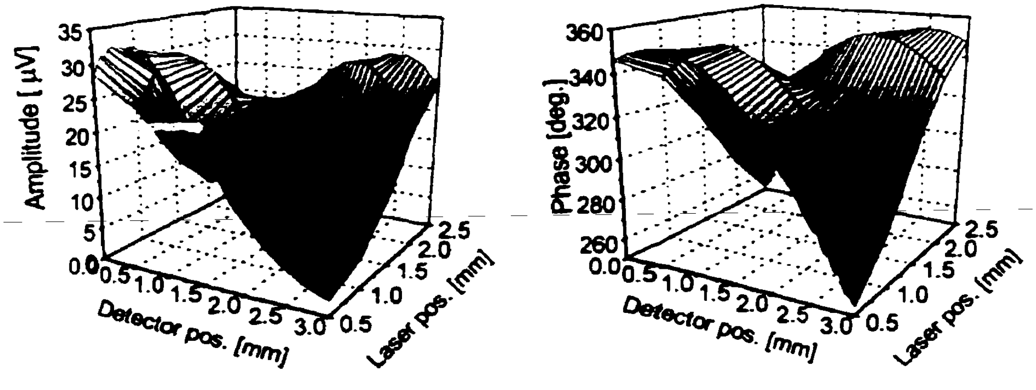

Figure 8.15 Transmission tomographic scan of 0.1mm deep defect. Amplitude and phase.

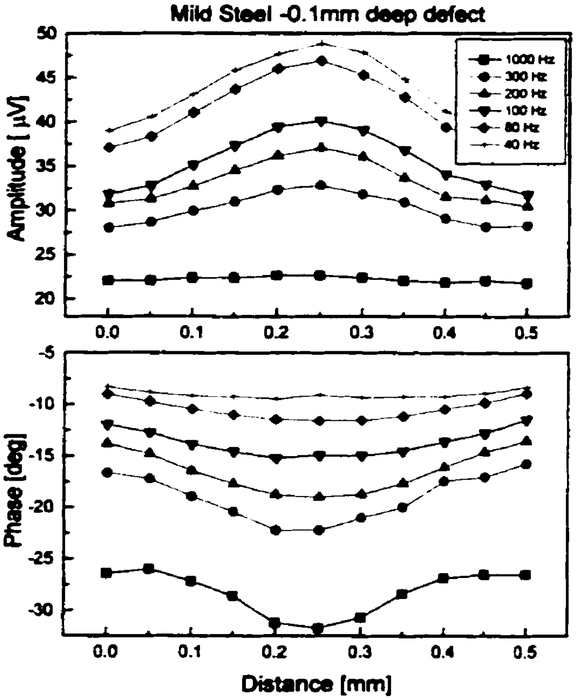

Figure 8.16 Amplitude and phase in backpropagation of the 2-D line scan for 40, 80, 100, 200, 300 and 1000Hz.

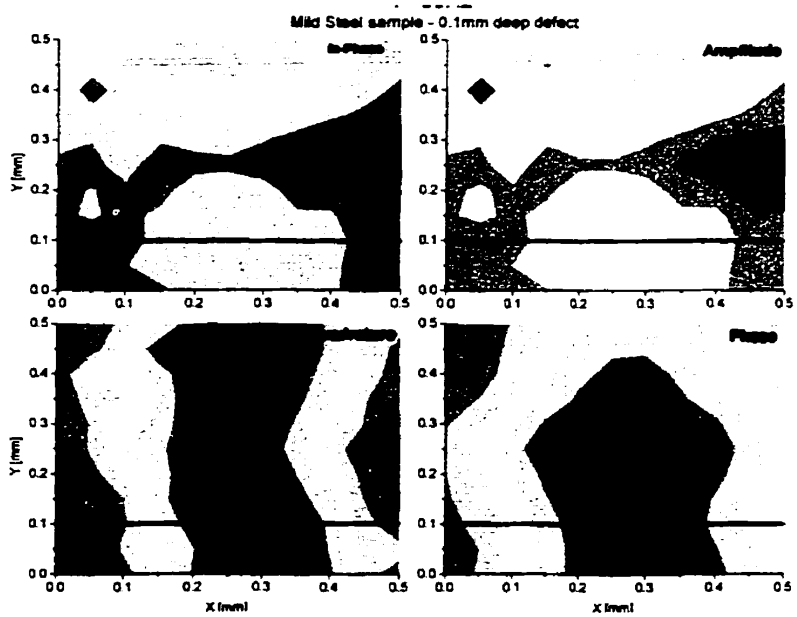

Figure 8.17 Thermal wave image of top view of Sample 2. From left clockwise: in-phase, amplitude, phase and quadrature. The black line is the location of the tomographic scan. F=80Hz.

A backpropagation tomographic scan at a modulation frequency of 80Hz with a thermal diffusion length of 0.25mm was then performed. The defect was 0.1mm deep into the material and the x-location was at the center (x=0.25mm) of 0.5mm scan. Figure 8.18 is the amplitude and phase of the tomographic scan in backpropagation with 11 laser positions, x_f = 0, 0.05, 0.1, 0.15, 0.2, 0.25, 0.3, 0.35, 0.4, 0.45, 0.5mm, and 21 detector positions. Above the tomogram the diagonal, which is equivalent to a 2-D scan, is shown for each signal channel (amplitude and phase). At the same location the tomographic experiments were performed at a frequency of 300Hz. The thermal diffusion length at this frequency is 0.13mm. The length of this scan is 0.3mm since there was no signal for higher scanning distance. Figure 8.19 is the backpropagation tomographic scan for seven laser positions, x_f = 0, 0.05, 0.1, 0.15, 0.2, 0.25mm, and 13 detector positions. The diagonal 2-D scan (x=y) is shown above the channels. This is created by the maximum of each scan (laser position spike).

Figure 8.20 is a backpropagation tomographic scan of a 0.2mm deep defect at a frequency of 80Hz. Both amplitude and phase have a minimum at the location of the defect. The defect is located at the center of the scan and 11 laser positions were collected, x_f = 0, 0.05, 0.1, 0.15, 0.2, 0.25, 0.3, 0.35, 0.4, 0.45, 0.5mm, with 21 detector positions. For the same location the tomographic experiment was repeated at a frequency of 300Hz with a thermal diffusion length of 0.13mm. The length of this scan is 0.3mm since again there was no signal for higher scanning distance. Figure 8.21 is the backpropagation tomographic scan for seven laser positions, x_f = 0, 0.05, 0.1, 0.15, 0.2, 0.25, and 0.3mm, with 13 detector positions.

The homogeneous field was also investigated in these experiments and Figures 8.22 and 8.23 show the field for both frequencies F=80Hz and F=300Hz, respectively. The response is shown on a two-dimensional graph. Each laser position corresponds to a maximum in the experimental data. The theoretical fields are also shown at each laser position and frequency. The agreement between theory (equation 6.41a,b) and experiment is excellent although there is a slight instrumental asymmetry on the right-hand side of the experimental data.

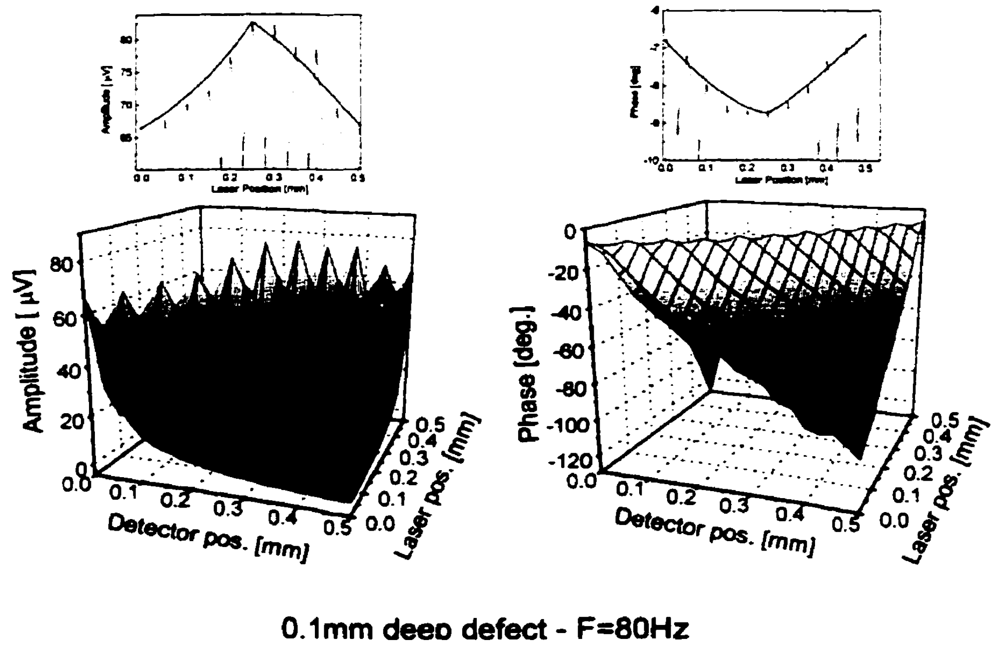

Figure 8.18 Backpropagation tomographic scan of 0.1mm deep defect. F=80Hz.

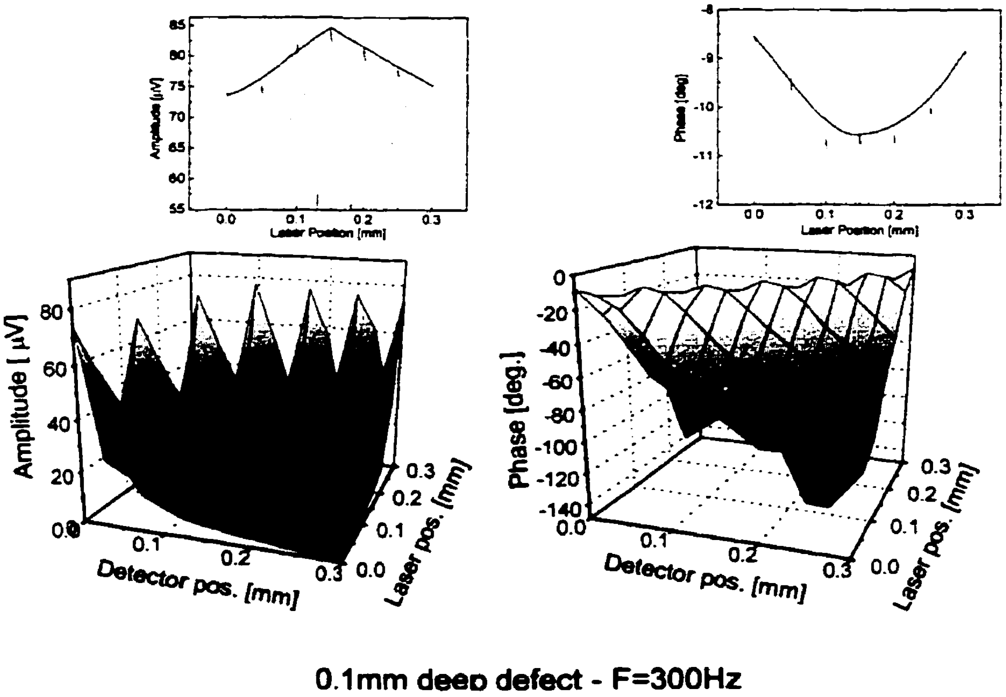

Figure 8.19 Backpropagation tomographic scan of 0.1mm deep defect. F=300Hz.

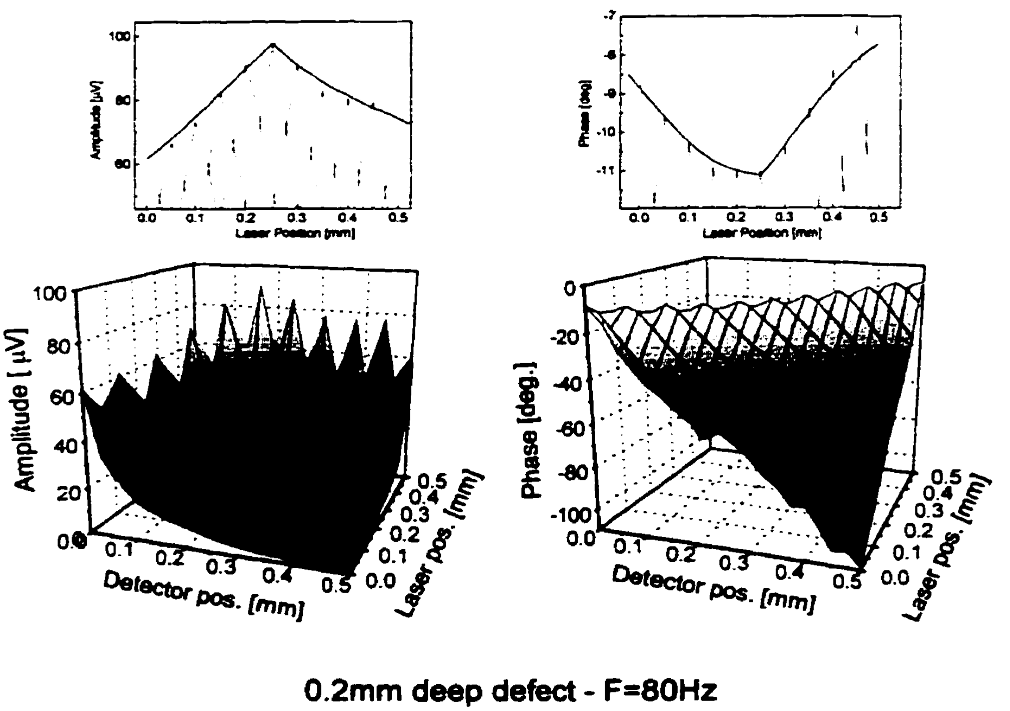

Figure 8.20 Backpropagation tomographic scan of 0.2mm deep defect. F=80Hz.

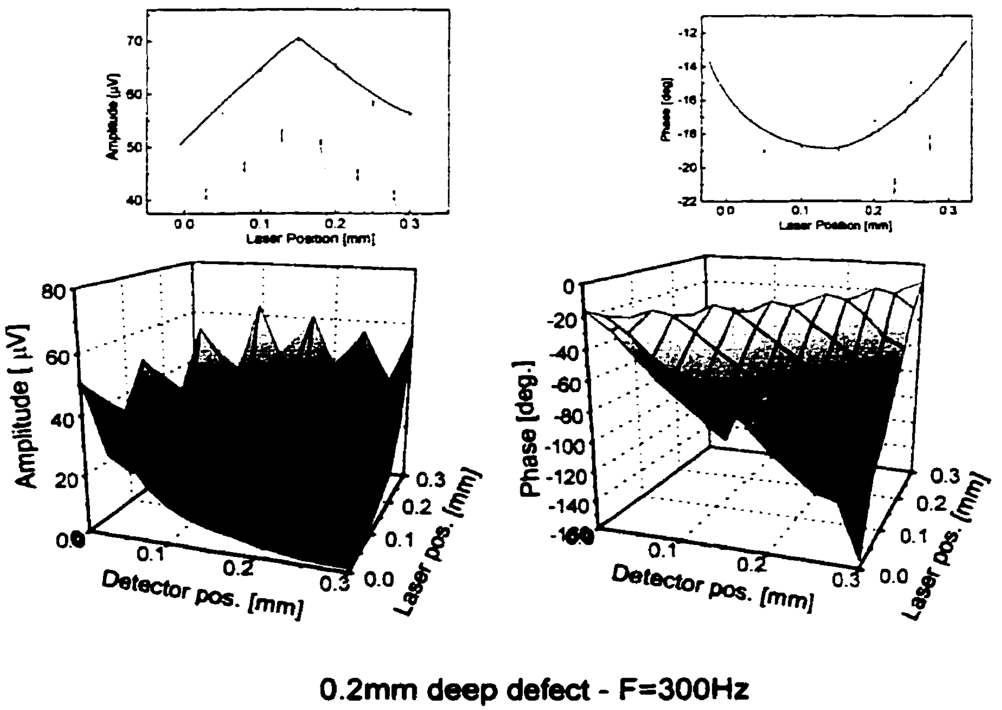

Figure 8.21 Backpropagation tomographic scan of 0.2mm deep defect. F=300Hz.

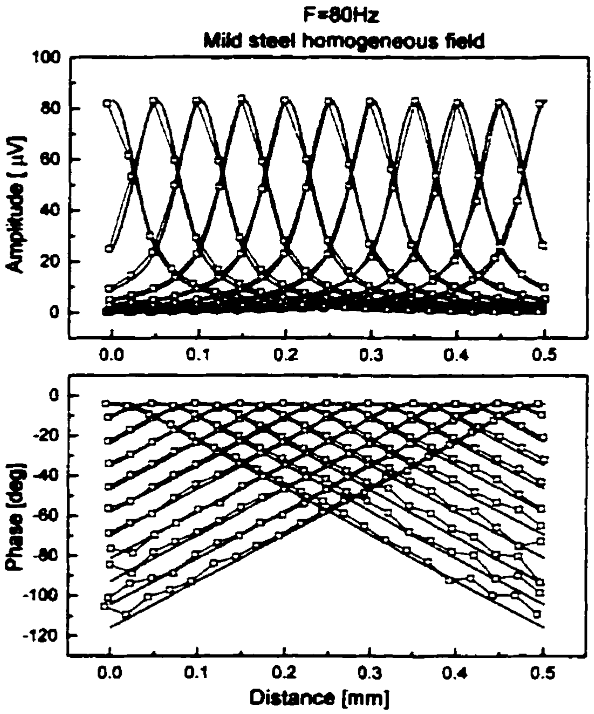

Figure 8.22 Homogeneous field of sample 2 at F=80Hz. Experiment (square); Theory (solid).

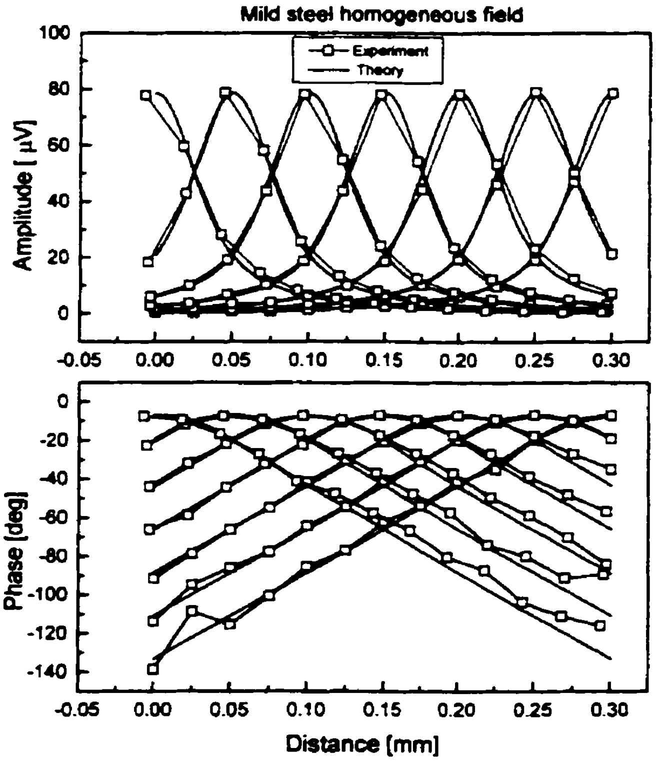

Figure 8.23 Homogeneous field of sample 2 at F=300Hz. Experiment (square); Theory (solid).

Chapter 9

Real Tomographic Inversions and Discussion

9.1 Introduction

In this chapter, real tomographic reconstructions from experimental data obtained in backpropagation and transmission mode presented in Chapter 8, are shown. The reconstructions are produced by the Born approximation, with the methodology developed in Chapters 6 and 7.

In Section 9.2, the reconstruction method used is briefly summarized. In Section 9.3, real tomographic inversions are shown with a discussion. Finally, conclusions and limitations of the method are discussed in Section 9.4.

9.2 Reconstruction Method

In reconstructing an image, only one set of experimental data, represented by one laser position and multiple detector points, is needed. Both amplitude and phase are used to describe the total surface field expressed in equation (7.7). The reconstructions are produced by the Born approximation following the flowchart in Table 7.2, and solving the linear system (7.18) with a regularization parameter. Equations (6.41a) and (6.41b) were used, respectively, for the calculation of the homogeneous backpropagation and transmitted thermal wave fields. The solution of the linear system is the object function, which is a real field with a zero imaginary part [39]. Numerically this value is not zero. An optimal solution to the linear system was obtained using the L-curve method. The object function reconstructed was the non-dimensional function (n^2(r)-1), where n(r) is the square-root ratio of the thermal diffusivity of the background to that of the defect, defined by equation (6.8d). The background thermal diffusivity, α, thermal conductivity, k, modulation frequency, f, and laser beam size, w, are the necessary input parameters for calculating the homogeneous thermal wave field. The input parameters for the inversion technique are as follows:

$$a_{steel1} = 1.1\text{x}10^{-5}\ \text{m}^2/\text{s},\ a_{steel2} = 1.55\text{x}10^{-5}\ \text{m}^2/\text{s},\ k_{steel} = 45\text{x}10^2\ \text{W/mK}$$

$$w = 27\,\mu\text{m}.$$

The expected magnitude of the non-dimensional object function, with a thermal diffusivity for the defect of α_{air}=2.2x10^{-5} m^2/s, is -0.5 and -0.3 for Sample 1 and 2, respectively. Experimentally, the total surface field was measured at 49 (transmission), 21 (backpropagation, F=80Hz) and 13 (backpropagation, F=300Hz) detector positions and the data was then interpolated to the desired number of points for a square matrix, using the cubic splines interpolation technique. Reconstructions for the transmission experiment were computed for n=10, so that the linear system consisted of 100 equations with 100 unknowns; for the backpropagation experiments n=15. The reconstructions were performed using a Pentium II 266 MHz CPU with 128Mb of RAM.

9.3 Tomographic Reconstructions of Steel and Discussion

9.3.1 Tomograms

The first reconstruction performed was that of the transmission experiment (Figure 8.15). Figure 9.1 is the average reconstruction of five laser position reconstructions obtained individually from the experimental data. In a previous work [72], it was found that averaging of reconstruction improves the final image since limited information is obtained through one laser position reconstruction. By averaging reconstructions information from different perspectives is obtained. The individual numerical reconstructions were performed with the laser position at x_l=0.5, 1.0, 1.5, 2 and 2.5mm. The experimental amplitude and phase data of the respective laser positions were used as input parameters for the inversion technique. The experimental data represented the total surface thermal-wave field of the imaged cross-section. The frequency used in this experiment was F=11Hz with a thermal diffusion length of 0.56mm. Figure 9.1 reconstructs the object function $F(x,y)$, with a contour of the reconstruction function at the bottom. The solid line on the contour of Figure 9.1 indicates the exact location and size of the defect, which was 0.6mm in diameter, centered at (x_c=1.5mm, y_c=1.6mm). The defect is shown at the correct x-position but it extends further to the back of the sample. The artifacts of the reconstruction diminish as a wider spectrum of spatial laser positions is used. The magnitude (contrast) of the defect is underestimated. In averaging, information was lost due to the fact that a few reconstructions underestimated the defect magnitude; the use of more laser positions for averaging reconstructions would ensure accuracy of the magnitude of the object function. Also, since detection occurred at the back surface of the sample only limited information is available for reconstructing the defect. The optimal regularization parameter for the reconstruction was retrieved using the L-curve method.

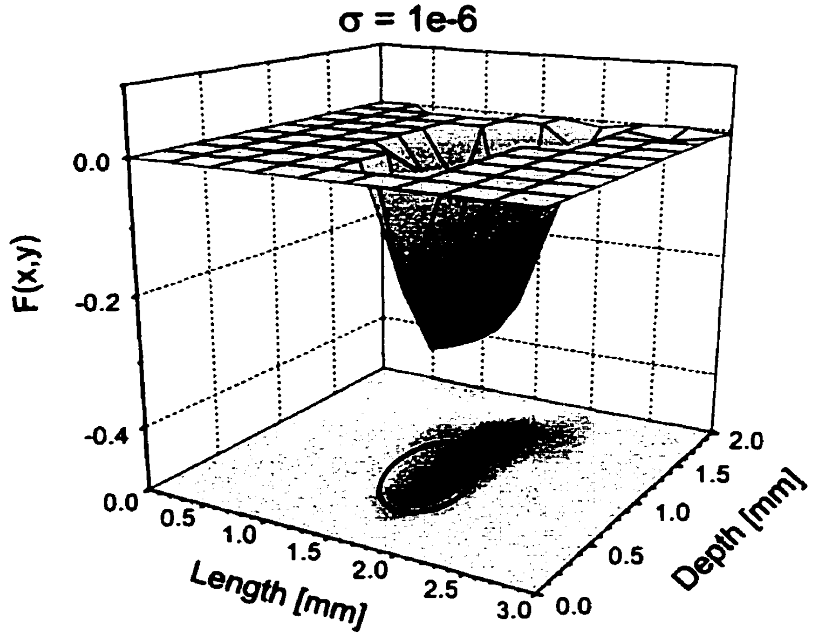

Figure 9.1 TSDT transmission reconstruction of Figure 8.14, average of 5 laser positions. True defect shown by solid line. Average regularization σ~1x10^{-6}.

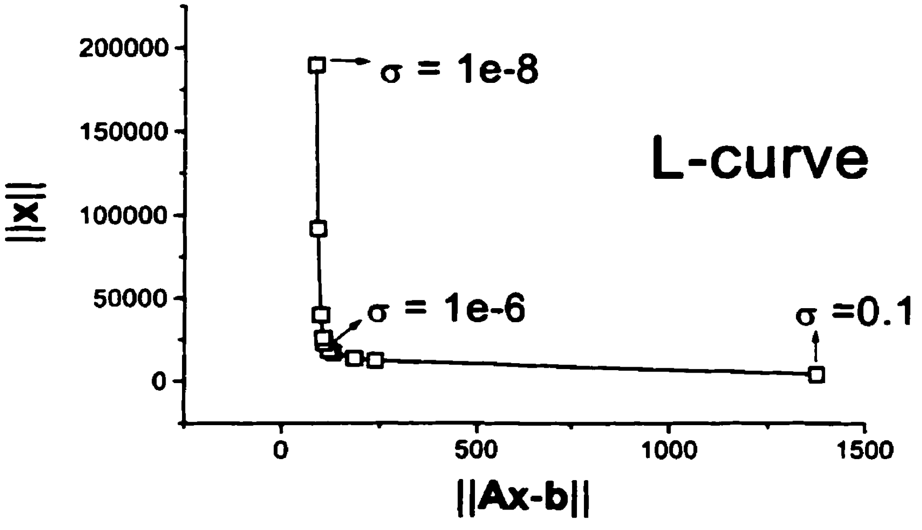

Figure 9.2 L-curve of x=1.5mm laser position reconstruction of Figure 9.1.

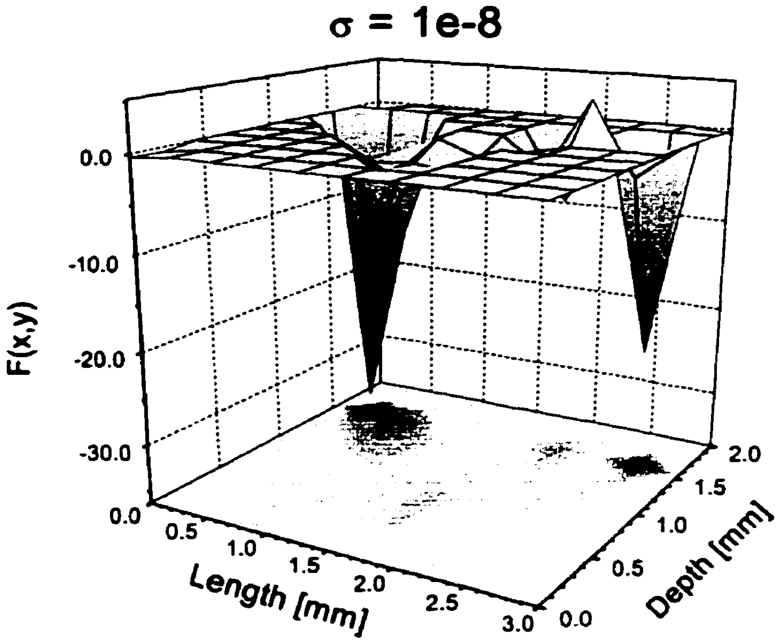

Figure 9.3 Reconstruction from the vertical part of the L-curve (Figure 9.2). Regularization $\sigma=1\times10^{-8}$.

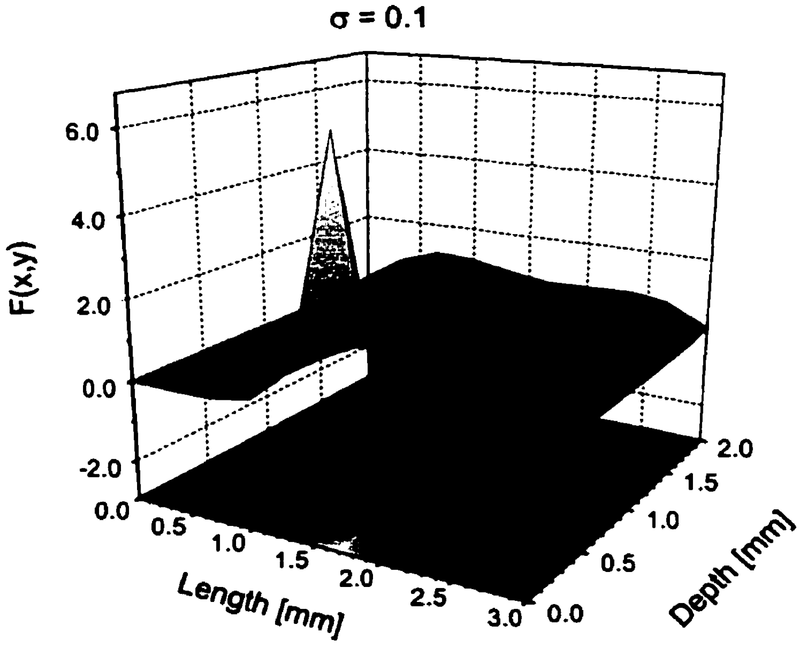

Figure 9.4 Reconstruction from the flat part of the L-curve (Figure 9.2). Regularization $\sigma=0.1$.

For each reconstruction performed at a specific laser position an L-curve was plotted for selecting the optimal solution corresponding to the corner regularization parameter, σ. For one laser position the L-curve is shown in Figure 9.2 and the optimal solution is $\sigma=1\times10^{-6}$. The average reconstruction was created by an average of all the optimal solutions. Figure 9.3 is the result of a reconstruction from the "vertical" part of the L-curve plot. The regularization parameter is $\sigma=1\times10^{-8}$. Perturbation noise dominates such a solution and the location of the defect is distorted. In Figure 9.4 an oversmoothed solution ("flat" part of the L-curve) is shown with the regularization parameter being $\sigma=0.1$. In this reconstruction the defect is overshadowed by the laser position x=1.5mm.

Backpropagation experiments were then performed with defects at two depths (0.1mm, 0.2mm) and at two modulation frequencies (F=80Hz, F=300Hz). These experiments were performed to test the limitations and resolution of the method at different depths. The next reconstruction was of the backpropagation experiment of a 0.1mm deep defect at F=80Hz (Figure 8.18). At this frequency the thermal diffusion length is 0.25mm. The defect was 0.3mm in diameter, centered at (x_c=0.15mm, y_c=0.25mm). Figure 9.5(a) is the average reconstruction of eleven laser positions at x_l=0, 0.05, 0.1, 0.15, 0.2, 0.25, 0.3, 0.35, 0.4, 0.45 and 0.5mm. The regularization parameter used for reconstruction was on the order of 10^{-4}. All subsequent experimental reconstruction in reflections had the same regularization parameter of 10^{-4}. The value of this regularization parameter assigns the transmission (regularity of 10^{-6}) problem as being less ill-defined when compared to the backpropagation one. An ill-defined problem provides a reasonable solution after being regularized. The regularization parameter is directly proportional to the ill-conditioning of the problem. The depth position of the defect is correctly reproduced but the image is smaller than the true defect size shown by the solid line. Also it is observed that the defect is somewhat asymmetric on the right hand side. This can be attributed to the asymmetry of the experimental data obtained by the photothermal microscope. The magnitude of the defect is underestimated at -0.25. Some artifacts exist at the left and back surfaces of the defect. As the number of laser positions increase these artifacts may decrease.

The same defect was reconstructed in backpropagation at F=300Hz with a diffusion length of 0.13mm. The reconstructed image corresponding to the experimental data of Figure 8.19 is shown in Figure 9.5(b). The reconstruction is the average of thirteen laser positions at x_l=0, 0.05, 0.1, 0.15, 0.2, 0.25, and 0.3mm. Although the front of the defect is reconstructed well the back boundary is shifted to the front at about two thermal diffusion lengths (0.26mm). This can be attributed to the fact that, in backpropagation the scatterer to be seen at about twice the diffusion length. Beyond a total distance of two thermal diffusion lengths, information is lost. The reconstruction as compared to Figure 9.5(a) is symmetrical. This is to be expected since for a 0.3mm scan the asymmetry of the instrument is much diminished.

The next reconstruction was the backpropagation experiment (Figure 8.20) of the 0.2mm deep defect with a 0.3mm diameter, centered at (x_c=1.5mm, y_c=0.35mm). The modulation frequency of the experiment was 80Hz, so that the thermal diffusion length was 0.25mm. Figure 9.6(a) is the average of all the reconstructions performed for each laser position. The location of the defect is in agreement with the exact position shown with the solid line. The front surface is precise but the back of the defect is degraded. An asymmetry in the reconstruction is again observed at the right-hand side. This reinforces the fact that this asymmetry is due to instrumental effects. Also at the back of the defect some artifacts are observed. With an increase in the number of laser positions, these artifacts could decrease.

Figure 9.6(b) is the backpropagation reconstruction of the same defect with F=300Hz. The experimental data is shown in Figure 8.21. The diffusion length is 0.13mm. The laser position is closer to the defect and above the edge of the defect. The front surface is reconstructed well whereas the back surface is reconstructed well up to about two thermal diffusion lengths from the front surface. At the front surface there are artifacts that would diminish with an increasing number of laser positions.

9.3.2 Image Error Analysis

In this section, error percentages of the reconstructions of Figures 9.1, 9.5(a), 9.5(b), 9.6(a), and 9.6(b) are calculated. The reconstructions are compared to the true images with respect to location, size and contrast. The true defect, although circular, in the analysis is represented as an ellipse, centered at x_c in the x-direction, and y_c in the y-direction, with a and b as its axes in the x- and y-direction, respectively. The error parameters are calculated below, and the subscripts *calc* and *exact* are used to represent the parameters calculated and their exact values (obtained from the knowledge of sample geometry), respectively. The parameters that will be examined are x_c, y_c, a, b and image contrast. The error is expressed as:

$$\mathrm{ERRp}=\frac{p_{calc}-p_{exact}}{p_{exact}}, \tag{9.1}$$

where p is the error parameter being examined. The calculated and exact values of each image, along with the error percentages, are tabulated. The first error examined is related to the defect location (Table 9.1). The error presented is an absolute value. The x_c-location and y_c-location are analyzed separately to clearly distinguish defect behavior. The second error deals with the defect size (Table 9.2). The shape of a defect is measured at the first contour level below the surface, and is defined at the same contrast in all the figures. This is the level where the defect is clearly formed, and there are no effects from surface anomalies. The error is negative if the size was underestimated, and positive if the size was overestimated. The eccentricity, *e*, of the defect is also calculated. Eccentricity indicates the degree of departure from circularity, and varies between 0 and 1. It is defined as:

$$e = \frac{\sqrt{a^2 - b^2}}{a}, \tag{9.2}$$

where a is the semimajor axis and b is the semiminor axis ($a>b$). When e=0, the ellipse is a circle. As eccentricity increases, the ellipse becomes flatter (depressed b), up to the extreme case, e=1, where the ellipse becomes a line segment. The eccentricity is used since all distortions in the images appear as ellipses. This is due to the fact that in these tomographic scans only one-sided information is obtained at the cross-section. The third error is associated with the defect contrast (Table 9.3). The contrast of a defect is taken as the largest minimum value produced by reconstruction. For an underestimated contrast, the error is negative.

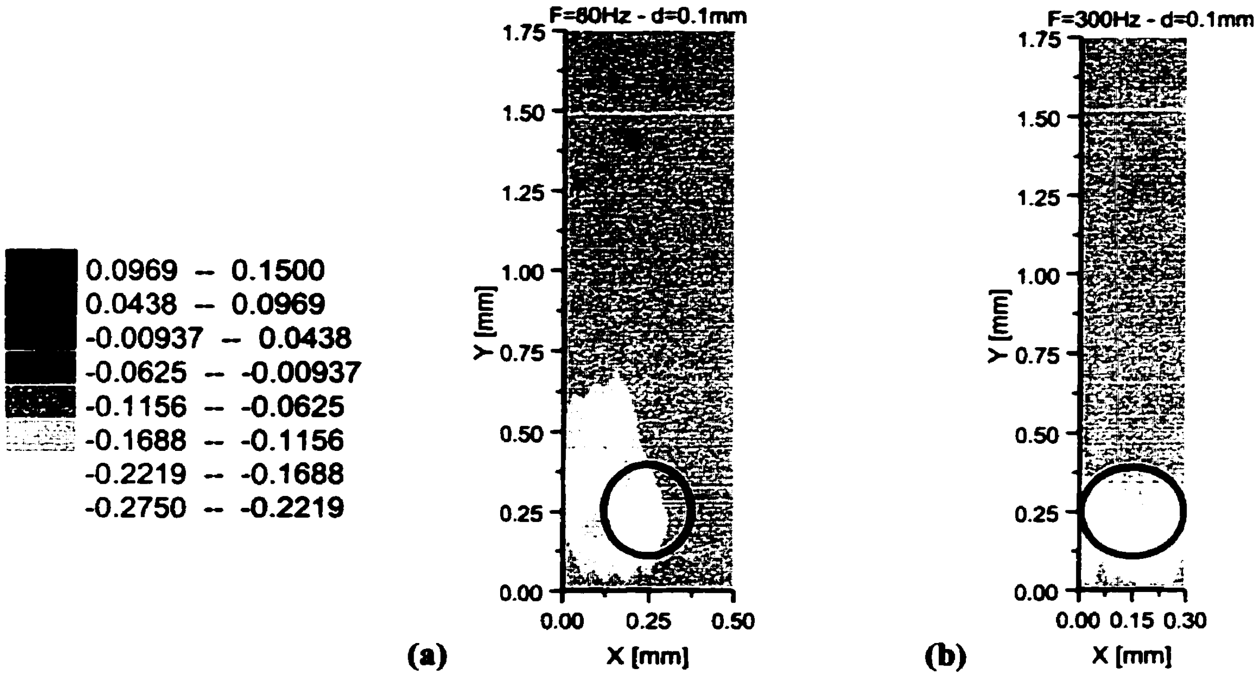

Figure 9.5 Average reconstruction of 0.1mm deep defect with 0.15mm diameter:a) F=80Hz, b) F=300Hz.

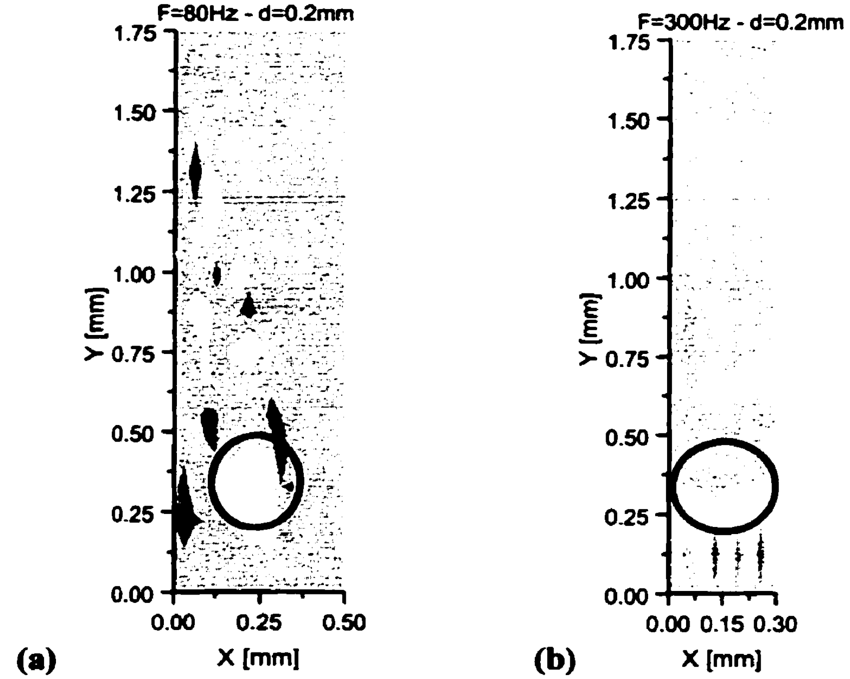

Figure 9.6 Average reconstruction of 0.1mm deep defect with 0.15mm diameter:a) F=80Hz, b) F=300Hz.

Reconstructions		Exact x_{center}	Exact y_{center}	Calculated x_{center}	Calculated y_{center}	Error(+/-) x-center	Error(+/-) y-center
1	Transmission F=11Hz Figure 9.1	1.5mm	0.4mm	1.6mm	0.57mm	6.7%	42.5%
2	Backpropagation F=80Hz Figure 9.5(a)	0.25mm	0.25mm	0.24mm	0.23mm	4%	8%
3	Backpropagation F=300Hz Figure 9.5(b)	0.15mm	0.25mm	0.15mm	0.19mm	0%	24%
4	Backpropagation F=80Hz Figure 9.6(a)	0.25mm	0.35mm	0.22mm	0.32mm	12%	8.6%
5	Backpropagation F=300Hz Figure 9.6(b)	0.15mm	0.35mm	1.5mm	0.26mm	0%	26%

Table 9.1 Errors related to exact defect location.

Reconstructions		Exact *a*-axis	Exact *b*-axis	Calcul. *a*-axis	Calcul. *b*-axis	Error *a*-axis	Error *b*-axis	Eccent *e*
1	Transmission F=11Hz Figure 9.1	0.3mm	0.3mm	0.2mm	0.5mm	-33%	67%	0.92
2	Backpropagation F=80Hz Figure 9.5(a)	0.15mm	0.15mm	0.12mm	0.2mm	-20%	33%	0.80
3	Backpropagation F=300Hz Figure 9.5(b)	0.15mm	0.15mm	0.15mm	0.19mm	0%	27%	0.61
4	Backpropagation F=80Hz Figure 9.6(a)	0.15mm	0.15mm	0.13mm	0.16mm	13%	6.7%	0.58
5	Backpropagation F=300Hz Figure 9.6(b)	0.15mm	0.15mm	0.15mm	0.08mm	0%	-47%	0.85

Table 9.2 Errors related to exact defect size.

Reconstructions		**Exact contrast**	**Calculated contrast**	**Error**
1	Transmission F=11Hz Figure 9.1	-0.5	-0.36	-28%
2	Backpropagation F=80Hz Figure 9.5(a)	-0.3	-0.25	-22%
3	Backpropagation F=300Hz Figure 9.5(b)	-0.3	-0.2	-20%
4	Backpropagation F=80Hz Figure 9.6(a)	-0.3	-0.25	-20%
5	Backpropagation F=300Hz Figure 9.6(b)	-0.3	-0.2	-33%

Table 9.3 Errors related to exact contrast.

The location of the center of the defect in the x-direction is accurate in all the reconstructions (Table 9.1). It is the y-coordinate of the defect center that is inaccurate. In transmission mode, the defect center is farther away than two thermal diffusion lengths measured from the back of the sample and as a result the defect shifts to the back surface, producing a large error. In backpropagation, as the frequency increases the y-center shifts to the front of the surface. As the defect moves closer to the back of the surface, the amount of y-location distortion is reduced, and the calculated value approaches the theoretical value.

The shape of a defect was examined in Table 9.2. In transmission, the image is elongated in the y-direction and depressed in the x-direction. The result is a defect reconstruction with eccentricity of almost 1 (e=0.91). For the 0.1mm deep defect in backpropagation the eccentricity decreases as the frequency is increased. For the 0.2mm deep defect the lower frequency gives a resonable eccentricity (e=0.58) but at the higher frequency the circular shape (e=0.85) is lost.

This is due to the fact that at this frequency the reconstruction is at the shallow depth of the cross-section. The next parameter that was tested was image contrast (Table 9.3). The reconstruction contrast defect is underestimated in both backpropagation and transmission mode. The averaging of more laser positions would reduce such errors. As the frequency is increased the contrast is decreased. Overall, contrast is reproduced well in all reconstructions. Taking into account the location, size and contrast of the defect, the best reconstructions were produced in backpropagation mode at F=80Hz. The most optimal of all is the case of 0.2mm deep defect at F=80Hz.

9.4 TSDT Limitations

In general, most of the error relating defect location was associated with the y-direction depression. This error occurred because the reconstruction information was obtained on a limited plane. Information obtained from a reconstruction depends on the laser position. A defect is delineated accurately on the side closer to the laser position, regardless of which mode of detection is used [72]. The experimental technique for obtaining the surface field is limited to providing information from the front or back of the sample. A tomographic scan along the perimeter of a cross-section would yield more information about the reconstructed cross section.

In conclusion, the Born approximation seems to be adequate for the materials and defect geometries utilized in this investigation. Assuming tubular (cylindrical) defects, such as drilled holes in aluminum, Kak and Slaney [67] have given a mathematical condition for the validity of the first Born approximation for general propagating fields that obey the conventional Helmholtz wave equation. This condition can be expressed as

$$a n_\delta < \frac{\lambda}{4} \tag{9.1}$$

where a is the radius of the cylindrical defect, n_δ is the *change* in the refractive index between the surrounding medium and the defect (equation 6.8d), and λ is the probe field wavelength ($\lambda_{th}=2\pi\mu$). For all the cases examined the criterion was calculated in Table 9.4. In all the cases the criterion was valid. One issue that arises from this table is that the criterion for reconstruction 2 is identical to that for reconstruction 4. With thermal waves this is not true since the depth of the defect is as important as the size. In the future perhaps a better criterion on the thermal wave Born approximation can be formulated.

Reconstructions		$\alpha * n_\delta$	criterion	$\pi\mu/2=\lambda_{th}/4$
1	Transmission 0.1mm deep /F=11Hz Figure 9.1	0.3*0.71= **0.213mm**	<	π*0.56/2= **0.880mm**
2	Backpropagation 0.1mm deep / F=80Hz Figure 9.5(a)	0.15*0.84= **0.126mm**	<	π*0.25/2= **0.393mm**
3	Backpropagation 0.1mm deep /F=300Hz Figure 9.5(b)	0.15*0.84= **0.126mm**	<	π*0.13/2= **0.204mm**
4	Backpropagation 0.2mm deep / F=80Hz Figure 9.6(a)	0.15*0.84= **0.126mm**	<	π*0.25/2= **0.393mm**
5	Backpropagation 0.2mm deep /F=300Hz Figure 9.6(b)	0.15*0.84= **0.126mm**	<	π*0.13/2= **0.204mm**

Table 9.4 Born approximation validity.

Based on these observations, a "guide" can be formulated for optimal reconstructions. Backpropagation reconstructions can better resolve defects close to the surface. The probing frequency and thus thermal diffusion length must be chosen with care. Large defects compared to the thermal diffusion length do not reconstruct as well as when the defect diameter is one thermal diffusion length. If the depth of the defect is deeper than the thermal diffusion length the defect will not be resolved depth wise. Therefore, for an optimum reconstruction the depth and size of the defect must be of the same order of one thermal diffusion length. This is consistent with the fact that in the cases examined the optimal reconstruction was that of a 0.2mm deep defect at F=80Hz.

9.5 Conclusions

In the previous work [72] the experimental field measured was broader than the theoretical field resulting in broader reconstructions. A major achievement of this work is that the broadening of images has been reduced. The L-curve method of finding an optimal reconstruction proved to be an effective tool for TSDT. The only limiting factor for the reconstructions is the validity of the Born approximation. It was found that for the geometries used in this work, the Born approximation yields a large number of satisfactory results. A tomographic scan along the perimeter of a cross-section would yield more information. Reconstructing a cross-section at different frequencies may prove effective for future superposition of images. The thermal diffusion length is a measure of the depth to which a cross-section can be imaged. A marked deterioration of images is observed as modulation frequency is increased beyond two thermal diffusion lengths as compared to the defect depth. The image restoration is lost with increasing depth and decreasing frequency. Optimal reconstructions can be obtained in backpropagation when the defect depth and size are of the order of one thermal diffusion length.

In the future, TSDT reconstructions can be performed for subsurface cracks like the one investigated in Section 8.6.1. This would give information, at certain cross-sections about the exact curvature, direction and depth of the crack.

Chapter 10

Conclusions and Recommendations

10.1 Overview of Depth Profilometry

Depth profilometry is an inverse problem that reconstructs thermal diffusivity profiles in a non-destructive way. The theoretical treatment of this problem approximates the thermal wave as a thermal harmonic oscillator (THO), and follows the Hamilton-Jacobi formalism [40] from classical mechanics. The theory satisfies all limiting cases of the problem geometry. From the theory, an inverse problem is developed which discretely solves for local thermal diffusivity as a function of depth. The profilometric nature of the problem arises from the fact that the depth is inversely proportional to the square-root of the modulating frequency. Experimentally, the problem requires one-dimensionality, and, therefore, a large incident beam is used so that lateral diffusion can be neglected.

Thermal wave depth profilometry finds substantial applications in surface treatment processes such as case hardening. Numerous photothermal researchers all over the world are currently seeking a solution to the depth profilometric problem. While many approaches to thermal diffusivity depth profiling have been introduced over the years, no study has rigorously examined the exact mechanism of thermal diffusivity. In the European community there is a consortium of groups attempting different methods to solve the problem. They have found a linear anti-correlation between microhardness and thermal diffusivity. It is however, the feeling of the author that although this may be true for the specific process of quenching, a simplified linear anti-correlation cannot be used as a universal formula for all heating process and steels. In this thesis, a low carbon steel (AISI 8620) was subjected to the carburizing, followed by quenching, which are two widely used industrial case hardening processes. While an anti-correlation between hardness and thermal diffusivity profiles was observed, several new observations were made. First, it was found that at greater depths, thermal diffusivity reconstructions showed a deviation from microhardness profiles, which became more substantial with increasing depth. The deviation was also more noticeable for quenched steels as compared to plain carburized steels. Therefore, the simplified linear anti-correlation noted in earlier studies [46] cannot be used for all cases. Second, the general shape of the thermal diffusivity profile was similar for both carburizing and quenching, which suggests that the shape of the profile is dominated by carbon diffusion. Third, it was observed that the martensite structure formed by quenching has a lower thermal diffusivity than the pearlite structure formed by carburizing. This suggests that the absolute magnitude of the thermal diffusivity profile is defined by the microstructure.

Futhermore, radiometric signals are influenced by surface roughness throughout the frequency spectrum. A novel method to account for surface roughness was developed, which is based on modeling roughness as a white Gaussian noise fitted to the effective frequency-domain roughness spectrum. This development is significant because it enables more efficient on-line non-destructive testing. The current methods for characterizing microhardness are destructive and time-consuming.

10.2 Overview of TSDT

An existing Thermal-wave Slice Diffraction Tomography (TSDT) technique for the detection of subsurface defects was improved. The existing method solves the Helmholtz pseudowave equation with a complex was number [66] for the temperature field generated in a material by an intensity-modulated laser beam incident on the surface. The pseudo-propagating temperature field is then expressed as the sum of the incident and scattered fields. The three-dimensional Green function and incident field are calculated by assuming Neumann boundary conditions [67]. The scattered field is expressed as a summation, over all individual point scatterers, represented by the Green function. Ultimately, the scattered field is expressed by a Fredholm integral equation of the first kind. Owing to the diffusive nature of the thermal wave field and the ill-conditioning of the inverse problem, conventional Fourier transform methods used in electromagnetic and acoustic tomography cannot be used [42]. Thus, the integral equation is solved using the Tikhonov regularization method.

In this thesis, a robust computational method for TSDT was developed. Most importantly, the L-curve method was used to resolve the difficulty of multiplicity of solutions, thereby obtaining an optimal solution to the inverse problem. Furthermore, a new tomographic high-resolution photothermal microscope, limited by the beam spot size (w=27μm), was constructed for the scans. Machined defects were made on mild steel samples to test the performance of TSDT. Scanned thermal wave data for one point source and multiple detection points were used as input to reconstruct a cross-sectional thermal diffusivity image. A final reconstruction was made by averaging over reconstructions of several source positions. It was concluded that when the defect depth and size were of the order of one thermal diffusion length, optimal reconstructions were obtained.

Photothermal radiometric detection microscopy is used as a method of collecting cross-sectional data, which are then numerically processed with the use of Tikhonov regularization to produce a tomogram. The implications of this work, besides establishing a reliable experimental foundation of TSDT, are quite broad in that it has the potential to address several other fields of tomographic science where strong dispersive attenuation presents a reconstruction problem. These fields include medical diffuse photon tomography, attenuated acoustical imaging, and geophysical tomography. There are other aspects that require further research in order to make TSDT a practical diffraction tomographic technique. Developments are presently being pursued to improve both the computational and experimental methodologies.

10.3 Overall Conclusions

Thermal wave inverse problems are ill-posed problems in that they either have no solution, no unique solution, or an unstable solution. It is only due to recent technological advances that these problems have become tractable computationally. The main difficulty with these problems is that a regularization method is needed to isolate a unique solution. Two important inverse problems were studied in this work: depth profilometry of hardened steels and tomography of subsurface defects. Tomography is a three-dimensional problem with a complicated theoretical/computational formulation but a relatively easy experimental formulation, whereas depth profilometry is a one-dimensional problem whose experimental replication is quite challenging.

In conclusion, the potential of thermal wave analysis lies in its ability of retrieving subsurface thermal inhomogeneities in a nondestructive manner. Both depth profilometry and diffraction tomography have their own unique advantages, and consequently, an immense potential for applicability to the metals industry. Depth profilometry can be used in the heat-treating industry as a replacement to microhardness testing. Depths in the μm-mm region can be observed for retrieving thermal diffusivity. The accuracy of the method decreases with increasing depth since experimentally the signal-to-noise ratio is low for low frequencies. The methodology can be used to identify changes that take place in a material as a result of surface modification processes such as: laser processing, case hardening and coating deposition. TSDT is also non-destructive, and finds practical applications for retrieving defects in the μm-mm region in backpropagation. One specific application can be in the automotive industry where roller bearings produce subsurface damage (cracks) in ceramics. Due to its high-resolution nature, TSDT can be used to accurately resolve defects of the order of the experimental beam spot size (27 μm in this work).

10.4 Future Work

10.4.1 Depth Profilometry

The current study has successfully studied the microhardness behaviour of rough low carbon steels subjected to carburizing and quenching. To produce an industrial-level instrument the work must be extended in the following ways:

(i) The heating process of carbonitriding must be investigated on AISI 8620 steel.

(ii) More steels under the categories of low, medium and high carbon steels must be studied; specifically, grades such as 10xx, 33xx, 86xx could be looked at.

(iii) These specific steels must undergo processes like carburizing, quenching and carbonitriding.

(iv) Comparison of all these steels must be made so that a global conclusion can be reached about the relationship between thermal diffusivity and microhardness. Care must be taken not to make any presumptions about the bulk thermal diffusivity. Therefore, the samples must be cross-sectioned and examined with a forward measurement so as to ensure uniqueness of the inversion results with respect to bulk values.

(v) In the numerical domain, the exact model developed by Miller et al. [58] can be tested to reconstruct real experimental data.

(vi) The signal acquisition speed can be increased by chirp modulation and Fast Fourier Transform analysis [105]. This will make the method more suitable for industrial applications.

10.4.2 TSDT

The current study has successfully obtained a tomographic process for the three-dimensional thermal wave field with sub-surface defects. This work can be extended in the following ways:

(i) The boundaries of the potential of TSDT can be further defined by studying classes of materials with widely different sub-surface structures and thermal transport properties.

(ii) Other methods besides the Tikhonov regularization method must be investigated for solving the ill-condition thermal wave problem. The wavelet based method developed by Miller et al. [73] can be tested with real experimental data.

(iii) The experimental time can be reduced by introducing an array detector.

(iv) An experimental method can be developed to obtain tomographic scans from all perspectives of the sample.

References

[1] A.G. Bell, "Upon the Production of Sound by Radiant Energy", Phil. Mag. **11**, 510 (1881).

[2] A. Rosencwaig and A. Gersho, "Theory of the Photoacoustic Effect with Solids", J. Appl. Phys. **47**, 64 (1976).

[3] A. Rosencwaig, Photoacoustics and Photoacoustic Spectroscopy, (Wiley and Sons, N. Y 1980).

[4] L.J. Inglehart, "Optical Beam Deflection of Thermal Waves in Opaque Solids", Ph.D. Thesis (1984).

[5] H.S. Carslaw and J.C. Jaeger, Conduction of Heat in Solids. (Oxford,Clarendon Press), 2nd edn.,(1959).

[6] S.G. Burnay, T.L. Williams, and C. H. Jones, eds.. Applications of Thermal Imaging. (Adam Hilger, Bistol and Philadelphia), pp. 226-228 (1988).

[7] F. A. McDonald, "Photoacoustic Effect and the Physics of Waves", Am. J. Phys. **48**, 41 (1980).

[8] M. Bertolotti, G. L. Liakhou, R. Li Voti, S. Paoloni and C. Sibillia, "Thermal Wave Reflection and Refraction: Theoretical and Experimental Evidence", J. Appl. Phys. **85**(7), 3540 (1999).

[9] C. A. Bennett, Jr., and R. R. Patty, "Thermal Wave Interferometry: A potential Application of the Photoacoustic Effect", Appl. Opt., **21**(1), 49 (1982).

[10] J. Shen and A. Mandelis, "Thermal-Wave Resonator Cavity", Rev. Sci. Instrum., **66**(10), 4999 (1995).

[11] A. Mandelis, Green Functions and Mathematical Methods of Diffusion-Wave Fields, Springer-Verlag (in press).

[12] R.L Thomas, L.D. Fauro, and P.K. Kuo, "Thermal Wave Imaging for Non-Destructive Evaluation", Can. J. Phys. **64**, 1234 (1986).

[13] Y.H. Wong, R.L. Thomas, and G.F. Hawkins, "Surface and Sub-Surface Structure of Solids by Laser Photoacoustic Spectroscopy", Appl. Phys. Lett. **32**,538 (1978).

[14] Y.H. Wong, R.L. Thomas, and J.J. Pouch, "Sub-surface Structures of Solids by Scanning Photoacoustic Microscopy", Appl. Phys. Lett. **35**, 368 (1979).

[15] M. Munidasa and A. Mandelis in, Principles and Perspectives of Photothermal and Photoacoustic Phenomena, (A. Mandelis, ed., Elsevier Science Publishing Co. Inc., New York), 300-358 (1992).

[16] G. Busse, "Optoacoustic Phase Angle Measurement for Probing a Metal", Appl. Phys. Lett. **35**, 759 (1979).

[17] R.L. Thomas, J.J. Pouch, Y.L. Wong, L.D. Favro, P.K. Kuo, and A. Rosencwaig, "Sub-surface Flow Detection in Metals by Photoacoustic Microscopy", J. Appl. Phys. **51**, 1152 (1980).

[18] L.C. Aamodt and J.C. Murphy, "Effect of Three-Dimensional Heat Flow Near Edges in Photothermal Measurements", Appl. Opt. **21**, 116 (1982).

[19] G. Busse and A. Ograbeck, "Optoacoustic Images", J. Appl. Phys. **51**, 3576 (1980).

[20] P.K. Kuo, L.D. Favro, L.J. Inglehart, and R.L. Thomas, "Photoacoustic Phase Signatures of Closed Cracks", J. Appl. Phys. **53**, 1258 (1982).

[21] M. Luukkala and A. Penttinen, "Photoacoustic Microscope", Electron. Lett. **15**, 325 (1979).

[22] P.K. Kuo and L.D. Favro, "A Simplified Approach to Computations of Photoacoustic Signals in Gas-Filled Cells", Appl. Phys. Lett. **40**, 1012 (1982).

[23] W. Jackson and N.M. Amer, "Piezoelectric Photoacoustic Detection: Theory and Experiment", J. Appl. Phys. **51**, 3343 (1980).

[24] G. Busse, "Imaging with the Optoacousitc Effect", Optics and Laser Technology, **12**, 149 (1980).

[25] G. Busse and A. Rosencwaig, "Subsurface Imaging with Photoacoustics", Appl. Phys. Lett. **36**, 815 (1980).

[26] E. Brandis, A. Rosencwaig, "Thermal Wave Microscopy with Electron Beams", Appl. Phys. Lett. **37**, 98 (1980).

[27] H. Coufal, "Photothermal Spectroscopy using Pyroelectric Thin-Film Detector", Appl. Phys. Lett., 44(1), **59** (1984).

[28] H. Coufal and A. Mandelis, "Photopyroelectric Sensors for Photothermal Analysis of Condensed Phases" Ferroelectrics **118**, 379 (1991).

[29] T. Baumann, F. Dacol, and R.L. Melcher, "Transmission Thermal Wave Microscopy with Pyroelectric Detection", Appl. Phys. Lett. **43**, 71 (1983).

[30] A.C. Boccara, D. Fournier and J. Badoz, "Thermo-optical Spectroscopy: Detection by the Mirage Effect", Appl. Phys. Lett. **36**, 130 (1980).

[31] L.C. Aamodt and J.C. Murphy, "Photothermal Measurements Using a Localized Excitation Source", J. Appl. Phys. **52**, 4903 (1981).

[32] P. E. Nortal and S.O. Kanstad, Physics Scripta **20**, 659 (1979).

[33] G. Busse, "Optoacoustic and Photothermal Material Inspection Techniques", Appl. Opt. **21**, 107 (1982).

[34] M.V. Luukkala, "Photoacoustic Microscopy at Low Modulation Frequencies", in <u>Scanned Image Microscopy</u>, E.Ash ed. (Academic Press, N.Y.),273(1980).

[35] G. Busse and K.F. Renk, "Stereoscopic Depth Analysis by Thermal Wave Transmission for Non-Destructive Evaluation", Appl. Phys. Lett. **42**, 366 (1983).

[36] A. Mandelis, F. Funak and M. Munidasa, "Generalized Methodology for Thermal Diffusivity Depth Profile Reconstruction in Semi-Infinite and Finitely Thick Inhomogeneous Solids", J. Appl. Phys. **80** (10), 5570 (1996).

[37] J. Jaarinen and M. Luukkala, "Numerical Analysis of Thermal Waves in Stratified Media for Non-Destructive testing Purposes", J. Phys. (Paris) **44**, C6-503 (1983).

[38] H. J. Vidberg, J. Jarrinen and D. O. Riska, "Inverse Determination of the Thermal-Conductivity Profile in Steel from the Thermal-Wave Surface Data", Can. J. Phys. **64**, 1178 (1986).

[39] A. Mandelis, S. B. Peralta and J. Thoen, "Photoacoustic Frequency-Domain Depth Profiling of Continuously Inhomogeneous Condensed Phases: Theory and Simulations for the Inverse Problem", J. Appl. Phys. **70** , 1761 (1991).

[40] A. Mandelis, "Hamilton-Jacobi Formulation and Quantum Theory of Thermal Wave Propagation in the Solid State", J. Math. Phys. **26**, 2676 (1985).

[41] A. Mandelis, E. Schoubs, S.B. Peralta and J. Thoen, "Quantitative Phototacoustic Depth Profilometry of Magnetic Field-Induced Thermal Diffusivity Inhomogeneity in the Liquid Crystal Octylcyanobiphenyl", J. Appl. Phys. **70**, 1771 (1991).

[42] T. C. Ma, M. Munidasa and A. Mandelis, "Photoacoustic Frequency-Domain Depth Profilometry or Surface-layer Inhomogeneities: Application to Laser Processed Steels", J. Appl. Phys. **71**, 6029 (1992).

[43] M. Munidasa, T.C. Ma, A. Mandelis, S.K. Brown and L. Mannik, "Non-Destructive Depth Profiling of Laser-Processed Zr-2.5Nb Alloy by IR Photothermal Radiometry", Mater. Sci. Eng. **A159**, 111 (1992).

[44] C. Glorieux, J. Fivez and J. Thoen, "Photoacoustic Investigation of the Thermal Properties of Layered Materials: Calculation of the Forward Signal and Numerical Inversion Procedure", J. Appl. Phys. **73**, 684 (1993).

[45] J. Fivez and J. Thoen, "Thermal Waves in Materials with Linearly Inhomogeneous Thermal Conductivity", J. Appl. Phys. **75**, 7696 (1994).

[46] T. T. N. Lan, U. Seidel and H.G. Walther, "Theory of Microstructural Depth Profiling by Photothermal Measurements", J. Appl. Phys. **77**(9), 4739 (1995).

[47] T. T. N. Lan, U. Seidel, H. G. Walther, G. Goch and B. Schmitz, "Experimental Results of Photothermal Microstructural Depth Profiling", J. Appl. Phys. **78**, 4108 (1995).

[48] J. Fivez and J. Thoen, "Thermal Waves in Materials with Inhomogeneous Thermal Conductivity", J. Appl. Phys. **79**, 2225 (1996).

[49] J. F. Power and M. C. Prystay, "Expectation Minimum (EM): A New Principle for the Solution of Ill-Posed Problems in Photothermal Science", Appl. Spectr. **49**(6), 709 (1995).

[50] J. F. Power and M. C. Prystay, "Nondestructive Optical Depth Profiling in Thin Films through Robust Inversion of the Laser Photopyroelectric Effect Impulse Response", Appl. Spectr. **49**(6), 725 (1995).

[51] C. Glorieux and J. Thoen, "Thermal Depth Profile Reconstruction by Neural Network Recognition of the Photothermal Frequency Spectrum", J. Appl. Phys. **80**, 6510 (1996).

[52] F. Funak, A. Mandelis and M. Munidasa, "Photothermal Frequency-Domain Depth Profilometry of a Discrete Inhomogeneous Surface Layer on Homogeneous Substrate", J. Phys.(Paris) IV, Colloque C7, vol. **4**, 95 (1994).

[53] V. V. Aleshin and V. A. Vysloukh, "Continued Fraction Method in Inverse Problem of Photothermal Diagnostics", Appl. Phys. A **64**, 579 (1997).

[54] R. Kolarov and T. Velinov, "Real-time Depth Profile Reconstruction of the Thermal Conductivity of Inhomogenous Solids", J. Appl. Phys. **83** (4),1878 (1998).

[55] R. Li Voti, M. Bertolotti and C. Sibilia, "Thermal Conductivity and Diffusivity Depth Profiles by Photothermal Technique: The Direct Inverse Problem", in X. Maldague editor, III International Workshop - Advances in Signal Processing for NDE of Materials, Vol. 3 of Topics in Non-Destructive Evaluation Series, ASNT, 379 (1998).

[56] M. H. Xu, J. C. Cheng and S. Y. Zhang, "Reconstruction Theory of Thermal Conductivity Depth Profiles by the Modulated Photoreflectance Technique", J. Appl. Phys., **84**(2), 675 (1998).

[57] M. Munidasa, F. Funak and A. Mandelis, "Application of Generalized Methodology for Quantitative Thermal Diffusivity Depth Profile Reconstruction in Manufactured Inhomogeneous Steel-Based Materials", J. Appl. Phys. **83** (5) 3495(1998).

[58] H. G. Walther and V. Aleshin, "Inspection of Inhomogeneous Samples by Combined Laterally Scanned and Frequency Resolved Photothermal Measurements", J. Appl. Phys. **86** (11), 6512 (1999).

[59] E. Miller, I. Yavuz, L. Nicolaides and A. Mandelis, "A Basis Adaptive, Inverse Scattering Aprroach to Photothermal Depth Profilometry", Circ. and Sing. Process. (special issue: July 2000).

[60] G. Busse, "Thermal Wave Non-Desrtuctive Depth Profiling with Stereoscopic Photothermal Detection", J. Phys. **44**, 471 (1983).

[61] D. Fournier, F. Lepoutre and A.C. Boccara, "Tomographic Approach for Photothermal Imaging using the Mirage Effect", J. Phys. **44**, 479 (1983).

[62] A. Mandelis and M. Mieszkowski, "Thermal Wave Sub-Surface Defect Imaging and Tomography Apparatus", U.S. Patent Number 4, 950, 897; Date: August 21, 1990.

[63] M. Munidasa and A. Mandelis, "Photopyroelectric Thermal-Wave Tomography of Aluminum with Ray-Optic Reconstruction", J. Opt. Soc. Am. **A 8**, 1851 (1991).

[64] M. Munidasa, A. Mandelis, and C. Ferguson, "Resolution of Photothermal Tomographic Imaging of Sub-surface defects in Metals with Ray-Optic Reconstruction", Appl. Phys. **54**, 244 (1992).

[65] A. Yarai, K. Sakamoto, and T. Nakanishi, "High Signal-to Noise Ratio and High Resolution Detection Techniques for Photopyroelectric Thermal Wave Imaging Reconstruction", Jpn. J. Appl. Phys., **33**, 3255 (1994).

[66] A. Mandelis, "Theory of Photothermal Wave Diffraction Tomography via Spatial Laplace Spectral Decomposition", J. Phys. A: Math. General **24**,2485 (1991).

[67] A.C. Kak and M. Slaney, Principles of Computerized Tomographic Imaging, (IEEE Press, New York, 1988).

[68] O. Pade and A. Mandelis, "Thermal-Wave Slice Tomography using Wave-Field Reconstruction", Inverse Problems, **10**, 185 (1994).

[69] O. Pade and A. Mandelis, "Computational Thermal-Wave Slice Tomography with Backpropagation and Transmission Reconstructions", Rev. Sci. Instrum. **64**, 3548 (1993).

[70] L. Nicolaides and A. Mandelis, "Image-Enhanced Thermal-Wave Slice Diffraction Tomography with Numerically Simulated Reconstructions", Inverse Problems **13**, 1393 (1997).

[71] A. Mandelis, "Green's Functions in Thermal Wave Physics: Cartesian Coordinate Representations", J. Appl. Phys.,**78** (2), (1995).

[72] L. Nicolaides, M. Munidasa and A. Mandelis, "Thermal-Wave Infrared Radiometric Slice Diffraction Tomography with Back-Scattering and Transmission Reconstructions: Experimental", Inverse Problems **13**, 1413 (1997).

[73] E. L. Miller, L. Nicolaides and A. Mandelis, "Nonlinear Inverse Scattering Methods for Thermal-Wave Slice Tomography: A Wavelet Domain Approach", J. Opt. Soc. Am. A, **15**(6), 1545 (1998).

[74] B. A. Findlayson, The Method of Weighted Residuals and Variational Principles, (Academic, New York, 1972), chap. 7.

[75] W.H.Press, S.A. Teukolsky, W.T. Vetterling and B.P. Flannery, Numerical recipes in C, 2nd ed. (Cambridge Univ. Press, Cambridge, p.398 (1992).

[76] D. Vergne and G. Busse, "Remote Inspection of Coatings with Thermal Wave Radiometry", Infrared Phys. **29**, 839 (1989).

[77] EG&G Judson Optoelectronics, Infrared Detectors, (1993).

[78] ASR850 DSP Lock-in Amplifier Operating Manual and Programing Reference, Stanford Research Sytems Inc., (1992).

[79] L. Qian and P. Li, "Photothermal radiometry measurement of thermal diffusivity", Appl. Opt., **29** (28), 4241 (1990).

[80] Y. S. Touloukian, R.W. Powell, C. Y. Ho and M. C. Nicolaou, Thermophysical properties of matter, Vol. 10 (Plenum, N.Y 1973).

[81] C. Hudson, Structure and Metals, (Flarepath Printers Ltd., Great Britain), Chap. 4 (1973).

[82] B. K. Bein, S. Krueger and J. Pelzl, "Photoacoustic measurement of effective thermal properties of rough and porous limiter graphite", Can. J. Phys., **64**, 1208 (1985).

[83] W. Kiepert, B. K. Bein, J. H. Gu, J. Pelzl and H. G. Walther, "Roughness Effects on Transient Surface Heating and Thermal Properties, Simulated by Finite Element Solutions of the Diffusion Equation", in Progress in Natural Science Suppl. Vol. ***6*** (S.-Y. Zhang, Ed., Taylor & Francis, Beijing), p. S-317 (1996).

[84] A. C. Boccara and D. Fournier, "Thermal wave investigation of transport properties I", in Photoacoustic and Thermal Wave Phenomena in Semiconductors, ed. A. Mandelis (Elsevier, New York), p. 308 (1987).

[85] P. M. Morse and H. Feshbach, Methods of Theoretical Physics, (McGraw-Hill, N.Y, 1953) Ch.7.

[86] K.J. Langenberg, Applied Inverse Problems, (Notes on Summer School on "Applied Inverse Problems", Fachgebiet Theoretische Elektrotechnik der Gesamthochschule, Kassel, GHK-TET, Kassel 1986) Ch.3.

[87] M. Abramowitz and A. Stegun, Handbook of Mathematical Functions, 9th ed. (National Bureau of Standards, Washington DC, 1970).

[88] C. Hansen, T.Sekii, and H. Shibahashi, "The Modified Truncated SVD Method for Regularization in General Form", SIAM J. Sci. Stat. Comput. **13**, No.5, 1142 (1992).

[89] V.A. Morozov, Regularization Methods for ill-Posed Problems, (CRC Press Inc.,Florida,1993).

[90] E. Kreyszig, Advanced Engineering Mathematics, 7th ed.,(J. Wiley & Sons Inc., N.Y.,1993) Ch. 18.

[91] Y. Jaluria, Computer Methods for Engineering, (Allyn and Bacon, Inc., Massachusetts, 1988).

[92] A. Tarantola, Inverse Problem Theory, (Elsevier Science Publishers, B.V., 1987).

[93] A.N. Tikhonov, "On Stability Of Inverse Problems", Dokl. Acad. Nauuk USSR, **39**(5), 195 (1943).

[94] J. Hadamard, Lectures on the Cauchy Problem in Linear Partial Differential Equations, Yale University Press, New Haven (1923).

[95] H. Schafer and E. Sternin, "Inverse Ill-posed Problems in Experimental Data Analysis in Physics", Phys. in Can.,March/April,77 (1997).

[96] C. Hansen, "Analysis of Disrete Ill-Posed Problems by Means of the L-Curve", SIAM Review, **34**, No.4, 561 (1992).

[97] B. Hofmann, Regularization for Applied and Ill-Posed Problems, (Teubner, Leipzig, 1986).

[98] B.T. Smith, J.M. Boyle, J.J. Dongara, B.S. Garbow, Y. Ikebe, V.C. Klema, and C.B. Moler, Matrix Eigensystem Routines-EISPACK Guide, 2nd ed., Lecture notes in Computer Science, Vol.6 (Spinger, N.Y., 1976).

[99] C. Hansen, "Numerical Tools for Analysis and Solution of Fredholm Integral Equations of the first Kind", Inv. Prob.,**8**, 849 (1992).

[100] C. Hansen and D. P. O'Leary, "The use of the L-curve in the regularization of discrete ill-posed problems", SIAM J. Sci. Comput., **14** (6), 1487 (1993).

[101] W. Press, S. Teukolsky, W. Vettering and B. Flannery, <u>Numerical Recipes in Fortran</u>, 2nd ed., (Cambridge University Press, 1992).

[102] S.J. Sheard and M. Somekh, "Semiconductor Assessment using Photothermal Radiometry", Infrared Phys., **28**, 287 (1988).

[103] J. R. Barla, D. N. Rose, J. E. Benci, J. P. Elder and H. Lin, "Contact Fatigue Behavior and Gas Cell Thermal Wave NDE of Sintered Reaction Bonded Silicon Nitride, Cer. Eng. and Sc. Proc. **17**(3), 255 (1996).

[104] S. Widjaja, K. Jakus and J. Ritter, "Hertzian indentation damage in alumina with R-curve behavior", Cer. Eng. and Sc. Proc., **16** (4), 579 (1995).

[105] A. Mandelis, "Time-Delay-Domain and Pseudo-Random Noise Photoacoustic and Photothermal Wave Spectroscopies. A review of the State-of-the-Art", IEEE Trans. Sonics Ultrasonics, **UFFC-33**, 590 (1986).

Appendix A

UNTREATED CROSS-SECTION

x300

100 μm

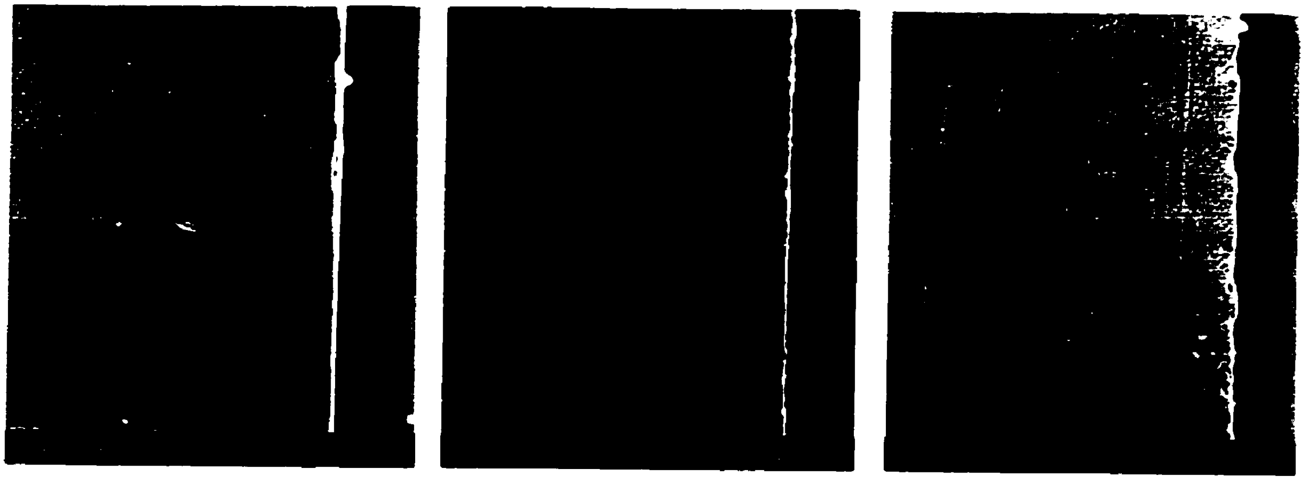

Sample 31 Sample 33 Sample 32

x1500

20 μm

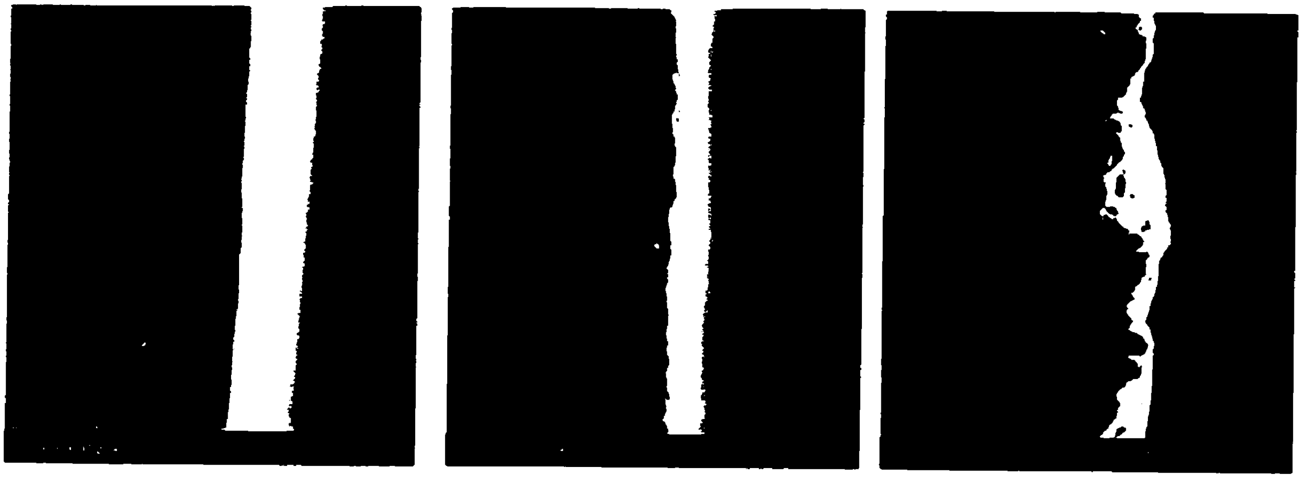

Sample 31 Sample 33 Sample 32